CHEMICAL LOOPING FOR SELECTIVE OXIDATIONS

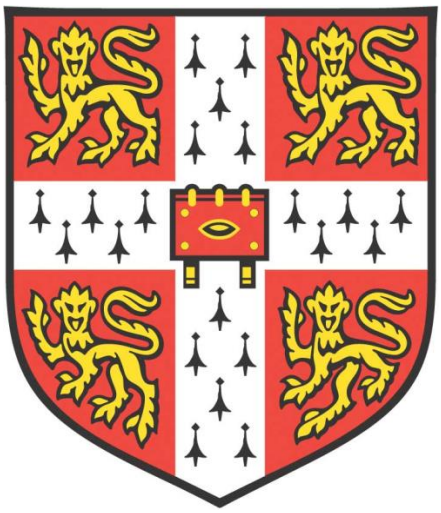

Martin Siu Chun Chan

Trinity College

Department of Chemical Engineering and Biotechnology

University of Cambridge

This dissertation is submitted for the degree of Doctor of Philosophy

August 2018

To Ewa, without whom this definitely maybe would have turned out a bit differently.

DECLARATION

This Dissertation is the result of my own work and includes nothing which is the outcome of work done in collaboration except where specifically indicated in the text. It has not been previously submitted, in part or whole, to any university or institution for any degree, diploma, or other qualification.

In accordance with the Department of Engineering guidelines, this thesis does not exceed 65,000 words, and contains less than 150 figures.

Signed:_____

Date:_____

Martin Siu Chun Chan

Department of Chemical Engineering and Biotechnology

University of Cambridge

CHEMICAL LOOPING FOR SELECTIVE OXIDATIONS

ABSTRACT

This Dissertation describes the development of chemical looping for selective oxidations. Chemical looping is a reactor technology that achieves simultaneous reaction and separation. For a large subset of reactions (*viz.* abstraction or insertion of oxygen), this technology is based upon the use of oxygen carriers. These materials, typically metal oxides, reversibly store and release oxygen, and there is growing interest in using these materials for selective oxidations. This Dissertation describes work on the development of oxygen carriers for selective oxidations, including foundational work on a method for analysing periodic non-catalytic gas-solid reactions, of which chemical looping selective oxidations are a subset.

The oxygen chemical potential of $Ca_2Fe_2O_5$ was exploited to improve the efficiency of the steam-iron process to produce hydrogen. The ability of reduced $Ca_2Fe_2O_5$ to convert a higher fraction of steam to hydrogen than chemically unmodified Fe was demonstrated in a packed bed. This demonstrates how the oxygen chemical potential might be manipulated and exploited for chemical looping reactions. The oxygen chemical potential determines the selectivity in thermodynamically-controlled selective oxidations, and, depending on the reaction mechanism, kinetically-controlled selective oxidations.

A generic method for enhancing the oxygen-carrying capacity of oxygen carriers for use in selective oxidations is presented, where one material that is selective in the reaction is deposited on the surface of a second material acting as a reservoir of oxygen and as a support. The presence of ceria in the support was found to supply lattice oxygen additional to that provided by the bismuth oxide, without affecting the selectivity of bismuth oxide. The surface chemistry was decoupled from the bulk properties of the support, thus simplifying the design and formulation of composite oxygen carriers.

Building upon the concepts of oxygen chemical potential and composite oxygen carriers, chemical looping epoxidation was demonstrated for the first time. The oxygen carrier was composed of Ag, for its unique catalytic properties, and $SrFeO_3$ as the support, for its high oxygen chemical potential at low temperatures. A reaction mechanism was proposed based on the observations.

Nonlinear frequency response theory was used to analysis a periodic non-catalytic gas-solid reaction. Generalised frequency response functions (which are higher order analogues to traditional, linear transfer functions) were derived to obtain the nonlinear frequency response of the archetypal reactor. Such a method lies between the traditional frequency response theorem and numerical methods in terms of accuracy and speed. A niche application was proposed for the analysis of experimental kinetics, avoiding convolution of measurements with the response time of measuring equipment.

In summary, this Dissertation describes how materials might be formulated for selective oxidations in chemical looping mode. This was demonstrated for an industrially-significant reaction for the production of ethylene. A novel application of nonlinear frequency response theory was also demonstrated for chemical looping reactions.

Martin S.C. Chan

ACKNOWLEDGEMENTS

I thank my supervisor Prof John Dennis for his vision, inspiration, and guidance over the course of my studies, as well as Dr Stuart Scott for his teaching and advice. I also thank Peter Davidson for his mentorship and advice since my undergraduate days. Thanks go to former and current members of the Combustion and Scott groups for sharing their knowledge and expertise, before I knew how to fend for myself: Drs Peng Dai, Felix Donat, Francisco García-García, Robert Grant, Wenting Hu, Ross Hubble, Mohammad Ismail, Cindy Lau, and Wen Liu. Special thanks go to Dr Ewa Marek for the countless discussions, encouragement, and her patience during the most trying times.

Much of this research would not have been possible without the aid given by the support staff. I thank Weiyao Ma, Kevin Swann, John Gannon, Mark Scudder, Sebastien Cosnefroy, Lee Pratt, Andy Hubbard, Gary Chapman, Jon Summerfield, Dr Simon Butler, Peter Claxton, Christopher Bawden, Roz Williams, Zlatko Saracevic, Wayne Skelton-Hough, Chris Amey, Jon Cowper, and Dr Iain Morrison for the endless list of help and assistance. Thanks also go to Tamsin Bell from Laura Torrente's group, Dr Matthew Dunstan and Dr Michael Gaultois from Clare Grey's group, and Dr Gareth Williams from Johnson Matthey.

I wish to thank my colleagues for the pleasure of working with them over the past few years: Herme Baldovi, Zach Bond, Sam Gabra, Belén González, Richard Goerke, Paul Hodgson, Mauro Malizia, Clayton Rabideau, Michael Sargent, Matthias Schnellmann, and Yaoyao Zheng. Tea-time Tiddlywinks is especially acknowledged.

The EPSRC, Trinity College and the IChemE are all acknowledged for their generous funding.

Lastly, I wish to thank my family for their unending and unconditional support, and my friends for their irreplaceable influence on my life.

CONTENTS

1 INTRODUCTION

1.1 Background

The need to reduce the environmental burdens of products and manufacturing, and to develop sustainable processes, has led to an increased call for 'process intensification'. The definition of this concept has evolved over time. A recent definition is 'the development of innovative apparatus and techniques that offer drastic improvements in chemical manufacturing and processing, substantially decreasing equipment volume, energy consumption, or waste formation, and ultimately leading to cheaper, safe, sustainable technologies' (Boodhoo and Harvey, 2013). To this end, interest has been growing in chemical looping technologies because of their inherent ability to perform reaction and separation in a single unit operation. An example is depicted in Figure 1.1 for chemical looping combustion (CLC), where an oxygen carrier, typically a metal oxide (*e.g.* Fe_2O_3), reacts with a fuel to generate CO_2 and H_2O and becomes reduced in the process (*e.g.* to Fe). The reduced oxygen carrier is then conveyed to a second reactor, where it reacts with air to regenerate the lattice oxygen (*e.g.* back to Fe_2O_3), before being recirculated back to react with the fuel again. Similar to membrane reactors, the feed streams are separated. However, this is a spatial separation in membrane reactors, whereas it is temporal in chemical looping reactors (in the frame of reference of the oxygen carrier) (Thursfield *et al.*, 2012). Its most prominent application is currently the chemical looping combustion of carbonaceous fuels. Considerable research has been undertaken on CLC (*e.g.* Dennis and Scott, 2010; Fan *et al*., 2012; Lyngfelt, 2014). The principle relies on the use of an oxygen carrier material (typically a transition metal oxide) and exploiting the relative ease of separating gases from solids rather than separating gaseous mixtures. As

shown in Figure 1.1, the carrier oxidises the fuel in one reactor, becoming reduced in the process. The reduced carrier is then conveyed to a second reactor where it is reoxidised with air, before being returned to the fuel reactor to complete the cycle. This method of combustion has the key advantage of producing a pure stream of CO_2, undiluted with N_2, ready for capture and storage in the Earth, with minimal energy penalty compared to other separation technologies such as amine scrubbing or oxy-fuel combustion (Wolf *et al.*, 2005; Dennis and Scott, 2010). CLC was shown to be more favourable than competing carbon capture technologies in a study that modelled the UK electricity system, even displacing some renewable technologies (Schnellmann *et al.*, 2018). Can chemical looping be as effective for the production of chemicals as it was shown for power generation?

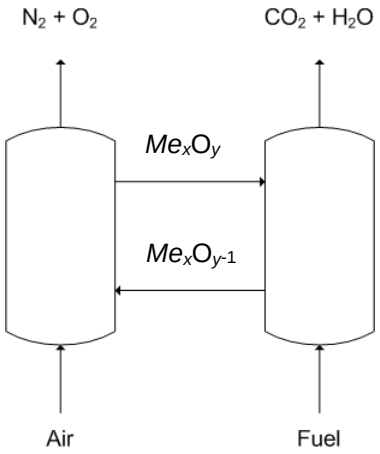

Figure 1.1. Schematic diagram of chemical looping combustion (CLC). Me_xO_y and Me_xO_{y-1} denotes the oxidised and reduced forms of the oxygen carrier, respectively. The use of coupled fluidised beds, circulating the oxygen carrier, allows for steady state operation.

Historical processes based on chemical looping include the steam-iron process for the production of hydrogen (Messerschmitt, 1908), and the Brin process for air separation (Jensen, 2009). Both have been superseded, respectively, by the steam reforming of methane, and by cryogenic air separation or pressure swing adsorption. More recently there was also DuPont's process for the selective oxidation of *n*-butane to maleic anhydride. Despite the complexity of this reaction, involving the transfer of 14 electrons and 7 oxygen atoms on the surface of the catalyst, it remains a rare example of a chemical looping selective oxidation which had been conducted on an industrial scale (Hudgins *et al.*, 2013). The plant operated for a decade before it was shut down and dismantled. Various reasons have been given in the open literature for the closure of the plant, citing

technical problems associated with incomplete reoxidation of the carrier (Yates and Lettieri, 2016), and, or, a rapidly changing market (Lintz and Reitzmann, 2007). The general idea of conveying solid lattice oxygen to a selective oxidation, in the absence of gaseous oxygen, is shown conceptually in Figure 1.2. This is depicted for a circulating fluidised bed reactor (moving solids, fixed gas flows), but this can also be performed in a cyclically operated packed bed reactor (fixed solids, switching gas flows), or even in a rotary reactor (fixed solids, fixed gas flows, moving reactor) (Zhao *et al.*, 2014).

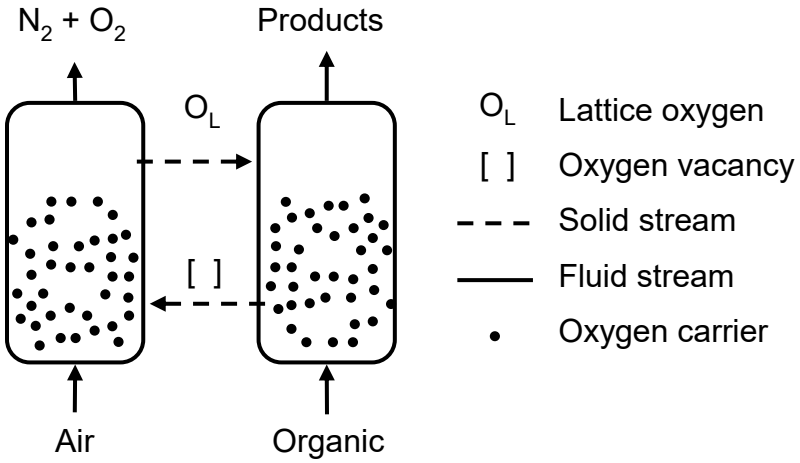

Figure 1.2. Schematic diagram of chemical looping selective oxidation for organic syntheses.

Using chemical looping to supply oxygen has substantial advantages for selective oxidations, owing largely to the complete substitution of gaseous oxygen for lattice oxygen. In conventional oxidation using gaseous oxygen or air, the requirement to operate below the explosion limit requires substantial recycle of reactants and, should there be a lack of mixedness, presents a safety hazard, or, at least, an opportunity for partial oxidation of the feed to unwanted carbon oxides. Using chemical looping to convey the oxygen as lattice oxygen to the reaction would achieve an inherent separation between the air and organic streams, offering the advantages of (i) safety, as the risk of forming explosive mixtures is minimised, (ii) eliminating the need to operate in oxygen-lean conditions, allowing for higher single-pass conversions and decreasing the need for recycling, (iii) potentially improved selectivities (Shekari and Patience, 2010), and (iv) avoiding the need to purify gaseous oxygen or the organic product from diluents such as nitrogen. In the light of these advantages, interest in chemical looping as a technology for the production of chemicals has been gradually increasing (Khadzhiev *et al.*, 2015; Chung

et al., 2016; Elbadawi *et al.*, 2016; Fleischer *et al.*, 2016; Gao *et al.*, 2016; Neal *et al.*, 2016).

Chemical looping reactions involving the transfer of oxygen are largely described by a mechanism in which some species *A* reacts with lattice oxygen, O_L, to form the product *P* and a vacancy [ ], which is then regenerated by gaseous oxygen. This mechanism is commonly referred to as a Mars-van Krevelen mechanism (Mars and van Krevelen, 1954), originally described by Wagner and Hauffe in 1938 (Lintz and Reitzmann, 2007). This is depicted in the following reaction scheme:

$$A_{(g)} + O_L \rightleftharpoons P_{(g)} + [\ ] \tag{1.1}$$

$$\frac{1}{2}O_{2(g)} + [\ ] \rightleftharpoons O_L \tag{1.2}$$

Conventionally, this mechanism is most often used to describe heterogeneous oxidation catalysts (but not all, since some catalysts are non-reducible), when reactions 1.1 and 1.2 occur concurrently, but not necessarily contiguously, on the surface. Chemical looping can be envisaged as separating these two steps temporally, with a timescale spanning a few seconds to tens of minutes. Variations of reactions 1.1 and 1.2 are possible, for example the supply of oxygen might be from steam, so that reaction 1.2 consumes steam to produce hydrogen whilst regenerating O_L (*i.e.* chemical looping production of hydrogen):

$$H_2O_{(g)} + [\ ] \rightleftharpoons O_L + H_{2(g)} \tag{1.3}$$

Another variation is that discrete solid phases, instead of vacancies, might be formed, for example if the oxygen carrier is iron oxide, then reactions 1.1 and 1.2 might be:

$$A_{(g)} + 3Fe_2O_{3(s)} \rightleftharpoons P_{(g)} + 2Fe_3O_{4(s)} \tag{1.4}$$

$$\frac{1}{2}O_{2(g)} + 2Fe_3O_{4(s)} \rightleftharpoons 3Fe_2O_{3(s)} \tag{1.5}$$

The Mars-van Krevelen mechanism enables chemical looping for oxygen abstraction and insertion, because the formation of *P* uses lattice oxygen, rather than gas-phase oxygen. For example, an iron molybdate oxygen carrier was found to be able to selectively oxidise methanol to formaldehyde in the absence of molecular oxygen, releasing 49% of all its solid oxygen at 350°C, or in terms of oxygen carrying capacity, 16 wt% based of the highest oxide (equivalent to 73 monolayers of oxygen atoms, assuming that each

monolayer contained 10^{19} m^{-2} of oxygen atoms) (House *et al.*, 2007). Further examples include the use of vanadium pyrophosphate to produce maleic anhydride from *n*-butane (0.34 wt% at 400°C), and a Mo-V-Sb oxide to produce acrylic acid from propane (0.52 wt% at 400°C) (Godefroy *et al.*, 2010).

The equilibrium constant for the reoxidation of the oxygen carrier, *e.g.* reactions 1.2 and 1.5, is directly related to the partial pressure of oxygen, pO_2, in equilibrium with the material. This partial pressure is a useful quantity in the analysis of chemical looping reactions, being a thermodynamic property of the oxygen carrier material, and is a measure of the chemical potential of oxygen in the material. It provides the driving force for the transfer of oxygen to (or from) the gas phase. A material that exerts a high pO_2 is usually more suited for performing oxidations, generally combustions. Materials with very high pO_2 (≥ 0.1 bar) can be used to release gaseous oxygen, given sufficient kinetics. At the other end of the spectrum, materials with low pO_2 are easier to oxidise (meaning simply that the minimum sufficient partial pressure of oxygen required to oxidise the material is lower), so mild oxidants such as steam and carbon dioxide can be used to produce hydrogen or carbon monoxide (where a lower pO_2 means that the ratio of steam:hydrogen or carbon dioxide:carbon monoxide is lower), provided that the material can be reduced in the first place. Materials with extremely low pO_2 might be effectively inert.

To engineer chemical looping selective oxidations, it is important to understand how selectivity arises in a particular reaction. The main product is usually formed from partial oxidation, whilst the competing side product is usually CO_2 from complete combustion. The side product could also sometimes be solid carbon in the form of coke. The aim, when performing a selective oxidation, is to maximise the production of the main product whilst minimising the production of any side products.

1.1.1 Thermodynamically controlled selective oxidations

For a small subset of reactions, it turns out that the main product is thermodynamically favoured over the side products. In these cases, selectivity can be achieved merely by allowing the reactor to approach equilibrium conditions in the appropriate chemical environment. The selectivity of such reactions is said to be thermodynamically controlled. For example, in the partial oxidation of methane, the main product is syngas (CO and H_2), whereas the competing reaction is combustion:

$$2\mathrm{CH_{4(g)}} + \mathrm{O_{2(g)}} \rightleftharpoons 2\mathrm{CO_{(g)}} + 4\mathrm{H_{2(g)}} \qquad \Delta H°_{298\ \mathrm{K}} = -72\ \mathrm{kJ/mol} \qquad (1.6)$$

$$\frac{1}{2}\mathrm{CH_{4(g)}} + \mathrm{O_{2(g)}} \rightleftharpoons \frac{1}{2}\mathrm{CO_{2(g)}} + \mathrm{H_2O_{(g)}} \qquad \Delta H°_{298\ \mathrm{K}} = -401\ \mathrm{kJ/mol} \qquad (1.7)$$

Writing the equilibrium constants K_p in terms of the partial pressures:

$$K_{\mathrm{p,POM}} = \frac{p\mathrm{CO}^2 p\mathrm{H}_2^4}{p\mathrm{CH}_4^2 p\mathrm{O}_2}\frac{1}{P°^3} \qquad (1.8)$$

$$K_{\mathrm{p,comb}} = \frac{p\mathrm{CO}_2^{0.5} p\mathrm{H_2O}}{p\mathrm{CH}_4^{0.5} p\mathrm{O}_2} \qquad (1.9)$$

where $K_{\mathrm{p,POM}}$ is the equilibrium constant for reaction 1.6, $K_{\mathrm{p,comb}}$ is the equilibrium constant for reaction 1.7, $P° = 1$ bar is the standard pressure and pI is the partial pressure of species I. Above ~700°C, the equilibrium constant for reaction 1.6 is greater than for reaction 1.7, and increases exponentially with temperature (Fan *et al.*, 2015), such that $K_{\mathrm{p,POM}} \gg K_{\mathrm{p,comb}}$. Writing new equilibrium constants for the chemical looping versions of the reactions, $K_{\mathrm{p,CL}}$ (noting that the oxygen carrier, being a solid phase, has activities of unity), and relating them to the homogeneous versions:

$$K_{\mathrm{p,CL,POM}} = \frac{p\mathrm{CO}^2 p\mathrm{H}_2^4}{p\mathrm{CH}_4^2}\frac{1}{P°^4} = K_{\mathrm{p,POM}}\frac{p\mathrm{O}_2}{P°} \qquad (1.10)$$

$$K_{\mathrm{p,CL,comb}} = \frac{p\mathrm{CO}_2^{0.5} p\mathrm{H_2O}}{p\mathrm{CH}_4^{0.5}}\frac{1}{P°} = K_{\mathrm{p,comb}}\frac{p\mathrm{O}_2}{P°} \qquad (1.11)$$

Since $p\mathrm{O}_2$ is fixed by the oxygen carrier material at equilibrium, it becomes possible to choose a material with appropriate $p\mathrm{O}_2$ such that $K_{\mathrm{p,CL,POM}} \gg 1$, but with $K_{\mathrm{p,CL,comb}} \ll 1$ (recalling that the homogeneous thermochemistry, not including the oxygen carrier, has already led to $K_{\mathrm{p,POM}} \gg K_{\mathrm{p,comb}}$). Thus, a high conversion of methane is achieved with $\frac{p\mathrm{CO}^2 p\mathrm{H}_2^4}{p\mathrm{CH}_4^2}\frac{1}{P°^4} \gg 1$, and at high selectivity with $\frac{p\mathrm{CO}_2^{0.5} p\mathrm{H_2O}}{p\mathrm{CH}_4^{0.5}}\frac{1}{P°} \ll 1$. Here, $p\mathrm{O}_2$ should not be too high, otherwise $K_{\mathrm{p,CL,comb}} > 1$: it should also be not too low, otherwise $K_{\mathrm{p,CL,POM}} < 1$. This shows that materials with mild oxidising potentials are suitable for the partial oxidation of methane and the production of syngas (Fan *et al.*, 2015).

Another side reaction is the deposition of coke, and a similar analysis can also be used to determine a range of materials able, thermodynamically, to oxidise coke (to CO), but not syngas (Fan *et al.*, 2015). However, it is often difficult to reach, in practice,

thermodynamic equilibrium between contacting solids such as between coke and the oxygen carrier, because diffusion in the solid state is generally slow and the area of solid-solid contact is often small. This means that, whilst the thermodynamics might be favourable for attaining selectivity, slow reaction kinetics might prohibit equilibria from being reached and so lead to a degraded selectivity. Therefore, to maintain selectivity, coking must usually be kinetically inhibited from forming in the first place. This is an example of kinetically-controlled selectivity and is usually more difficult to achieve than thermodynamic control, because the competing kinetic processes, involving active sites, is generally still a challenging science.

Thermodynamic selectivity is usually improved by limiting the presence of oxygen. This is not necessarily true for kinetic selectivity where an increase in oxygen content can improve selectivity. For example, sometimes an optimum oxygen content exists, as seen in the production of ethylene oxide (Stegelmann *et al.*, 2004), propylene oxide (Khatib and Oyama, 2015), styrene oxide (Lambert *et al.*, 2005) and maleic anhydride (Shekari and Patience, 2010). Selective oxidations with potentially significant industrial impact, such as the oxidative coupling of methane, oxidative dehydrogenation of light alkanes, and the epoxidation of higher alkenes, are all kinetically controlled, and is arguably why many have yet to be commercialised.

1.1.2 Kinetically-controlled selective oxidations

In kinetically-controlled selective oxidations, irrespective of the thermodynamics, the desired products and reactants can potentially be combusted, which is inevitably kinetically-controlled with, frequently, rapid kinetics. These features are captured in a simplified reaction network of a series-parallel type, shown in Figure 1.3 (A) for the epoxidation of ethylene (Linic and Barteau, 2003). Here, ethylene is partially oxidised to ethylene oxide with rate constant k_1, but can also be combusted with rate constant k_2. The desired product, ethylene oxide, can also be combusted with rate constant k_3. The mechanism captured by k_1 and k_2 is sometimes referred to as the 'primary chemistry', whereas k_3 is sometimes referred to as the 'secondary chemistry' (Tan *et al.*, 1987; Torres *et al.*, 2007). The series reaction, rate constant k_3, captures the observation of decreasing selectivity with increasing conversion (eventually everything is combusted, for a sufficiently large residence time), shown qualitatively in Figure 1.3 (B). This is why industrial epoxidation reactors are usually operated at small conversions with small residence times, of the order of 1 s, with high yields achieved by separation of the

products and recycling of the reactants (Rebsdat and Mayer, 2012). The parallel reaction, rate constant k_2, captures the observation of imperfect selectivity at differential conversions. The strong correlation of selectivity with conversion, shown in Figure 1.3 (B), means that rigorous comparisons of selectivity for different catalysts and conditions must be made at isoconversions, a point often neglected in the open literature. The first challenge is to formulate a catalyst, or oxygen carrier, with appropriate active sites. In this simplified model for example, this means $k_1 > k_2$ and $k_1 > k_3$.

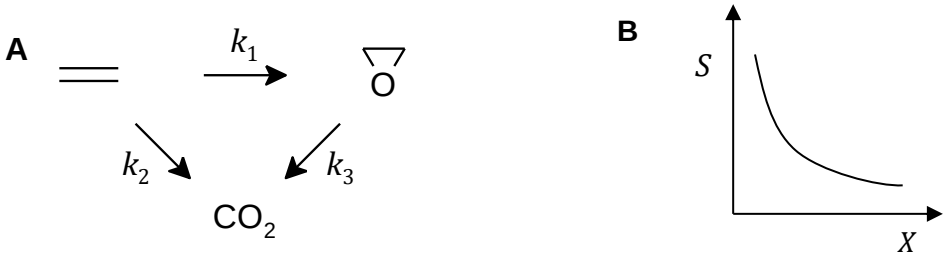

Figure 1.3. (A) Simplified reaction network of a series-parallel type, using the epoxidation of ethylene as an example. (B) Typical qualitative trend of how selectivity varies with conversion for kinetically controlled selective oxidations, with features captured by a series-parallel network.

1.1.3 Oxidative dehydrogenation of light alkanes

The oxidative dehydrogenation (ODH) of light alkanes is a reaction with the potential to upgrade a constituent of natural gas to a useful and more valuable intermediate. Compared to thermal dehydrogenation, the ODH of alkanes to olefins is not equilibrium-limited and is exothermic, but has yet to be implemented industrially despite the identification of many promising catalysts (Cavani *et al.*, 2007; Gärtner *et al.*, 2013). This section is focused mainly on the ODH of ethane. The thermal dehydrogenation (DH) of ethane is:

$$\mathrm{C_2H_{6(g)}} \rightleftharpoons \mathrm{C_2H_{4(g)}} + \mathrm{H_{2(g)}} \qquad \Delta H^\circ_{773\,\mathrm{K}} = +140\ \mathrm{kJ\ mol^{-1}} \tag{1.12}$$

For a feed of pure or diluted ethane, the equilibrium conversion to ethylene achievable by DH is related to its equilibrium constant, the dilution ratio, and the pressure through the following:

$$K_{\mathrm{p,DH}} = \frac{X^2}{(1-X)(1+X+I)}\left(\frac{P}{P^\circ}\right) \tag{1.13}$$

where $K_{\mathrm{p,DH}}$ is the equilibrium constant for reaction 1.12, I is the dilution ratio (the molar ratio of inert gases to ethane), P is the pressure of the system, $P^\circ = 1$ bar is the standard

pressure and X is the conversion of ethane. This relationship shows that the conversion may be increased by (i) increasing $K_{\mathrm{p,DH}}$ or (ii) decreasing the initial partial pressure of ethane, as shown in Figure 1.4, where $K_{\mathrm{p,DH}}$ was calculated from tabulated data in Haynes (2017). $K_{\mathrm{p,DH}}$ can be increased by increasing the temperature, but this, kinetically, promotes unselective side reactions such as coke deposition and pyrolysis (Gray and McCaffrey, 2002; Zimmermann and Walzl, 2009). Using inert gases means that downstream separation is required, and use of vacuum pressures complicates the engineering design. Removing the hydrogen product *in situ* is therefore an interesting alternative for increasing the conversion. In a sense, this is accomplished by ODH (effectively the hydrogen is combusted to steam, and steam does not hydrogenate ethylene). Two predominant approaches have been reported for performing ODH (Cavani *et al.*, 2007), (i) a 'two-step' process combining DH with sequential selective combustion of hydrogen to drive the forward reaction, typically working at temperatures > 700°C where the homogeneous reaction is significant, and (ii) a 'single-step' process, or 'true ODH', with a single catalyst (or oxygen carrier) activating the alkane and producing the alkene and steam, typically working at temperatures < 500°C. A review of two-step ODH is now presented, followed by a review of single-step ODH.

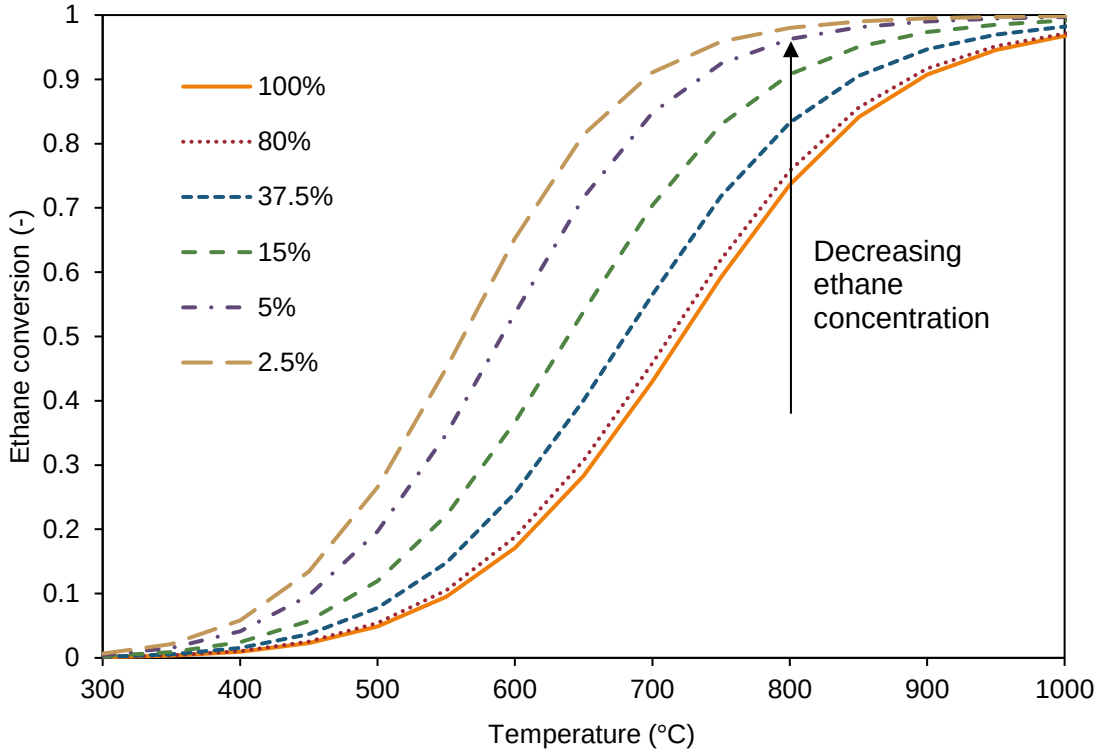

Figure 1.4. Conversion of ethane in thermal dehydrogenation as a function of temperature and the initial mol% of ethane (system pressure at 1 bara). Calculated from tabulated data in Haynes (2017).

Tsikoyiannis *et al.* (1999) proposed implementing two-step ODH by combining a conventional dehydrogenation catalyst (typically based on Pt) with an oxygen carrier to combust selectively the evolved hydrogen, thereby driving the forward reaction beyond the thermodynamic limits in thermal dehydrogenation. This was demonstrated for the dehydrogenation of propane to propylene, using supported Bi_2O_3 as the oxygen carrier and Pt-Sn-ZSM-5 as the dehydrogenation catalyst. A yield of propylene of 48%, with about 90% selectivity was achieved, an improvement of 140% over the equilibrium yield for DH alone. However, a rapid decline to 33% yield by the tenth cycle was observed, attributed to the loss of dispersion of Bi_2O_3 (Grasselli *et al.*, 1999a). Development of an appropriate oxygen carrier for selective hydrogen combustion (SHC) is recognised as a crucial aspect in two-step ODH. Doped ceria has also been shown to be selective and stable for this reaction over many cycles, but has yet to be demonstrated in combination with a dehydrogenation step (de Graaf *et al.*, 2004; Blank *et al.*, 2007; Beckers *et al.*, 2009).

Another crucial aspect in two-step ODH is the development of the DH catalyst, because of rapid coking (Larsson *et al.*, 1996). The predominant conventional DH catalysts are based on either chromium oxide or platinum (Caspary *et al.*, 2008; Zimmermann and Walzl, 2009). Chromia-based catalysts are probably unsuitable because steam, produced during ODH, poisons the catalyst (Kocoń *et al.*, 2005). Therefore, a two-step process should probably use a Pt-based catalyst. However, a clean Pt surface cokes immediately upon exposure to hydrocarbons (Larsson *et al.*, 1998). This is especially taxing for a chemical looping process because this effectively introduces a penalty on selectivity for each regeneration treatment with oxygen, although, in principle, it would be possible to regenerate the oxygen carrier separately from the Pt catalyst. Furthermore, low concentrations of hydrogen, as in an ODH environment, exacerbate coking (Waku *et al.*, 2004). Although hydrogen is converted to steam, which can inhibit coking (Sattler *et al.*, 2014), apparently steam does not inhibit as strongly as hydrogen on an equivalent molar basis, as indicated by the experiments conducted by Waku *et al.* (2004), where coking was more severe when hydrogen was combusted to steam in a batch system. In contrast, however, a separate study found steam to be more effective than hydrogen for inhibiting coke (Kogan *et al.*, 2001). These studies might not necessarily be in conflict because of different experimental conditions employed. Kogan *et al.* (2001) used (i) higher partial pressures of steam (or hydrogen), (ii) higher temperatures and (iii) a Pt-Sn/θ-Al_2O_3 catalyst, as opposed to a Pt/Na-[Fe]ZSM5 catalyst used by Waku *et al.* (2004). Other experimental differences could also have been significant. In any case, additional steam (or hydrogen) could be added to the feed, as in the Steam Active Reforming (STAR) process developed by the Uhde company (Sattler *et al.*, 2014).

Use of a dehydrogenation catalyst could be avoided if the operating temperature were sufficiently high, by exploiting homogeneous, gas-phase dehydrogenation. The only material required then is the oxygen carrier to perform selective hydrogen combustion. This has been demonstrated for the ODH of ethane using sodium tungstate-promoted Mn-Mg-O (Neal *et al.*, 2016; Yusuf *et al.*, 2017), and sodium tungstate-promoted Mn-Si-O (Yusuf *et al.*, 2018). The most effective oxygen carrier was found to be sodium tungstate-promoted Mg_6MnO_8, achieving an ethylene yield of 68% at 89% selectivity. No results were reported which exceeded the equilibrium yield for DH, which is 76-86% at the reported experimental conditions of 800-850°C and 80 mol% ethane at atmospheric pressure, as indicated in Figure 1.4. These manganese oxides promoted by sodium tungstate are similar to materials typically researched for oxidative coupling of methane

(OCM), which is explained by the observation that, during OCM, ethane is formed *in situ* and subsequently dehydrogenated to ethylene (Takanabe and Iglesia, 2009). Another high temperature ODH oxygen carrier, a Li-promoted La-Sr-Fe oxide perovskite, was reported to have achieved an ethylene yield of 32% at 85% selectivity, in chemical looping mode. However, the reactor was still at a very high temperature of 700°C, so the homogeneous reaction was small but significant, converting ~3% of the ethane fed at > 95% selectivity to ethylene (Gao *et al.*, 2016). The oxygen carrier did contribute a higher proportion of the reaction at lower temperatures (a minimum of 650°C was examined), so it could be considered as a single-step material. The yield of 32% was, again, below the equilibrium yield for DH, which is 56% at 700°C, 37.5 mol% ethane at atmospheric pressure, as indicated in Figure 1.4. Nevertheless, the processes using these high temperature oxygen carriers (*i.e.* the Mn- and La-Sr-Fe-based oxides) still offered advantages over conventional steam cracking, such as lower energy requirements because ODH is exothermic.

A variety of catalysts and oxygen carriers have been developed for single-step ODH. The most promising material appears to be Mo-V-Te-Nb-O (Lwin *et al.*, 2017), achieving > 90% selectivity to ethylene at conversions of 45-65%, operating catalytically with oxygen and ethane in the feed at mild temperatures of 250-450°C at pressures of 0.1 – 30 barg (Arnold *et al.*, 2009). There are reports of even higher selectivities and conversions (Arnold *et al.*, 2009; Gaffney and Mason, 2017). A process is currently being developed exploiting this catalyst (Baroi *et al.*, 2017). Two examples were found using this material in chemical looping mode. One group used this material in a laboratory-scale, riser-regenerator reactor with coupled fluidised beds (reactor volume 0.125 L), achieving 90% selectivity to ethylene at a conversion of 13% at 575°C (Gerzeliev *et al.*, 2016). The same formulation appeared to perform much better in ideal conditions during pulsed-feeding experiments, achieving 95% selectivity at 67% conversion at 600°C in a separate study by the same workers (Khadzhiev *et al.*, 2015), but this discrepancy was not discussed in either publication. It might be speculated that this was caused by the operation in the circulating fluidised beds, leading to suboptimal control of the reaction. For example, the residence time distribution of the solids in a fluidised bed could lead to a wider range of oxidation states of the carrier, which could give rise to different active sites that are less selective. The flow pattern in a fluidised bed could also have led to back mixing of the gas, leading to combustion of the products. Not enough information was given to calculate the corresponding equilibrium yields for DH. Another group used this material for the

ammoxidation of propane, where ~2% of the total lattice oxygen was removed and regenerated during pulsed-feeding experiments (Grasselli *et al.*, 2006).

Boron nitride, an inorganic analogue of graphene, was discovered to be a highly effective ODH catalyst for the production of propylene (Hermans *et al.*, 2015; Grant *et al.*, 2016), achieving a selectivity of 80% at a conversion of 21%, operating catalytically at 530°C (Shi *et al.*, 2017a). It was also applied to the ODH of ethane, achieving a selectivity of 80% at a conversion of 63%, operating catalytically at 600°C with 16.7 mol% ethane (an equilibrium DH yield would have been 35%) (Shi *et al.*, 2017b). It should be noted that allylic C-H bonds, present in propylene but not in ethylene, are weaker, leading to a lower activation energy for further oxidation, which partially explains why the ODH of propane is more difficult than ethane (Cavani *et al.*, 2007). Some mechanistic studies suggest the active site being at the zigzag edges (Huang *et al.*, 2017; Shi *et al.*, 2018), whereas a separate study suggested active surface sites, although these are not necessarily contradictory (Grant *et al.*, 2017). An isotopic tracer experiment using $^{18}O_2$ found that isotopic scrambling only occurred when ethane was present in the oxygen feed, suggesting that $O_{2(g)}$ is activated only in the presence of the alkane (Huang *et al.*, 2017). Furthermore, no apparent conversion of propane or products were observed when oxygen was absent from the feed. *Operando* DRIFTS indicated that ethane was activated to form surface ethyl species but no products were evolved (with no oxygen in the feed), with these surface species desorbing as ethylene in a subsequent step when only oxygen was fed, without any ethane (Huang *et al.*, 2017). These observations suggest that chemical looping operation with this boron nitride would be challenging. A family of boron-based materials was found to be similarly active and selective in ODH, including boron carbide, titanium boride, nickel boride, cobalt boride, hafnium boride, tungsten boride and elemental boron (Grant *et al.*, 2017).

To conclude this section, Siluria Technologies is developing a process and associated catalysts for the oxidative coupling of methane (OCM) and the ODH of ethane (Peplow, 2017). Details of the process and the catalysts are protected. Reportedly, the catalysts are based on promoted inorganic nanowire oxides, grown using viruses as templates (Zurcher *et al.*, 2011), and, remarkably, are active for OCM at temperatures as low as 200-300°C (Farrell *et al.*, 2016). Currently, this process for OCM (and ODH) appears to be nearest to commercialisation (Peplow, 2017).

1.1.4 Epoxidation of alkenes

Ethylene oxide (EO) is an industrially-significant chemical intermediate, with a global production of 26 million tonnes in 2013 (McAteer *et al.*, 2017). It is used in the synthesis of polymers, antifreeze, surfactants, solvents *etc*. The predominant technology for its production is the epoxidation of ethylene with air or purified oxygen. This technology and the associated catalyst is well-developed, obtaining selectivities of up to 90% for ethylene oxide (Rebsdat and Mayer, 2012). Silver is the only catalyst used because no other material matches its performance (Rebsdat and Mayer, 2012). No examples of chemical looping epoxidation were found in the open literature, except for arguably one study by Park *et al.* (1983). There, chemical looping operation was performed using Ba-promoted Ag supported on silica or alumina, to probe mechanistic details rather than as a route for industrial application. However, their reaction was conducted only up to 150°C, much lower than industrial conditions. They also did not use a reducible oxide support. Estimating the value of the largest apparent oxygen capacity from their results, 0.007 wt%, and the ratio of oxygen released to surface silver, 0.064, suggests that only adsorbed oxygen was participating in the looping reaction, which is probably caused by the aforementioned key differences (*i.e.* inert support, and low reaction temperature). It should be noted that Park *et al.* (1983) posited that molecular oxygen is the selective species in epoxidation, which is contrary to the current consensus that atomic oxygen is the species, specifically electrophilic oxygen adatoms (Bukhtiyarov and Knop-Gericke, 2011; Chen *et al.*, 2018).

A patent assigned to Standard Oil Development Co. described chemical looping selective oxidation in a circulating fluidised bed system, for the production of aromatic compounds such as phthalic anhydride (Rollman, 1949). Possible application to other selective oxidations were also mentioned, including ethylene to ethylene oxide, but no examples or evidence were given to suggest that epoxidation had actually been performed. As shown by the experiments by Park *et al.* (1983), use of silver alone for chemical looping cannot achieve competitive performances. It is unlikely that other materials were discovered at that time, or since. This highlights the challenge for chemical looping operation, because the most viable material, silver, does not oxidise (and store lattice oxygen) easily. However, a chemical looping mode of operation, utilising only lattice oxygen and removing gaseous molecular oxygen, might promote more selective oxygen species on the catalyst surface. A brief review of the mechanistic features of silver-catalysed epoxidation of ethylene is given in chapter 4.

Ethylene oxide is the only epoxide produced industrially *via* the direct oxidation of the alkene with gaseous oxygen. Propylene and higher alkenes are much more difficult to oxidise selectively in the gas phase, and so currently have no analogous industrial process. Instead, propylene oxide is produced from the chlorohydrin or the hydroperoxide process. Both produce side products and require complex purification schemes (Khatib and Oyama, 2015). The difficulty of epoxidation of higher alkenes with oxygen is often ascribed to the presence of allylic hydrogen, which is absent in ethylene (Khatib and Oyama, 2015). Density functional theory (DFT) calculations suggest that copper catalysts would be more selective than silver, which was supported by ultra-high vacuum experiments displaying apparent perfect selectivity to *trans*-methylstyrene oxide (Lambert *et al.*, 2005). However, a review still showed Ag to be the best material, with the best sample, Ag/WO_3, achieving a selectivity of 83% to propylene oxide at a conversion of 15.5% at 250°C and 20 bara (Khatib and Oyama, 2015). The challenge in using copper is that, under industrial conditions, it tends to oxidise easily (Khatib and Oyama, 2015). One study showed that illumination with visible light can keep copper in a reduced state, thereby maintaining the selectivity for propylene oxide (Marimuthu *et al.*, 2013). Subjecting copper catalyst to anaerobic pulses of propylene (*i.e.* chemical looping experiments) has shown that copper lattice oxygen is perfectly selective (> 97%) for acrolein and produces no propylene oxide at 250°C (He *et al.*, 2013). In contrast, a slightly different experiment, in which a step increase in propylene was fed to a stream of oxygen passing steadily over a silver oxide catalyst, showed that the catalyst, promoted with sodium chloride and sodium hydrogen sulphate, is > 90% selective to propylene oxide at temperatures of 150-170°C (Kobayashi, 1980). The selectivity fell rapidly to a steady state value of < 8% (the other product being CO_2), ascribed to the regeneration of the active oxygen species being slow. It might also be speculated that this collapse of selectivity was caused by the surface being reduced, or participation of coke in the reaction. The identity of the active oxygen species (atomic, molecular or lattice) was not determined.

Oxygen adatoms on silver are also generally considered to be the selective species for the epoxidation of higher alkenes, similar to ethylene epoxidation (Nijhuis *et al.*, 2006; Khatib and Oyama, 2015). However, a recent paper has proposed, based on DFT, that molecular oxygen is the selective oxygen species (Dai *et al.*, 2017). No experimental support was given. The DFT calculations showed that molecular oxygen adsorbed on Ag (111) (and other metals) is very selective for propylene oxide, much more than atomic

oxygen adsorbed on either Ag (111) or Ag (100). The selectivity of molecular oxygen adsorbed on Ag (100) was omitted without explanation, which raises suspicions because of experimental observations that propylene oxide is formed on Ag (100), but not at all on Ag (111) (Pulido *et al.,* 2012). Nevertheless, the theoretical work by Dai *et al.* (2017) and the experimental work by Pulido *et al.* (2012) do not necessarily contradict each other – molecular oxygen adsorbed on Ag (100) could turn out to be more selective than atomic oxygen on Ag (100). The identity of the selective oxygen species is important because chemical looping operation could affect the distribution of the various oxygen species on the surface.

1.1.5 Rates of reaction with time-varying feeds

Chemical looping reactions are inherently transient. The solid looping agent passes through a range of chemical states. The bulk solid might undergo discrete phase changes (*e.g.* Fe_2O_3, Fe_3O_4, $FeO_{1+\delta}$ and Fe) and, or, continuous changes in a non-stoichiometric phase (*e.g.* $FeO_{1+\delta}$). The composition of the surface of the solid at the gas-solid interface can also change similarly (*e.g.* the surface of Fe_2O_3 is different to that of Fe), in addition to having a dynamic population of adsorbed species exposed to a changing gas environment. Physical, morphological changes to the solid particles are also common. For the design of reactors, an adequate mathematical expression of the kinetics is necessary. This requires that reaction kinetics are accurately measured, which can be challenging for transient processes such as chemical looping. True steady state measurements, where the reactor is kept at a fixed state, are either impossible to set up or inadequate because models based on steady state measurements do not predict the performance of periodic reactors (Renken *et al.,* 2013). Moreover, various candidate kinetic mechanisms, each with different transient behaviours, might all fit a set of steady state measurements. This makes it difficult to discriminate among different mechanisms based on steady state measurements alone (Renken *et al.*, 2013). However, using dynamic measurements makes it possible to discriminate kinetic mechanisms and potentially ensures accurate prediction of the periodic performance (Renken *et al.,* 2013).

Input modulation is one method of performing dynamic measurements on a reactor (other methods include feeding pulses, or step changes in feed concentration). This is where some variable, *e.g.* concentration in the feed or temperature of the reactor, is deliberately forced to oscillate about some mean value, and the response of the reactor is measured. The full dynamic response can be measured, revealing kinetic information. Alternatively,

the time-averaged response can also be measured, but the response to a changing frequency of modulation has been recommended (Renken *et al.*, 2013) to ensure sensitivity in the test among kinetic models. Historically, there have also been studies of input modulation to enhance the performance of reactors. For example, in epoxidation, the selectivity for ethylene oxide was found to improve when the feed, a mixture of ethylene, oxygen and nitrogen, was modulated (with oxygen and ethylene oscillating in phase, and nitrogen varied to maintain a constant volumetric flow rate) (Renken *et al.*, 1976). Nevertheless, industrially, it would appear that feed modulation has not been exploited to improve performance. However, the development of chemical looping is an opportunity to revisit this technique, because chemical looping reactors are already input-modulated. With appropriate kinetic information, it might be possible to inform the optimal modulation policy, if one exists.

1.2 Objectives

The aim was to develop chemical looping for selective oxidation reactions. Firstly, oxygen carriers need to be developed, requiring an understanding of the thermodynamics of the reactions, as well as understanding how selectivity arises. The overall objective was to demonstrate that chemical looping selective oxidation is feasible and to demonstrate this for the oxidative dehydrogenation of ethane and the epoxidation of ethylene. The other objective was to explore if feed modulation can be employed with chemical looping to enhance the performance of the reactor.

Specifically, the objectives of this Dissertation are to investigate:

- The effect of the chemical potential of oxygen of an oxygen carrier on a reaction.
- How to formulate oxygen carriers for selective oxidations.
- If epoxidation can be performed in chemical looping mode.
- Mathematical methods of analysing the frequency response of periodic reactors.

This Dissertation has been structured with each chapter focusing on one of these objectives. Chapter 2 demonstrates the potential of using different oxygen carriers to shift the thermodynamics of reaction. Chapter 3 demonstrates how composite oxygen carriers be made to achieve selective chemical looping reactions. Linking chapters 2 and 3, chapter 4 applies both principles for the production of ethylene oxide, a crucial chemical intermediate. Chapter 5 investigates the applicability of a novel method for analysing the response of nonlinear periodic reactors.

Parts of the work in this Dissertation have been disclosed in an invention, first patent application GB1713951.0. Some of the research in this Dissertation has also been published, as listed below:

- Chan, M.S.C., Liu, W., Ismail, M., Yang, Y., Scott, S.A., Dennis, J.S., 2016. Improving hydrogen yields, and hydrogen:steam ratio in the chemical looping production of hydrogen using $Ca_2Fe_2O_5$. *Chem. Eng. J.*, **296**, 406–411. doi:10.1016/j.cej.2016.03.132
- Chan, M.S.C., Baldovi, H.G., Dennis, J.S., 2018. Enhancing the capacity of oxygen carriers for selective oxidations through phase cooperation: bismuth oxide and ceria–zirconia. *Catal. Sci. Technol.*, **8**, 887–897. doi:10.1039/C7CY01992K
- Chan, M.S.C., Marek, E., Scott, S.A., Dennis, J.S., 2018. Chemical looping epoxidation. *J. Catal.*, **359**, 1–7. doi:10.1016/j.jcat.2017.12.030

Research outside the scope of this Dissertation has also been undertaken over the duration of this Ph.D. Some of this work has been published in the following:

- Ismail, M., Liu, W., Chan, M.S.C., Dunstan, M.T., Scott, S.A., 2016. Synthesis, Application, and Carbonation Behavior of $Ca_2Fe_2O_5$ for Chemical Looping H_2 Production. *Energy & Fuels*, **30**, 6220–6232. doi:10.1021/acs.energyfuels.6b00631
- Gaultois, M.W., Dunstan, M.T., Bateson, A.W., Chan, M.S.C., Grey, C.P., 2018. Screening and Characterization of Ternary Oxides for High-Temperature Carbon Capture. *Chem. Mater.*, **30**. doi:10.1021/acs.chemmater.7b04679

2 IMPROVING HYDROGEN YIELDS IN THE CHEMICAL LOOPING PRODUCTION OF HYDROGEN USING $Ca_2Fe_2O_5$

2.1 Introduction

The use of hydrogen as an energy vector is dependent on efficiently minimising the carbon emissions associated with its production (Dincer and Acar, 2015). The steam-reforming of methane is currently the dominant source of hydrogen but it is energy intensive and requires operation at large scale to be economic (Häussinger *et al.*, 2000; Kathe *et al.*, 2016). A proposed alternative to steam reforming is to use the chemical looping of iron oxide to produce H_2, otherwise known as the steam-iron process. Use of looping reactions for this purpose dates back to the late 19th and early 20th Century (Messerschmitt, 1908). This process is summarised in the following scheme:

(I) Successive reduction of the oxide by synthesis gas (or some hydrocarbon fuel) to produce CO_2 and H_2O (where z and z' refer to the non-stoichiometry of the wüstite phase (Fe_zO), and enthalpies of reaction correspond to z = 0.947 where appropriate):

$$3Fe_2O_{3(s)} + CO_{(g)} \rightleftharpoons 2Fe_3O_{4(s)} + CO_{2(g)} \qquad \Delta H^{\circ}_{1123\,K} = -38.1\ \text{kJ mol}^{-1} \qquad (2.1)$$

$$\frac{z}{4z-3}Fe_3O_{4(s)} + CO_{(g)} \rightleftharpoons \frac{3}{4z-3}Fe_zO_{(s)} + CO_{2(g)} \qquad \Delta H^{\circ}_{1123\,K} = +21.1\ \text{kJ mol}^{-1} \qquad (2.2)$$

$$\mathrm{Fe}_{z'}\mathrm{O}_{(s)} + \mathrm{CO}_{(g)} \rightleftharpoons \frac{1}{z'}\mathrm{Fe}_{(s)} + \mathrm{CO}_{2(g)} \qquad \Delta H^{\circ}_{1123\,\mathrm{K}} = -16.7\ \mathrm{kJ\ mol^{-1}} \qquad (2.3)$$

$$3\mathrm{Fe}_2\mathrm{O}_{3(s)} + \mathrm{H}_{2(g)} \rightleftharpoons 2\mathrm{Fe}_3\mathrm{O}_{4(s)} + \mathrm{H}_2\mathrm{O}_{(g)} \qquad \Delta H^{\circ}_{1123\,\mathrm{K}} = -4.5\ \mathrm{kJ\ mol^{-1}} \qquad (2.4)$$

$$\frac{z}{4z-3}\mathrm{Fe}_3\mathrm{O}_{4(s)} + \mathrm{H}_{2(g)} \rightleftharpoons \frac{3}{4z-3}\mathrm{Fe}_z\mathrm{O}_{(s)} + \mathrm{H}_2\mathrm{O}_{(g)} \qquad \Delta H^{\circ}_{1123\,\mathrm{K}} = +54.6\ \mathrm{kJ\ mol^{-1}} \qquad (2.5)$$

$$\mathrm{Fe}_{z'}\mathrm{O}_{(s)} + \mathrm{H}_{2(g)} \rightleftharpoons \frac{1}{z'}\mathrm{Fe}_{(s)} + \mathrm{H}_2\mathrm{O}_{(g)} \qquad \Delta H^{\circ}_{1123\,\mathrm{K}} = +16.8\ \mathrm{kJ\ mol^{-1}} \qquad (2.6)$$

(II) Oxidation of the reduced solid by H_2O to produce H_2 (reverse of reactions 2.5 and 2.6).

(III) Oxidation of the magnetite (Fe_3O_4) by air to generate heat (and remove any carbonaceous deposits):

$$2\mathrm{Fe}_3\mathrm{O}_{4(s)} + 0.5\mathrm{O}_{2(g)} \rightleftharpoons 3\mathrm{Fe}_2\mathrm{O}_{3(s)} \qquad \Delta H^{\circ}_{1123\,\mathrm{K}} = -244.1\ \mathrm{kJ\ mol^{-1}} \qquad (2.7)$$

This approach offers the advantages of (i) achieving an inherent separation of CO_2 if conducted in a packed bed reactor, (ii) being potentially thermally neutral, and (iii) the economics being less dependent on the scale of the process. As a consequence of (iii), a process based on chemical looping would be suited to the local production of H_2 from any gasified fuel. The advantages of a packed bed reactor configuration have been described previously by Bohn *et al.* (2008).

An important variable affecting the efficiency of the process is the conversion of steam to hydrogen by the reverse of reactions 2.5 and 2.6 in stage (II). Low conversions of steam require additional steam to be generated or recycled, both of which require additional inputs of energy (He and Li, 2014). Using unmodified iron oxide, the maximum conversion of the steam is limited by the thermodynamic equilibria of reactions 2.5 and 2.6, with equilibrium constants $K_{p2.5}$ and $K_{p2.6}$, which is related to the oxidising potentials of the phase transitions. The oxidising potential can be expressed in terms of partial pressures pO_2, pH_2O/pH_2, or pCO_2/pCO. For example at 1123 K, the conversion of steam to hydrogen by metallic iron and wüstite (Fe_zO) is thermodynamically limited to 62% and 21%, respectively, calculated from data obtained by Giddings and Gordon (1973). However, the formation of a ternary oxide phase, by mixing iron with other elements, could, potentially, enhance the stability of Fe^{2+} and Fe^{3+} under reducing environments, lowering the oxidising potentials of the transition from metallic Fe to Fe^{2+} and Fe^{3+} and

hence increasing the conversion of steam. Previous work on mixed oxides with the potential to improve steam conversion in the thermodynamic limit for the production of hydrogen include the Ca-Fe-O system (Ismail *et al.*, 2014) and the perovskite $La_{0.8}Sr_{0.2}FeO_{3-\delta}$ (LSF) (He and Li, 2015).

This chapter focused on $Ca_2Fe_2O_5$, a phase recently studied for its potential in chemical looping (Ismail *et al.*, 2014). It undergoes a single phase transition from Fe^{3+} to Fe^0 in:

$$2CaO_{(s)} + 2Fe_{(s)} + 3H_2O_{(g)} \rightleftharpoons Ca_2Fe_2O_{5(s)} + 3H_{2(g)} \qquad \Delta H^\circ_{1123\,K} = -107.9\ \text{kJ mol}^{-1} \qquad (2.8)$$

$$Ca_2Fe_2O_{5(s)} + 3CO_{(g)} \rightleftharpoons 2CaO_{(s)} + 2Fe_{(s)} + 3CO_{2(g)} \qquad \Delta H^\circ_{1123\,K} = +7.05\ \text{kJ mol}^{-1} \qquad (2.9)$$

where enthalpies have been calculated from the results of Jacob *et al.* (1999) (verified with MTData using the NPL Oxide Database (Davies *et al.*, 2002)). Notably, these two reactions occur at much lower oxidising atmospheres than with pure iron oxides, as seen in Figure 2.1. Therefore at 1123 K, $Ca_2Fe_2O_5$ can achieve a 75% conversion of steam over the entirety of its carrying capacity of oxygen, a marked increase from 62% for unmodified iron oxide over its wüstite-iron transition (Fe_zO-Fe) or 21% for the magnetite-wüstite transition (Fe_3O_4-Fe_zO). Whilst carbonation of the reduced and oxidised forms of $Ca_2Fe_2O_5$ may occur under certain conditions, this is thermodynamically infeasible in the experimental conditions described here.

The present work investigated the use of $Ca_2Fe_2O_5$ for the chemical looping production of hydrogen and to compare its performance against chemically unmodified iron oxide supported on ZrO_2, a system studied in an earlier work (Liu *et al.*, 2012). This is important in improving the efficiency of hydrogen generation *via* the steam-iron reaction.

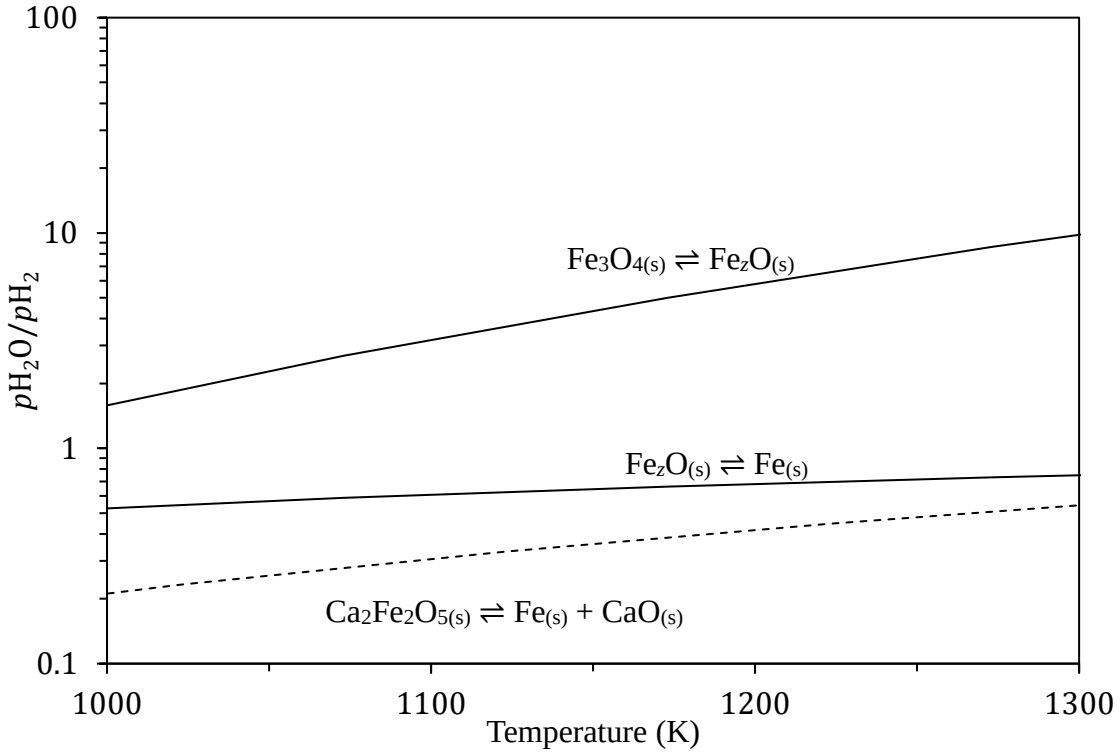

Figure 2.1. Baur-Glaessner phase diagram showing the phase transitions of the Fe-O system in different oxidising environments (the steam to hydrogen ratio, pH_2O/pH_2) as a function of temperature, calculated from experimental data (Giddings and Gordon, 1973). The phase transition for $Ca_2Fe_2O_5$-(Fe+CaO) (- -) is also shown, calculated from experimental data reported by Jacob *et al.* (1999).

2.2 Experimental

The oxygen carriers, (i) 60 wt% Fe_2O_3 supported on ZrO_2 (denoted Fe60Zr) and (ii) $Ca_2Fe_2O_5$, were synthesised using a modified Pechini method (Pechini, 1963; Cushing *et al.*, 2004). Briefly, stoichiometric quantities of the metal nitrates ($Fe(NO_3)_3 \cdot 9H_2O$, purity > 98 %, Sigma-Aldrich; $ZrO(NO_3)_2 \cdot xH_2O$, purity > 99.5 %, ZrO_2 content = 35.4 wt%, ACROS Organics; $Ca(NO_3)_2 \cdot 4H_2O$, purity > 99.0 %, Sigma-Aldrich) were dissolved in reverse osmosis water. Citric acid (purity > 99.5 %, Sigma-Aldrich) was then added with a citric acid to metal ion mole ratio of 1. Ethylene glycol (purity >99.75%, Sigma-Aldrich) was then added to the mixture with a glycol to citric acid mole ratio of unity. The mixture was then dried at 373 K in air for 12 h to produce a xerogel, which was then calcined at 1223 K in air for 3 h. The purity of the synthesised $Ca_2Fe_2O_5$ was verified by X-ray diffraction (XRD) and thermogravimetric analysis (TGA). The oxygen carrying capacity of the samples was measured using TGA by temperature-programmed reduction in H_2

and oxidation in air. For use in a packed bed, the calcined powders were compressed at 740 MPa for 3 minutes followed by crushing to a sieve size range of 300-425 μm.

The phase purity of freshly calcined and cycled $Ca_2Fe_2O_5$ was analysed using powder X-ray diffraction (XRD). Data was collected at atmospheric conditions on a Panalytical Empyrean diffractometer using Cu-Kα radiation, with a voltage of 40 kV and a current of 40 mA. The instrument was arranged in a Bragg-Brentano geometry. Samples were first ground to a fine powder (< 67 μm) before being loaded into the *ex situ* sample holders. Rietveld refinements were carried out using GSAS (Von Dreele and Larson, 2000) with the graphical user interface EXPGUI (Toby, 2001). Parameters refined included lattice parameters, thermal displacement parameters, Lorentzian coefficients and sample displacement.

The oxygen carrying capacities of the samples were quantified by temperature-programmed reduction (TPR) and oxidation (TPO) in a commercial cantilever-type thermogravimetric analyser (TGA/DSC1, Mettler Toledo). Temperature-control was achieved by an electrical heater in combination with a water-cooling circuit. A sketch of the arrangement inside the temperature-controlled reaction chamber is shown in Figure 2.2. Reactive gases were passed over the crucible through a capillary. The reaction chamber was also continuously flushed with flows of purge gas and protective gas, which effectively diluted the concentration of reactive gas exposed to the sample. The temperature programme was specified using commercial software (STAR software, Mettle Toledo). The gas programme was specified using a custom C++ script that also synchronised with the temperature programme. Approximately 20 mg of freshly calcined sample was placed in a 70 μL alumina crucible within the reaction chamber. The sample was initially dried for one hour at 393 K in a flow of N_2 (50 mL/min, all flows measured at 295 K, 1 atm), followed by TPR with an additional flow of 5 vol% H_2 in N_2 (50 mL/min) and then TPO with an additional flow of air (50 mL/min).

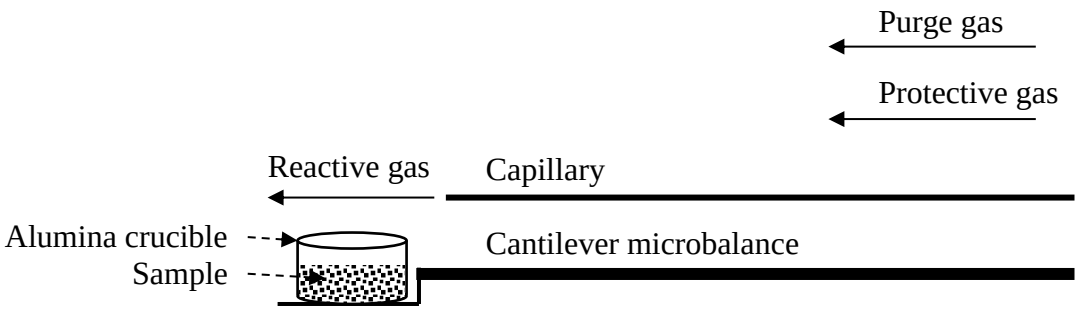

Figure 2.2. Schematic drawing of the apparatus inside the TGA.

The performance of the carriers was examined by reducing and oxidising the particles in a vertically-mounted packed bed reactor, consisting of a 10 mm I.D. tube of recrystallised alumina, at 1123 K. The packing consisted of, in order from bottom to the top, (i) 7.5 g of α-Al_2O_3, (ii) oxygen carrier and (iii) 10 g of α-Al_2O_3. The layer of oxygen carrier consisted of 0.9790 g of Fe60Zr or 1.0066 g of $Ca_2Fe_2O_5$, which corresponds to 0.59 g of Fe_2O_3, or (assuming zirconia and calcium oxide do not contribute) a theoretical carrying capacity of 11.1 mmol of O atoms. The arrangement of the experimental apparatus is shown in Figure 2.3. The temperature variation along the reactive bed was measured in the absence of gas flow to be < 2 K. Compressed gases were obtained from cylinders, consisting of 10.05 vol% CO in balance N_2 (BOC plc., certified 5 % accuracy), pure N_2 (purity > 99.998 %), and air (blended grade, O_2 content 19 – 22 %) (Air Liquide S.A.). Steam was generated by bubbling nitrogen through reverse osmosis water held at 298 K in a water bath, with the resulting humidity measured by a capacitive relative humidity sensor (HYT 271, IST AG). The feed lines were trace heated to 50°C to prevent condensation. The levels of steam were constant within a single cycle, but varied cycle to cycle because of changes in the laboratory temperature with the time of day. The off-gases were sequentially dried by a condenser held in an ice bath and a tube packed with $CaCl_2$ pellets. Gas analysis was performed by a non-dispersive infrared (NDIR) and paramagnetic analyser for CO, CO_2 and O_2 (Uras26 and Magnos206, EL3020, ABB), and a thermal conductivity analyser for H_2 (Caldos27, EL3020, ABB).

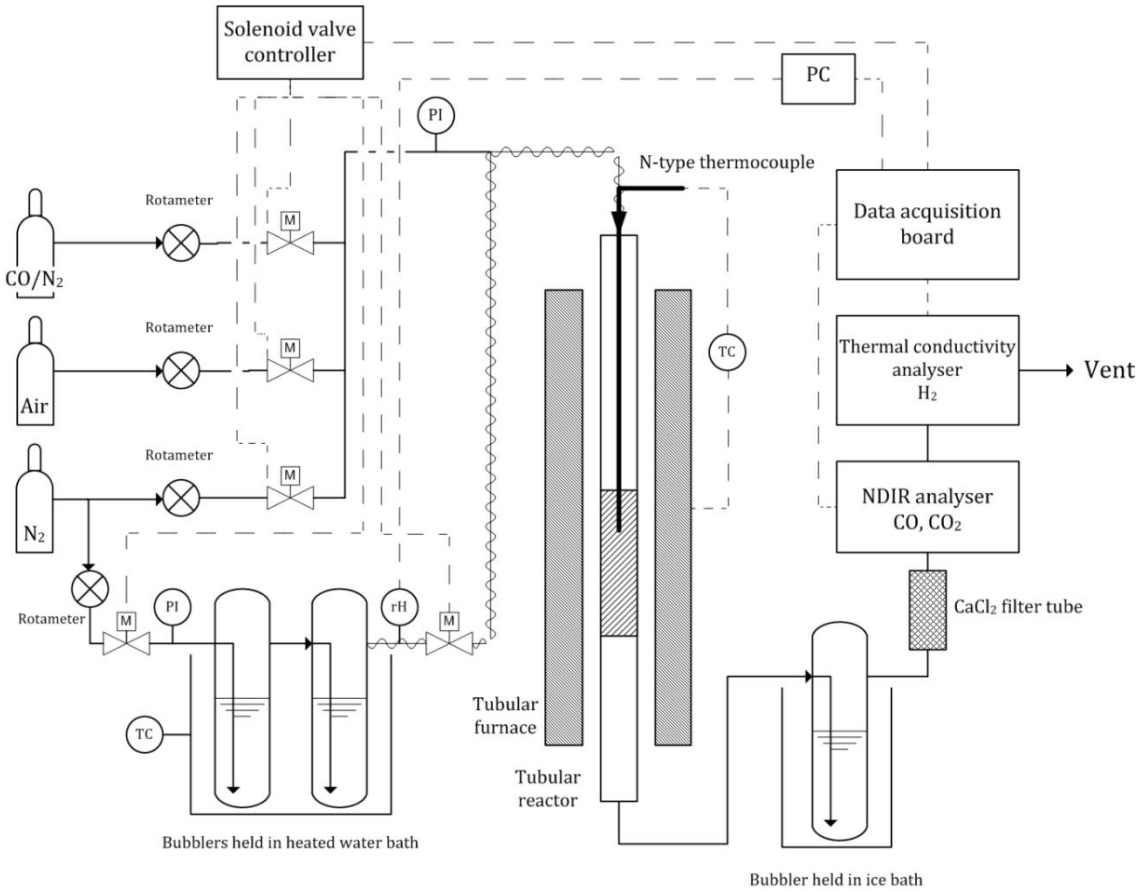

Figure 2.3. Schematic diagram of the packed bed reactor. Dashed lines are electronic or electrical signals. Solid lines are material streams. 'rH' represents the relative humidity sensor.

The performance of the rig was validated by measurement of the oxidising potential of the magnetite-wüstite transition in pure iron oxide. This was achieved by reducing a batch of iron oxide particles to wüstite, diluted in α-Al_2O_3 sand to maintain its reactivity, followed by oxidation in CO_2. Sufficiently large space times allowed equilibrium to be reached between the off-gas and the exit of the bed. This was confirmed by a period, or periods, of constant $[CO_2]/[CO]$ ratios in the off-gas, thus yielding the oxidising potential of the magnetite-wüstite transition. The measured ratio was $[CO_2]/[CO] = 3.25$ which is in agreement with the theoretical value of 3.3 (Giddings and Gordon, 1973).

The temperature of 1123 K was chosen to emulate the effluent from a typical gasifier, and because carbonation is infeasible at these conditions. The oxygen carriers were reacted in sequential stages, summarised in Table 2.1. The durations of each stage were chosen to allow each reaction to reach completion, which was indicated by no further conversion of the inlet gases. This was intended to sample as many phase transitions as possible in the carrier. The duration of reduction of $Ca_2Fe_2O_5$ was longer because its rate

of reduction with CO was strongly limited by thermodynamics. The flow rates during oxidation with steam were chosen to be sufficiently low for equilibrium to be established between H_2O, H_2 and the oxygen carrier, confirmed by a period, or periods, of constant off-gas composition. Further confirmation was indicated by the conversion of steam being unchanged when the flow rate was further decreased. The reactor was purged with N_2 for 3 minutes between each stage.

Table 2.1. Conditions of each stage in the chemical looping experiments. Flows were measured at 295 K, 1 atm.

Stage	Inlet concentration (vol%)	Total flow rate (ml/min)	Duration (min)	
			Fe60Zr	$Ca_2Fe_2O_5$
Reduction with CO	10.1	230	99	172
Oxidation with H_2O	2.5-3.5[a]	96	198	198
Oxidation with O_2	2.3	300	30	30

[a] Measured online by a capacitive relative humidity sensor (HYT 271, IST AG). Some variation arose from changes in the laboratory temperature.

During oxidation with steam, the instantaneous conversion of steam at a particular time was calculated using:

$$x_{\mathrm{H_2O}}(t) = \frac{\text{instantaneous molar flow rate of } \mathrm{H_2} \text{ leaving the bed}}{\text{instantaneous molar flow rate of } \mathrm{H_2O} \text{ entering the bed}} = \frac{1}{\frac{y_{\mathrm{H_2O,in}}}{1-y_{\mathrm{H_2O,in}}}} \frac{y_{\mathrm{H_2}}(t)}{1-y_{\mathrm{H_2}}(t)} \tag{2.10}$$

where y_i is the mole fraction of species i in the off-gas measured on a dry basis, and $y_{\mathrm{H_2O,in}}$ is the measured mole fraction of steam in the feed.

The cumulative conversion of steam was calculated using:

$$X_{\mathrm{H_2O}}(t) = \frac{\text{total moles of } \mathrm{H_2} \text{ leaving the bed}}{\text{total moles of } \mathrm{H_2O} \text{ entering the bed}}$$

$$= \frac{1}{\frac{y_{\mathrm{H_2O,in}}}{1 - y_{\mathrm{H_2O,in}}}} \frac{\int_{t_{\mathrm{start}}}^{t} \frac{y_{\mathrm{H_2}}(t)}{1 - y_{\mathrm{H_2}}(t)} dt}{t - t_{\mathrm{start}}} \tag{2.11}$$

where t_{start} is the time when H_2 was first detected by the analyser.

The conversion of the bed of oxygen carrier was calculated, assuming dilute gases, using:

$$X_{\mathrm{O}}(t) = \frac{\text{accumulated moles of O in reactor}}{\text{oxygen carrying capacity of sample}}$$

$$= \frac{\dot{N}_{\mathrm{N_2}}}{n_{\mathrm{O}}} \int_{t_{\mathrm{start}}}^{t} \left(\frac{y_{\mathrm{H_2}}(t)}{1 - y_{\mathrm{H_2}}(t)} - \frac{2y_{\mathrm{CO_2}}(t)}{1 - y_{\mathrm{CO_2}}(t)} - \frac{y_{\mathrm{CO}}(t)}{1 - y_{\mathrm{CO}}(t)} \right) dt \tag{2.12}$$

where $\dot{N}_{\mathrm{N_2}}$ is the molar flow rate of N_2 and n_{O} is the nominal molar oxygen carrying capacity of the carrier.

2.3 Results

The *ex situ* XRD patterns of the oxidised $Ca_2Fe_2O_5$ samples before and after cycling, shown in Figure 2.4, showed that phase segregation was reversible during repeated transitions between $Ca_2Fe_2O_5$ and a two-phase mixture of CaO and Fe, and that the carrier did not segregate into CaO and Fe_2O_3.

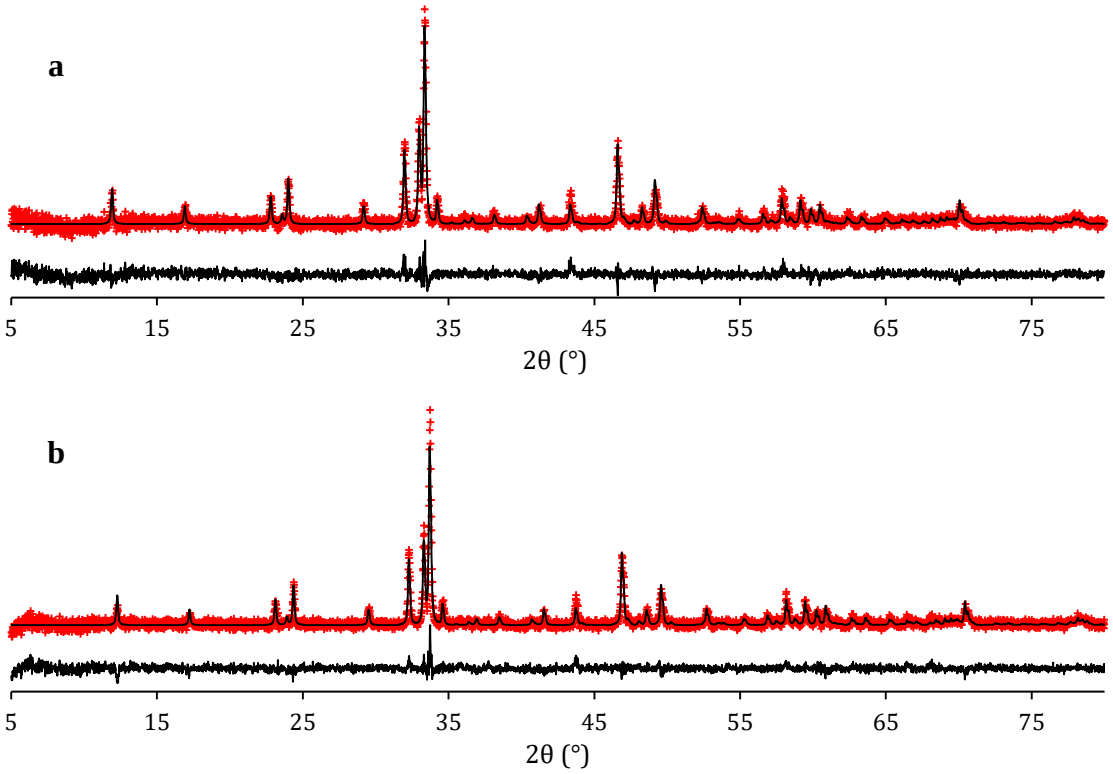

Figure 2.4. Rietveld refined XRD patterns of oxidised $Ca_2Fe_2O_5$ (a) freshly calcined and (b) after 10 cycles.

The measured temperatures and changes in mass of the samples during TGA are shown in Figure 2.5. The oxygen carrying capacity was calculated by assuming the changes in mass during oxidation were solely due to the carrier gaining lattice oxygen, and were found to deviate by no more than 2% from the nominal compositions for both $Ca_2Fe_2O_5$ and Fe60Zr.

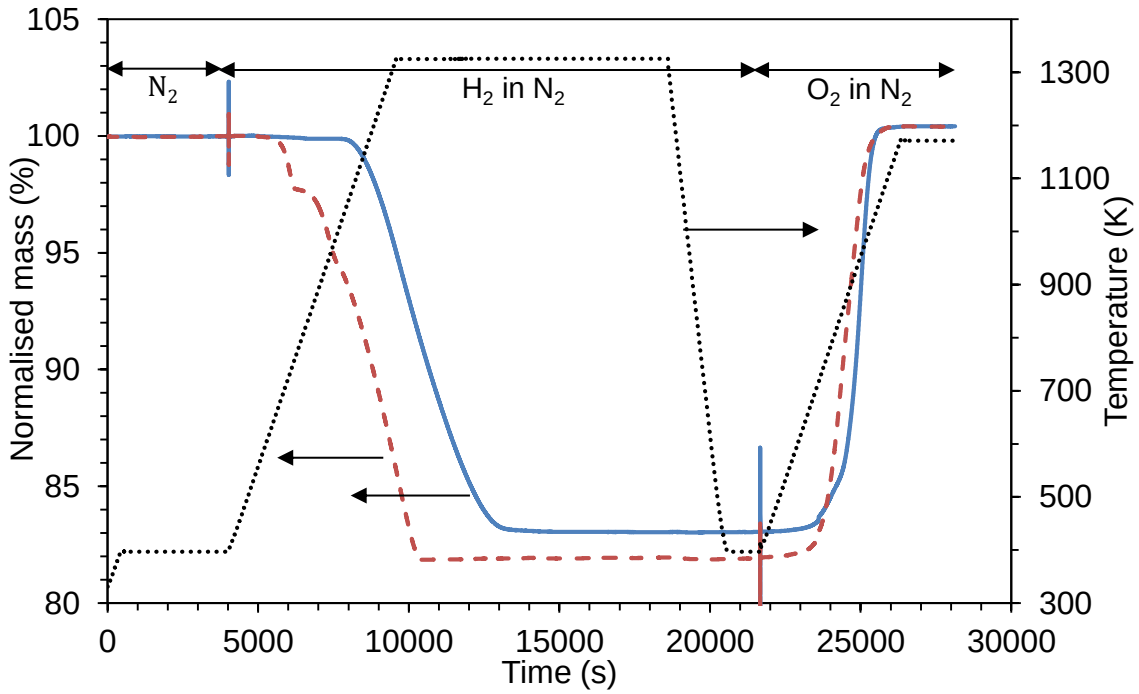

Figure 2.5. Normalised sample mass during the temperature-programmed reduction in H_2 and temperature-programmed oxidation in O_2 (all gases diluted in N_2). Solid, dashed and dotted lines correspond to the mass of $Ca_2Fe_2O_5$, mass of Fe60Zr and the temperature respectively.

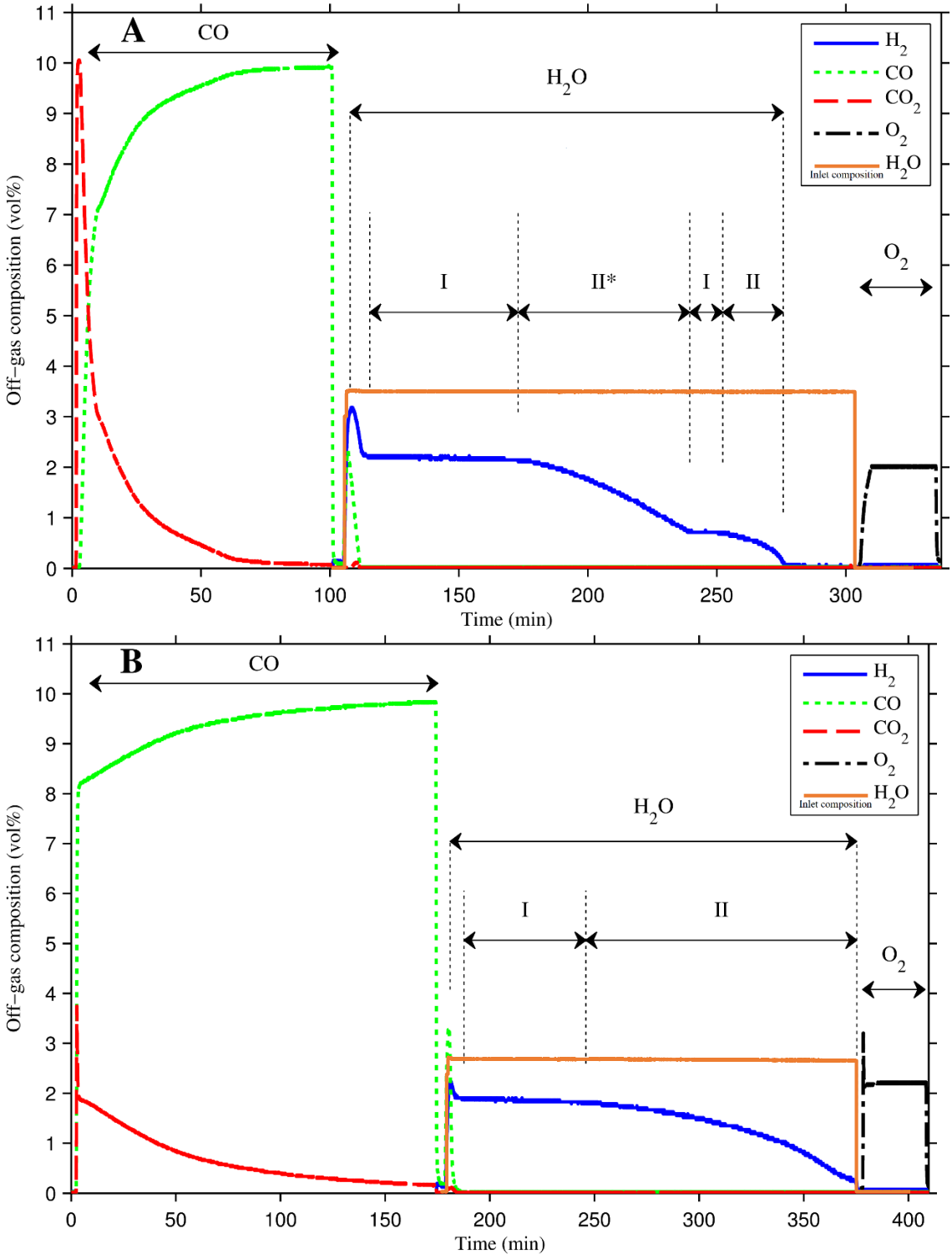

Figure 2.6. Off-gas mole fraction profiles for **(A)** Fe60Zr and **(B)** $Ca_2Fe_2O_5$. Initially 10 vol% CO is fed into the bed, followed by steam and finally air. The measurements for steam correspond to the feed composition at the inlet of the reactor, not the off-gas. The packed bed was purged with N_2 between each step. The regimes governing the conversion of steam are labelled as I equilibrium-limited and II rate-limited. II* indicates that non-stoichiometric effects may also have been significant.

The variation in composition of the off-gases from the reactor with time are shown in Figure 2.6, which reflects the rate of reaction and the conversion of the bed. The lower concentration of hydrogen produced by $Ca_2Fe_2O_5$, compared to Fe60Zr, was caused by the lower humidity of the feed due to variations in the ambient temperature affecting the saturator.

Reduction with CO

Initially, the sample was reduced with CO until negligible amounts of CO_2 were measured at the outlet (residual conversions of CO were attributed to carbon deposition by the reverse Boudouard reaction and was consistent with the evolution of carbon oxides observed during oxidation steps). Initially for Fe60Zr, in Figure 2.6 (A), CO was fully converted to CO_2, corresponding to the transition of Fe_2O_3 to Fe_3O_4 with its high oxidising potential (reaction 2.1). The concentration of CO_2 then quickly dropped with time as the bed was progressively reduced and Fe_2O_3 was consumed. The point of inflection at t = 10 min indicated the depletion of Fe_3O_4, beyond which the majority of the reaction was due to the reduction of Fe_zO to Fe. The outlet concentration did not equilibrate with the oxygen carrier because the conversion was limited by the rate of reaction. As the lattice oxygen was depleted, the rate of reaction slowed and the conversion of CO fell.

For $Ca_2Fe_2O_5$, in Figure 2.6 (B), an initial spike of CO_2 was observed which was probably due to contaminants in the reactor (XRD and TGA results, shown in Figures 2.4 and 2.5, suggested that the sample itself is pure, and control experiments in the packed bed containing only α-Al_2O_3 detected oxygen-carrying capacities of up to 3 mol% of the nominal loading). As the bed became depleted in $Ca_2Fe_2O_5$, the concentration of CO_2 dropped as the rate of reaction decreased, similar to the behaviour observed for Fe60Zr, but without an obvious point of inflection. Differences in reduction behaviour can be seen where Fe60Zr, with its higher oxidising potential, gave higher conversions of CO than $Ca_2Fe_2O_5$, and was fully reduced in a shorter time.

Oxidation with H_2O

During oxidation with steam, both materials exhibited an initial spike in H_2, probably owing to reaction with the carbon deposited during the CO reduction, indicated by the accompanying evolution of CO and CO_2. Aside from this initial removal of carbon, two distinct regimes can be observed, namely (I) equilibrium-limited and (II) rate-limited, both being marked in Figure 2.6. Generally in the equilibrium-limited regime, both the chemical kinetics and mass transfer are fast enough for the reaction to be limited by the

supply of the reacting gas. The conversion will then reach the thermodynamic limit at the exit from the bed. In essence, the oxides in the bed act as a redox buffer to constrain the local oxidising potential of the gas. This means that the composition profile in the equilibrium-limited regime will be constant and correspond to the oxidising potential of the material at the exit of the bed. In Figure 2.6 (A), two plateaux can be seen in the mole fraction of H_2. The measured values of y_{H_2O}/y_{H_2} at these plateaux are 0.63 and 3.87, respectively, and are in agreement with the predicted values of 0.63 and 3.85 for the Fe_zO-Fe and Fe_3O_4- Fe_zO transitions at 1123 K, respectively. The reactor was operating in the equilibrium-limited regime at these plateaux.

For wüstite (Fe_zO), the stability of its non-stoichiometry resulted in a continuously decreasing oxidising potential as the lattice oxygen content fell at the outlet, and hence a decaying conversion of steam over time. This situation could have been confounded with the rate-limited regime, and may have been observed between the first and second plateaux for Fe60Zr, marked as II* in Figure 2.6 (A). The rate-limited regime is associated with the depletion of lattice oxygen, leading to a gradual decrease in the rate and hence the conversion of gas. This behaviour was observed after the second plateau during the decline in y_{H_2}. For the situation in $Ca_2Fe_2O_5$, Figure 2.6 (B), one equilibrium-limited period is initially observed followed by a rate-limited period. The observed oxidising potential here was consistent with the single redox buffer described by reaction 2.8 (*i.e.* its equilibrium constant).

Oxidation with air

When air was fed, the delayed breakthrough of O_2 showed that further oxidation occurred with Fe60Zr, because Fe_3O_4 does not react with steam, the reverse of reaction 2.4 being thermodynamically infeasible. No further oxidation was observed for $Ca_2Fe_2O_5$, which indicates that steam is sufficient to fully oxidise the material, consistent with reaction 2.8 (the initial overshoot in the concentration of O_2 is an experimental artefact caused by the mixing of pressurised air and N_2). Lastly, no CO_x was evolved, indicating that the steam was sufficient to remove all carbon deposits.

2.4 Discussion

The following is an analysis for predicting the behaviour of an idealised equilibrium reactor when it is producing H_2, for comparison with the observed experimental results. Consider the situation where a reactor contains an initially fully reduced oxygen carrier.

Steam is fed to the reactor, with H_2 and steam exiting the reactor. An unsteady state molar balance of oxygen around the reactor then states (neglecting the inventory of oxygen in the gas phase, which is acceptable since the molar density of the solid is much greater than that of the gas):

$$\dot{N}_{\mathrm{H_2O,in}} = \dot{N}_{\mathrm{H_2O,out}} + \frac{dn}{dt} \tag{2.13}$$

where $\dot{N}_{i,\mathrm{in}}$ and $\dot{N}_{i,\mathrm{out}}$ are the molar flows of species i into and out of the reactor, respectively, n is the number of moles of O within the reactor and t is time.

A molar balance of hydrogen states:

$$\dot{N}_{\mathrm{H_2O,in}} = \dot{N}_{\mathrm{H_2O,out}} + \dot{N}_{\mathrm{H_2,out}} \tag{2.14}$$

Equations 2.13 and 2.14 then give:

$$\dot{N}_{\mathrm{H_2,out}} = \frac{dn}{dt} \tag{2.15}$$

The definition of the instantaneous conversion of steam (equation 2.10) states:

$$x_{\mathrm{H_2O}}(t) = \frac{\dot{N}_{\mathrm{H_2,out}}}{\dot{N}_{\mathrm{H_2O,in}}} \tag{2.16}$$

The definition of the conversion of the bed of oxygen carrier (equation 2.12) states:

$$X_{\mathrm{O}}(t) = \frac{n}{n_{\mathrm{O}}} \tag{2.17}$$

where n_{O} is the total oxygen-carrying capacity of the reactor.

Equations 2.15-2.17 then give:

$$dt = \frac{n_{\mathrm{O}}}{\dot{N}_{\mathrm{H_2,out}}} dX_{\mathrm{O}} = \frac{n_{\mathrm{O}}}{\dot{N}_{\mathrm{H_2O,in}} x_{\mathrm{H_2O}}} dX_{\mathrm{O}} \tag{2.18}$$

Introducing now the definition of the cumulative conversion of steam (equation 2.11):

$$X_{\mathrm{H_2O}} = \frac{\int_0^t \dot{N}_{\mathrm{H_2,out}}\, dt}{\int_0^t \dot{N}_{\mathrm{H_2O,in}}\, dt} \tag{2.19}$$

Equations 2.18 and 2.19 then finally give:

$$X_{\mathrm{H_2O}} = \frac{X_{\mathrm{O}}}{\int_0^{X_{\mathrm{O}}} \frac{1}{x_{\mathrm{H_2O}}} dX_{\mathrm{O}}} \tag{2.20}$$

It is now required to evaluate the integral by determining how the instantaneous conversion of steam $x_{\mathrm{H_2O}}$ varies with the conversion of the bed X_{O}. Now if the oxidation state of the bed changes uniformly from an initially fully reduced state, then any local molar ratio of lattice oxygen to iron can be related to the bulk conversion of the bed:

$$\frac{n}{n_{\mathrm{Fe}}} = \frac{n_{\mathrm{O}}}{n_{\mathrm{Fe}}} X_{\mathrm{O}} = \frac{3}{2} X_{\mathrm{O}} \tag{2.21}$$

where the factor of 3/2 corresponds to the fully oxidised state being Fe_2O_3. The oxidising potential of the oxygen carrier is dependent on the local ratio of (active) lattice oxygen to iron (with numerical values given below appropriate for 1123 K (Giddings and Gordon, 1973; Barin, 1995)):

$$\log\left(\frac{p\mathrm{O_2}}{1\ \mathrm{bar}}\right) = \begin{cases} 1.0531M + B & 0 < \frac{n}{n_{\mathrm{Fe}}} < 1.0531 \quad \mathrm{I-W\ transition} \\ \frac{n}{n_{\mathrm{Fe}}} M + B & 1.0531 < \frac{n}{n_{\mathrm{Fe}}} < 1.1217 \quad \mathrm{W\ phase\ field} \\ 1.1217M + B & 1.1217 < \frac{n}{n_{\mathrm{Fe}}} < \frac{4}{3} \quad \mathrm{W-M\ transition} \\ -7.48 & \frac{4}{3} < \frac{n}{n_{\mathrm{Fe}}} < \frac{3}{2} \quad \mathrm{M-H\ transition} \end{cases} \tag{2.22}$$

where $p\mathrm{O_2}$ is the partial pressure of oxygen in equilibrium with the oxygen carrier, *M* and *B* are temperature-dependent empirical constants reported by Giddings and Gordon (1973). $\log p\mathrm{O_2} = -7.48$ for the magnetite-haematite transition was calculated from tabulated data (Barin, 1995). I, W, M and H denote iron, wüstite, magnetite and haematite, respectively. Equations 2.21 and 2.22 allows $p\mathrm{O_2}$ to be expressed as a function of X_{O}.

The equilibrium constant for the combustion of H_2, $K_{\mathrm{H_2}}$, can be used to express the oxidising potential in terms of an equivalent ratio of steam to H_2 (*i.e.* the equilibrium constant for the reduction of the oxygen carrier *K*):

$$K = p\mathrm{H_2O}/p\mathrm{H_2} = K_{\mathrm{H_2}} p\mathrm{O_2}^{1/2} \tag{2.23}$$

which specifies the equilibrium ratio of steam to hydrogen as a function of X_{O}.

In this ideal case, it is assumed that the kinetics are sufficiently fast for the gases to be always in equilibrium with the oxygen carrier, so $x_{\mathrm{H_2O}}$ can be calculated from the equilibrium constant, which, in turn, is specified by the state of conversion of the bed.

$$x_{\mathrm{H_2O,ideal\ ii}} = \frac{1}{K(X_\mathrm{O}) + 1} = f(X_\mathrm{O}) \tag{2.24}$$

where the dependence of $K(X_\mathrm{O})$ on the conversion of the bed is specified by equations 2.21-2.23. This final relationship then allows the integral in equation 2.20 to be evaluated, yielding one of the idealised profiles in Figure 2.7 (D), discussed below.

The observed conversions of steam varying with the conversion of the bed are shown in Figure 2.7. The conversions of the bed have been normalised to reflect the difference in H_2-production capacity between unmodified iron oxide and $Ca_2Fe_2O_5$, being 88.9% and 100% of the oxygen carrying capacity, respectively. Figure 2.7 also shows ideal scenarios where the conversion of the gas was constantly equilibrium-limited, assuming that the oxidation state of the bed changed either (i) in sharp fronts propagating axially or (ii) uniformly along the bed. The behaviour of ideal case (ii) is described by equations 2.20 and 2.24. It is apparent that the results match more closely to case (ii), suggesting there has been considerable dispersion along the bed (any mixing in the gas-phase would blur gradients both in the gas and solid phase, departing from case i).

In Figure 2.7 it can be seen that $Ca_2Fe_2O_5$ showed markedly higher conversions of up to 75% compared to 62% for Fe60Zr and, owing to its single phase transition, maintained a higher cumulative conversion across all states of conversion of the bed. Fe60Zr maintained 62% conversion as long as metallic iron was sufficiently active in the bed. When the metallic iron became depleted, the conversion dropped as the next least oxidising material is wüstite. The oxidising potential of wüstite is a function of its oxygen stoichiometry 1/*z* in Fe_zO (Giddings and Gordon, 1973), so as the wüstite phase was enriched in oxygen from $Fe_{0.950}O$, the equilibrium conversion of steam declined. The first decline in the conversion of steam was likely to be a convolution of (i) consumption of Fe and (ii) enrichment of the wüstite phase. Once wüstite became fully enriched (*i.e.* $Fe_{0.891}O$, in equilibrium with magnetite), magnetite (Fe_3O_4) started to form. This magnetite-wüstite redox buffer then briefly maintained the conversion of steam at 21% until the wüstite was consumed, with no further hydrogen produced.

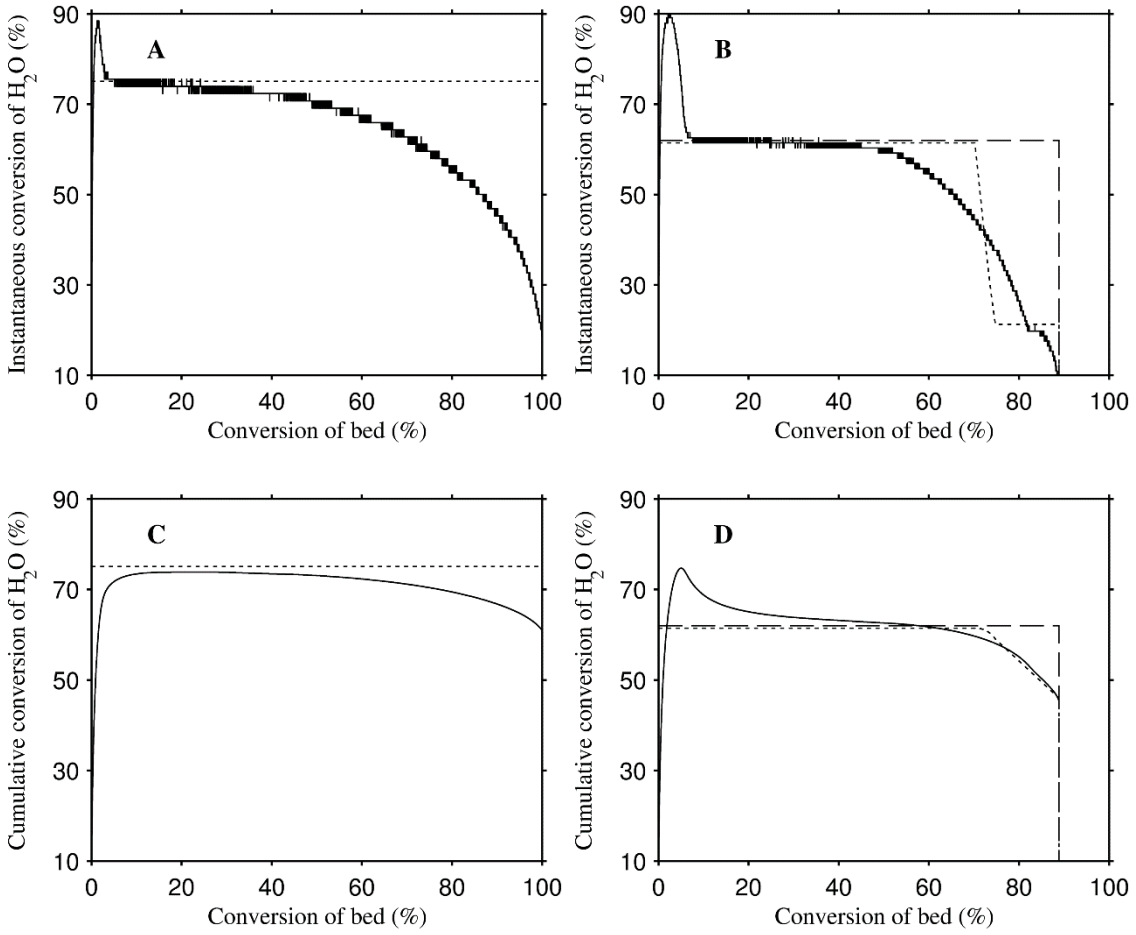

Figure 2.7. Conversions of steam *versus* the conversion of the bed of oxygen carrier. (A, B) Instantaneous conversions for $Ca_2Fe_2O_5$ and Fe60Zr, respectively. (C, D) Cumulative conversions for $Ca_2Fe_2O_5$ and Fe60Zr, respectively. Solid lines, dashed lines and dotted lines correspond respectively to experimental observations, the ideal case with sharp axial fronts, and the case with a uniform distribution of oxidation states (with equilibrium being attained at all times in the last two cases).

The enhancement of the conversion of steam through the use of $Ca_2Fe_2O_5$ over that of chemically unmodified iron oxide has been demonstrated. Furthermore, all of the oxygen carrying capacity in $Ca_2Fe_2O_5$ was available to produce hydrogen, whereas for Fe60Zr only oxygen from oxidising Fe to Fe_3O_4 is available (which is 89 mol% of the oxygen present in Fe_2O_3). This was sustained throughout the 10 cycles tested. XRD patterns of the fresh and cycled material, shown in Figure 2.4, also showed that $Ca_2Fe_2O_5$ was able to be fully regenerated and did not segregate into Fe_2O_3 and CaO. In Figure 2.7, the deviation of the conversion plots from ideality is due to the reactivity of the carrier decreasing as it nears full conversion. Use of longer beds or lower flow rates would be able to improve the conversion profiles, as suggested by assumptions adopted in a

modelling study of fixed beds operating at equilibrium (Heidebrecht and Sundmacher, 2009).

Drawbacks were observed in that $Ca_2Fe_2O_5$ gave a lower conversion of CO during reduction which could contaminate the CO_2 stream and render carbon capture and storage more difficult. Here, low conversions of CO arose from a decreased rate of reduction, but even at equilibrium at 1123 K, the maximum conversion of CO attainable by $Ca_2Fe_2O_5$ would be 23%, compared to 77% or 100% for Fe60Zr depending on if oxidation with air is used. This could be alleviated by using $Ca_2Fe_2O_5$ in a polishing operation (illustrated in Figure 2.8), where the mixture of H_2 and H_2O from the outlet of a bed of unmodified iron oxide would be fed into a bed of reduced $Ca_2Fe_2O_5$. With this arrangement at 1123 K, only 17% of the H_2-production capacity (on a molar basis) needs to be provided by the $Ca_2Fe_2O_5$ stage, with the other 83% provided by the unmodified Fe stage (assuming ideal breakthrough occurs in both beds simultaneously). This requires a smaller loading of $Ca_2Fe_2O_5$ than if all of the H_2-production capacity were to be provided by $Ca_2Fe_2O_5$ alone, thus drastically decreasing the time for complete reduction whilst achieving enhanced conversions of steam.

A further improvement would be, during the reduction step, to reverse the flow of syngas so that it is first fed to $Ca_2Fe_2O_5$ and then unmodified iron. Reversal of the flow maximises both the respective conversions of CO and H_2O during the reduction and oxidation steps, whereas the staged polishing arrangement decreases the amount of $Ca_2Fe_2O_5$ required for the enhancement in the conversion of steam. This configuration has also been proposed by other workers (He and Li, 2015; Kathe *et al.*, 2016). The reactive gases are sequentially exposed to materials of increasing driving force (*i.e.* decreasing oxidising potential for the oxidation step, or increasing oxidising potential for the reduction step).

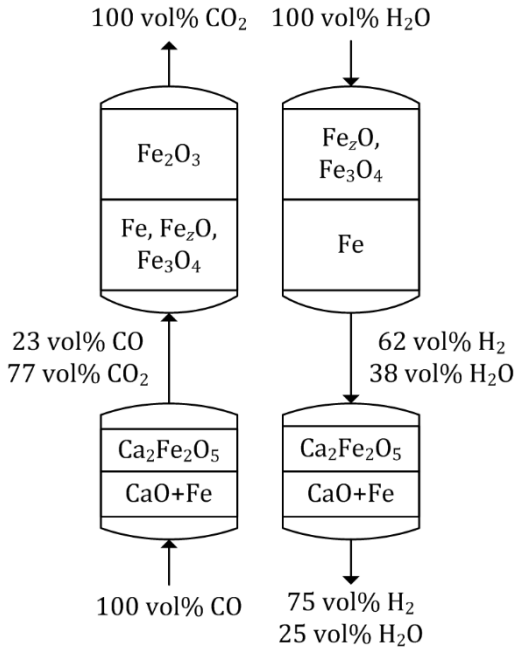

Figure 2.8. Illustration of the polishing concept in combination with reversal of the flows operating at 1123 K. The flow direction during reduction (left) and oxidation (right) are reversed in order to maximise the conversion of the feed gases.

2.5 Conclusions

The performance of a rationally-designed oxygen carrier $Ca_2Fe_2O_5$ was verified by comparison with 60 wt% Fe_2O_3-ZrO_2 (Fe60Zr). Experiments conducted in a packed bed reactor confirmed that, at 1123 K, $Ca_2Fe_2O_5$ achieved higher conversions of steam of 75% compared to 62% for Fe60Zr. This came at the cost of lower conversions of CO, but this can be offset with adaptations in the process design. A proposed modification is a polishing operation where the composition of the product gases (H_2 and steam) from a bed of unmodified iron oxide is polished in a subsequent bed of $Ca_2Fe_2O_5$, thus decreasing the required amount of $Ca_2Fe_2O_5$. The flow may also be reversed during oxidation and reduction, maximising the respective conversions of CO and H_2O.

3 ENHANCING THE CAPACITY OF OXYGEN CARRIERS FOR SELECTIVE OXIDATIONS THROUGH PHASE COOPERATION: BISMUTH OXIDE AND CERIA-ZIRCONIA

3.1 Introduction

Selective oxidation reactions constitute an important class of reactions undertaken industrially for the production of organic intermediates. The predominant approach is to perform these reactions catalytically over transition metal oxides by co-feeding the organic reactant with the oxidant, typically molecular oxygen. A chemical looping mode of operation, sometimes referred to as 'cyclic', 'redox' or 'anaerobic' mode, has been suggested by several workers (Vrieland and Murchison, 1996; Creaser *et al.*, 1999; Kuang *et al.*, 1999; Tsikoyiannis *et al.*, 1999; de Graaf *et al.*, 2004; Patience and Bockrath, 2010), but has often been overlooked in favour of operating in steady state with co-feed of the organic molecule and gaseous oxygen for its simplicity in implementation.

An important example of a semi-commercial application of this technology was Dupont's process for oxidising *n*-butane to maleic anhydride, undertaken in a circulating fluidised

bed (CFB) (Patience and Bockrath, 2010). Although this process had seen significant improvement through its lifetime between the 1980s and the 2000s (Contractor *et al.*, 1988), vanadium pyrophosphate was used as the oxygen carrier (or catalyst, depending on the reactor configuration) and suffered from a low oxygen-carrying capacity, of the order of 0.2 wt% (kg O/kg carrier). Oxygen carriers used for combustion typically range from 5–25 wt%. For chemical syntheses, lower capacities necessitate lower partial pressures of reactant, otherwise the carrier quickly becomes severely reduced which tends to cause coking. Lower capacities might, to some extent, be compensated for by adjusting operating parameters such as using a higher solid circulation rate (as in circulating fluidised beds) or higher frequency of cycling (as in packed bed reactors) but at an economic trade-off with higher operating costs. Higher capacities are therefore advantageous for chemical looping operation (Godefroy *et al.*, 2010).

In general, a suitable oxygen carrier needs to be (i) highly active, (ii) highly selective, (iii) highly stable with respect to repeated cycles of redox, (iv) have a sufficiently high oxygen-carrying capacity, and (v) be sufficiently cheap to manufacture. The problem is compounded because the selectivity and activity of the material might change substantially as its oxidation state alters with progress of the reaction (*e.g.* combustion may be prominent when the carrier is fully oxidised, whereas coking may occur when the carrier is deeply reduced). For some reactions, one material might not possess all relevant properties. Here, the proposition is to use structured composite materials for kinetically-controlled selective oxidations, with the surface decorated with selective active sites. This selective phase is stabilised on an active support, *e.g.* an oxygen-permeable solid that can provide additional lattice oxygen to the active sites. Lattice oxygen may be drawn from the solid itself if it is reducible. The hypothesis is that the gas preferentially reacts with the selective phase, which, in turn, is regenerated with oxygen from the electrolyte either by bulk diffusion or by reverse spillover at the triple phase boundary. The resulting synergistic composite is then both selective and stable, performing better than the sum of the separate components, enabled by phase cooperation (Grasselli, 2002, 2014). Side reactions of the gas with the electrolyte may be much slower than with the selective active sites or be physically inhibited by the selective phase acting as a barrier. This approach is easier than screening for a single material with all the required properties.

This chapter demonstrates this proposed concept for a model reaction scheme, chosen to be the selective combustion of hydrogen in the presence of ethylene. This reaction has had some historical interest in the context of the oxidative dehydrogenation (ODH) of

light alkanes, specifically the two-step process (Tsikoyiannis *et al.*, 1999; Beckers *et al.*, 2009). This reaction was chosen because it is possible to analyse rapidly and quantitatively the gaseous products H_2O and CO_2. Accordingly, the reactions during the reduction step in the chemical looping cycle are reactions 3.1 and 3.2, with reoxidation described by reaction 3.3 (applicable for a Bi-based oxygen carrier):

$$\frac{1}{3}\mathrm{Bi_2O_{3(s)}} + \mathrm{H_{2(g)}} \rightleftharpoons \frac{2}{3}\mathrm{Bi_{(l)}} + \mathrm{H_2O_{(g)}} \qquad \Delta H°_{500°C} = -50.6\ \mathrm{kJ\ mol^{-1}} \qquad (3.1)$$

$$2\mathrm{Bi_2O_{3(s)}} + \mathrm{C_2H_{4(g)}} \rightleftharpoons 4\mathrm{Bi_{(l)}} + 2\mathrm{CO_{2(g)}} + 2\mathrm{H_2O_{(g)}} \quad \Delta H°_{500°C} = -148.1\ \mathrm{kJ\ mol^{-1}} \qquad (3.2)$$

$$\frac{2}{3}\mathrm{Bi_{(l)}} + \frac{1}{2}\mathrm{O_{2(g)}} \rightleftharpoons \frac{1}{3}\mathrm{Bi_2O_{3(s)}} \qquad \Delta H°_{500°C} = -196\ \mathrm{kJ\ mol^{-1}} \qquad (3.3)$$

For the selective combustion of hydrogen in the presence of hydrocarbons, bismuth oxide (Grasselli *et al.*, 1999b) and doped ceria (Rothenberg *et al.*, 2003; Beckers and Rothenberg, 2010) have previously been demonstrated to be selective carriers. Bismuth oxide and metallic bismuth have low melting points (817°C and 272°C, respectively) which makes them prone to deactivation. Stabilisation with a support is therefore necessary, but this decreases the gravimetric oxygen-carrying capacity if it is inert. A possible candidate active support is ceria, which is stable and conducts oxide ions but needs to be doped to be selective. These dopants could be Bi or W (Rothenberg *et al.*, 2003; Beckers *et al.*, 2009). Zirconia is often mixed with ceria to increase its stability and oxygen-carrying capacity at a given temperature (Kim *et al.*, 2006; Montini *et al.*, 2016). A combination of bismuth oxide supported on ceria-zirconia has been shown to be active, selective and stable (de Graaf *et al.*, 2004), but the effect of the support on the innate selectivity of bismuth has not been established. The effect of the composition of the support was also not established. Ceria is also interesting because it has similar lattice parameters to those of certain polymorphs of bismuth oxide, thereby promoting phase cooperation (Grasselli, 2014). This chapter explores the effect of an active support on the selectivity. Accordingly, a range of ceria-zirconia supported bismuth oxides was prepared, and their performances for reactions 3.1 and 3.2 were evaluated in a packed bed reactor in chemical looping mode.

3.2 Experimental

3.2.1 Preparation of oxygen carriers

The oxygen carriers were composed of 25 wt% Bi_2O_3 supported on $Ce_xZr_{1-x}O_{2-\delta}$. The ceria-zirconia supports were synthesised using a citrate-gel method (Kaspar *et al.*, 2003); the resulting particles were subsequently wet-impregnated with a solution of bismuth nitrate, dried, and then calcined. Briefly, stoichiometric quantities of $Ce(NO_3)_3{\cdot}6H_2O$ (Sigma-Aldrich, purity 99% trace metals basis), $ZrO(NO_3)_2{\cdot}xH_2O$ (Sigma-Aldrich, purity 99 %, 35.9 wt% ZrO_2) and citric acid (Sigma-Aldrich, purity ≥ 99.5%) with a citric acid to metal ion ratio of 2:1 were dissolved in reverse osmosis water. The total concentration of metal ions was 1 M. The mixture was then heated in an oven to dryness at 120°C for 12 h, forming a xerogel, which was subsequently calcined in a furnace at 200°C for 1 h. The resulting brown gel was crushed and calcined again at 600°C for 3 h, yielding a fine powder of $Ce_xZr_{1-x}O_{2-\delta}$. Bismuth was then added to the supports by wet impregnation. Thus, $Bi(NO_3)_3{\cdot}5H_2O$ (Sigma-Aldrich, purity ≥98%) was dissolved in pH 0 nitric acid (Fisher Scientific) to prevent precipitation. The acidified bismuth nitrate solution (bismuth concentration 0.477 M) was then mixed with the ceria-zirconia support in a ratio of 3 mL of solution per gram of support, with ultrasonication in a bath for 10 min to aid mixing. The slurry was then heated in an oven at 120°C to dryness for 12 h, followed by calcination in a furnace at 600°C for 3 h. For experiments in a packed bed, the powders were pelletised by compression at 100 MPa, crushed, then sieved to a sieve size range of 212 – 300 µm. Five oxygen carriers were synthesised in this study and are denoted Bi25Ce*x*Zr where x = [0, 25, 50, 75, 100] refers to the mole percent of ceria in the ceria-zirconia support (*e.g.* 25 wt% Bi_2O_3 supported on $Ce_{0.50}Zr_{0.50}O_{2-\delta}$ is denoted as Bi25Ce50Zr). The loading of 25 wt% Bi_2O_3 was chosen to ensure the support was covered by Bi_2O_3. The theoretical loading of Bi_2O_3 required for a monolayer coverage over CeO_2 was estimated from the surface density of oxygen on CeO_2. The surface densities are 7.9 atoms/nm^2, 9.6 atoms/nm^2 and 6.8 atoms/nm^2 for the (111), (110) and reconstructed (100) planes of CeO_2, respectively (Mullins, 2015). Using the highest value of 9.6 atoms/nm^2 to give a conservative estimate, and taking a specific surface area of, say, 50 m^2/g CeO_2, this corresponds to 0.80 mmol surface O/g CeO_2. The ratio of Bi:O in Bi_2O_3 then specifies the loading of Bi, which is 0.53 mmol Bi/g CeO_2. This corresponds to 0.124 g Bi_2O_3/g CeO_2, or 11.1 wt% Bi_2O_3. The ceria-zirconia supports used had less than the assumed value of 50 m^2/g, which makes this estimate conservative. An excess loading of 25 wt% was used to give additional margin for *e.g.* non-uniform coverage.

3.2.2 Characterisation

A thermogravimetric analyser (TGA/DSC1, Mettler Toledo), described previously in section 2.2, was used to measure the oxygen-carrying capacity of the samples by temperature-programmed reduction (TPR). The TPR in diluted H_2 was performed at a heating rate of 10°C/min from 150°C to 600°C, followed by holding at 600°C for 10 min. Approximately 40 mg of freshly-calcined sample was placed in a 70 µL alumina crucible within the reaction chamber. The sample was initially dried for 10 minutes at 600°C in a flow of Ar (50 mL/min, all volumetric flow rates reported were measured at 293 K and 1 atm), followed by the TPR with an additional flow of 5 vol% H_2 in N_2 (50 mL/min). The oxygen-carrying capacity was calculated by assuming that the change in mass during reduction was solely due to the carrier losing lattice oxygen. A subsequent temperature-programmed oxidation (TPO) was then performed, where the flow of H_2 was substituted for air (50 mL/min).

Powder X-ray diffraction (XRD) was used to analyse the crystalline phases of the oxygen carriers. The patterns were measured on a commercial instrument (Empyrean, PANalytical) using Cu-Kα radiation with a voltage of 40 kV and a current of 40 mA. Samples were first ground to a fine powder (< 67 µm) before being loaded into the *ex situ* sample holders. The instrument was arranged in a Bragg-Brentano geometry. The reference patterns used to identify the phases were ICSD-60900 (m-ZrO_2), ICSD-85322 (t-ZrO_2), ICSD-88759 (CeO_2), ICSD-94229 (α-Bi_2O_3), ICSD-417638 (β-Bi_2O_3), ICSD-98144 (δ-Bi_2O_3).

X-ray photoelectron spectrometry (XPS) was used to analyse the surface composition of the oxygen carriers. The spectrometer (ESCALAB 250Xi, Thermo Fisher Scientific) was equipped with an Al-Kα (1486.6 eV) X-ray source, and the analysis was conducted under an ultrahigh vacuum ($<10^{-10}$ mbar). Binding energies were calibrated using the C(1s) peak (284.6 eV).

Nitrogen physisorption isotherms were measured at -196°C using a Micromeritics ASAP 2020 instrument. Approximately 0.10 g of sample was used, which was degassed under vacuum at 150°C for 1 h prior to the measurements. The isotherms were modelled using the Brunauer, Emmett and Teller (BET) method (Brunauer *et al.*, 1938).

Transmission Electron Microscopy (TEM) was used to analyse the morphology of the oxygen carriers. The samples were prepared by ultrasonically dispersing the powdered oxygen carriers in deionised water. A droplet of this transparent suspension was loaded

onto holey carbon film on a 400 mesh copper grid (Agar Scientific), followed by drying in a vacuum oven at 80°C. High-resolution TEM (HRTEM) images were obtained using a Tecnai F20 system at 200 kV with a high brightness field emission gun (FEG). High angle annular dark field (HAADF) scanning TEM (STEM) was coupled with energy-dispersive X-ray spectroscopy (EDX), performed with an Oxford EDX detector, to obtain elemental maps of the materials.

3.2.3 Packed bed reactor

The downflow packed bed reactor consisted of an 8 mm i.d., 560 mm long quartz tube with a sintered disc fixed 255 mm from the bottom, mounted vertically. The tube was inserted into the bore of an electrically-heated furnace, the ends of which were plugged with insulating refractory fibres. The output of the furnace was controlled by a type N thermocouple with a mineral-insulated Nicrobell D sheath inserted into the bed. The bed was packed above the sintered disc, with a bottom layer of 3 g of coarse SiC (Alfa Aesar, 46 grit) to position the active bed in the isothermal region of the furnace, then a middle layer with the carrier (diluted with SiC to eliminate limitations on heat transfer), then finally another layer of 2.5 g of SiC on top to preheat the feed. Both ends of the quartz tube were connected to Swagelok Ultra-Torr® vacuum fittings and sealed with fluorocarbon FKM O-rings. All upstream tubing was metal with compression fittings to minimise any ingress of moisture and oxygen. The line from the reactor outlet to the housing of the humidity sensor was trace heated to prevent condensation of moisture.

The feed gases to the reactor were supplied from cylinders (Air Liquide), and consisted of separate cylinders of (i) 5.4 vol% ethylene, (ii) 4.81 vol% H_2, (iii) 5.03 vol% O_2, and (iv) pure N_2 (purity > 99.998 %). The balance gas was always N_2. Gas flows were manipulated by calibrated rotameters. The gas analysis was accomplished by a set of online analysers in series. These were, in order from upstream to downstream: for H_2O (IST, HYT 271, capacitive polymer humidity and temperature sensor), H_2 (ABB, EL3020 Caldos27, thermal conductivity), CO, CO_2 (ABB, EL3020 Uras26, NDIR), and O_2 (ABB, EL3020 Magnos206, paramagnetic). A drying tube packed with $CaCl_2$ was fitted between the humidity sensor and thermal conductivity sensor to remove moisture. The gas channels (H_2, CO, CO_2, and O_2) were calibrated using certified gas cylinders (4.81 vol% H_2 in balance N_2, 10.0 vol% CO in balance N_2, 10.0 vol% CO_2 in balance N_2, and 5.03 vol% O_2 in balance N_2). The H_2O channel was calibrated by feeding calibrated concentrations of H_2 (mixed by diluting a calibrated flow of 4.81 vol% H_2 with a

calibrated flow of pure N_2, and verified by measurement with the thermal conductivity detector) through a packed bed of copper oxide held at 400°C – the outlet of which was assumed to contain H_2O equal to the concentration of H_2 at the inlet (this was supported by the constant levels of H_2O measured by the sensor not decreasing over time, which meant that total conversion of H_2 to H_2O was achieved). The error in the measurement of H_2O was found to be no more than 3% relative to the actual concentration. Offline gas chromatography (GC) equipped with a flame ionization detector (FID) was used to measure CH_4, C_2H_6 and C_2H_4 (Agilent, 6850), with separation achieved by a porous layer open tubular column (Agilent, GS-GasPro). The FID signals were calibrated using external standards from certified gas mixtures (50.65 vol% C_2H_6 in balance N_2, and 5.4 vol% C_2H_4 in balance N_2), with the exception of CH_4 being calibrated by multiplying the response factor for C_2H_6 by two (*i.e.* the effective carbon number of C_2H_6, 2.0, divided by the effective carbon number of CH_4, 1.0) (Scanlon and Willis, 1985). The gas samples were withdrawn through a septum seal on the reactor exhaust line.

In the integral bed experiments, 0.10 g of the carrier, diluted with 0.80 g of SiC, was loaded into the packed bed to measure selectivity and activity. The chemical looping operation consisted of two stages: (i) reduction in a mixture of 2.5 vol% H_2, 2.5 vol% C_2H_4, (ii) oxidation in 5 vol% O_2, with nitrogen purges between stages. The operating temperature ranged from 450 to 550°C. The reducing feed was an equimolar mixture of H_2 and C_2H_4 to emulate the products from a catalytic dehydrogenation process. C_2H_6 was omitted for simplicity because it has been shown to be much less reactive than C_2H_4 (Tsikoyiannis *et al.*, 1999). Each stage progressed until no further reaction was observed. The hydrogen and carbon molar balances between the feed and the products were always within ±5%. A control was performed at 550°C in which the reactor was packed with only SiC: no detectable conversions of H_2 or C_2H_4 were measured. All packed bed experiments were analysed using standard diagnostic criteria for heat and mass transfer limitations: axial dispersion (Mears, 1971b; Gierman, 1988); bed dilution (Berger *et al.*, 2002); particle external (Froment *et al.*, 2011) and internal mass transfer (Vannice, 2005); particle external and internal heat transfer and bed radial heat transfer (Mears, 1971a). It was revealed that the only limitation on the observed rates of reaction were at higher conversions due to the supply of reactant. The oxygen-carrying capacity of the materials was calculated by integrating the oxygenated products in the off-gas, using:

$$n_{\mathrm{O}} = \frac{F}{W} \int_{t_{\mathrm{start}}}^{t_{\mathrm{end}}} y_{\mathrm{H_2O}}(t)\, dt \tag{3.4}$$

where n_O is the specific oxygen-carrying capacity of the sample, F is the total molar flow rate of gas, W is the mass of the oxygen-carrier loaded into the bed, and y_{H_2O} is the mole fraction of steam. Also, t_{start} is the time when steam was first detected and t_{end} the time when the reaction ended (*i.e.* when there was no further conversion of the gases). The contribution from CO_2 was neglected because it was negligibly small and subject to noise; in fact, CO_2 contributed only 2% to the measured capacity in the worst case, for Bi25Ce100Zr at 550°C.

For kinetic measurements, the packed bed reactor (*n.b.* a fluidised bed reactor was unsuitable because the prepared particles were too friable) was operated in differential mode, *i.e.* the conversion of the feed was less than 10% at all times, to minimise axial gradients in chemical composition. This was achieved by varying the flow rate and the mass of the carrier loaded into the bed; the residence time here was much smaller than in the integral bed experiments. Because of the short bed lengths, the oxygen carrier in these experiments was pelletised to 90 – 150 µm sieve diameter (with 120 grit SiC, Alfa Aesar, used as the inert diluent) to minimise the influence of bed dilution on the measured kinetics, by increasing the bed length:particle diameter ratio (Berger *et al.*, 2002). In a typical experiment, the bed was packed and heated to the desired temperature (in the range 450 – 550°C). A cycle consisted of an oxidation step in 5 vol% O_2, then a subsequent purge in N_2 for 3 min, then a reduction step in 4.81 vol% H_2 until no products were detected. The molar flowrate of the evolved steam during the reduction step gave a measure of the kinetics at that particular temperature. For any temperature, the cycle was repeated to check for deactivation of the carrier; deviation in the measured activity (*viz.* the apparent first order rate constant for the combustion of H_2 at zero conversion of the carrier) was usually less than 5%. The temperature was then ramped to a higher setpoint to measure the apparent activation energy. At the end of the series of experiments, deactivation of the carrier was checked again by repeating an earlier experiment; deviation in the measured activity was usually less than 10%.

The concentration profiles of steam, from the differential bed, were deconvoluted from the response of the humidity sensor by using a first order lag model. Thus, the deconvoluted mole fraction of steam was calculated using:

$$y_{corrected}(t) = y_{measured}(t) + t_{mix}\frac{dy_{measured}(t)}{dt} \tag{3.5}$$

where $y_{\text{corrected}}$ is the deconvoluted mole fraction of steam, y_{measured} is the measured value, and t_{mix} is the characteristic response time of the humidity sensor which was determined experimentally from a step change of steam to the sensor at various flow rates (the equivalent 'mixing volume' was determined to be 28 mL, corresponding to t_{mix} between 3.4 – 11.0 s for the utilised flow rates of 150 – 500 mL/min). The derivative was calculated using a central difference scheme spanning six intervals in time (Fornberg, 1988):

$$\left(\frac{dy}{dt}\right)_i = \frac{y_{i+3} - 9y_{i+2} + 45y_{i+1} - 45y_{i-1} + 9y_{i-2} - y_{i-3}}{60(t_{i+1} - t_{i-1})} \tag{3.6}$$

where y_i is the i^{th} measurement of the concentration at time t_i.

The response time of the sensor t_{mix} was generally greater than the characteristic reaction time by at least a factor of 5 (this is discussed in section 3.3.4). Practical limitations on t_{mix} arose because of significant pressure drops along the bed at higher flow rates – flow rates above 500 mL/min were not used because the pressure drop exceeded 0.2 bar.

The corrected mole fraction of steam was used to calculate the specific rate of reaction, r, at time t, using:

$$r(t) = \frac{F}{W} y_{\text{corrected}}(t) \tag{3.7}$$

The conversion of the solid, X_{O}, was calculated using:

$$X_{\text{O}}(t) = \frac{\text{cumulative moles of O released}}{\text{total moles of O released}} = \frac{\int_{t_{\text{start}}}^{t} y_{\text{H}_2\text{O}}(t)\, dt}{\int_{t_{\text{start}}}^{t_{\text{end}}} y_{\text{H}_2\text{O}}(t)\, dt} \tag{3.8}$$

The peak conversion of H_2, X_{H_2}, was calculated using:

$$X_{\text{H}_2} = \frac{\max(y_{\text{corrected}}(t))}{y_{\text{H}_2,\text{in}}} \tag{3.9}$$

where $\max(y_{\text{corrected}}(t))$ is the highest deconvoluted mole fraction of H_2O observed during the reduction step, and $y_{\text{H}_2,\text{in}}$ is the mole fraction of H_2 in the feed. The peak conversion of C_2H_4, $X_{\text{C}_2\text{H}_4}$, was calculated on a C-mole basis from experiments where only C_2H_4 was fed, using:

$$X_{\text{C}_2\text{H}_4} = \frac{1}{2} \frac{\max(y_{\text{CO}_2}(t))}{y_{\text{C}_2\text{H}_4,\text{in}}} \tag{3.10}$$

where $\max(y_{CO_2}(t))$ is the highest mole fraction of CO_2 observed during the reduction step, and $y_{C_2H_4,in}$ is the mole fraction of C_2H_4 in the feed.

The rate constant for the combustion of species i, k_i, was calculated from the peak conversion X_i using:

$$k_i = \frac{F}{WP} \ln \frac{1}{1 - X_i} \tag{3.11}$$

where F is the total molar flowrate of gas, W is the mass of oxygen carrier in the packed bed, P is the absolute pressure (1 bara), and X_i is the peak conversion of species i. This expression assumes that the reactor behaved like a plug-flow reactor with first order kinetics; this was verified as given in section 3.3.3, below. Comparing the peak conversions of gas simplifies the kinetic analysis and avoids complications associated with structural changes in the solid as the reaction progresses.

3.3 Results

3.3.1 Characterisation

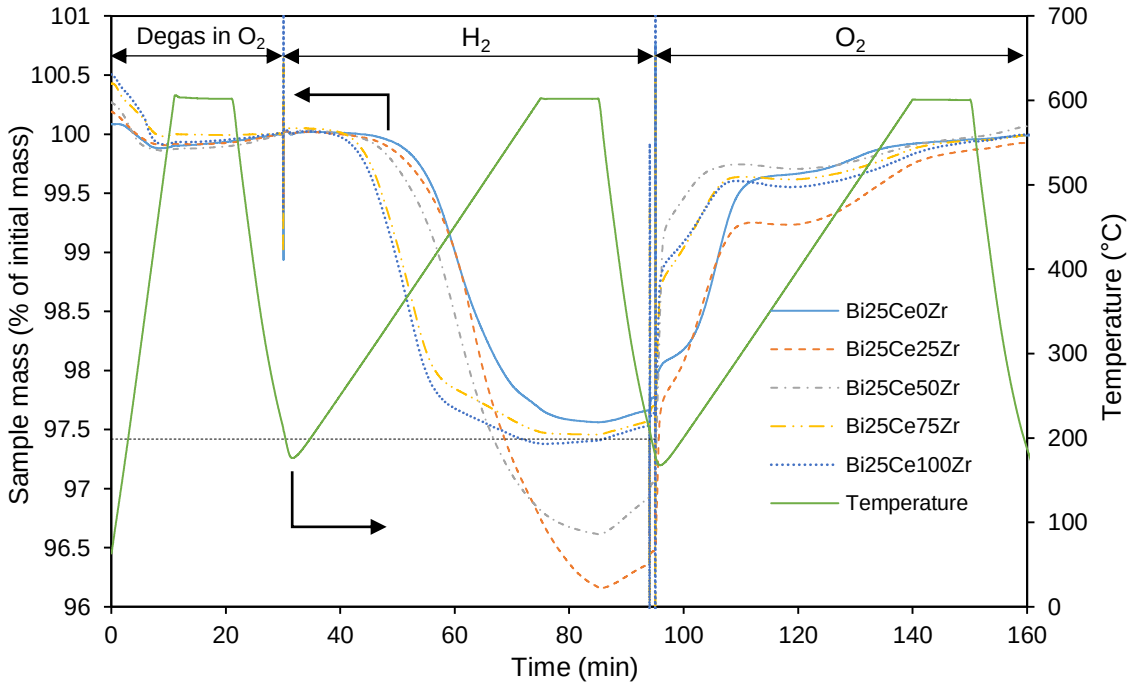

Figure 3.1. Thermogravimetric analysis (TGA) of the supported bismuth oxide samples. The samples were first degassed in flowing air, followed by TPR in H_2 and TPO in air. The temperature was ramped from 150°C to 600°C at a rate of 10°C/min. The initial mass was taken at the start of the TPR at 30 min. The spikes in the mass are artefacts caused

by the switching of gases. The dashed horizontal line at 97.42 wt% represents the theoretical mass of a completely reduced sample of Bi25Ce0Zr.

Figure 3.1 shows how the mass of the prepared oxygen carriers varied during the thermogravimetric analysis (TGA). The onset of reduction by H_2 occurred approximately at 270-360°C, with a higher ceria content resulting in lower temperatures. The samples lost varying amounts of mass by the end of the TPR, which was caused by the different degrees of reducibility of the supports. The bismuth oxide component was almost completely reduced, as shown by the total mass lost by the Bi25Ce0Zr sample (2.44 wt%, close to the expected value of 2.58 wt%, marked at 97.42 wt%). Two samples, Bi25Ce25Zr and Bi25Ce50Zr, were not completely reduced by the end of the TPR. A large increase in mass was observed at the start of the TPO, indicating that reoxidation is fast. All samples were able to regenerate their original mass by the end of the TPO. Table 3.1 shows the characterisation of the oxygen carriers by N_2-physisorption and TGA. Before impregnation with 25 wt% Bi_2O_3 (but after the first calcination at 600°C), the surface areas generally increased with an increase in Zr content, with the exception of the sample of pure zirconia. After impregnation and the final calcination at 600°C, a significant amount of area was lost, possibly due to either the low melting point of pure Bi_2O_3 at 817°C facilitating sintering, or the hot concentrated nitric acid destroying the internal pore structure during impregnation. This resulted in a low surface area in the final product. The oxygen-carrying capacity of Bi25Ce0Zr was measured by TGA to be 2.44 wt%, which is sufficient to verify the bismuth loading of 25 wt%, corresponding to 2.58 wt%. The oxygen-carrying capacities showed that the addition of Ce increased the capacity, as expected. However, the precise values of the capacities, when measured by TGA, were different to those measured in the packed bed experiments. This was because of both the different temperature (TPR up to 600°C in the TGA, and isothermal at 450 – 550°C in the packed bed) and the sample in the TGA having undergone only a single cycle. In the packed bed experiments, the capacity displayed in the first cycle tended to be smaller (as low as 92% of the second cycle) than in subsequent cycles. Nevertheless, both reactors were generally in agreement, showing that intermediate ceria-zirconia compositions had a higher capacity.

Table 3.1. Characterisation by N_2-physisorption and TGA of the oxygen carriers. Surface areas of the carriers before and after impregnation with 25 wt% Bi_2O_3 are shown. The temperature-programmed reduction in diluted H_2 was performed at a heating rate of 10°C/min from 150°C to 600°C.

	BET surface area (m^2/g)		Oxygen-carrying capacity (g O/g carrier, %)
	Before impregnation	After impregnation	
Bi25Ce0Zr	3.7	2.5	2.44
Bi25Ce25Zr	45.6	3.7	3.84
Bi25Ce50Zr	39.8	5.2	3.38
Bi25Ce75Zr	33.3	7.2	2.54
Bi25Ce100Zr	11.1	7.6	2.66

Figure 3.2 shows the X-ray diffraction patterns for the materials before and after impregnation with 25 wt% Bi_2O_3. It can be seen that the supports were apparently present in the fluorite phase, but the broad peaks meant that phases of lower symmetry cannot be excluded (Montini *et al.*, 2016), with the exception of the ZrO_2 sample which presented both monoclinic and tetragonal phases. The peak positions shift with the addition of zirconia because the smaller size of the Zr^{4+} cation compared to the Ce^{4+} cation decreases the lattice parameter. Upon the addition of bismuth oxide, some samples presented additional peaks of low intensity which were attributed to α-Bi_2O_3. It was also found that β-Bi_2O_3 was present in Bi25Ce0Zr (*i.e.* 25 wt% Bi_2O_3 supported on ZrO_2), consistent with previous reports (Chen and Eysel, 1996; Jovalekić *et al.*, 2008). For the samples containing ceria, the low intensities of the bismuth phases could have been owing to a combination of (i) bismuth forming amorphous layers not detectable by diffraction, (ii) the doping of bismuth into the ceria or ceria-zirconia lattice, or (iii) broad overlapping peaks. There is also evidence of shifted peak positions upon the addition of Bi_2O_3, most apparent for the pure CeO_2 support, suggesting doping of the fluorite structure.

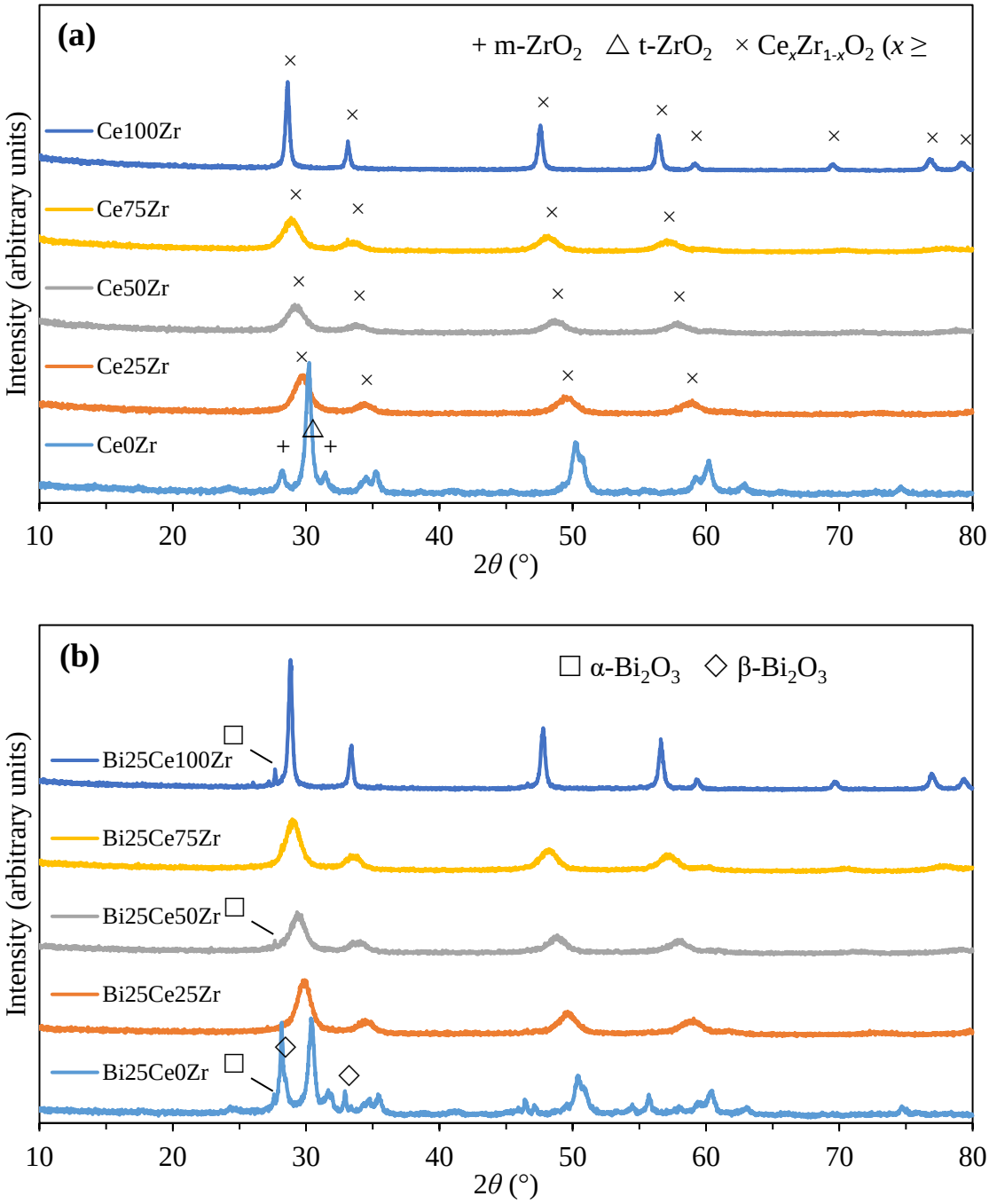

Figure 3.2. Powder X-ray diffraction patterns of the freshly calcined samples of (a) support and (b) supports impregnated with 25 wt% Bi_2O_3. Only peaks unique to each phase are marked. The apparent missing peaks at higher 2θ in the ceria-zirconia samples were likely to have been caused by low signal-to-noise ratios, owing to peak-broadening.

Table 3.2 summarises the near-surface (depth < ~10 nm) elemental compositions of the oxygen carriers, as measured by XPS. There was a deviation in the XPS measurements from the mean composition, because XPS is a surface-sensitive technique. It can be seen that (a) the surface is enriched with Bi, as expected from the impregnation procedure, and also (b) the Ce:Zr ratio is less than the bulk ratio, in agreement with other workers (de

Graaf *et al.*, 2004). Table 3.2 also shows the results for Bi25Ce75Zr reduced in H_2, showing a lower amount of Bi than in the freshly-calcined sample; this has also been reported by other workers and was attributed to the metallic bismuth phase dewetting the ceria-zirconia surface, with the bismuth oxide phase wetting the surface again when it was reoxidised (de Graaf *et al.*, 2004). As discussed in section 3.4, volatilisation of bismuth might also have been significant.

Table 3.2. Summary of XPS analysis on the oxygen carriers showing the oxygen-free composition of the surface of the powdered samples. The expected mean composition (calculated from the quantities of reagents in the preparation method) is also shown for comparison.

	XPS measurements			Mean composition		
	Bi mol%	Ce mol%	Zr mol%	Bi mol%	Ce mol%	Zr mol%
Bi25Ce0Zr	32	0	68	15.0	0	85.0
Bi25Ce25Zr	35	5.2	59	16.2	20.9	62.8
Bi25Ce50Zr	38	11	51	17.4	41.3	41.3
Bi25Ce75Zr	47	23	31	18.6	61.0	20.3
Bi25Ce100Zr	69	31	0	19.8	80.2	0
Reduced Bi25Ce75Zr	19	33	48	18.6	61.0	20.3

TEM images were obtained for Bi25Ce50Zr. In Figure 3.3 (a), it can be seen that the samples were composed of nanocrystalline particles. Fringe patterns were also visible, with an interplanar spacing of 0.30 nm corresponding to the (111) plane of ceria-zirconia. Under these *ex situ* conditions, amorphous material can also be seen on the surface. Figure 3.3 (b) shows EDS maps, confirming that Bi was homogeneously dispersed over the surface of each particle. The mean metal composition in Figure 3.3 (b) was found to be: 40% Ce, 37% Zr and 24% Bi. This differed from Table 3.2 because EDS is not as surface-sensitive because the incident electrons penetrate to a much greater depth, whereas photoelectrons in XPS can only escape from near the surface. This means that the XPS measurement is more relevant in this context of heterogeneous catalysis.

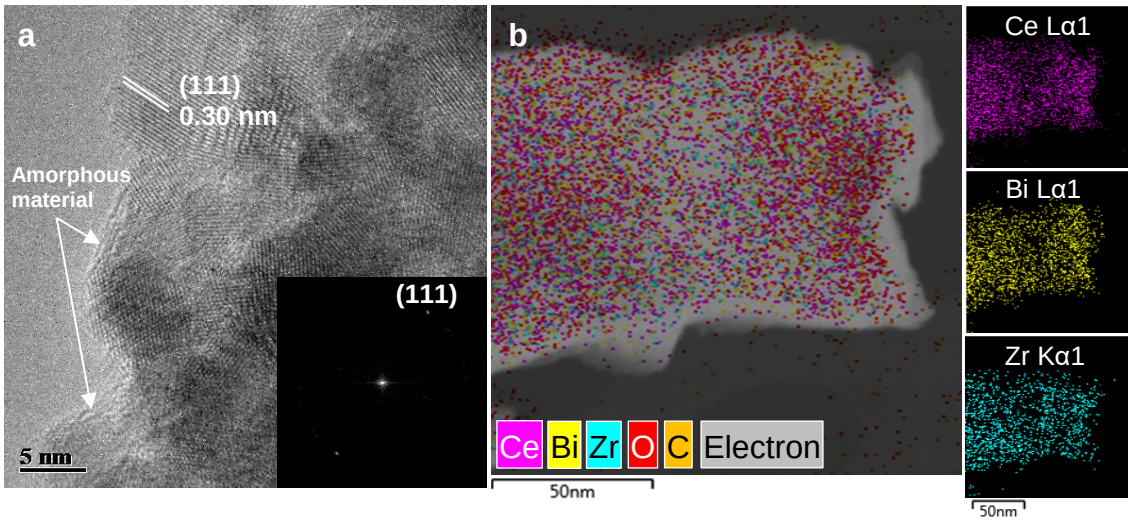

Figure 3.3. TEM images of fresh samples of Bi25Ce50Zr. (a) HRTEM image with fringe patterns corresponding to the (111) plane of ceria-zirconia. Inset: fast Fourier Transform (FFT). (b) HAADF-STEM image and EDS elemental maps of Bi Lα1, Ce Lα1 and Zr Kα1.

3.3.2 Packed bed reactor

Figure 3.4 shows a typical profile of the concentrations of components in the effluent gas during a chemical looping experiment in the integral bed. During the reduction stage, when C_2H_4 and H_2 were fed to the packed bed of carrier, the combustion products were composed almost entirely of steam, with only a small amount of CO_2 being detected (close to the resolution of the data acquisition at 0.01 vol%) at the start of the reaction, but decaying quickly. Furthermore, GC analysis did not detect any consumption of the ethylene. The rate of production of steam fell with the depletion of lattice oxygen. During the subsequent oxidation stage, consumption of gaseous O_2 was convoluted with the response of the analyser (the mixing time constant of the analyser, measured in response to a step change at the input of the sampling train, was 11 s, whereas the time constant observed during an oxidation stage at a lower temperature of 450°C was 12 s), suggesting that oxidation of the carrier with O_2 is fast. Tiny concentrations of CO_2 were detected, owing to the combustion of the small amounts of coke deposited during the preceding reduction. No CO was detected. This high inertness of the carrier towards C_2H_4, in the presence of H_2, was observed for all five carriers, across the temperature range 450 – 550°C.

The oxygen carriers differed in their activities and in their oxygen-carrying capacities. Figure 3.5 shows that as the Ce content of the support increased, the conversion of H_2

increased. Also shown are the conversions of C_2H_4 from a separate experiment where only 5.4 vol% C_2H_4 was fed to the reactor. The conversions were significantly higher than in the case where H_2 was co-fed with the ethylene. This shows that the activity towards the combustion of C_2H_4 was strongly dependent on the composition of the gas. Nonetheless, the degree of oxidation of the ethylene was substantially less than that of H_2, as seen in Figure 3.5. Figure 3.6 shows that the oxygen-carrying capacity of each sample increased with temperature, and is higher for the intermediate ratios of Ce:Zr, consistent with existing studies (Kim *et al.*, 2006). Bi25Ce0Zr displayed a capacity consistent with its loading of 25 wt% Bi_2O_3, *i.e.* 0.25 × 10.3 = 2.58 wt%, which again confirms the loading of bismuth (pure Bi_2O_3 has a capacity of 10.3 wt%). The supports were able to contribute additional lattice oxygen with the bismuth oxide without adversely affecting the selectivity, despite ceria-zirconia itself not being selective (Rothenberg *et al.*, 2003; de Graaf *et al.*, 2004). The capacity of a bismuth-free sample, $Ce_{0.75}Zr_{0.25}O_2$, was found to be 1.40 wt% at 550°C, so the expected oxygen-capacity of the composite carrier with the addition of 25 wt% Bi_2O_3, assuming an ideal mixture, would then be (0.75 × 1.40) + (0.25 × 10.3) = 3.63 wt%. This is consistent with the measured value shown in Figure 3.6 of 3.67 wt%, which confirms that the oxygen-carrying capacity of the ceria-zirconia phase is not affected by the addition of bismuth. Furthermore, the selectivity of the oxygen contained in the support was enhanced by the presence of a selective surface; this was apparent when comparing the amount of CO_2 evolved per mass of support with and without Bi_2O_3, which were 18 and 34 [µmol CO_2]/[g $Ce_{0.75}Zr_{0.25}O_2$], respectively, despite both supports releasing the same total amount of oxygen. Lastly, the sample with pure ceria as the support did not contribute much additional lattice oxygen, despite being the most active; the lack of zirconia meant that bulk ceria was less reducible.

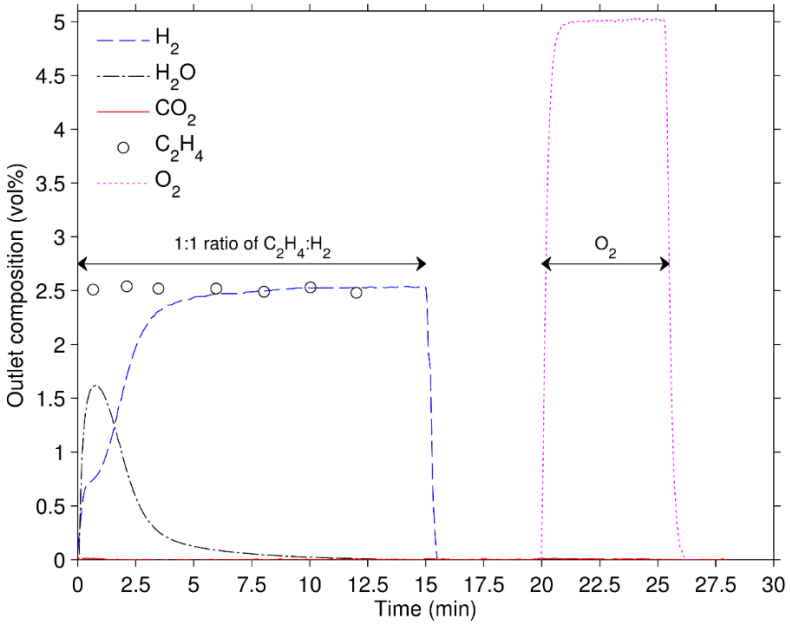

Figure 3.4. Concentration profile at the reactor outlet during a typical cycle, here shown for 0.10 g of Bi25Ce0Zr at 550°C, 1 atm. Feed gases: 2.5 vol% C_2H_4, 2.5 vol% H_2 during reduction, 5.0 vol% O_2 during oxidation, with a purge of N_2 in between stages. Total flows were constant at 100 mL/min as measured at 293 K and 1 atm. CO_2 signals were small and close to the resolution of the data acquisition (0.01 vol%).

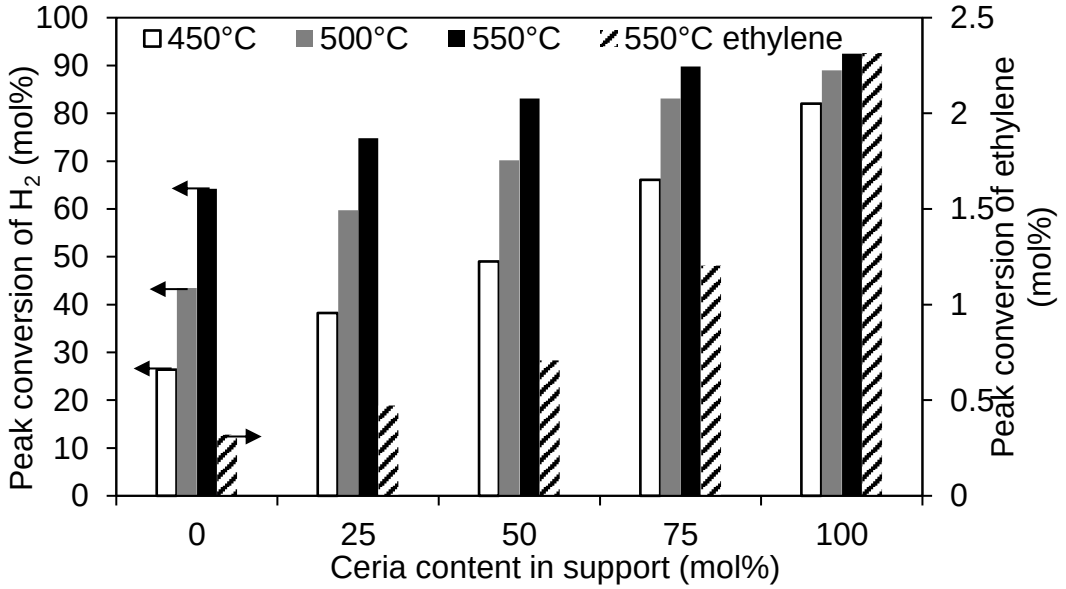

Figure 3.5. Activities of the Bi25Ce*x*Zr carriers during the reduction stage of the packed bed experiments. Conditions: 0.10 g of carrier, 1 atm. Feed gas: 2.5 vol% C_2H_4, 2.5 vol% H_2, at a total flow of 100 mL/min as measured at 293 K and 1 atm. Note that the conversion of C_2H_4 corresponds to experiments where only 5.4 vol% C_2H_4 (and no H_2) is fed.

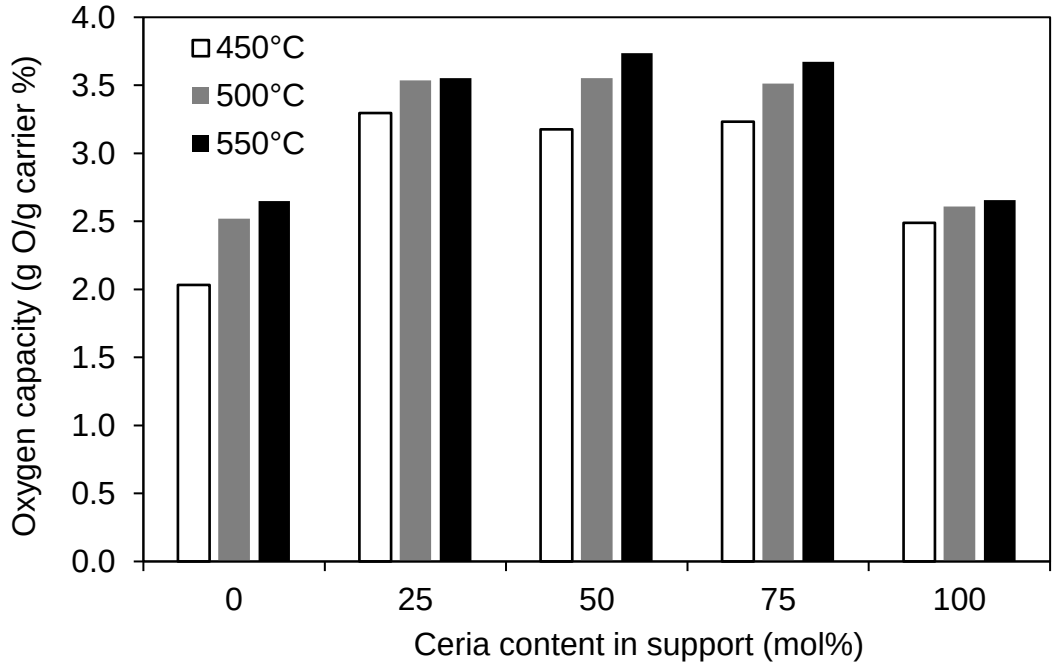

Figure 3.6. Oxygen-carrying capacities of the Bi25Ce*x*Zr carriers measured in the packed bed experiments. Conditions: 0.10 g of carrier, 1 atm. Feed gas: 2.5 vol% C_2H_4, 2.5 vol% H_2, at a total flow of 100 mL/min as measured at 293 K and 1 atm.

3.3.3 Kinetic measurements in a differential bed

Figure 3.7 shows the variation of the rate of reaction with the concentration of hydrogen. A linear fit with a fixed intercept of zero correlates the measurements well (R^2 = 0.997), which confirms the reduction of bismuth oxide is first order with respect to hydrogen.

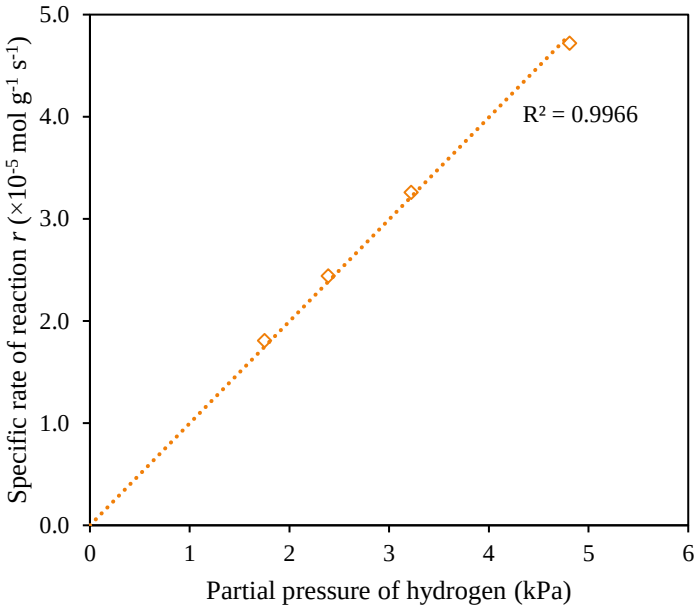

Figure 3.7. Variation of the specific rate of reaction with the partial pressure of hydrogen, shown for Bi25Ce75Zr.

Figure 3.8 shows how the rates of reaction varied with the conversion of the oxygen carriers. In all samples except Bi25Ce100Zr, an initial period of constant rate of reaction can be observed for up to 30 % conversion of the solid. As the solid conversion increases, the rate falls because the reaction becomes starved of lattice oxygen. The overall form of the curves of r against X_O is largely similar. The response of the sensor became more significant for the most active samples, Bi25Ce75Zr and Bi25Ce100Zr, indicated by the maxima being reached at higher values of X_O (*i.e.* greater than ~10%). The possible influence of the response of the sensor on the measured kinetics is examined further in section 3.3.4.

The maximum rates of reaction in Figure 3.8 were used to calculate the apparent first order rate constants according to equation 3.11. These rate constants are shown in the Arrhenius plot in Figure 3.9 and in Table 3.3. These linear fits only use $T \leq 500°C$ for Bi25Ce75Zr and $T \leq 475°C$ for Bi25Ce100Zr because of convolution with the sensor at the higher temperatures for these samples. It can be seen that the apparent activation energies do not vary significantly for any of the samples (with the exception of Bi25Ce75Zr), which suggests a similar rate-determining step. The similar selectivities in these bismuth-containing samples, also shown in Table 3.3, also suggest a common active site.

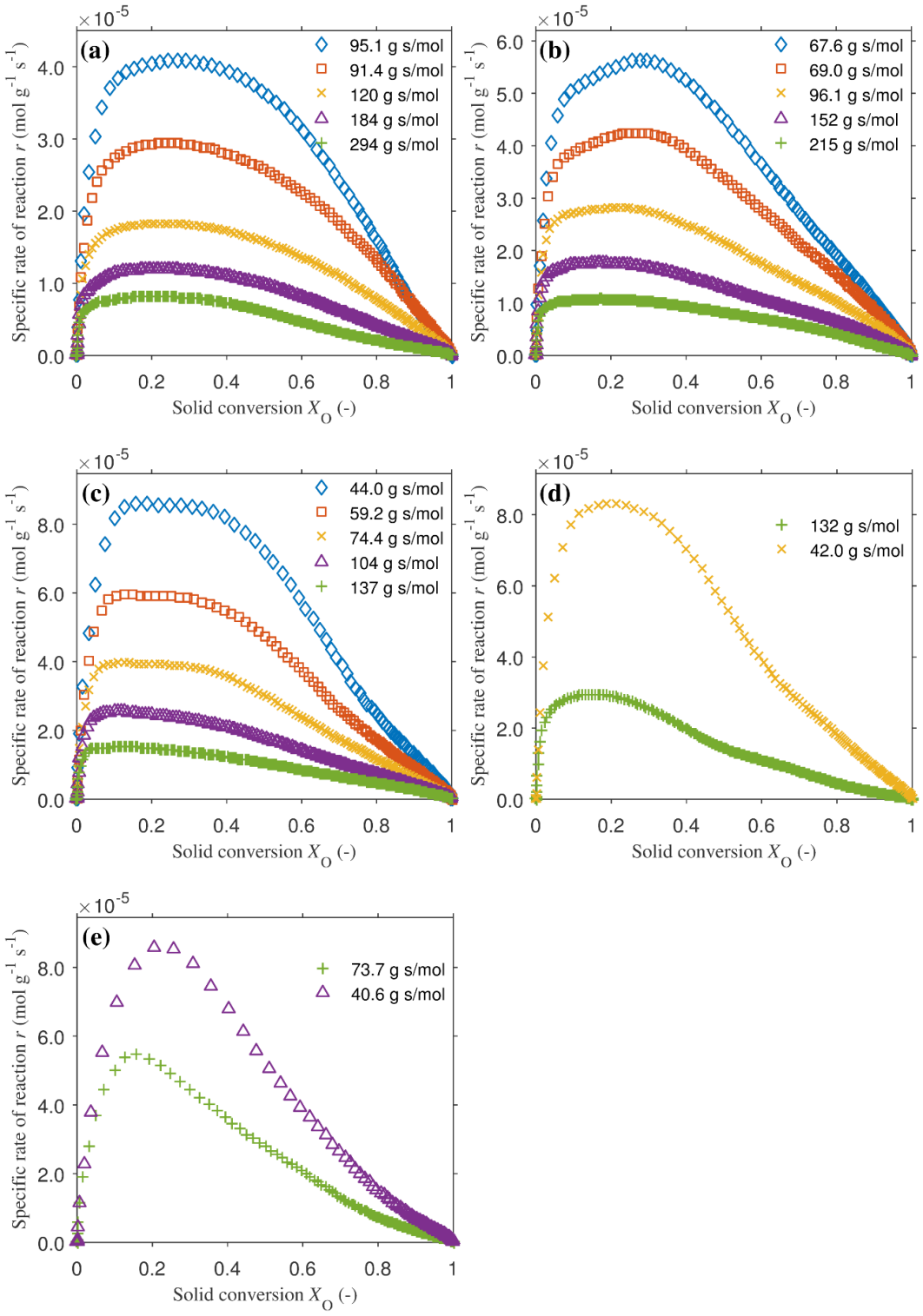

Figure 3.8. Variation of the specific rate of reaction, r, with the conversion of a differential bed of oxygen carrier, X_O. Legend entries denote values of the ratio of the mass of oxygen carrier to the total molar flow rate, W/F, at each temperature: + 450°C, △ 475°C, × 500°C, □ 525°C, ◇ 550°C. The feed gas was 4.81 vol% H_2 in N_2. The conversion of H_2 was < 10%, and the effectiveness factor was estimated to be unity in all cases. (a) Bi25Ce0Zr, (b) Bi25Ce25Zr (c) Bi25Ce50Zr (d) Bi25Ce75Zr (e) Bi25Ce100Zr.

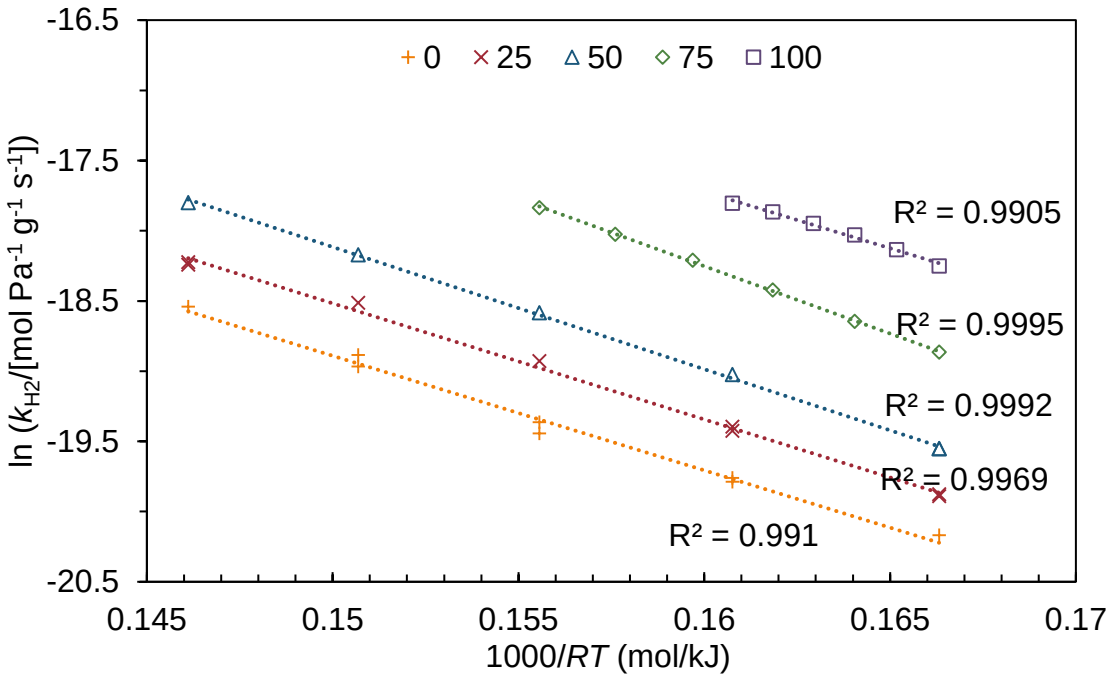

Figure 3.9. Arrhenius plot showing the variation of the rate constant for the combustion of H_2, k_{H_2}, with temperature, T for the supported bismuth oxide oxygen carriers. Legend entries refer to x in Bi25CexZr. The linear fits only use only use $T \leq 525°C$ for Bi25Ce75Zr and $T \leq 500°C$ for Bi25Ce100Zr, due to convolution with the response time of measurement at higher temperatures.

Table 3.3. Apparent activation energies and rate constants for the reduction of supported bismuth oxide in either hydrogen or ethylene. The selectivity $S = k_{H_2}/k_{C_2H_4}$ is also shown. The rate constants and selectivities were measured at 550°C (or, for Bi25Ce75Zr and Bi25Ce100Zr only, were extrapolated to 550°C). The errors in the activation energy indicate the 95% confidence interval.

	E_{a,H_2}	$k_{H_2} \times 10^9$	$k_{C_2H_4} \times 10^{11}$	$S = \frac{k_{H_2}}{k_{C_2H_4}}$
	kJ mol^{-1}	mol Pa^{-1} g^{-1} s^{-1}	mol Pa^{-1} g^{-1} s^{-1}	-
Bi25Ce0Zr	82 ± 8	8.9	2.0	441
Bi25Ce25Zr	83 ± 5	12	3.0	410
Bi25Ce50Zr	87 ± 3	19	4.5	417
Bi25Ce75Zr	96 ± 3	45	7.6	589
Bi25Ce100Zr	80 ± 10	61	15	411

3.3.4 Influence of heat and mass transfer on the measured kinetics

This section describes a set of standard diagnostic criteria used to determine whether a particular transport phenomenon could have influenced the measured kinetics (*viz.* cause a deviation from the intrinsic kinetics by more than 5% (EUROKIN, 2012)).

Axial Dispersion

The flux of chemical species due to axial dispersion in a packed bed can act to decrease the apparent rate of reaction. The following criterion is satisfied if the effect of axial dispersion can be neglected (Mears, 1971b; Gierman, 1988):

$$\frac{h_{\mathrm{bed}}}{d_{\mathrm{p}}} > \frac{8}{Bo} n \ln \frac{1}{1-X} \tag{3.12}$$

where h_{bed} is the axial length of the reactive bed (including inert diluting particles), d_{p} is the particle diameter, $Bo \equiv u d_{\mathrm{p}}/D_{\mathrm{ax}}$ is the Bodenstein number, u is the superficial velocity of the gas, D_{ax} is the axial dispersion coefficient, $n = 1$ is the order of reaction, and X is the conversion of the reactant. D_{ax} was calculated using a correlation reported by Delgado (2006, equations 18 and 19).

Bed Dilution

Bed dilution is the mixing of reactive particles with inert particles, and is used to alleviate the effects of heat transfer across the bed. However, bed dilution itself can influence the rate of reaction due to local bypass effects. The following criterion is satisfied if the effect of bed dilution can be neglected (Berger *et al.*, 2002):

$$b < \frac{1}{1 + 10 X d_{\mathrm{p}}/h_{\mathrm{bed}}} \tag{3.13}$$

where b is the volume of inert particles as a fraction of the total volume of solids.

External Mass Transfer

Diffusion through the stagnant film surrounding the reactive particles (*i.e.* external mass transfer) can limit the observed rate of reaction. The following criterion is satisfied if the effect of external mass transfer can be neglected (Froment *et al.*, 2011):

$$\frac{r_{\mathrm{v,obs}}}{k_{\mathrm{g}} a C_{\mathrm{bulk}}} < \frac{0.05}{n} \tag{3.14}$$

where $r_{\mathrm{v,obs}}$ is the observed rate of reaction per unit volume of reactive particle, k_{g} is the external mass transfer coefficient, a is the external surface area per unit volume of

reactive particle, C_{bulk} is the concentration of the reactant in the bulk, and C_{surface} is the concentration of the reactant at the external surface of the particle. k_{g} was calculated using a correlation reported by Wakao and Funazkri (1978).

Internal Mass Transfer

Diffusion within the pores of the reactive particles (*i.e.* internal mass transfer) can limit the observed rate of reaction. The following criterion is satisfied if the effect of internal mass transfer can be neglected for a first order reaction (Vannice, 2005):

$$\frac{r_{\mathrm{v,obs}}\left(d_{\mathrm{p}}/6\right)^{2}}{C_{\mathrm{surface}}D_{\mathrm{eff}}} < 0.067 \tag{3.15}$$

where D_{eff} is the effective diffusivity of the reactant within the pores of the particle, and was calculated using:

$$D_{\mathrm{eff}} = \frac{\varepsilon_{\mathrm{p}}}{\tau} D_{\mathrm{m}} \tag{3.16}$$

where ε_{p} is the porosity of the particle, τ is the tortuosity of the pores and D_{m} is the molecular diffusivity of the reactant. D_{m} was calculated using Chapman-Enskog theory (Bird *et al.*, 2007), and it was assumed that there were no pores sufficiently small to give a Knudsen component. The absence of limitations due to external mass transfer means $C_{\mathrm{surface}} = C_{\mathrm{bulk}}$.

Radial Heat Transfer across the Bed

Interparticle heat transfer along the radius of the bed may be neglected if the following criterion is satisfied (Mears, 1971a):

$$\frac{r_{\mathrm{v,obs}}|\Delta_{\mathrm{r}}H|(1-\varepsilon_{\mathrm{b}})(1-b)d_{\mathrm{t}}^{2}}{32\lambda_{\mathrm{eff,r}}} < \frac{0.05RT^{2}}{E_{\mathrm{a}}} \tag{3.17}$$

where $\Delta_{\mathrm{r}}H$ is the enthalpy of reaction, ε_{b} is the voidage of the bed, d_{t} is the diameter of the bed, $\lambda_{\mathrm{eff,r}}$ is the effective radial thermal conductivity of the bed, R is the molar gas constant, T is the temperature of the bed and E_{a} is the apparent activation energy of the reaction. The value of $\lambda_{\mathrm{eff,r}}$ was calculated using a correlation reported by Specchia *et al.* (1980).

External Heat Transfer

Conduction of heat through the stagnant film surrounding the reactive particles (i.e. external heat transfer) can affect the observed rate of reaction. The following criterion is satisfied if the effect of external heat transfer can be neglected (Mears, 1971a):

$$\frac{r_{\mathrm{v,obs}}|\Delta_{\mathrm{r}}H|d_{\mathrm{p}}^2}{6\alpha_{\mathrm{p}}} < \frac{0.05RT^2}{E_{\mathrm{a}}} \tag{3.18}$$

where α_{p} is the heat transfer coefficient between the particle and the bulk gas. α_{p} was calculated using a correlation by Wakao *et al.* (1979).

Internal Heat Transfer

Conduction of heat through the pores of the reactive particles (*i.e.* internal heat transfer) can affect the observed rate of reaction. The following criterion is satisfied if the effect of internal heat transfer can be neglected (Mears, 1971a):

$$\frac{r_{\mathrm{v,obs}}|\Delta_{\mathrm{r}}H|d_{\mathrm{p}}^2}{60\lambda_{\mathrm{p}}} < \frac{0.05RT^2}{E_{\mathrm{a}}} \tag{3.19}$$

where λ_{p} is the thermal conductivity of the reactive particle. λ_{p} was estimated conservatively to be 0.1 W m^{-1} K^{-1} (Satterfield, 1991).

Evaluation of Criteria

Table 3.4 shows the variables and parameters evaluated for the experiment conducted for Bi25Ce100Zr at 475°C (corresponding to the highest measured k_{H_2}, which is most susceptible to transport limitations). Table 3.5 shows the evaluation of the criteria applied to this experiment, and it can be seen that all criteria were satisfied and consequently the measured rates of reaction reflected the intrinsic kinetics.

Table 3.4. Variables used in the evaluation of the diagnostic criteria. Experimental conditions: total flow of 465 mL/min (as measured at 293 K, 1 atm) of 4.81 vol% H_2 in balance N_2, bed contains 0.0129 g of Bi25Ce100Zr of size 90 – 150 µm, temperature 748 K, pressure 1 atm.

Variable	Value	Comments	Ref.
a	5.16×10^{4} $m^2\ m^{-3}$	Assumed spherical particles	
b	0.95		
C_{bulk}	0.773 mol m^{-3}		
C_p	1.1 kJ kg^{-1} K^{-1}	Isobaric specific heat capacity of N_2	
$C_{surface}$	0.773 mol m^{-3}	Valid because criterion 3.14 applied	
D_{ax}	2.2×10^{-4} $m^2\ s^{-1}$	Criterion 3.12 was insensitive to deviations in D_{ax} of 500%	(Delgado, 2006)
D_{eff}	1.0×10^{-4} $m^2\ s^{-1}$		
D_m	3.6×10^{-4} $m^2\ s^{-1}$	Diffusivity of H_2 in N_2. Insensitive if varied by factor of 10	(Bird *et al.*, 2007)
d_p	116 µm		
d_t	8 mm		
E_a	100 kJ mol^{-1}	Conservative estimate. Measured value was 80 kJ mol^{-1}	
h_{bed}	4 mm		
k_g	7.6 m s^{-1}		(Wakao and Funazkri, 1978)
n	1		
u	0.39 m s^{-1}		
$r_{v,obs}$	178 mol m^{-3} s^{-1}		
T	748 K		
X	0.0724		
α_p	1100 W m^{-2} K^{-1}		(Wakao *et al.*, 1979)
$\Delta_r H$	-51 kJ mol^{-1}	Reaction: $\frac{1}{3}Bi_2O_{3(s)} + H_{2(g)} \rightleftharpoons \frac{2}{3}Bi_{(l)} + H_2O_{(g)}$	(Barin, 1995)
ε_b	0.38	Estimated, typical value	
ε_p	0.4	Estimated. Criterion 3.15 was insensitive for $\varepsilon_p > 0.006$	
$\lambda_{eff,r}$	0.6 W m^{-1} K^{-1}		(Specchia *et al.*, 1980)
λ_g	0.049 W m^{-1} K^{-1}	Thermal conductivity of gas, from Eucken formula	(Bird *et al.*, 2007)
λ_{inert}	97 W m^{-1} K^{-1}	Thermal conductivity of SiC particles	(Nilsson *et al.*, 1997)
λ_p	0.1 W m^{-1} K^{-1}	Conservative estimate	(Satterfield, 1991)
μ	3.3×10^{-5} Pa s	Dynamic viscosity of gas, from Chapman-Enskog theory	(Bird *et al.*, 2007)
ρ	0.436 kg m^{-3}	Density of gas	
τ	1.4	Estimated, typical value	

Table 3.5. Evaluation of the diagnostic criteria using the values reported in Table 3.4, establishing the absence of significant deviations from the intrinsic kinetics.

Criterion	Eqn.	LHS	RHS
$\frac{h_{\mathrm{bed}}}{d_{\mathrm{p}}} > \frac{8}{Bo} n \ln \frac{1}{1-X}$	(3.12)	34	2.9
$b < \frac{1}{1 + 10X d_{\mathrm{p}}/h_{\mathrm{bed}}}$	(3.13)	0.95	0.98
$\frac{r_{\mathrm{v,obs}}}{k_{\mathrm{g}} a C_{\mathrm{bulk}}} < \frac{0.05}{n}$	(3.14)	5.8×10^{-4}	0.05
$\frac{r_{\mathrm{v,obs}} \left(d_{\mathrm{p}}/6\right)^2}{C_{\mathrm{surface}} D_{\mathrm{eff}}} < 0.067$	(3.15)	8.6×10^{-4}	0.067
$\frac{r_{\mathrm{v,obs}} \lvert\Delta_{\mathrm{r}} H\rvert (1-\varepsilon_{\mathrm{b}})(1-b) d_{\mathrm{t}}^2}{32 \lambda_{\mathrm{eff,r}}} < \frac{0.05 R T^2}{E_{\mathrm{a}}}$	(3.17)	0.9 K	2.3 K
$\frac{r_{\mathrm{v,obs}} \lvert\Delta_{\mathrm{r}} H\rvert d_{\mathrm{p}}^2}{6 \alpha_{\mathrm{p}}} < \frac{0.05 R T^2}{E_{\mathrm{a}}}$	(3.18)	0.2 K	2.3 K
$\frac{r_{\mathrm{v,obs}} \lvert\Delta_{\mathrm{r}} H\rvert d_{\mathrm{p}}^2}{60 \lambda_{\mathrm{p}}} < \frac{0.05 R T^2}{E_{\mathrm{a}}}$	(3.19)	0.02 K	2.3 K

Limitation of the sensor response time on the measured kinetics

In general, measurements of the rates of gas-solid reactions could be influenced by limitations in heat and mass transfer and also by the response of the analysers. Estimates of the rates of heat and mass transfer, and qualification with standard diagnostic criteria, have shown that the rates of reaction were not likely to have been influenced by these phenomena. To estimate the impact on the rate of reaction due to convolution with the response of the sensor, a characteristic reaction time, τ, was defined:

$$\tau = t(y = \max(y)\, e^{-1}) - t_{\mathrm{start}} \tag{3.20}$$

i.e. τ is the time taken for the rate of reaction to fall to a factor of $e^{-1} = 0.368$ from the maximum, measured from the start of the reaction. The ratio of the reaction time to the response time, τ/t_{mix}, then gives an indication of how severely the measurements were affected by convolution with the sensor; these are summarised in Table 3.6. It can be seen that the humidity sensor responded sufficiently quickly for samples Bi25Ce0Zr, Bi25Ce25Zr and Bi25Ce50Zr, because τ/t_{mix} is an order of magnitude greater than unity. The samples richer in ceria (Bi25Ce75Zr and Bi25Ce100Zr) reacted much quicker,

such that τ/t_{mix} was closer to unity. For these samples, the response time might have affected the kinetic measurements despite the deconvolution procedure, but probably not to a significant extent.

Table 3.6. Characteristic reaction times compared to the response time of the humidity sensor, appropriate for the kinetic experiments.

	450°C		500°C		550°C	
	τ	τ/t_{mix}	τ	τ/t_{mix}	τ	τ/t_{mix}
	s	-	s	-	s	-
Bi25Ce0Zr	124	11	69	15	37	10
Bi25Ce25Zr	179	16	70	14	38	11
Bi25Ce50Zr	122	11	54	9	26	7
Bi25Ce75Zr	59	5	22	6	-	
Bi25Ce100Zr	24	4	16[a]	5[a]	-	

[a] Measurement was taken at 475°C

3.4 Discussion

The similarity in the selectivities, activation energies, and form of the curves of rate *vs* solid conversion, independent of the composition of the support, indicates that the gas was reacting with the same solid component in all the samples, Bi_2O_3. This similarity might have been caused by Bi_2O_3 wetting the ceria-zirconia surface, as suggested by de Graaf *et al.* (2004). XPS shows that the surface composition is enriched with Bi and depleted with Ce; a higher ratio of Bi to Ce would be favourable for maintaining the selectivity (because Bi active sites are selective, whereas Ce active sites are not). TEM images also show that bismuth was spread homogeneously over the particles. The result is that the most abundant exposed active sites are on Bi_2O_3, as opposed to CeO_2, which explains the similar selectivities. If the rate-limiting step occurred during the gas-solid reaction (as opposed to, say, transport of ions across the Bi_2O_3-support interface or in the bulk of the support), then this would lead to the similar apparent activation energies. This apparent independence of the surface reaction from the bulk properties of the support is beneficial because this simplifies the design and formulation of oxygen carriers. A significant dependence would have removed a degree of freedom in the design process. Where strong metal-support interaction is necessary, this might limit (but not completely

exclude all) the range of possible oxygen carriers – a set of oxygen carriers might exist conferring the strong metal-support interaction.

Enhanced oxygen-carrying capacities were observed for the samples with a mixture of ceria and zirconia as the support. This enhancement, in combination with consistently high values of selectivity, demonstrates a synergistic effect between the selective bismuth oxide phase and the ceria-zirconia phase. The cyclic stability and oxygen-carrying capacity of ceria-zirconia complemented the selectivity and capacity of bismuth oxide, resulting in a composite material that performed better than either material in isolation. This synergy might be described as 'phase cooperation' (Grasselli, 2014) and is likely to have been facilitated by similar lattice parameters. The lattice parameters for the potentially relevant structures are similar; 5.4112 Å (fluorite), 5.6446 Å (tetragonal, *c*-axis), and 5.6549 Å (fluorite), for CeO_2, β-Bi_2O_3, and δ-Bi_2O_3, respectively. In general, this could be readily applied in the design of selective oxygen carriers for chemical syntheses. This presents a solution to previous attempts at a chemical looping arrangement, which have, in some cases, been beset by poor oxygen-carrying capacities (Contractor, 1999; Godefroy *et al.*, 2010). This principle is explored in chapter 4 with a different pair of materials, Ag and $SrFeO_3$.

An additional set of preliminary experiments were conducted to examine the performance of Bi25Ce75Zr in combination with a proprietary Pt-based catalyst, for the two-step ODH of ethane to ethylene. The Pt catalyst was intended to dehydrogenate the ethane, forming ethylene and hydrogen in the following reaction:

$$C_2H_{6(g)} \rightleftharpoons C_2H_{4(g)} + H_{2(g)} \qquad \Delta H°_{500°C} = 140 \text{ kJ mol}^{-1} \qquad (3.21)$$

The Bi-based oxygen carrier was present to combust selectively the hydrogen generated, thereby driving the reaction forward beyond nominal thermodynamic yield (*i.e.* the equilibrium yield that would have been achieved in thermal dehydrogenation). A heterogeneous mixture of particles of the supported Pt catalyst and particles of the oxygen carrier was loaded into the packed bed reactor. A feed of 50 vol% C_2H_6 was introduced, and a mixture of C_2H_4 and H_2O was observed at the outlet of the reactor, confirming that ODH was occurring. The results are shown in Figure 3.10. An initial concentration of 3.6 vol% C_2H_4 was produced, which exceeded the nominal thermodynamic yield, which has not yet been reported for the two-step ODH of ethane. If only thermal dehydrogenation had occurred and had proceeded to equilibrium, then, at these conditions (feed of 50 vol% C_2H_6, 450°C and 1 atm), only 1.6 vol% C_2H_4 would have been produced (calculated using

standard Gibbs free energies of formation tabulated by Haynes (2017)). A small but significant amount of CO_2 was also produced with a peak concentration of 0.53 vol%, which is higher than shown in *e.g.* Figure 3.4, because of the different feed compositions. This two-step ODH experiment contained a high concentration of C_2H_6, but no C_2H_4 or H_2 in the feed. The lack of hydrogen is significant because its presence was shown to inhibit the combustion of propylene (Tsikoyiannis *et al.*, 1999), here, it might be speculated that the combustion of ethane (and ethylene) is also similarly inhibited by hydrogen. As the reaction proceeded, the oxygen carrier became depleted and the concentration of H_2O and CO_2 fell. The concentration of H_2 increased accordingly as a result, because dehydrogenation continued. As the oxygen carrier became fully reduced, the concentration of C_2H_4 fell to 1.7 vol%, close to the nominal thermodynamic yield. Following a purge at 12.5 min, the reactor was fed 5 vol% O_2 to regenerate the oxygen carrier. At the start of this oxidation step at 20 min, CO_2 and H_2O was evolved, indicating the presence of coke. At 22 min, O_2 was observed at the reactor outlet, and increased to the inlet concentration of 5 vol%, indicating no further consumption of O_2. A subsequent cycle showed a similar performance, giving some indication of the overall stability of the mixture of Pt catalyst and oxygen carrier. However, when the temperature was increased to 500°C, the performance degraded with cycling. The rate of degradation was significantly more rapid than when either material (the Pt catalyst or the oxygen carrier) was cycled in isolation. A possible explanation could be volatilisation of bismuth from the oxygen carrier, which could deposit on and deactivate Pt active sites. Volatilisation was investigated by TGA, where a sample of 15 wt% Bi_2O_3 supported on $Ce_{0.50}Zr_{0.50}O_{2-\delta}$ was exposed to an extended reduction in H_2 isothermally at a higher temperature of 550°C (the higher temperature was chosen to exaggerate the effect for detection), shown in Figure 3.11. The expected oxygen carrying capacity for this sample is 2.86 wt% (contributions of 1.55 wt% from Bi_2O_3 and 1.32 wt% from $Ce_{0.50}Zr_{0.50}O_{2-\delta}$). When H_2 was passed over the sample, it lost mass as it became reduced. The total mass lost during the first reduction cycle was 3.17 wt% (at 22 min), which is 0.31 wt% greater than expected from its oxygen carrying capacity. This extra loss in mass could have been caused by vaporisation of bismuth. When the sample was reoxidised (at 25 min), there was a deficit in the mass of 0.54 wt%, compared to initial mass. This shows that some of the mass was lost irreversibly, which, again, could have been caused by volatilisation. A second, extended reduction step led to 3.78 wt% of the sample mass lost (at 271 min), which is 0.92 wt% higher than its nominal oxygen carrying capacity. After the second

reoxidation, the deficit in mass compared to the initial mass was 1.32 wt% (at 275 min). This deficit after reoxidation is largely accounted for by the additional mass lost during the reduction steps (0.31 + 0.92 = 1.23 wt%). These observations are consistent with volatilisation of the sample. Another notable feature during reduction with H_2 is an apparent point of inflection, at times of 10 min and 41 min (marked by asterisks (*) in Figure 3.11), for the first and second cycle respectively. These points of inflection occurred when the sample was nearly fully reduced (*i.e.* lost > 90% of its available oxygen, assuming its lost mass up to that point is only oxygen), and could be speculated to be the onset of volatilisation. This could suggest that available oxygen in the sample inhibits volatilisation.

Volatilisation was not detected in the previous set of TGA experiments (shown in Figure 3.1, where the initial sample mass was recovered after reoxidation), and this might be speculated to have been caused by the different experimental conditions. In the previous TGA experiments, a TPR was used, whereas here, the reduction was performed isothermally – as the temperature increased during the TPR, more oxygen from ceria became activated which could have been sufficient to inhibit volatilisation. Volatilisation was also not detected during the packed bed experiments because vapour could have condensed on downstream surfaces that are still sufficiently hot to be active. Volatilisation might have been the actual cause for deactivation during previous attempts at using bismuth for two-step ODH. Previously, deactivation was attributed to an increase in the average crystallite size of bismuth oxide, and was said to have led to a loss of dispersion (Tsikoyiannis *et al.*, 1999), which is an inadequate explanation because bulk reduction and oxidation are facile at these temperatures. Other workers noted the appearance of a yellow band (the colour of bismuth oxide) at the outlet of their reactor after reduction at 600°C (Beckers *et al.*, 2009). During the packed bed experiments, the oxygen carrier could easily have become completely reduced, leading to volatilisation of bismuth and subsequent deposition on Pt. This might be avoided by avoiding deep reduction of the oxygen carrier, but this would be challenging to implement in an integral packed bed reactor.

Further development would be necessary to utilise bismuth oxide and Pt for two-step ODH, where issues of volatilisation and coking would need to be addressed. Coking on Pt might be inhibited by supporting the Pt on the oxygen carrier, as shown by Pt on $Ce_xZr_{1-x}O_2$ for the reforming of methane with CO_2 (Noronha *et al.*, 2001). Mobile oxygen from the carrier could prevent the accumulation of coke, although, depending on the exact

mechanism of this effect, there will be a risk of coke being merely oxidised to CO_x. Even if coke is oxidised during the reduction step, as opposed to the oxidation step as seen in Figure 3.10, then the net effect is still the loss of selectivity towards ethylene.

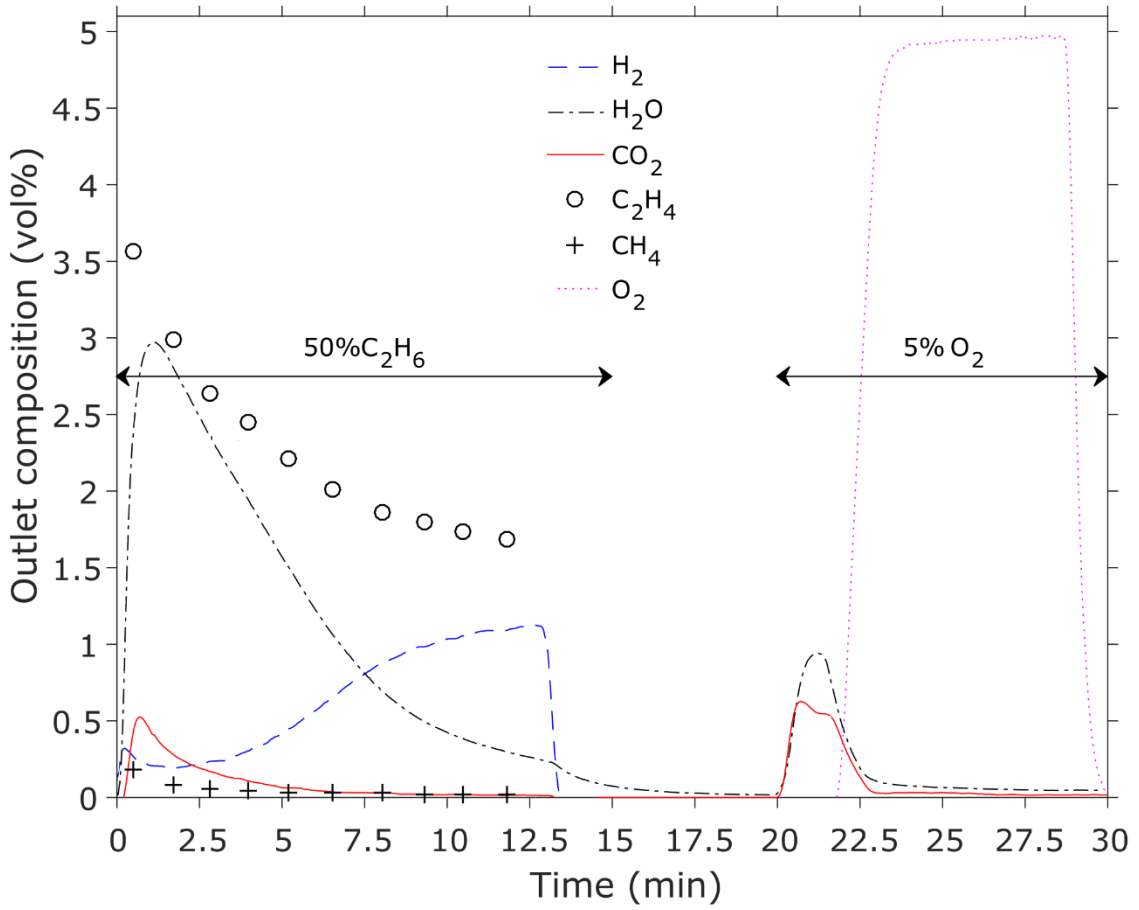

Figure 3.10. Concentration profile of the first cycle during two-step ODH. A mixture of Bi25Ce75Zr and a proprietary Pt catalyst was loaded into the reactor. The temperature was 450°C, at a pressure of 1 atm. Feed gases: 50.65 vol% C_2H_4 during reduction, 5.0 vol% O_2 during oxidation, with a purge of N2 in between stages. Total flows were constant at 100 mL/min as measured at 293 K and 1 atm.

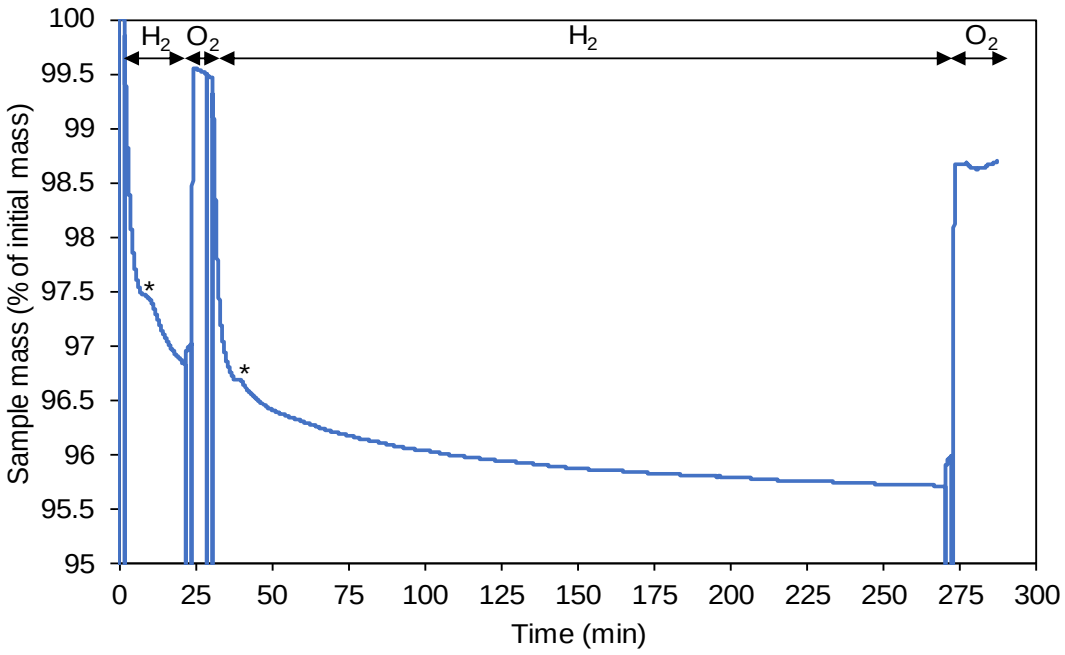

Figure 3.11. Thermogravimetric analysis (TGA) of 15 wt% Bi_2O_3 supported on $Ce_{0.50}Zr_{0.50}O_{2-\delta}$ during isothermal cycling at 550°C. The labelled gases, H_2 or O_2, denote the periods in which they were fed. The asterisks (*) mark points of inflection observed during the reduction in H_2. The spikes in the mass are artefacts caused by the switching of gases. The irreversible loss of mass might be caused by volatilisation of bismuth when the sample was deeply reduced.

3.5 Conclusions

The oxygen-donating capacity of an oxygen carrier consisting of bismuth oxide supported on ceria-zirconia was enhanced by the support. It was found that intermediate ratios of ceria-zirconia had higher oxygen-carrying capacities, and that this extra capacity did not significantly detract from the innate selectivity of the bismuth oxide for the combustion of H_2 over C_2H_4. The selectivity of the surface was apparently decoupled from the bulk properties of the support. This demonstrates a potential solution in increasing the capacity of oxygen carriers for chemical syntheses; a selective phase may be deposited on an oxygen carrier without significant detriment to the function of either material. The first iteration in developing a formulation may simply be to select an existing catalyst, viable in conventional co-feeding mode, to deposit on the surface of a suitable oxygen carrier material. This approach would be easier than screening for a single material that possesses all the required properties.

4 CHEMICAL LOOPING EPOXIDATION

4.1 Introduction

A key intermediate species in the mechanism for the epoxidation of ethylene is the oxygen adatom (O_a), which is the selective oxygen species responsible for the epoxidation and, depending on its electrophilicity, combustion (Lambert *et al.*, 2005). In the conventional process, where ethylene and gaseous oxygen are co-fed to the reactor, O_a is generated from the dissociative adsorption of $O_{2(g)}$. Ethylene can then adsorb on to the silver surface to react with O_a (*i.e.* a Langmuir-Hinshelwood mechanism) and form an oxametallacycle intermediate, which then forms either ethylene oxide (EO) or acetaldehyde (Linic *et al.*, 2004). The acetaldehyde is usually rapidly combusted, and can also form from sequential isomerisation of ethylene oxide on acid sites *e.g.* silver and alumina (Bukhtiyarov and Knop-Gericke, 2011). An alternative mechanism at high coverages of oxygen on silver is where ethylene in the gas phase can react with O_a to form ethylene oxide (*i.e.* an Eley-Rideal mechanism), said to be a more selective pathway (Özbek and van Santen, 2013). The presence of oxygen vacancies on the surface then promotes the pathway involving the oxametallacycle, lowering the selectivity (Özbek and van Santen, 2013). To date, there have been no reports of O_a being directly supplied from a solid oxidant, probably because of the challenging requirements imposed on such a material. Working catalysts typically operate at partial pressures of O_2 of up to 2 bar and temperatures of 200–300°C (Rebsdat and Mayer, 2012), where evidence suggests the existence of surface silver oxide phases (Michaelides *et al.*, 2003; Reichelt *et al.*, 2007; Piccinin *et al.*, 2010).

Here, it is therefore posited that the solid oxidant needs to have a high chemical potential of oxygen, μ_{O2}, to stabilise these active phases, or at least to ensure a sufficiently high surface coverage of O_a. Such a high μ_{O2} at these temperatures is rare among solid oxides. Sufficiently fast ionic conduction is also required to replenish O_a during the reaction, but oxide ion conduction is typically slow at these temperatures. Lastly, the solid oxidant needs to be regenerable without significant loss of oxygen-storage capacity and kinetic activity.

A recent, large-scale *in silico* screening of materials has identified $SrFeO_3$ as a potential oxygen carrier for chemical looping combustion (Lau *et al.*, 2017). It was found that $SrFeO_3$ can release $O_{2(g)}$ reversibly over many cycles of thermal decomposition followed by reoxidation at low temperatures (~673 K, pO_2 = 0.15 bar), demonstrating its favourable μ_{O2} and kinetics. Crucially, bulk $SrFeO_3$ does not react with CO_2 significantly (Lau *et al.*, 2017) and thereby deactivate with the formation of bulk carbonate, a problem afflicting other possible materials with a similar μ_{O2} such as SrO_2/SrO and BaO_2/BaO (Jensen, 2009). Resistance against carbonation is necessary because significant levels of CO_2 are generated from side reactions during epoxidation.

These favourable properties suggested the possibility of interfacing $SrFeO_3$ with Ag; $SrFeO_3$ could then supply oxygen to Ag as bulk or subsurface oxygen (O_{ss}), where the oxygen could then diffuse to the silver surface to be presented as O_a to effect the epoxidation in the absence of $O_{2(g)}$. The concept is summarised in Figure 4.1. The catalyst would then be regenerated in air in a separate step to complete the chemical looping cycle.

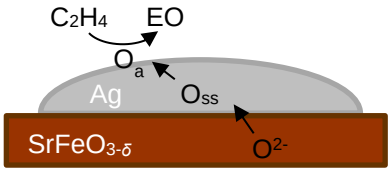

Figure 4.1. Chemical looping epoxidation using a silver-modified oxygen carrier

It is advantageous to perform selective oxidations using a solid oxidant, in the absence of $O_{2(g)}$, because this avoids flammable mixtures and renders a safer process. The conversion of ethylene is no longer limited by the supply of $O_{2(g)}$, decreasing the need to recycle unreacted ethylene – industrial processes tend to operate with limited amounts of O_2 with ethylene in excess (Rebsdat and Mayer, 2012). Furthermore, separation costs can be reduced by avoiding the need to separate N_2 (from purifying either O_2 or the products). Minimising recycling, and combining unit operations of reaction and separation, are both examples of process intensification (Charpentier, 2007; Van Gerven and Stankiewicz,

2009; Kim *et al.*, 2017). Lastly, improved selectivities might be achieved by the removal of $O_{2(g)}$ (Yusuf *et al.*, 2017).

In this chapter, epoxidation was investigated in the absence of $O_{2(g)}$ by using a solid oxygen carrier. The aim was not to show selectivities comparable with industrial ones, so common promoters were not used (*e.g.* Cs and Cl). Rather, the objective was to demonstrate the concept. The term 'catalyst' is used as an abbreviation for the 'catalyst-oxygen carrier' materials prepared in this study, where Ag acts as the catalyst and $SrFeO_3$ acts as the oxygen carrier.

4.2 Experimental

$SrFeO_3$ was prepared by a solid-state synthesis method. Stoichiometric amounts of $SrCO_3$ (0.72 mol) and Fe_2O_3 (0.36 mol) were mixed in a ball mill for 3 hours at 25 Hz. Ethanol (50 mL, 99.8%, Fisher Scientific) was added as a binder to improve mixing. The mixture was dried for 24 hours at 50°C, and sieved to 180-355 μm. The particles were then calcined in four stages, with each stage consisting of calcination at 1000°C for 3 hours, followed by cooling to room temperature.

Incipient wetness impregnation was used to dose Ag on to the supports, consisting of either $SrFeO_3$ or α-Al_2O_3. Prior to impregnation, $SrFeO_3$ was sieved to a size range of 212 – 300 μm, and α-Al_2O_3 (Alfa Aesar, product code 43862) was crushed and sieved to a size range of 212 – 300 μm. The volume of solution added was equal to the pore volume of the support, which was determined empirically beforehand by adding deionised water dropwise with stirring to a mass of support. The endpoint was taken to be when the granular matter just started to cohere, *i.e.* when the internal pores have been filled and the mixture is at the onset of the pendular regime, when the volume of water added was taken to be equal to the pore volume. The pore volume of $SrFeO_3$ was measured to be 0.24 mL/g, and the pore volume of α-Al_2O_3 was measured to be 0.26 mL/g. In a typical preparation of 15 wt% Ag/$SrFeO_3$, 1.3895 g of $AgNO_3$ (≥99.0%, Sigma-Aldrich) was dissolved in 1.2 mL water, which was then added dropwise to a batch of 5.0000g $SrFeO_3$ with agitation by a spatula. Correspondingly, in a typical preparation of 15 wt% Ag/Al_2O_3, 1.3895 g of $AgNO_3$ (≥99.0%, Sigma-Aldrich) was dissolved in 1.3 mL water, which was then added dropwise to a batch of 5.0000g Al_2O_3 with agitation by a spatula. The impregnated solids were then dried at 120°C for 12 h in static atmospheric air, before calcination at 500°C for 5 h with a ramp rate of 5°C/min in static atmospheric air.

A packed bed reactor was used to perform the epoxidation experiments and was operated in either chemical looping mode or co-feeding mode. The reactor consisted of an 8 mm i.d., 200 mm long quartz tube mounted vertically with a sintered disc fixed 75 mm from the bottom. The tube was wrapped with a high temperature dual-element heating tape (Omega, DHT052020LD). The output of the heating tape was controlled by a type K thermocouple with a mineral-insulated Inconel sheath inserted into the bed. The bed was packed above the sintered disc, with a bottom layer of α-Al_2O_3 (Boud Minerals, 425-710 µm) to position the active bed in the isothermal region of the reactor, then a middle layer with the catalyst, then finally another layer of 3 g of α-Al_2O_3 to distribute and preheat the feed. Both ends of the quartz tube were connected to Swagelok Ultra-Torr® vacuum fittings and sealed with fluorocarbon FKM O-rings. A 7 µm filter (Swagelok, SS-2TF-7) was fitted at the outlet of the reactor. *Ex situ* regeneration of the active material was performed by dismounting the reactor tube, containing the packed bed, from its fittings and placing it in a box furnace to be calcined at 400°C for 2 h in static air.

The feed gases to the reactor were supplied from cylinders (BOC), and consisted of 5.16 vol% C_2H_4 in balance N_2 (certified to 5% uncertainty, BOC), N_2 (purity > 99.998 %), and bottled purified air (contained approximately ~400 ppm CO_2). Gas flows were manipulated by calibrated rotameters and checked using a bubble film flowmeter at the start of each experiment. Gases were switched using digitally-controlled solenoid valves. Continuous online analysis of the gaseous products was achieved by a Fourier transform infrared (FTIR) analyser (MKS Instruments, Multigas 2030) equipped with a liquid N_2-cooled mercury-cadmium-telluride detector. Measurements were collected 2.5 h after filling the liquid N_2 dewar, once the background had settled. The 5.11 m gas cell was heated to 150°C. Each measurement consists of 8 scans of the band 800-4600 cm^{-1}, lasting 1.87 s, at a resolution of 0.5 cm^{-1}. The collected spectra were analysed for C_2H_4, CO_2, ethylene oxide, CO and H_2O, using software (MKS, MG2000). No acetaldehyde was detected. The analysis regions for each quantified species were adjusted to exclude interfering peaks from other species to eliminate any cross-sensitivities. Negligible amounts of CO were detected, < 40 ppm. H_2O was not quantified; its quantity was inferred from the stoichiometry of combustion, $C_2H_4 + 3/2O_2 \rightarrow CO_2 + H_2O$, *i.e.* 1 mol of CO_2 generated implied that 1 mol of H_2O was also generated, and that 3 mol of O was consumed. The measurements of gas concentrations were smoothed using a Savitzky-Golay filter of order two and a frame length of 15 (sampling frequency of 0.53 Hz); smoothed quantities were used in the calculations of instantaneous selectivity and

conversion, whereas raw quantities were used for the mean selectivity and conversion. These smoothed quantities, y_{smooth}, were then subsequently deconvoluted from the response of the analyser using a first-order lag model according to

$$y_{\text{dec},i}(t) = y_{\text{smooth},i}(t) + t_{\text{mix}} \frac{dy_{\text{smooth},i}(t)}{dt} \tag{4.1}$$

where $y_{\text{dec},i}$ is the deconvoluted mole fraction of species i and t_{mix} = 0.42 min was the response time of the analyser with a volumetric flow rate of 200 mL/min. Deconvoluted measurements were used only for presenting mole fractions and for the calculations of turnover frequency (TOF), but not used in any other analyses.

In the chemical looping experiments, the reactor was packed with 1.0 g α-Al_2O_3 for the bottom layer, with 2.000 g catalyst in the middle layer. A constant flow rate of 200 mL/min (measured at 293 K, 1 atm), was maintained at all times. The feed gases were switched automatically, with the base case cycling times of (i) reduction with 5.16 vol% C_2H_4 in balance N_2 for t_{red} = 1.5 min, (ii) purge with N_2 for 2 min, (iii) oxidation with compressed air for t_{ox} = 15 min, and (iv) purge with N_2 for 2 min.

Assuming dilute gases and small conversions, so that the total molar flow rate in and out of the reactor was constant, the overall carbon balance in a particular reduction stage was calculated according to

$$\text{Carbon balance} = \frac{\text{Total carbon detected}}{\text{Total carbon fed}} = \frac{\int_{t_{\text{start}}}^{t_{\text{end}}} \left(y_{C_2H_4} + y_{\text{EO}} + \frac{1}{2} y_{CO_2} + \frac{1}{2} y_{\text{CO}} \right) dt}{y_{C_2H_4,\text{feed}} \cdot t_{\text{red}}} \tag{4.2}$$

where y_i is the mole fraction of species i, t is time, and $y_{C_2H_4,\text{feed}}$ is the mole fraction of C_2H_4 in the feed. The start and end time for integration was the first and final point in time where EO was detected (the range of this time was not necessarily equal to t_{red} because of the response of the analyser). The carbon balance was always within 95 ± 5%, and usually within 98 ± 5%, which verifies that the rate of accumulation of coke in the reactor is small and may be neglected in subsequent analyses.

The cumulative amount of oxygen released by time t, in a particular cycle starting at time t_{start}, was calculated by integrating all the oxygenated gaseous products according to

$$\text{Mol O released}(t) = F \int_{t_{\text{start}}}^{t} \left(y_{\text{EO}} + 3y_{CO_2} + y_{\text{CO}} \right) dt \tag{4.3}$$

where F is the total molar flow rate, and the term $3y_{CO_2}$ accounts for oxygen released from both CO_2 and H_2O by assuming these two products are generated only from the combustion of C_2H_4.

In the co-feeding experiments, 2.0 g α-Al_2O_3 was used for the bottom layer with 1.000 g catalyst. The flows of C_2H_4 and air were mixed to a composition of 4 vol% C_2H_4, 4 vol% O_2 in balance N_2, at a total flow rate of 200 mL/min. The instantaneous carbon balance was calculated according to

$$\text{Instantaneous carbon balance, co-feeding}(t) = \left.\frac{y_{C_2H_4} + y_{EO} + \frac{1}{2}y_{CO_2} + \frac{1}{2}y_{CO}}{y_{C_2H_4,\text{feed}}}\right|_t \quad (4.4)$$

The carbon balance during co-feeding was always within 97 ± 3%.

The mean selectivity achieved in a particular reduction stage, $\bar{S}$, was calculated using

$$\bar{S} = \frac{\text{Total carbon in EO}}{\text{Total carbon in all products}} = \frac{\int_{t_{start}}^{t_{end}} y_{EO}\, dt}{\int_{t_{start}}^{t_{end}} \left(y_{EO} + \frac{1}{2}y_{CO_2} + \frac{1}{2}y_{CO}\right) dt} \quad (4.5)$$

The start time for integration was arbitrarily chosen to be the point when CO_2 was above 500 ppm, and the end time was chosen to be the point when C_2H_4 starts to decrease which signifies the start of the purge: these points in time were chosen to minimise the artificial influence of the response of the analyser.

The mean conversion of C_2H_4 achieved in a particular reduction stage, $\bar{X}$, was calculated using (assuming perfect carbon balance)

$$\bar{X} = \frac{\text{Total carbon in all products}}{\text{Total carbon fed}} = \frac{\int_{t_{start}}^{t_{end}} \left(y_{EO} + \frac{1}{2}y_{CO_2} + \frac{1}{2}y_{CO}\right) dt}{\int_{t_{start}}^{t_{end}} \left(y_{C_2H_4} + y_{EO} + \frac{1}{2}y_{CO_2} + \frac{1}{2}y_{CO}\right) dt} \quad (4.6)$$

The start time was chosen to be the point when CO_2 was above 500 ppm, and the end time was defined to be the point when C_2H_4 started to decrease which signified the start of the purge.

The instantaneous selectivity at time t was calculated using

$$S(t) = \frac{\text{Concentration of EO}}{\text{Concentration of carbon in products}} = \left.\frac{y_{EO}}{y_{EO} + \frac{1}{2}y_{CO_2} + \frac{1}{2}y_{CO}}\right|_t \quad (4.7)$$

The instantaneous conversion at time *t* was calculation using

$$X(t) = \frac{\text{Concentration of carbon in products}}{\text{Concentration of carbon in all species}} = \left. \frac{y_{\text{EO}} + \frac{1}{2}y_{\text{CO}_2} + \frac{1}{2}y_{\text{CO}}}{y_{\text{C}_2\text{H}_4} + y_{\text{EO}} + \frac{1}{2}y_{\text{CO}_2} + \frac{1}{2}y_{\text{CO}}} \right|_t \quad (4.8)$$

where the denominator was defined as such to minimise influence from the response of the analyser, but neglecting deposition of carbon. The definitions of instantaneous selectivity and conversion were equivalent to those used for the chemical looping case.

The turnover frequency (TOF) for the rate of production of EO and conversion of C_2H_4 was calculated according to

$$\text{TOF EO} = \frac{\text{rate of production of EO}}{\text{number of surface Ag atoms}} = \frac{F y_{\text{EO}}}{n_s m} \quad (4.9)$$

$$\text{TOF C}_2\text{H}_4 = \frac{\text{rate of conversion of C}_2\text{H}_4}{\text{number of surface Ag atoms}} = \frac{F\left(y_{\text{EO}} + \frac{1}{2}y_{\text{CO}_2}\right)}{n_s m} \quad (4.10)$$

where n_s is the moles of surface Ag atoms per unit mass of catalyst and m is the mass of catalyst. The approximation that the rate of reaction = Fy_i was used because the change in the total molar flow of gas can be neglected for dilute feeds with small conversion.

Brunauer, Emmett and Teller (BET) theory (Brunauer *et al.*, 1938) was used to model nitrogen physisorption isotherms measured at 77 K (Tristar 3000, Micromeritics). Prior to analysis, the samples were degassed at 150°C *in vacuo* for 1 h. A quantity of 1–2 g of the supported silver samples were used in each analysis.

Thermogravimetric analysis (TGA) was conducted using a TGA/DSC1 (Mettler Toledo), described previously in section 2.2. Approximately 20 mg of 15 wt% Ag/$SrFeO_3$ was loaded into a 70 µL alumina crucible. The sample was heated to 270°C in air. Five minutes after reaching the setpoint temperature, the gas was switched to N_2 for 2 min to purge. Ethylene was then fed to the sample for 30 min, followed by a 2 min purge with N_2, then air was fed for 60 min. Throughout the experiments, the TGA chamber was purged with protective and purge gas flows of Ar (50 mL/min each, measured at 293 K and 1 atm). The reactive gas was supplied through a capillary tube located above the crucible at 50 mL/min (measured at 293 K and 1 atm). The reactive gases fed from cylinders were air, N_2, 5.16% C_2H_4 in balance N_2 (all BOC, >99.99%). The actual concentrations of the specific gas components listed were approximately three times lower when in contact with the solid sample due to the dilution with the protective and purge gas.

Scanning electron microscopy (SEM) images were taken using a Leo GEMINI 1530 VP. The particulate samples of 15 wt% Ag/$SrFeO_3$ were mounted on copper tape. Images were taken at an accelerating voltage of 2.4 kV and a working distance of 5.4 – 5.6 mm. Distributions of particle size were measured from the SEM images with ImageJ (Schneider *et al.*, 2012). The analysis was carried out semi-automatically, using the 'Analyze Particles' function in ImageJ. The results were then inspected manually to correct for any false measurements, *e.g.* aggregated particles. Each analysed particle i was described by its projected area A_i, from which an equivalent diameter was calculated $d_i = 2\sqrt{A_i/\pi}$. The surface area-weighted mean diameter was then calculated using $d_{3,2} = \frac{\sum d_i^3}{\sum d_i^2}$, which was taken to be the mean crystallite size. 458 particles were measured for Ag/$SrFeO_3$, and 83 particles for Ag/Al_2O_3. The dispersion of silver, D, was calculated by assuming spherical particles, so

$$D = \frac{\text{number of surface Ag atoms}}{\text{total number of Ag atoms}} = \frac{\rho_s \pi d_{3,2}^2}{\rho_b \frac{\pi d_{3,2}^3}{6}} = \frac{6\rho_s}{\rho_b}\frac{1}{d_{3,2}} = \frac{6 \times 1.14 \times 10^{19}}{5.87 \times 10^{28}}\frac{1}{d_{3,2}[\text{m}]} = \frac{1.17}{d_{3,2}[\text{nm}]} \qquad (4.11)$$

where $\rho_s = 1.14 \times 10^{19}$ m^{-2} is the surface atom density of silver averaged over the (100), (110) and (111) planes, and $\rho_b = 5.87 \times 10^{28}$ m^{-3} is the bulk atom density of silver (fcc lattice parameter is 0.40853 nm). The moles of surface Ag atoms per unit mass of catalyst, n_s, can then be calculated from the loading of silver using $n_s = Dw/m_{\text{Ag}}$ where $w = 15$ wt% is the loading of Ag on the catalyst and $m_{\text{Ag}} = 108$ g mol^{-1} is its molecular weight.

Powder X-ray diffraction (XRD) was performed on the supported silver samples using Cu-Kα radiation with a voltage of 40 kV and current 40 mA (Empyrean, PANalytical). Samples were first ground to a fine powder (< 67 μm) before being loaded into the *ex situ* sample holders. The instrument was arranged in a Bragg-Brentano geometry. The diffractogram was collected in the range of 2θ from 10° to 150° over 67 min, with a step size 2θ = 0.0167°. The mean particle size of the silver crystallites was measured by Rietveld refinement of the diffraction patterns. The refined parameters were particle size, strain, unit cell and atomic displacement. The surface area-weighted mean diameter was calculated using the method reported by Popa and Balzar (2002). The lack of measurable peak-broadening in the Al_2O_3-supported sample suggested that the particles were at least 300 nm. Nevertheless, measurements for both Al_2O_3- and $SrFeO_3$-supported samples were consistent with SEM imaging.

4.3 Results

Figure 4.2 shows the XRD pattern obtained for the Ag/$SrFeO_3$ sample. Rietveld refinement shows that almost all the observed peaks can be explained by the presence of Ag and $SrFeO_3$. Modelling the effects of particle size and strain showed a mean Ag crystallite size of 110 ± 40 nm.

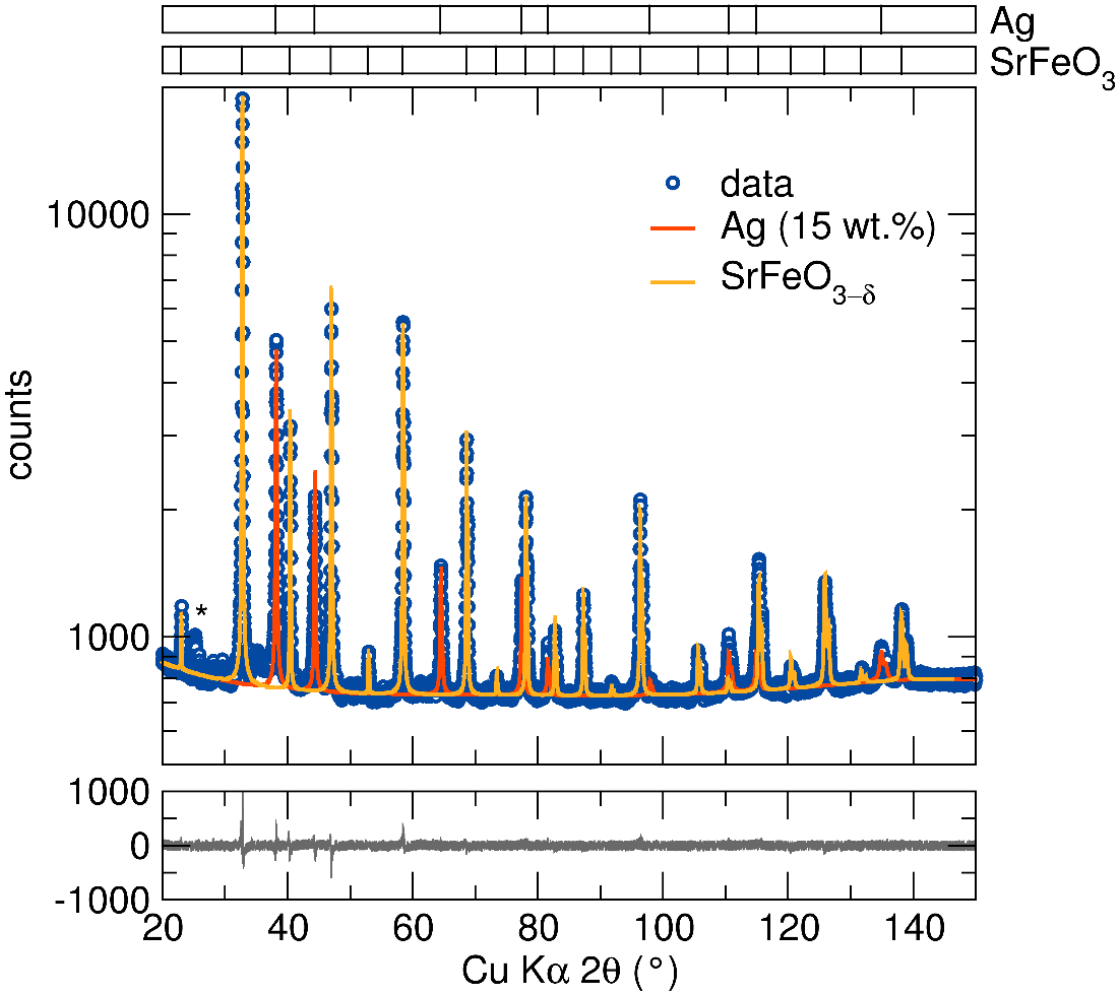

Figure 4.2. Refined pattern for 15 wt% Ag/$SrFeO_3$. The refined parameters were particle size, strain, unit cell and atomic displacement. Reflections from an unidentified secondary phase are indicated by asterisks.

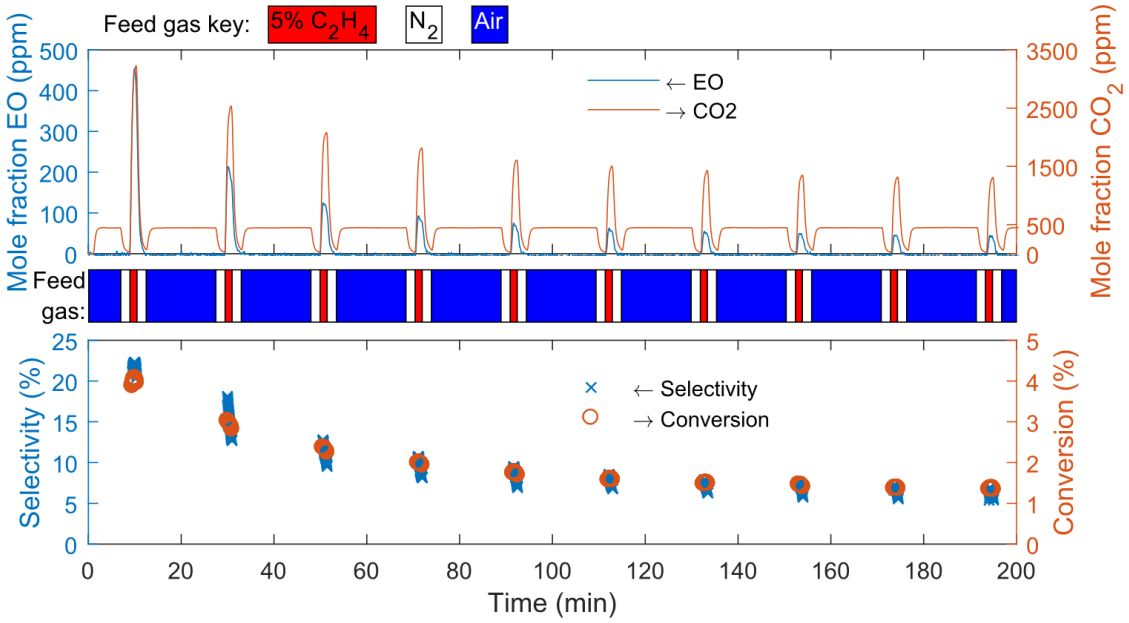

Figure 4.3. Mole fraction, selectivity and conversion profiles from a packed bed reactor operated in chemical looping mode, using 15 wt% Ag/$SrFeO_3$ as the catalyst. The background of CO_2 during oxidation steps was from compressed atmospheric air. Conditions: 270°C, 1 atm, 2.000 g catalyst, gas feed of 200 mL/min (as measured at 293 K, 1 atm). Cycling times: (i) t_{red} = 1.5 min reduction with 5.16 vol% C_2H_4 in balance N_2, (ii) 2 min purge with N_2, (iii) t_{ox} = 15 min oxidation with air, (iv) 2 min purge with N_2.

The catalyst, composed of 15 wt% Ag supported on $SrFeO_3$, was evaluated in a packed bed reactor (*n.b* here, the nonstoichiometric perovskite $SrFeO_{3-\delta}$ is abbreviated as $SrFeO_3$ for brevity: its characterisation was reported by Lau *et al.* (2017)). A typical experiment is shown in Figure 4.3, which shows how the mole fractions varied over 10 cycles. Within each cycle, air was first fed to the reactor (indicated by the background level of ~440 ppm CO_2 in the cylinder of compressed air) to charge the catalyst with oxygen, followed by a purge with N_2, then a switch to a feed of ethylene to produce EO and CO_2, followed by another purge. The selectivity and conversion achieved by the catalyst decayed gradually with cycling, before approaching an asymptote. This decay is probably caused by the slow rate of reoxidation of the perovskite. Thermogravimetric analysis, presented in Figure 4.4, shows that the rate of oxidation in air was indeed much slower than the rate of reduction in ethylene. This is supported by the results in Figure 4.5, which show the effect of varying the duration of reduction and oxidation. When the duration of oxidation was increased from t_{ox} = 7.5 min to 30 min, both the selectivity and conversion were maintained at higher values. A similar improvement was observed when the duration of reduction was decreased from t_{red} = 3 min to 1 min. The decrease in conversion is probably caused by the depletion of oxygen species, owing to the catalyst gradually becoming more

reduced with cycling. Cycling with 5 min reduction and 10 min oxidation (results not shown) led to the mole fraction of EO decaying to zero within four cycles. Accumulation of coke, indicated by slight elevations in the mole fraction of CO_2 (of the order of 10 ppm) during oxidation with air, may also have caused the decaying activity. The decrease in selectivity might be explained by the depletion of subsurface oxygen species, O_{ss}, when the catalyst was reduced. The decrease in abundance of O_{ss} would cause the degree of electrophilicity of O_a to decrease (Amorim de Carvalho *et al.*, 2007; Özbek and van Santen, 2013), resulting in the observed decrease in selectivity.

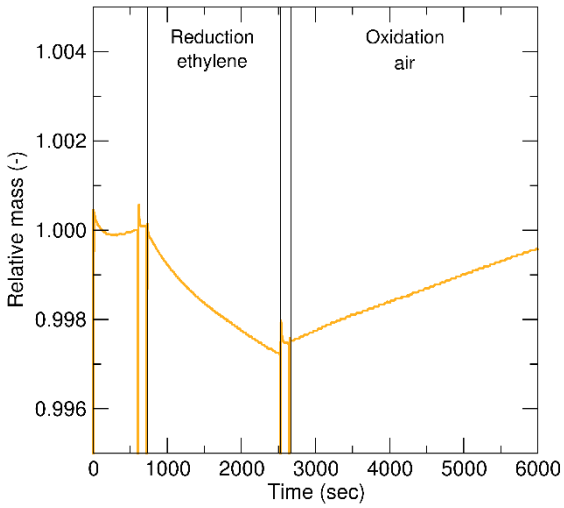

Figure 4.4. Variation of catalyst mass over a single cycle for a sample of 15 wt% $Ag/SrFeO_3$ measured by TGA. The temperature was fixed at 270°C. The spikes in the mass are artefacts caused by the switching of gases.

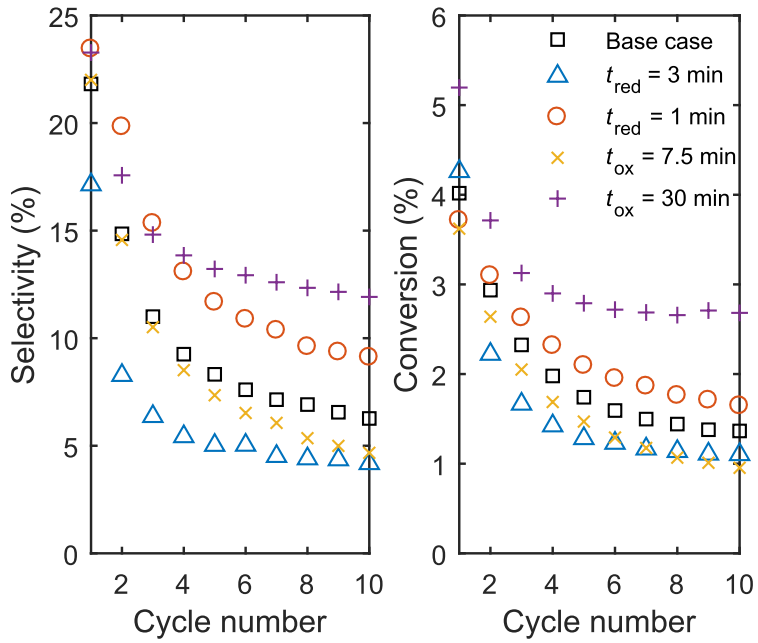

Figure 4.5. Effects of cycling times on the selectivity and conversion. Conditions: 270°C, 1 atm, 2.000 g of 15 wt% Ag/$SrFeO_3$, feed of 200 mL/min (as measured at 293 K, 1 atm). Cycling times (unless stated otherwise): (i) t_{red} = 1.5 min reduction with 5.16 vol% C_2H_4 in balance N_2, (ii) 2 min purge with N_2, (iii) t_{ox} = 15 min oxidation with air, (iv) 2 min purge with N_2.

The regenerability of the 15 wt% Ag/$SrFeO_3$ catalyst was examined further by calcining the cycled sample *ex situ* in static air at 400°C for 2 h, before subjecting it to the same ten cycles. This was repeated three times, shown in Figure 4.6. It can be seen that this treatment fully regenerated both the selectivity and activity of the catalyst, confirming that the oxidation step is probably the rate-limiting step in the cycle. Additionally, coke should have been effectively removed by this period of oxidation. Figure 4.6 also shows that the selectivity gradually improved over time, which might be related to the sintering of the Ag particles. The selectivity of Ag particles, for epoxidation, increases with their size (Christopher and Linic, 2010; Bukhtiyarov and Knop-Gericke, 2011). Scanning electron microscopy (SEM) images of the fresh and cycled catalysts, presented in Figure 4.7, show that Ag particles as small as 50 nm present on the fresh catalyst were no longer present on the cycled catalyst.

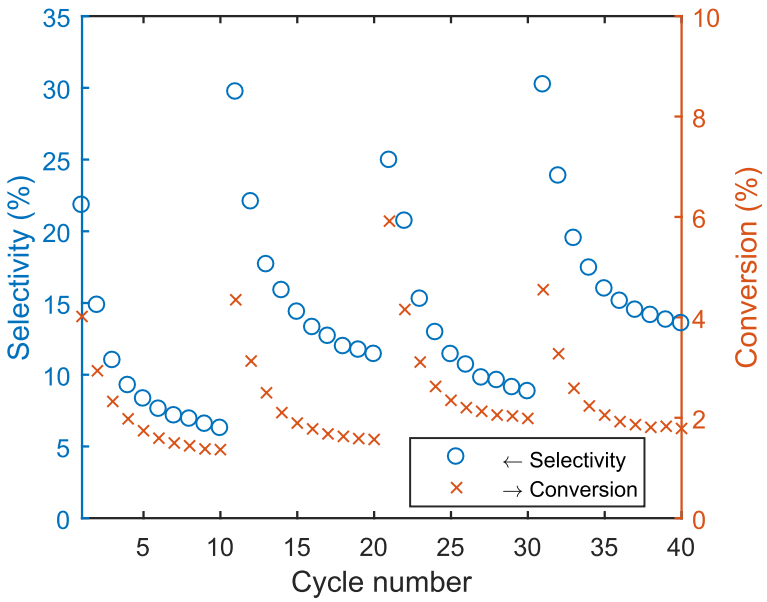

Figure 4.6. Effect of extended *ex-situ* reoxidation at 400°C for 2 h, performed after every 10th cycle. Conditions: 270°C, 1 atm, 2.000 g of 15 wt% Ag/$SrFeO_3$, feed of 200 mL/min (as measured at 293 K, 1 atm). Cycling times: (i) t_{red} = 1.5 min reduction with 5.16 vol% C_2H_4 in balance N_2, (ii) 2 min purge with N_2, (iii) t_{ox} = 15 min oxidation with air, (iv) 2 min purge with N_2.

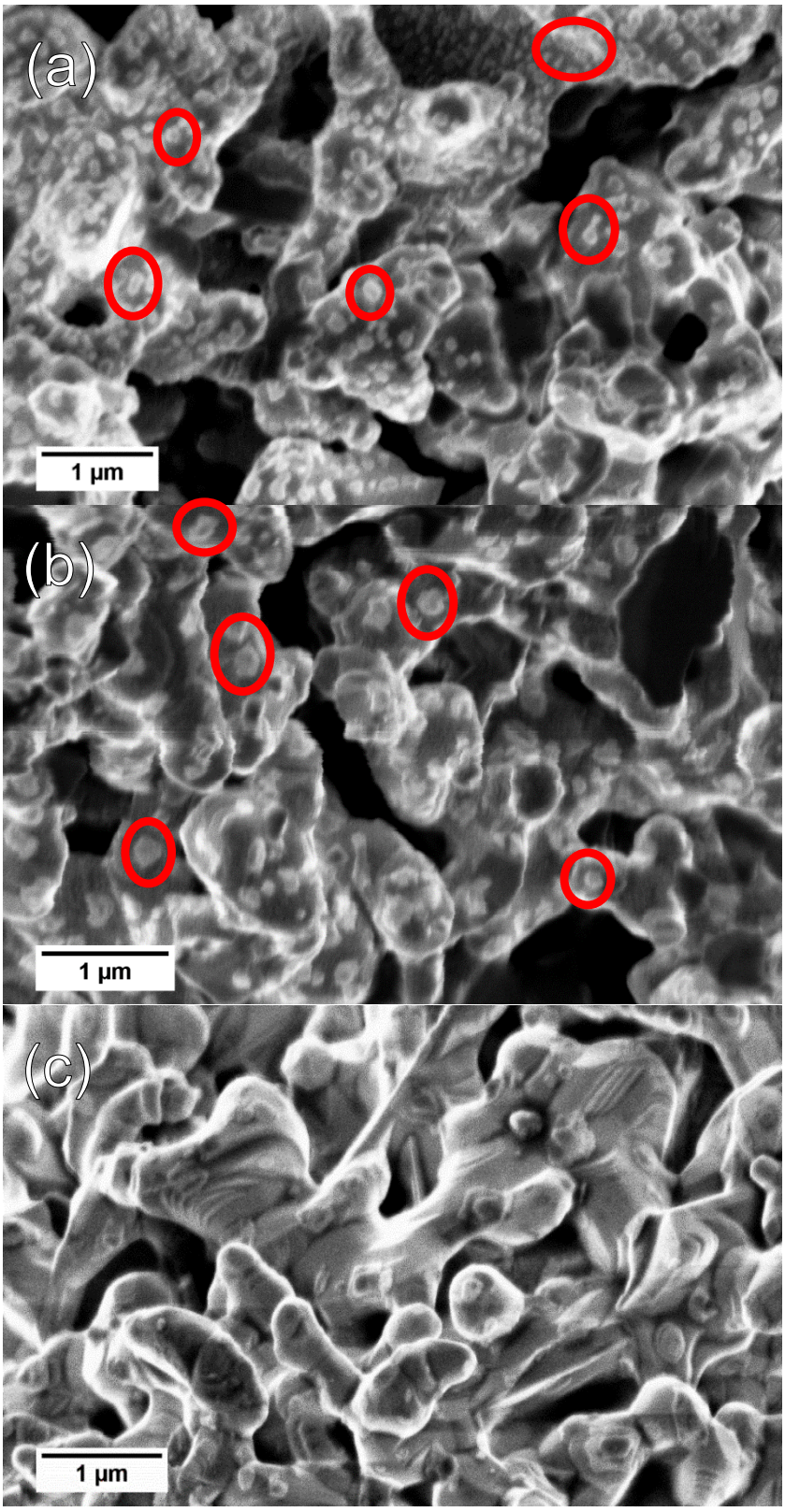

Figure 4.7. SEM images of 15 wt% Ag/$SrFeO_3$ (a) initial state after first calcination at 500°C for 5 h, (b) cycled and regenerated multiple times, and (c) bare $SrFeO_3$. Ag crystallites as small as 50 nm are present in (a), whereas only crystallites > 100 nm appear in (b). Selected individual and clusters of crystallites have been circled in red for clarity.

Generally, over the course of one cycle, the instantaneous selectivity of the carrier decreased as it became more reduced. This is shown in Figure 4.8 for the sample which had been regenerated three times at 400°C for 2 h (*i.e.* cycles 31-40 in Figure 4.6). The trend is consistent with the mechanism proposed earlier, that reduction of the catalyst led to a gradual depletion of O_a and O_{ss}, resulting in the decreasing selectivity. Interestingly, the first cycle after each calcination step always exhibited a maximum in selectivity and conversion (*n.b.* the early maxima for subsequent cycles are probably artefacts of the response time of the gas analyser, or noise). This gradual improvement in the selectivity during the first cycle in Figure 4.8 might be due to carbon deposition which selectively poisoned unselective sites (Collett and McGregor, 2016). Figure 4.8 also shows that the oxygen carrying capacity of the sample was of the order of 0.1 wt%, which is an order of magnitude higher than previously reported for conventional Ag/Al_2O_3, namely ~0.007 wt% (Park *et al.*, 1983).

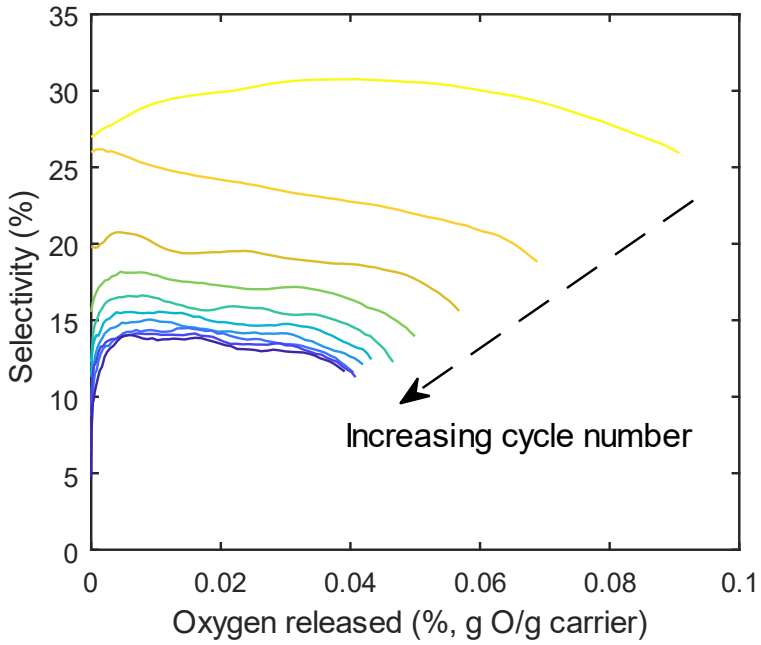

Figure 4.8. Variation of instantaneous selectivity with degree of reduction of catalyst, expressed as the total amount of oxygen released. Each line corresponds to one cycle. Conditions: 270°C, 1 atm, 2.000 g of 15 wt% $Ag/SrFeO_3$, feed of 200 mL/min (as measured at 293 K, 1 atm). Cycling times: (i) t_{red} = 1.5 min reduction with 5.16 vol% C_2H_4 in balance N_2, (ii) 2 min purge with N_2, (iii) t_{ox} = 15 min oxidation with air, (iv) 2 min purge with N_2.

4.4 Discussion

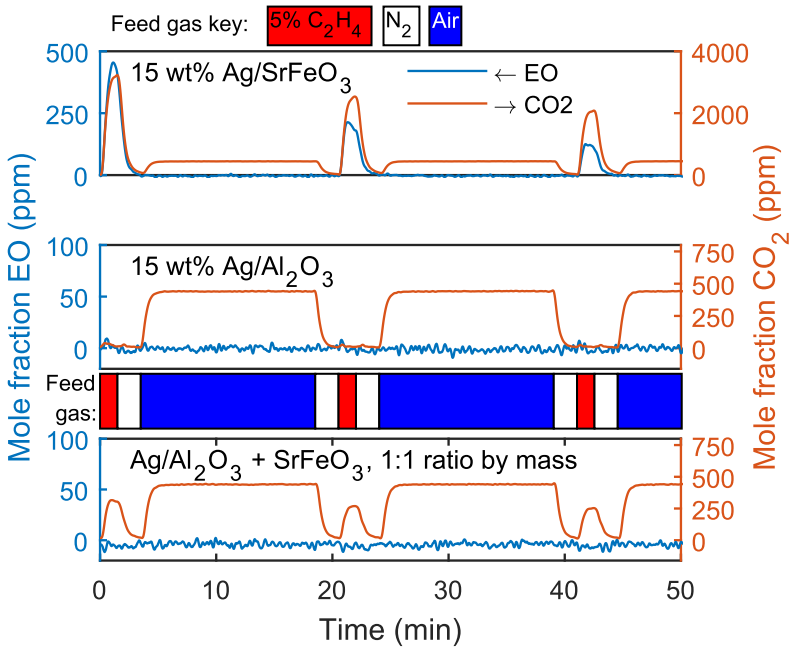

Figure 4.9. Effect of the support on the performance in chemical looping mode. Conditions: 270°C, 1 atm, 2.000 g of catalyst, feed of 200 mL/min (as measured at 293 K, 1 atm). Cycling times: (i) t_{red} = 1.5 min reduction with 5.16 vol% C_2H_4 in balance N_2, (ii) 2 min purge with N_2, (iii) t_{ox} = 15 min oxidation with air, (iv) 2 min purge with N_2.

The performance of $Ag/SrFeO_3$ was in stark contrast with those of (i) 15 wt% Ag/Al_2O_3 and (ii) a heterogeneous mixture of particles of 15 wt% Ag/Al_2O_3 with particles of $SrFeO_3$, shown in Figure 4.9. The 15 wt% Ag/Al_2O_3 catalyst yielded only barely detectable levels of EO (~10 ppm) with instantaneous selectivities of up to ~30% in the first cycle, and no detectable EO in subsequent cycles. The production of CO_2 also quickly fell to insignificant levels (< 30 ppm). This is because neither Ag nor Al_2O_3 can carry enough oxygen over from the preceding oxidation step in the cycle, so the subsequent reaction with ethylene became starved of oxygen. With the addition of separate particles of $SrFeO_3$ to the bed, only CO_2 was produced. This is because the perovskite could not generate O_a by itself nor did it supply any oxygen to Ag/Al_2O_3, which prevented epoxidation from occurring and so only combustion occurred. This also shows that some CO_2 evolved in the reaction with $Ag/SrFeO_3$ must have originated from reaction with the part of the $SrFeO_3$ surface not covered with Ag. Therefore, the selectivity could be improved simply by increasing the coverage of $SrFeO_3$ with Ag. The experiment with bare $SrFeO_3$ also eliminates the possibility of $SrFeO_3$ supplying oxygen to Ag *via* gaseous transport at this temperature. Hence, the performance of 15 wt% $Ag/SrFeO_3$ must have originated from the intimate physical contact between Ag and

$SrFeO_3$, suggesting possible mechanisms: (i) solid state oxygen diffused from $SrFeO_3$ to Ag, as hypothesised, (ii) the oxygen storage capacity of Ag became enhanced, or (iii) Ag facilitated adsorption and diffusion of ethylene to the $SrFeO_3$ boundary to react with lattice oxygen from $SrFeO_3$, *i.e.* triple phase boundaries. However, because of the magnitude of the effect, the mechanism of (ii) seems unlikely; if one assumes that all the oxygen in the products originated solely from Ag, then the bulk chemical state of the silver phase would be written as $AgO_{0.08}$ (for the first cycle with t_{red} = 3 min), which is far higher than the limit of solubility (O:Ag molar ratio ~10^{-6}) (Assal *et al.*, 1997). Moreover, bulk silver oxide is not thermodynamically stable at these conditions (Assal *et al.*, 1997). Adsorbed oxygen also cannot account for the capacity because the amount of oxygen released exceeded the number of surface Ag sites. As shown in Table 4.1, the molar ratio of O released to surface Ag = 7.7 exceeded an adsorption stoichiometry of 1, which is generally assumed for chemisorption analyses (Lu *et al.*, 2005), and is also two orders of magnitude higher than previously observed, 0.064, for anaerobic epoxidation of ethylene by Ag on an inert support (Park *et al.*, 1983). Furthermore, adsorbed oxygen should also be accessible by Ag/Al_2O_3 and yet it did not exhibit much activity, probably because oxygen desorbed from Ag during the N_2 purge, which would be significant at these temperatures (Busser *et al.*, 2002). Triple phase boundaries producing CO_2 through the mechanism of (iii) cannot yet be excluded, but the formation of ethylene oxide through this mechanism is unlikely because epoxidation proceeds from the formation of oxametallacycles (Linic *et al.*, 2004). $SrFeO_3$ is not known to support the formation of oxametallacycles. In conclusion, $SrFeO_3$ most probably donated oxygen to Ag to be presented as adatoms on the Ag surface through the mechanism of (i). This might well be exploitable in catalyst-oxygen carrier systems other than $Ag\text{-}SrFeO_3$ shown herein and applicable to selective oxidations other than the epoxidation of ethylene.

The Ag/Al_2O_3 and $Ag/SrFeO_3$ catalysts were also examined in a co-feeding mode, using gas-phase oxygen, where the feed was a premixed stream of O_2 (4 vol%) and C_2H_4 (4 vol%), with 200 mL/min total flow (as measured at 293 K and 1 atm) and 1.000 g catalyst (half the catalyst loading compared to the chemical looping experiments). After 5 h on stream, Ag/Al_2O_3 achieved a conversion of 1.6% at a selectivity of 27%, whilst $Ag/SrFeO_3$ achieved a conversion of 6% at a selectivity of 5.7%. Turnover frequencies (TOF) from these co-feeding experiments are shown in Table 4.1. TOFs were also calculated for the $Ag/SrFeO_3$ sample in chemical looping mode, shown in Figure 4.10. Whilst the TOF apparently increased up to ~0.03 wt% of oxygen released, this is probably

an artefact caused by the response time of the analyser. It is feasible for the TOF to have linearly decayed right from the start, which is typical for certain types of gas-solid reactions, and that convolution with the analyser masked this initial period. TOF then decayed from maxima of 1.1 × 10^{-2} C_2H_4 s^{-1} and 0.24 × 10^{-2} EO s^{-1}, because the oxygen was depleted. The observed TOFs in this study were within the generally-observed range of 10^{-3}–10^{-1} s^{-1} for unpromoted supported polycrystalline Ag catalysts (Seyedmonir *et al.*, 1990; Lu *et al.*, 2005). It is not surprising that the chemical looping TOF was on the lower end of this range, because the lattice oxygen from $SrFeO_3$ has additional resistances for transport to the Ag active sites compared to gaseous oxygen.

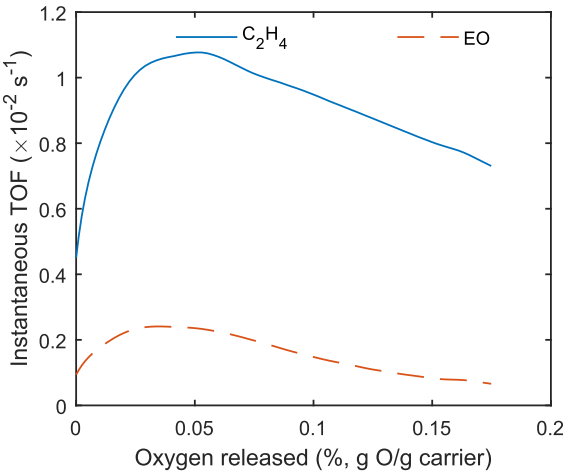

Figure 4.10. Turnover frequencies, based on the rates of C_2H_4 conversion and EO production, varying with the degree of reduction during the first cycle. Conditions: 270°C, 1 atm, 2.000 g of 15 wt% Ag/$SrFeO_3$, feed of 200 mL/min (as measured at 293 K, 1 atm). Reduction in 5.16 vol% C_2H_4 over a period of 3 min.

The diffusion of oxygen through the particles of silver, or the perovskite lattice, could have influenced the observed rates of reaction. This effect is characterised by a mass transfer Biot number, $\mathrm{Bi_m}$, defined as:

$$\mathrm{Bi_m} = \frac{\text{diffusional resistance}}{\text{surface resistance}} = \frac{k_\mathrm{O} L}{D_\mathrm{O}} \tag{4.12}$$

where L is the length scale (equal to $d/3$ for a sphere with diameter d), D_O is the diffusivity of oxygen through silver, 2.6 × 10^{-11} m^2 s^{-1} at 270°C (Gryaznov *et al.*, 1973), and k_O is an apparent first order rate constant defined by:

$$r_\mathrm{O} = k_\mathrm{O} A C_{\mathrm{C_2H_4}} \tag{4.13}$$

where r_O is the rate of reaction of oxygen at the surface (measured by the rate of production of oxygenated products weighted by the number of oxygen atoms per molecule), A is the surface area of the silver and $C_{C_2H_4}$ is the concentration of ethylene in the bulk gas. For the most active sample, $r_O = \frac{F(y_{EO}+3y_{CO_2})}{m} = 8.0 \times 10^{-7}$ mol s^{-1} g^{-1} (the factor of 3 includes the oxygen in water co-produced with carbon dioxide during combustion), resulting in a rate constant of:

$$k_O = \frac{r_O}{AC_{C_2H_4}} = \frac{8.0 \times 10^{-7}}{0.8 \times 1.19} = 8.4 \times 10^{-7} \text{ m s}^{-1} \quad (4.14)$$

This corresponds to a Biot number of:

$$\text{Bi}_m = \frac{8.4 \times 10^{-7} \times \frac{107 \times 10^{-9}}{3}}{2.6 \times 10^{-11}} = 1.2 \times 10^{-3} \quad (4.15)$$

which is small and shows that diffusional gradients in the silver crystallites are small. The group D_O/k_O has dimensions of length and is sometimes referred to as the effective oxygen diffusional length scale (Dueso *et al.*, 2015). In this case, the diffusional length scale evaluates to 30 μm, which suggests that silver particles much smaller than this length scale should not be significantly limited by diffusion of oxygen. Influence of diffusion through the perovskite lattice was not determined (no diffusion coefficients at these temperatures were found in the literature).

Whilst the selectivities and TOFs shown in the chemical looping experiments were worse than those of the conventional co-feeding experiments, they were within an order of magnitude and it is noted that there are many degrees of freedom available to optimise the performance of both, or separately, the catalyst and the oxygen carrier, in addition to the operating parameters. No such optimisation was undertaken in producing these results, but should form the subject of future work. It is noteworthy that the instantaneous performance near the start of chemical looping operation briefly surpassed the co-feeding operation, and that this could be reliably reproduced with a long regenerating treatment at elevated temperatures in air – it is speculated that tuning the material properties for faster reoxidation to sustain this early transient will be particularly important.

Finally, in section 4.1, it was originally posited that a high chemical potential of oxygen is required to attain selectivity. This might be supported by the observations in Figure 4.5, where longer reductions (or shorter oxidations) led to a solid of lower chemical potential, hence the accelerated degradation in selectivity with cycling. Similarly, in Figure 4.6, the

restoration of the original selectivity could have corresponded to the restoration of the original oxidation state of the oxygen carrier (and hence the original high chemical potential of oxygen). The decaying instantaneous selectivity within a cycle, shown in Figure 4.8, could also be similarly explained – as the oxygen carrier became reduced, its chemical potential of oxygen decreased.

Table 4.1. Characterisation and turnover frequencies (TOF), based on C_2H_4 conversion or EO production, of the prepared catalysts. The uncertainty in the mean particle size measurements correspond to a 95% confidence interval.

Sample	BET surface area	Mean particle size XRD	Mean particle size SEM	Silver dispersion SEM	Moles of surface Ag	Chemical looping[a]				Co-feeding	
						Oxygen released	O released / Surface Ag	TOF C_2H_4	TOF EO	TOF C_2H_4	TOF EO
	$m^2\ g^{-1}$	nm	nm	-	mol Ag g^{-1}	mol O g^{-1}	-	$\times10^{-2}\ s^{-1}$	$\times10^{-2}\ s^{-1}$	$\times10^{-2}\ s^{-1}$	$\times10^{-2}\ s^{-1}$
15 wt% $Ag/SrFeO_3$	0.92	110±40	107±3	1.09×10^{-2}	1.5×10^{-5}	1.2×10^{-4}	7.7	1.1	0.24	2.2	0.13
15 wt% Ag/Al_2O_3	0.22	>300	2740±80	4.27×10^{-4}	5.9×10^{-7}	[b]	[b]	[b]	[b]	15	4.3

[a] First cycle with reduction time t_{red} = 3 min. Maximum instantaneous values for TOF.

[b] No detected activity

4.5 Conclusions

The epoxidation of ethylene in the absence of gaseous oxygen depended crucially upon the intimate contact between the catalyst, Ag, and the oxygen carrier, $SrFeO_3$. This intimate contact suggests that solid state transport of oxygen from $SrFeO_3$ to Ag was responsible for the observed performance, but further study is needed to confirm this mechanism. Effects of the operating conditions were studied, which showed that the oxidation step in the cycle is probably the bottleneck, being slower than the reduction step, and that further attention on this part of the process is crucial. Comparable, although currently inferior, performance with conventional co-feeding justifies further development of this technology.

5 ANALYSIS OF GAS-SOLID REACTIONS USING GENERALISED FREQUENCY RESPONSE FUNCTIONS

5.1 Introduction

Nonlinear systems are ubiquitous in chemical engineering (*e.g.* in chemical reactions with non-first order kinetics, and, or, with rate constants involving with Arrhenius-type behaviour). The analysis of such operations may sometimes be simplified when the process is at steady state, but it becomes complicated when unsteady operation is required either by necessity (such as in adsorption beds and catalytic converters) or by choice (such as in chromatographic operations, batch systems, and chemical looping reactors).

An input, oscillating about some mean value (*i.e.* input modulation), to a nonlinear system can sometimes produce an enhanced performance over the steady state that had no input modulation (with the same mean input) (Silveston *et al.*, 1995). For example, the rate of reaction, yield or selectivity in a reactor might be improved by modulating the feed concentration (Yadav and Rinker, 1989). This can sometimes be rationalised by envisaging the oscillations as merely allowing the system to sample a range of steady states, where the time constant of the system is much smaller than the period of the oscillations (and provided that the system is stable). The performance is then a time-average of this range of sampled steady states. If the rate law is convex (*e.g.* reactions

higher than first order), then the time-averaged rate of reaction must necessarily be greater than the steady state which was not oscillating. A stronger effect of "global enhancement" has also been reported (Yadav and Rinker, 1989), where the performance with input modulation is greater than any steady state that had no input modulation. In this case, the optimum steady state input is not necessarily equal to the mean of the optimum oscillating input. Global enhancement cannot be explained by an averaging over a set of steady states, since it exceeds the optimum steady state. In some cases, global enhancement is said to originate from surface dynamics in heterogeneous reactions (Yadav and Rinker, 1989).

In oscillatory systems, the analysis can sometimes be simplified by linearisation, but this technique is generally applicable only when the deviations about some initial steady state are small. This allows the "frequency response theorem" to be applied (Stephanopoulos, 1983), which relates the amplitude ratio and phase angle of the response to properties of the system. However, this linearised system is inherently limited because the oscillations are necessarily sinusoidal about the steady state. In other words, the time-averaged performance of oscillatory operation is predicted to be the same as the steady state. Therefore, it cannot predict improved or diminished performances that are often possible in nonlinear systems. The difference between the time-averaged performance of oscillatory operation and the performance of the corresponding steady state operation is sometimes referred to as the 'DC component' of the response to the oscillating input.

The frequency response theorem has been extended to describe nonlinear systems using a Volterra series. This extension has been used to analyse a variety of systems in control, acoustics, aeroelastics, and electronics (Cheng *et al.*, 2017). In the past decade, it has been applied to chemical processes, and has been exploited to predict rapidly the DC component of the output response (Marković *et al.*, 2008; Nikolic Paunic and Petkovska, 2013; Nikolić *et al.*, 2015). The DC component is particularly important in evaluating whether periodic operation of a chemical process can allow for enhanced performance over some steady state operation, because the DC component directly measures the time-averaged performance of a process relative to the steady state. The prediction of the DC component relies upon the use of "generalised frequency response functions" (GFRFs), which are higher order extensions to the transfer function encountered in the linear frequency response theorem.

The use of generalised frequency response functions is more accurate than the linear frequency response theorem. However, depending on the magnitude of the truncated

terms in the Volterra series, numerical methods might be significantly more accurate than GFRFs. Nevertheless, GFRFs have the advantage of being able to evaluate quickly the response of a nonlinear system across a continuous range of frequencies, whereas numerical methods have to sample a discrete set of frequencies, as well as ensuring that transients have decayed. Therefore, GFRFs could be seen as a method that lies between the linear frequency response theorem and numerical methods, both in terms of accuracy and speed.

GFRFs have been applied to homogeneous and heterogeneous reactors, adsorption systems, membrane reactors and electrochemical systems. This chapter examines its novel application to periodic non-catalytic gas-solid reactions (*e.g.* chemical looping reactions), which is an example of a multiple input multiple output (MIMO) system. A simple physical model of a gas-solid reactor is constructed, which is then solved using either a numerical method or GFRFs. Both methods are then compared and contrasted.

5.2 Methods

5.2.1 Model of gas-solid reactor

In this idealised scenario, heat and mass transfer effects were assumed to be negligible so that the rates of reaction were controlled by intrinsic kinetics. The reaction was also assumed to be isothermal, conserves the number of moles of gas, and also does not change the structure of the solid. The system was also assumed to be weakly nonlinear, as discussed later in section 5.2.2. The overall reaction is chosen to be of the form $A + B \rightarrow$ Products. The mechanism proceeds *via* a solid intermediate, so that the overall reaction is composed of the following elementary reactions:

$$A + S \rightarrow \text{Products} + [\ ] \tag{5.1}$$

$$B + [\ ] \rightarrow \text{Products} + S \tag{5.2}$$

where [ ] is some vacancy in the solid, *S*. This type of mechanism includes Mars-van Krevelen reactions. An example of such a reaction is chemical looping combustion, where *A* is some hydrocarbon fuel, *B* is oxygen, *S* is lattice oxygen and the products are CO_2 and H_2O. The following rate laws were assumed for reactions 5.1 and 5.2, respectively:

$$r_1 = -k_A c_A (1 - X) \tag{5.3}$$

$$r_2 = -k_B c_B X \tag{5.4}$$

i.e. first order with respect to the gaseous reactants, with a uniform solid reaction. r_1 and r_2 are the rates of reactions 5.1 and 5.2 respectively, k_A and k_B are first order rate constants, c_A and c_B are the concentrations of *A* and *B*, and X is the fractional conversion of the solid (X varies between 0 and 1, where 0 corresponds to a state saturated with S, and 1 corresponds to a state saturated with vacancies [ ]). The nonlinearity here arises from the products of the output variables $c_A X$ and $c_B X$, which, for large perturbations from a steady state, prohibits the use of linear methods such as the frequency response theorem. This is a relative simple example of a gas-solid reaction, but GFRFs may be derived for arbitrarily complicated rate laws (including non-polynomial expressions, where Taylor expansions may be used to convert expressions to polynomial forms). The point of the current study is to demonstrate the applicability of GFRFs to such reactions.

The reaction is conducted in a continuous stirred tank reactor (CSTR), where the contents of the reactor are well-mixed and are the same as the outlet conditions. Such a reactor may be used to model fluidised beds with no cross-flow, or differential packed bed reactors. The reactor model is shown in Figure 5.1. The reactor is initially at some steady state, when at time $t = 0$, the feed concentrations c_{A0} and c_{B0} are forced to oscillate, and the response of the outlet concentrations c_A and c_B (as well as the conversion of the solid X) are to be predicted. In chemical looping, *A* and *B* are never co-fed, which can be modelled in this way if *e.g.* c_{A0} and c_{B0} were two square wave functions 180° out of phase (an additional period of $c_{A0} = 0$ and $c_{B0} = 0$ might be introduced to emulate a purge step, which would be necessary for a chemical looping system with back mixing such as a CSTR).

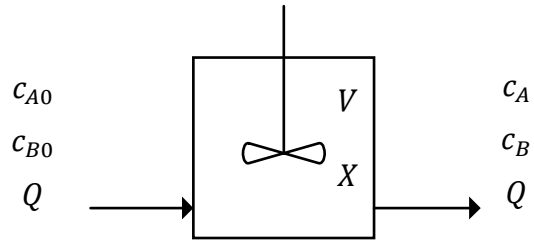

Figure 5.1. Continuously stirred tank reactor (CSTR). The volumetric flow through the reactor is Q and assumed to be constant. The concentrations of *A* and *B* in the feed are c_{A0} and c_{B0} respectively, whereas the concentrations in the outlet are c_A and c_B. The volume of the reactor is V, and the solid contents in the reactor are at a conversion X.

Material balances over the reactor, of *A*, *B*, and *S*, give the following nonlinear differential equations:

$$\tau \frac{dc_A}{dt} = c_{A0} - c_A - k_A \tau c_A (1 - X) \tag{5.5}$$

$$\tau \frac{dc_B}{dt} = c_{B0} - c_B - k_B \tau c_B X \tag{5.6}$$

$$n_O \frac{dX}{dt} = -k_B V c_B X + k_A V c_A (1 - X) \tag{5.7}$$

where $\tau = V/Q$ is the residence time of gas, n_O is the maximum number of moles of *S* (or [ ]) in the reactor (for example, it could be the total oxygen carrying capacity in the reactor). These differential equations are non-dimensionalised using $\theta = t/\tau$ for the time ordinate, and the following substitutions for the time-dependent variables c_{A0}, c_{B0}, c_A, c_B and X:

$$c_{A0}(\theta) = c_{A0s}\big(1 + \tilde{c}_{A0}(\theta)\big) \tag{5.8}$$

$$c_{B0}(\theta) = c_{B0s}\big(1 + \tilde{c}_{B0}(\theta)\big) \tag{5.9}$$

$$c_A(\theta) = c_{As}\big(1 + \tilde{c}_A(\theta)\big) \tag{5.10}$$

$$c_B(\theta) = c_{Bs}\big(1 + \tilde{c}_B(\theta)\big) \tag{5.11}$$

$$X(\theta) = X_s\left(1 + \tilde{X}(\theta)\right) \tag{5.12}$$

where subscript *s* denotes steady state conditions, and an accent tilde denotes a dimensionless deviation variable. Substituting equations 5.8-5.12 into equations 5.5-5.7 results in:

$$\frac{d\tilde{c}_A}{d\theta} = \frac{c_{A0s}}{c_{As}}(1 + \tilde{c}_{A0}) - (1 + \tilde{c}_A) - k_A \tau (1 + \tilde{c}_A)\left(1 - X_s\big(1 + \tilde{X}\big)\right) \tag{5.13}$$

$$\frac{d\tilde{c}_B}{d\theta} = \frac{c_{B0s}}{c_{Bs}}(1 + \tilde{c}_{B0}) - (1 + \tilde{c}_B) - k_B \tau (1 + \tilde{c}_B) X_s\big(1 + \tilde{X}\big) \tag{5.14}$$

$$X_s \frac{d\tilde{X}}{d\theta} = -k_B \tau \alpha_B (1 + \tilde{c}_B) X_s\big(1 + \tilde{X}\big) + k_A \tau \alpha_A (1 + \tilde{c}_A)\left(1 - X_s\big(1 + \tilde{X}\big)\right) \tag{5.15}$$

where the substitutions $\alpha_A = V c_{As}/n_O$ and $\alpha_B = V c_{Bs}/n_O$ have been used for convenience, α being a dimensionless group interpreted as the ratio of the gas molar capacity to the solid molar capacity. Equations 5.13-5.15 can be used to solve for the initial steady state conditions by setting all deviation variables and their derivatives to zero, yielding:

$$0 = \frac{c_{A0s}}{c_{As}} - 1 - k_A \tau (1 - X_s) \tag{5.16}$$

$$0 = \frac{c_{B0s}}{c_{Bs}} - 1 - k_B \tau X_s \tag{5.17}$$

$$0 = -k_B \tau \alpha_B X_s + k_A \tau \alpha_A (1 - X_s) \tag{5.18}$$

Given the initial steady state feed conditions c_{A0s} and c_{B0s}, the steady state output variables c_{As}, c_{Bs} and X_s can be solved simultaneously using equations 5.16-5.18. The expressions for these steady state variables are cumbersome and are not shown here.

The differential equations 5.13-5.15 may be further simplified by subtracting from them the steady state equations 5.16-5.18, resulting in:

$$\frac{d\tilde{c}_A}{d\theta} = \frac{c_{A0s}}{c_{As}}\tilde{c}_{A0} - \tilde{c}_A\left(1 + k_A\tau(1 - X_s)\right) + k_A\tau X_s\tilde{X} + k_A\tau X_s\tilde{c}_A\tilde{X} \tag{5.19}$$

$$\frac{d\tilde{c}_B}{d\theta} = \frac{c_{B0s}}{c_{Bs}}\tilde{c}_{B0} - \tilde{c}_B(1 + k_B\tau X_s) - k_B\tau X_s\tilde{X} - k_B\tau X_s\tilde{c}_B\tilde{X} \tag{5.20}$$

$$\begin{aligned} X_s\frac{d\tilde{X}}{d\theta} = {} & -k_B\tau\alpha_B X_s\tilde{c}_B + k_A\tau\alpha_A(1 - X_s)\tilde{c}_A + (k_A\tau\alpha_A + k_B\tau\alpha_B)X_s\tilde{X} \\ & + k_B\tau\alpha_B X_s\tilde{c}_B\tilde{X} + k_A\tau\alpha_A X_s\tilde{c}_A\tilde{X} \end{aligned} \tag{5.21}$$

Typically, at this point, equations 5.19-5.21 are linearised by assuming that deviations are small, allowing the higher order terms such as $\tilde{c}_A\tilde{X}$ and $\tilde{c}_B\tilde{X}$ to be neglected and resulting in a set of coupled linear differential equations. Instead, the following procedure is undertaken. Firstly, the following oscillatory inputs were used:

$$\tilde{c}_{A0} = \frac{a}{2}\left(e^{i\omega\theta} + e^{-i\omega\theta}\right) \tag{5.22}$$

$$\tilde{c}_{B0} = \frac{b}{2}\left(e^{iu\theta} + e^{-iu\theta}\right) \tag{5.23}$$

where a and b are the amplitudes of oscillation, and ω and u are the dimensionless angular frequencies. Setting $a = -b$, these functions correspond simply to two sinusoidal oscillations that are 180° out of phase. The time-averaged input is the same as the steady state input. It should be noted that, in general, any oscillatory function with an arbitrary number of harmonic frequencies may be used, and any arbitrary phase shift between the two inputs can also be used.

The coupled nonlinear ordinary differential equations 5.19-5.21, together with the initial conditions $\tilde{c}_A(\theta = 0) = 0, \tilde{c}_B(\theta = 0) = 0, \tilde{X}(\theta = 0) = 0$ and oscillatory inputs described by equations 5.22 and 5.23, specify the time-dependent behaviour of the reactor $\tilde{c}_A(\theta)$, $\tilde{c}_B(\theta)$, and $\tilde{X}(\theta)$. The following sections now describe the two methods used to solve these equations. The first method uses GFRFs, whereas the second method uses a conventional numerical method.

5.2.2 Approximate solution with generalised frequency response functions (GFRFs)

The mathematics underpinning generalised frequency responses have been described by Weiner and Spina (1980). In brief, consider an oscillatory input, composed of any number of harmonics, expressed as:

$$x(t) = \sum_{k=1}^{N} a_k e^{i\omega_k t} \tag{5.24}$$

where a_k is the amplitude and $|\omega_k|$ is the frequency of the k^{th} term. It has been shown that the response of a weakly nonlinear system (*viz.* a system that can be expressed in polynomial form) may be expressed as a Volterra series (Volterra, 1959):

$$y(t) = \sum_{n=1}^{\infty} y_n(t) \tag{5.25}$$

$$y_n(t) = \sum_{k_1=1}^{N} \sum_{k_2=1}^{N} \dots \sum_{k_n=1}^{N} a_{k_1} a_{k_2} \dots a_{k_n} G_n\left(\omega_{k_1}, \omega_{k_2}, \dots, \omega_{k_n}\right) e^{i(\omega_{k_1}+\omega_{k_2}+\dots+\omega_{k_n})t} \tag{5.26}$$

where $G_n\left(\omega_{k_1}, \omega_{k_2}, \dots, \omega_{k_n}\right)$ is the n^{th} order GFRF (and G_1 is equivalent to the transfer functions obtained in the linear Frequency Response Theorem). In practical applications of this method, the infinite series in equation 5.25 may be truncated to some finite order to some arbitrary level of accuracy. This is expressed as:

$$y(t) \approx \sum_{n=1}^{M} y_n(t) \tag{5.27}$$

where M is some finite order.

The objective is to find expressions for $G_n\left(\omega_{k_1}, \omega_{k_2}, \dots, \omega_{k_n}\right)$ in terms of physical parameters, which then allows the output $y(t)$ to be reconstructed in terms of these physical parameters. This is accomplished by substituting the expressions for $x(t)$ and $y(t)$ using equations 5.24 and 5.27. Harmonic probing is then applied to the resulting equations. This is done by equating the coefficients of terms that have the same frequencies and amplitudes and is possible only for polynomial equations, hence the aforementioned limitation to weakly nonlinear systems. The result is a system of algebraic equations relating G_n to the physical parameters. This system of algebraic

equations may then be solved in order from first to higher order G_n. With the resulting G_n, the output $y(t)$ may then be reconstructed.

For systems with two inputs, say input $x(t)$ as defined in equation 5.24 and input $z(t)$ defined by:

$$z(t) = \sum_{k=1}^{N} b_k e^{iu_k t} \tag{5.28}$$

then the output needs to include mixed-order terms that describe the combined effect of both inputs (additional inputs will also require the interaction between the mixed-order terms), so that equation 5.27 is modified to:

$$y(t) \approx \sum_{n=1}^{M} y_{x,n}(t) + \sum_{n=2}^{M} y_{xz,n}(t) + \sum_{n=1}^{M} y_{z,n}(t) \tag{5.29}$$

where $y_{x,n}(t)$, $y_{z,n}(t)$ and the mixed-order output $y_{xz,n}(t)$ are defined by:

$$y_{x,n}(t) = \sum_{k_1=1}^{N} \sum_{k_2=1}^{N} \dots \sum_{k_n=1}^{N} a_{k_1} a_{k_2} \dots a_{k_n} G_{x,n}\left(\omega_{k_1}, \omega_{k_2}, \dots, \omega_{k_n}\right) e^{i(\omega_{k_1}+\omega_{k_2}+\dots+\omega_{k_n})t} \tag{5.30}$$

$$y_{z,n}(t) = \sum_{k_1=1}^{N} \sum_{k_2=1}^{N} \dots \sum_{k_n=1}^{N} b_{k_1} b_{k_2} \dots b_{k_n} G_{z,n}\left(u_{k_1}, u_{k_2}, \dots, u_{k_n}\right) e^{i(u_{k_1}+u_{k_2}+\dots+u_{k_n})t} \tag{5.31}$$

$$y_{xz,n}(t) = \sum_{m=1}^{n-1} \sum_{k_1=1}^{N} \dots \sum_{k_m=1}^{N} \dots \sum_{k_n=1}^{N} a_{k_1} \dots a_{k_m} b_{k_{m+1}} \dots b_{k_n} G_{xz,n}\left(\omega_{k_1}, \dots, \omega_{k_m}, \dots, u_{k_n}\right) e^{i(\omega_{k_1}+\dots+u_{k_m}+\dots+u_{k_n})t} \tag{5.32}$$

To apply this method to the current situation of the gas-solid reactor, which is a multiple-input and multiple-output (MIMO) system, the following expressions for the outputs were used, being equations 5.29-5.35 relabelled appropriately for $\tilde{c}_A$, $\tilde{c}_B$ and $\tilde{X}$, and with appropriate dimensions for ω and u:

$$
\begin{aligned}
&\tilde{c}_A(\theta) \\
&= \sum_{n=1}^{M}\Bigg[\sum_{k_1=1}^{N}\sum_{k_2=1}^{N}\dots\sum_{k_n=1}^{N} a_{k_1}a_{k_2}\dots a_{k_n}F_{x,n}\left(\omega_{k_1},\omega_{k_2},\dots,\omega_{k_n}\right)e^{i(\omega_{k_1}+\omega_{k_2}+\dots+\omega_{k_n})\theta} \\
&+ \sum_{m=1}^{n-1}\sum_{k_1=1}^{N}\dots\sum_{k_m=1}^{N}\dots\sum_{k_n=1}^{N} a_{k_1}\dots a_{k_m}b_{k_{m+1}}\dots b_{k_n}F_{xz,n}\left(\omega_{k_1},\dots,\omega_{k_m},\dots,u_{k_n}\right)e^{i(\omega_{k_1}+\dots+u_{k_m}+\dots+u_{k_n})\theta} \\
&+ \sum_{k_1=1}^{N}\sum_{k_2=1}^{N}\dots\sum_{k_n=1}^{N} b_{k_1}b_{k_2}\dots b_{k_n}F_{z,n}\left(u_{k_1},u_{k_2},\dots,u_{k_n}\right)e^{i(u_{k_1}+u_{k_2}+\dots+u_{k_n})\theta}\Bigg]
\end{aligned}
\tag{5.33}
$$

$$
\begin{aligned}
&\tilde{c}_B(\theta) \\
&= \sum_{n=1}^{M}\Bigg[\sum_{k_1=1}^{N}\sum_{k_2=1}^{N}\dots\sum_{k_n=1}^{N} a_{k_1}a_{k_2}\dots a_{k_n}G_{x,n}\left(\omega_{k_1},\omega_{k_2},\dots,\omega_{k_n}\right)e^{i(\omega_{k_1}+\omega_{k_2}+\dots+\omega_{k_n})\theta} \\
&+ \sum_{m=1}^{n-1}\sum_{k_1=1}^{N}\dots\sum_{k_m=1}^{N}\dots\sum_{k_n=1}^{N} a_{k_1}\dots a_{k_m}b_{k_{m+1}}\dots b_{k_n}G_{xz,n}\left(\omega_{k_1},\dots,\omega_{k_m},\dots,u_{k_n}\right)e^{i(\omega_{k_1}+\dots+u_{k_m}+\dots+u_{k_n})\theta} \\
&+ \sum_{k_1=1}^{N}\sum_{k_2=1}^{N}\dots\sum_{k_n=1}^{N} b_{k_1}b_{k_2}\dots b_{k_n}G_{z,n}\left(u_{k_1},u_{k_2},\dots,u_{k_n}\right)e^{i(u_{k_1}+u_{k_2}+\dots+u_{k_n})\theta}\Bigg]
\end{aligned}
\tag{5.34}
$$

$$
\begin{aligned}
&\tilde{X}(\theta) \\
&= \sum_{n=1}^{M}\Bigg[\sum_{k_1=1}^{N}\sum_{k_2=1}^{N}\dots\sum_{k_n=1}^{N} a_{k_1}a_{k_2}\dots a_{k_n}H_{x,n}\left(\omega_{k_1},\omega_{k_2},\dots,\omega_{k_n}\right)e^{i(\omega_{k_1}+\omega_{k_2}+\dots+\omega_{k_n})\theta} \\
&+ \sum_{m=1}^{n-1}\sum_{k_1=1}^{N}\dots\sum_{k_m=1}^{N}\dots\sum_{k_n=1}^{N} a_{k_1}\dots a_{k_m}b_{k_{m+1}}\dots b_{k_n}H_{xz,n}\left(\omega_{k_1},\dots,\omega_{k_m},\dots,u_{k_n}\right)e^{i(\omega_{k_1}+\dots+u_{k_m}+\dots+u_{k_n})\theta} \\
&+ \sum_{k_1=1}^{N}\sum_{k_2=1}^{N}\dots\sum_{k_n=1}^{N} b_{k_1}b_{k_2}\dots b_{k_n}H_{z,n}\left(u_{k_1},u_{k_2},\dots,u_{k_n}\right)e^{i(u_{k_1}+u_{k_2}+\dots+u_{k_n})\theta}\Bigg]
\end{aligned}
\tag{5.35}
$$

where F, G and H are the GFRFs for $\tilde{c}_A$, $\tilde{c}_B$ and $\tilde{X}$, respectively. These expressions were substituted into the differential equations 5.19-5.21 and harmonic probing was applied to solve for the GFRFs. In this study, GFRFs up to and including third order were used (*i.e.* $M = 3$).

For the current reactor model and its associated inputs, it is not always possible to distinguish GFRFs associated with the same frequency and amplitude (*e.g.* $G_{xz,3}(\omega,-\omega,u)$ is associated with the same frequency and amplitude as $G_{xz,3}(-\omega,\omega,u)$ of a^2be^{iut}, causing them to appear in the same equations during harmonic probing). Such GFRFs were assumed to be equal to each other, which is effectively averaging their contributions.

The expressions for the GFRFs were then substituted back into equations 5.33-5.35 to reconstruct the outputs as a function of time. The terms with the same frequencies were

collected to express the output as a sum of the DC component and the first and higher harmonics. This was expressed as (using $\tilde{X}$ as an example):

$$\tilde{X}(\theta) = \tilde{X}_{\mathrm{DC}} + \tilde{X}_{\mathrm{I}}(\omega\theta) + \tilde{X}_{\mathrm{II}}(2\omega\theta) + \tilde{X}_{\mathrm{III}}(3\omega\theta) + \cdots \tag{5.36}$$

For the DC component, the constant terms (*i.e.* the coefficients of e^0) were collected, recognising that when $\omega = u$ the asymmetric mixed terms become constants:

$$\begin{aligned}\tilde{X}_{\mathrm{DC}} &= \left(\frac{a}{2}\right)^2 H_{x,2}(\omega,-\omega) + \left(\frac{a}{2}\right)^2 H_{x,2}(-\omega,\omega) + \frac{a}{2}\frac{b}{2}H_{xz,2}(\omega,-u) \\ &\quad + \frac{a}{2}\frac{b}{2}H_{xz,2}(-\omega,u) + \left(\frac{b}{2}\right)^2 H_{z,2}(u,-u) + \left(\frac{b}{2}\right)^2 H_{z,2}(-u,u) \\ &= 2\left(\frac{a}{2}\right)^2 H_{x,2}(\omega,-\omega) + \frac{a}{2}\frac{b}{2}\left(H_{xz,2}(\omega,-u) + \mathrm{Conjugate}\left[H_{xz,2}(\omega,-u)\right]\right) \\ &\quad + 2\left(\frac{b}{2}\right)^2 H_{z,2}(u,-u)\end{aligned} \tag{5.37}$$

Here, $\mathrm{Conjugate}[x]$ denotes the complex conjugate of x, noting that GFRFs with negative arguments are complex conjugates of each other (Li and Billings, 2006), *e.g.* $H_{xz,2}(-\omega,u)$ is the complex conjugate of $H_{xz,2}(\omega,-u)$. For pairs of asymmetric unmixed second order GFRFs, *e.g.* $H_{x,2}(\omega,-\omega)$ and $H_{x,2}(-\omega,\omega)$, these must also be equal because they are unmixed and differ only by the permutation of its arguments (Li and Billings, 2006).

To express the first and higher harmonics, it is convenient to define a new function $\Upsilon_n(n\omega)$, where n is the order of the respective harmonic. $\Upsilon_n(n\omega)$ is the Fourier transform of the n^{th} harmonic in the reconstructed output (Petkovska and Morgenstern, 2013). In the current system Υ_1, Υ_2 and Υ_3 were found to be:

$$\begin{aligned}\Upsilon_1(\omega) &= 2\left(\frac{a}{2}\right)H_{x,1}(\omega) + 2\left(\frac{b}{2}\right)H_{z,1}(u) + 6\left(\frac{a}{2}\right)^3 H_{x,3}(\omega,\omega,-\omega) \\ &\quad + 6\left(\frac{b}{2}\right)^3 H_{z,3}(u,u,-u) + 4\left(\frac{a}{2}\right)\left(\frac{b}{2}\right)^2 H_{xz,3}(\omega,u,-u) \\ &\quad + 4\left(\frac{a}{2}\right)^2\left(\frac{b}{2}\right)H_{xz,3}(\omega,-\omega,u) + 2\left(\frac{a}{2}\right)^2\left(\frac{b}{2}\right)H_{xz,3}(\omega,\omega,-u) \\ &\quad + 2\left(\frac{a}{2}\right)\left(\frac{b}{2}\right)^2 H_{xz,3}(-\omega,u,u)\end{aligned} \tag{5.38}$$

$$\Upsilon_2(2\omega) = 2\left(\frac{a}{2}\right)^2 H_{x,2}(\omega,\omega) + 2\left(\frac{b}{2}\right)^2 H_{z,2}(u,u) + 2\left(\frac{a}{2}\right)\left(\frac{b}{2}\right)H_{xz,2}(\omega,u) \tag{5.39}$$

$$Y_3(3\omega) = 2\left(\frac{a}{2}\right)^3 H_{x,3}(\omega,\omega,\omega) + 2\left(\frac{b}{2}\right)^3 H_{z,3}(u,u,u) + 2\left(\frac{a}{2}\right)^2\left(\frac{b}{2}\right) H_{xz,3}(\omega,\omega,u) + 2\left(\frac{a}{2}\right)\left(\frac{b}{2}\right)^2 H_{xz,3}(\omega,u,u) \tag{5.40}$$

This allows $\tilde{X}_{\mathrm{I}}(\omega\theta)$, $\tilde{X}_{\mathrm{II}}(2\omega\theta)$ and $\tilde{X}_{\mathrm{III}}(3\omega\theta)$ to be compactly expressed as:

$$\tilde{X}_{\mathrm{I}}(\omega\theta) = |Y_1|\cos(\omega\theta + \arg(Y_1)) \tag{5.41}$$

$$\tilde{X}_{\mathrm{II}}(2\omega\theta) = |Y_2|\cos(2\omega\theta + \arg(Y_2)) \tag{5.42}$$

$$\tilde{X}_{\mathrm{III}}(3\omega\theta) = |Y_3|\cos(3\omega\theta + \arg(Y_3)) \tag{5.43}$$

5.2.3 Exact solution with numerical method

A numerical method of solution to equations 5.19-5.21 was used as a basis for comparison with the GFRF approach. The NDSolve function in Mathematica was used, which calls the LSODA solver (Wolfram Research Inc., 2017). The solution obtained with this method was taken to be 'exact' and provided a means for gauging the errors arising from *e.g.* truncation of the Volterra series in section 5.2.2. The numerical method also provided a means for inspecting the stability of the system.

The numerical values for the parameters are summarised in Table 5.1. Despite the implied symmetry between *A* and *B* in using these values, the method is not limited to cases where these reactions are symmetric.

Table 5.1. Values for the parameters and derived parameters in the gas-solid reactor.

Parameter			Value
$\tau = V/Q$	Mean residence time of gas in the reactor	s	1
k_A	First order rate constant for the reaction of *A*	s^{-1}	1
k_B	First order rate constant for the reaction of *B*	s^{-1}	1
c_{A0s}	Initial steady state concentration of *A* in the feed	kmol m^{-3}	1
c_{B0s}	Initial steady state concentration of *B* in the feed	kmol m^{-3}	1
c_{As}	Initial steady state concentration of *A* in the reactor	kmol m^{-3}	2/3
c_{Bs}	Initial steady state concentration of *B* in the reactor	kmol m^{-3}	2/3
X_s	Initial steady state conversion of solid	-	1/2
$\alpha_A = Vc_{As}/n_O$	Molar ratio of *A* to the solid capacity	-	10
$\alpha_B = Vc_{Bs}/n_O$	Molar ratio of *B* to the solid capacity	-	10

5.3 Results

5.3.1 Generalised frequency response functions

Figures 5.2, 5.3 and 5.4 show how the frequency response functions (FRFs) vary with the dimensionless frequency of the oscillations in the feed concentrations of *A* and *B*. In Figure 5.2 it can be seen that, by comparing the magnitude of F_x to F_z, $\tilde{c}_A$ is more sensitive to oscillations in *A* than *B*, as expected. It can also be seen that higher order FRFs are smaller in magnitude, which suggests that the errors can be tolerable when truncating the Volterra series, depending on the amplitudes of the oscillations. The magnitudes also decay as the frequency of oscillations increase, which is expected because the volume of the reactor acts to damp out frequencies much faster than its time constant (*i.e.* its residence time).

The symmetry between *A* and *B* (arising from the numerical parameters in Table 5.1) is evident when comparing Figure 5.2 and Figure 5.3. It can be seen that F_x is equivalent to G_z (*i.e.* the response of $\tilde{c}_A$ to $\tilde{c}_{A0}$ is equivalent to the response of $\tilde{c}_B$ to $\tilde{c}_{B0}$), and F_z is equivalent to G_x. F_{xz} is also equivalent to G_{xz} (with the equivalent combination of orders in the inputs, *i.e.* $F_{xz,3}(\omega,\omega,u)$ is equivalent to $G_{xz,3}(\omega,u,u)$).

The response of $\tilde{X}$ to *A* or *B* are also symmetric, as shown in Figure 5.4, but with the opposite signs. H_x is equivalent to $-H_z$. The third order mixed FRFs are also symmetric.

The symmetric second order mixed FRF, $H_{xz,2}(\omega, u)$, was found to be zero for all frequencies.

The second order asymmetric GFRFs are shown in Figure 5.5, which are the components that contribute to the DC offset in the output. These show that oscillations caused the time-averaged concentrations $\tilde{c}_A$ and $\tilde{c}_B$ to deviate from their steady state values. In this specific situation, the deviation is positive, which means that the mean rate of reaction has decreased due to this periodic operation. The mixed responses have double the magnitude of the unmixed response and are negative, which means that if *A* and *B* oscillate in phase, there would be no DC offset. However, if *A* and *B* oscillate with a phase difference of 180°, then this would increase the DC offset. For the response of $\tilde{X}$, the GFRF in response to oscillation *A* and *B* have opposite signs, as expected. The asymmetric second order mixed FRF, $H_{xz,2}(\omega, -u)$ is shown to be purely imaginary. $H_{xz,2}(-\omega, u)$ was also found to be purely imaginary with a phase difference of 180° (as expected, since they are complex conjugates), which means they give no contribution to the DC offset of $\tilde{X}$. This is expected because the DC offset of $\tilde{X}$ caused by simultaneous oscillations (at the same frequency) of *A* and *B* must be zero if they are kinetically symmetric, *i.e.* when both *A* and *B* oscillate, the time-averaged value of $\tilde{X}$ should not deviate from its steady state value of 0.5, if *A* and *B* are symmetric.

Lastly, it can be seen that the GFRFs have a low frequency limit tending to some constant value. They also have a high frequency limit tending to zero modulus, when the time period of oscillations become much greater than the time constant of the reactor (its residence time, in this case).

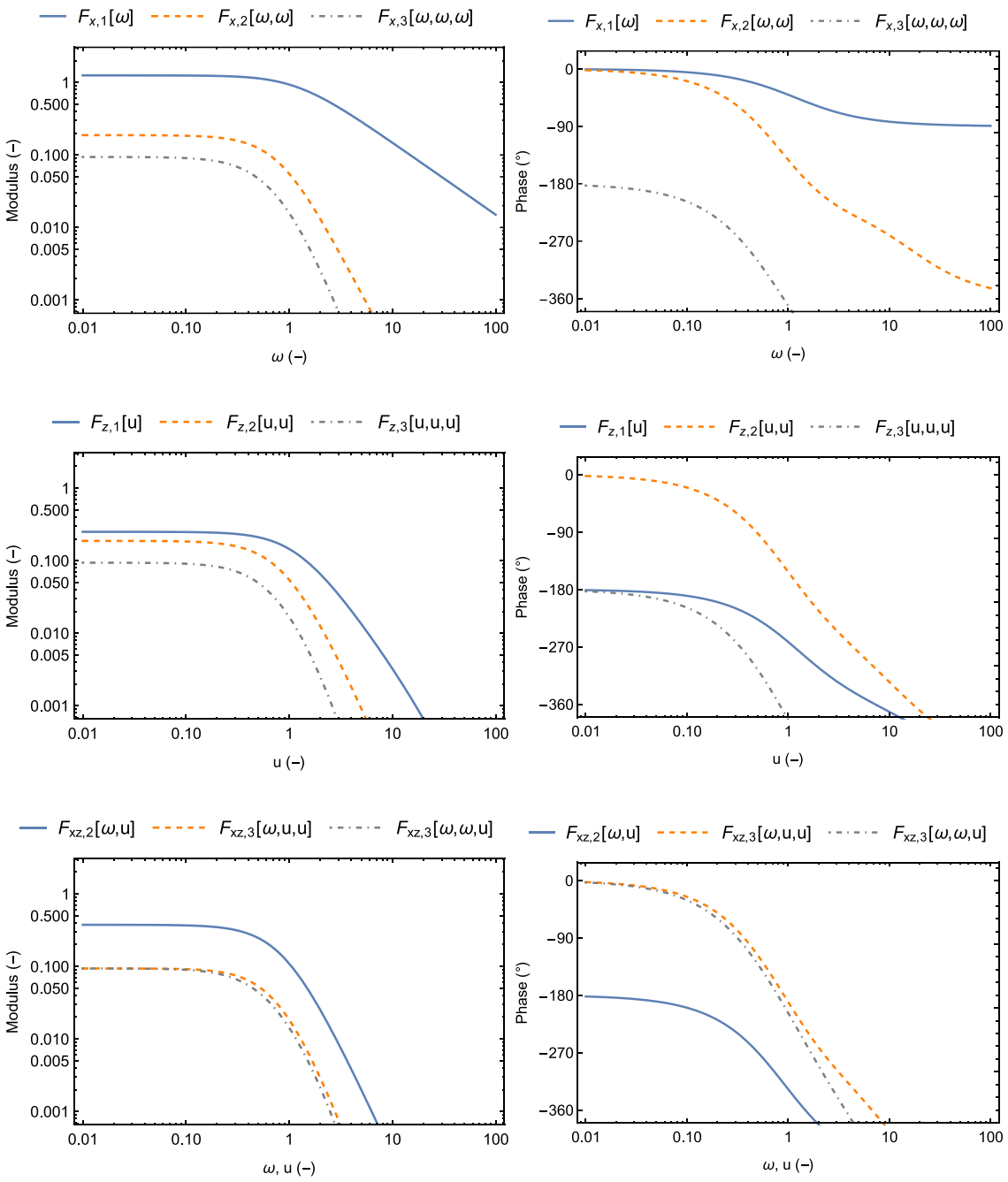

Figure 5.2. Bode plots of the generalised frequency response functions relating $\tilde{c}_A$ to the inputs.

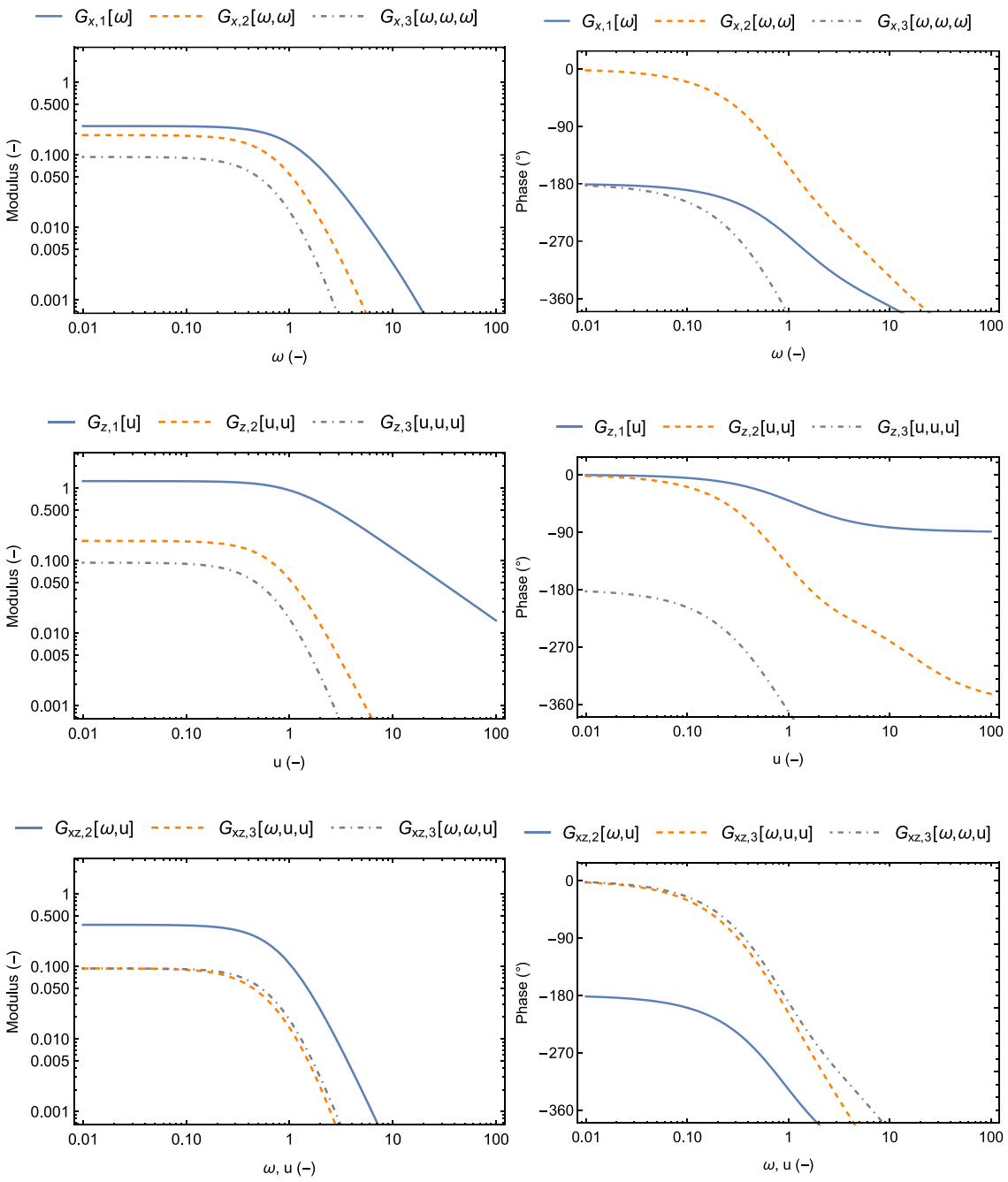

Figure 5.3. Bode plots of the generalised frequency response functions relating $\tilde{c}_B$ to the inputs.

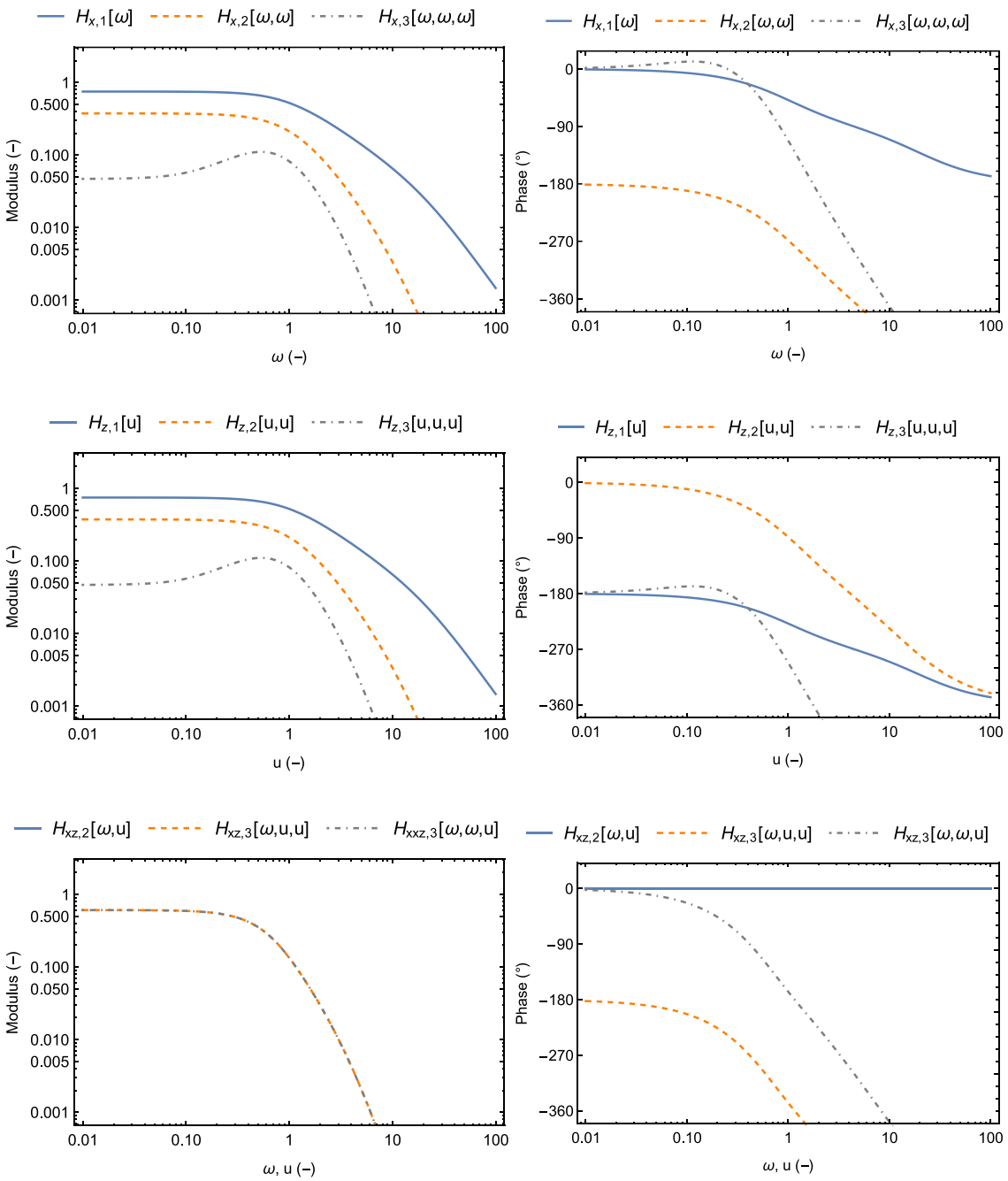

Figure 5.4. Bode plots of the generalised frequency response functions relating $\tilde{X}$ to the inputs.

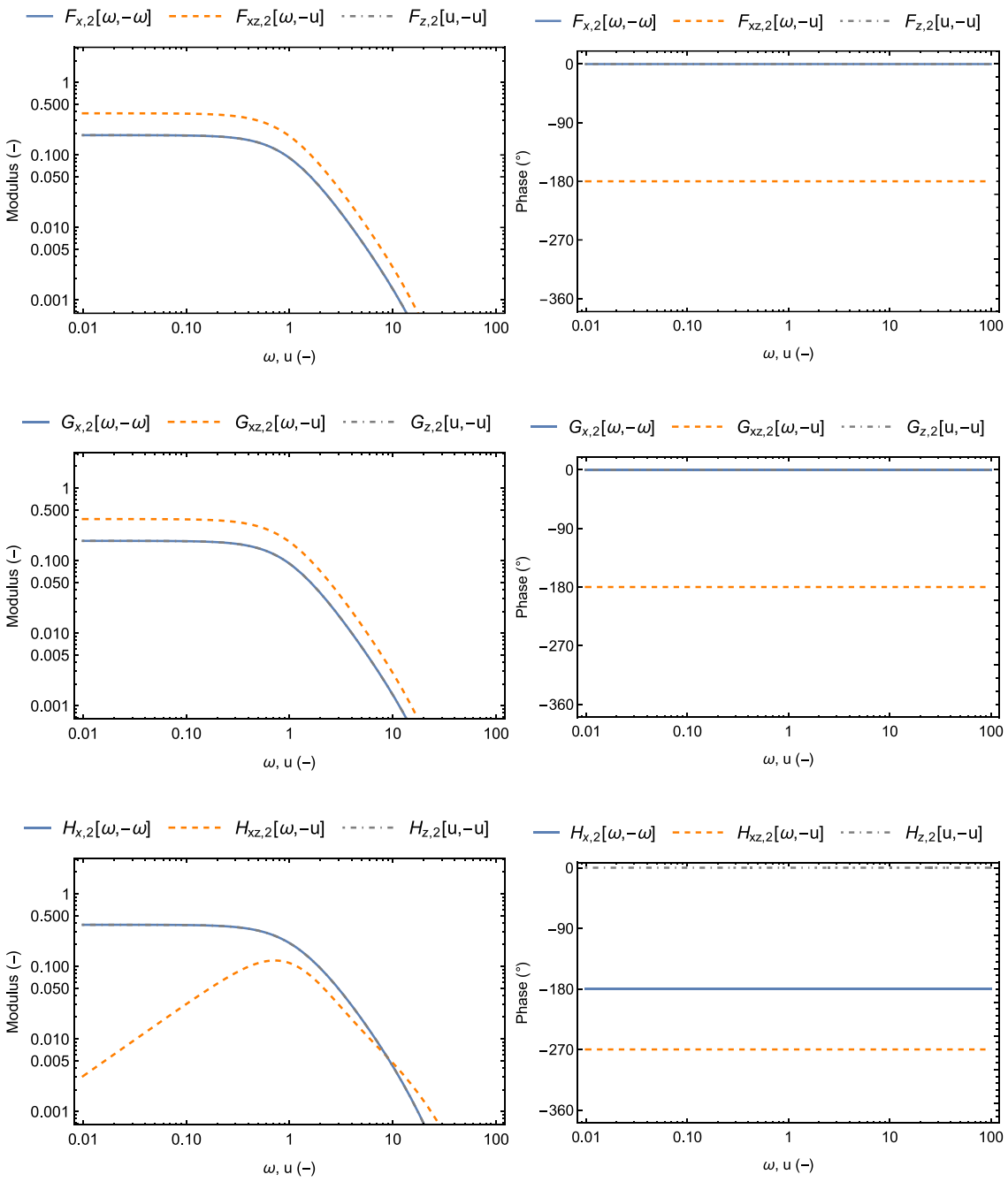

Figure 5.5. Bode plots of the second order asymmetric GFRFs which are directly proportional to the DC component of the response. The moduli and arguments of the unmixed GFRFs overlap exactly, except for $H_{x,2}(\omega,-\omega)$ and $H_{z,2}(u,-u)$ which have opposite signs.

5.3.2 Comparison with numerical solution

The GFRFs obtained in section 5.3.1 were used to reconstruct the output responses (expressed in equations 5.36-5.43 for $\tilde{X}(\theta)$). These were then compared to the exact solutions obtained using the numerical method. Figure 5.6 shows the effect of including

higher order GFRFs. The simplest construction, using only the first order GFRFs, correspond to only one harmonic. This response is equivalent to that predicted if the linear frequency response theorem had been used. It does not predict a DC offset, whereas the numerical solution does. Furthermore, $\tilde{X}$ exceeds -1 and 1, which is not physical because X must be between 0 and 1, so $\tilde{X}$ must be greater than -1, and, when $X_s = 0.5$, $\tilde{X}$ must be less than 1. When second order GFRFs are included, the DC offsets in $\tilde{c}_A$ and $\tilde{c}_B$ are largely accounted for, but the effect on $\tilde{X}$ is small. Finally, when third order GFRFs are included, the errors in $\tilde{X}$ are largely eliminated. The effect on $\tilde{c}_A$ and $\tilde{c}_B$ are small. Higher order GFRFs are necessary to account for the remaining deviations from the numerical model.

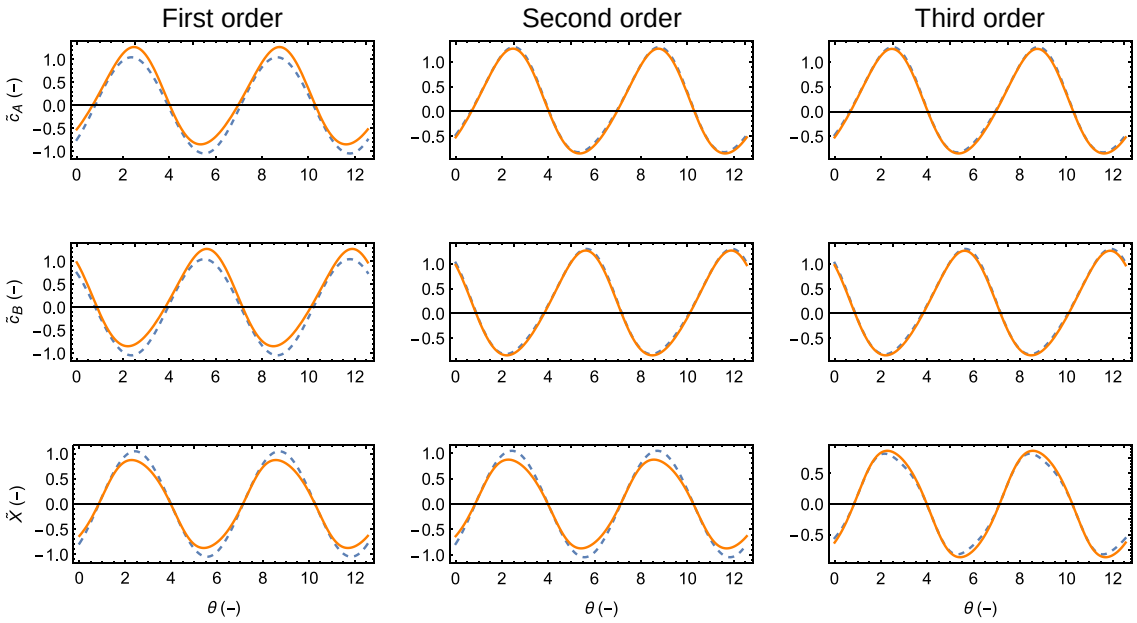

Figure 5.6. Comparison of output responses when calculated with GFRFs (--) and an exact numerical method (–). Dimensionless amplitude $a = -b = 1.0$, dimensionless frequency $\omega = 0.01$.

The effect of varying the input frequency is shown in Figure 5.7. It can be seen that even with a maximum amplitude of 1, GFRFs are accurate for frequencies higher than $\omega = 1$. This might be expected because the time constant of the reactor effectively damps out oscillations with smaller time periods. As a result, nonlinear effects will be smaller and so can be more easily described with low order GFRFs. At $\omega = 100$, the output closely resembles simple sinusoids of a single harmonic with no DC component. For low frequencies $\omega = 0.01$, the errors are large. This might be expected because the degree of nonlinearity is larger with high amplitudes at low frequencies, because this kind of operation allows for large changes in $\tilde{X}$. When $\tilde{X}$ approaches -1 or 1, then (for $X_s = 0.5$)

X approaches 0 or 1, so that the rate of reaction tends to zero. This means the response of $\tilde{X}$ will tend towards a square-wave function, which will require many more harmonics to describe accurately. Therefore, higher order GFRFs will be required with low frequency and large amplitudes. Figure 5.8 shows how the errors vary with the amplitude, for a low dimensionless frequency of $\omega = 0.01$. It can be seen that for small amplitudes of $a = -b = [0.25, 0.50]$, the two methods agree well. As the amplitude increases to 0.75 and 1.0, the error in the GFRF method grows, especially in the response of $\tilde{X}$.

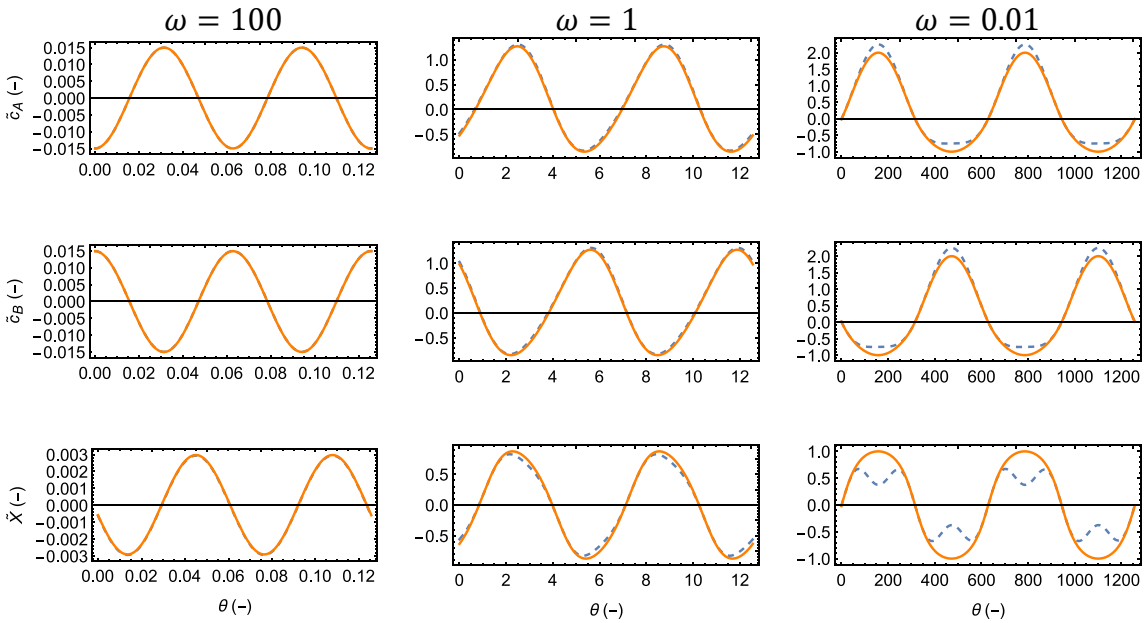

Figure 5.7. Comparison of output responses with varying frequency when calculated with GFRFs (--) and an exact numerical method (–). Dimensionless amplitude $a = -b = 1.0$.

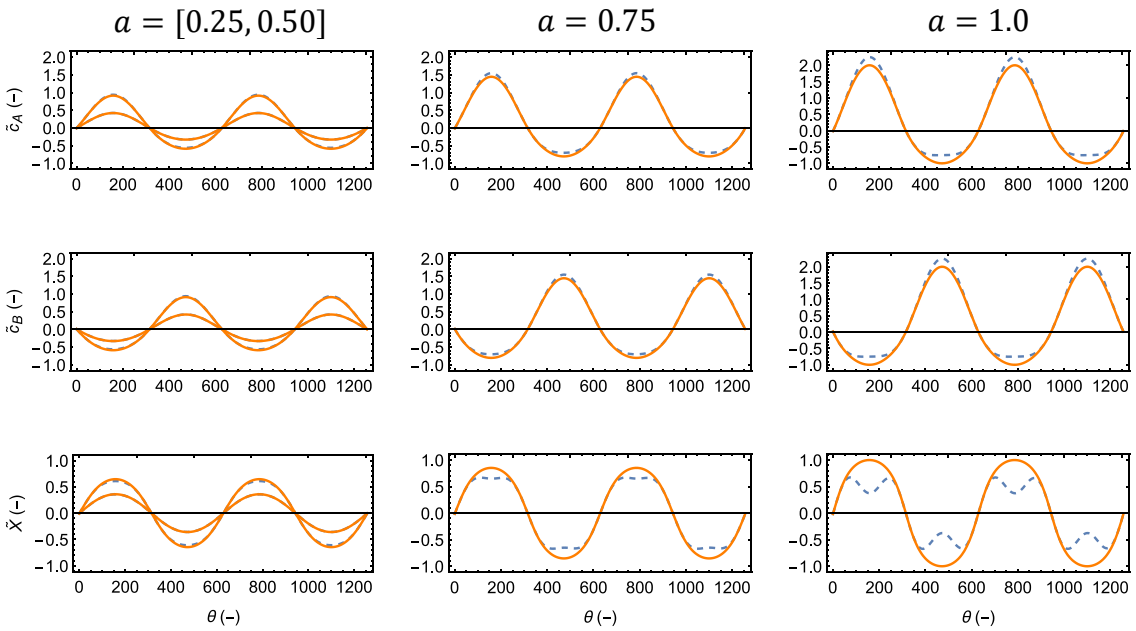

Figure 5.8. Comparison of output responses with varying amplitude when calculated with GFRFs (--) and an exact numerical method (–). Dimensionless frequency $\omega = 0.01$.

5.4 Discussion

From Figure 5.6, it is evident that the use of GFRFs provides a substantial improvement in accuracy over the linear frequency response theorem. Nevertheless, errors are still substantial within regimes that are characterised by low frequencies, shown in Figure 5.7, and large amplitudes, shown in Figure 5.8. In these regimes, the oscillations in X become large, tending towards limiting values of 0 and 1 where nonlinear behaviour becomes more significant, thus requiring higher order harmonics to be included. Whilst it is possible to include higher orders, the computation becomes more expensive and so the use of GFRFs loses its advantage of speed over the numerical method. Additionally, the expressions for the GFRFs are cumbersome and so it is difficult to extract analytical trends by inspection (*i.e.* physical interpretation). Numerical methods suffer from the same problem. However, the use of GFRFs does allow the Bode plots to be obtained quicker than with the numerical method.

Some practical applications might be highly nonlinear. For example, in chemical looping reactors, depending on the operating conditions, the conversion of solid could swing from a deeply reduced stated to a highly oxidised state (*i.e.* X operates close to 0 and 1). In such cases the use of GFRFs might be inappropriate. More complicated reaction mechanisms, involving intermediate species, might also need additional sets of GFRFs (essentially increasing the number of outputs in the MIMO system), which adds computational expense.

One possible area of useful application is for the measurement of chemical kinetics in gas-solid reactions. A perennial problem in experiments is the need for fast response in the measurement system. For example, during spectrophotometric analysis of gaseous species evolved in a reaction, a large path length for absorption is required to improve the signal-to-noise ratio. This might necessitate a large volume of the gas cell, which promotes back-mixing and therefore obscures the chemical kinetics. A higher gas flow might be used but this requires a larger reactor and therefore more solid sample. By operating the experiment in a periodic fashion, this eliminates the time constant of the measurement system. Instead, a steady state measurement of the DC response is sufficient to extract kinetic information, which is convenient because the DC response would be unaffected by the time constant of the measurement system. Only the oscillatory input to the reactor needs to be characterised accurately. In this situation, the use of GFRFs allows for the evaluation for kinetic models to be compared to experimental data.

5.5 Conclusions

This chapter has demonstrated the viability of using generalised frequency response functions (GFRFs), which extends the traditional linear frequency response theorem to nonlinear systems, to analyse periodic non-catalytic gas-solid reactions. Chemical looping reactors are an example of such a system. A simple model of a generic gas-solid reactor was constructed and solved using GFRFs, as well as a numerical method serving as a basis for comparison. Depending on the operating parameters, the degree of error varied. The error generally increased with the degree of nonlinearity in the reactor, generally caused by a combination of low frequencies and large amplitudes. This operating policy allowed the solid phase to approach full conversion, which resulted in much lower rates of reaction and hence led to significant nonlinearities. Because real reactors might operate in such a fashion, these errors might preclude GFRFs from being applied to such contexts (although these errors can be reduced by including higher order GFRFs, subject to computational power). An alternative application to the measurement of kinetics was proposed, which alleviates the problem of measurement techniques with slow response times.

6 CONCLUSIONS

This Dissertation investigated the feasibility of chemical looping selective oxidations. Prior work on chemical looping has been predominantly limited to high temperatures, > 700°C, where a substantial library of materials, able to act as oxygen carriers, has already been researched. The challenge in this investigation was to develop an oxygen carrier able to react at much lower temperatures, where selectivity can be achieved. The resulting oxygen carrier must also be able to present active sites that can perform the selective oxidation, because activity at lower temperatures by itself is not sufficient to achieve selectivity.

Chapter 2 began with the hypothesis that chemical looping reactions could be made more efficient by adjusting a thermodynamic property of the oxygen carrier, namely its equilibrium partial pressure of oxygen, pO_2. This was demonstrated with the identification and synthesis of $Ca_2Fe_2O_5$, which has a lower pO_2 than Fe_2O_3. When used in the chemical looping production of hydrogen, $Ca_2Fe_2O_5$ achieved a significantly higher conversion of steam to hydrogen than Fe_2O_3, as predicted by thermodynamic modelling. It was also observed that $Ca_2Fe_2O_5$ achieved a lower conversion of CO to CO_2, as predicted by the thermodynamics. A reactor configuration was proposed which would combine the high conversion of fuel achieved by Fe_2O_3 with the high conversion of steam achieved by $Ca_2Fe_2O_5$. Whilst this has practical applications for the steam-iron process, the key idea of this chapter, of designing oxygen carriers using pO_2 as a key parameter, was brought forward to be applied to selective oxidations.

Chapter 3 was concerned with achieving selectivity for a particular reaction. The set of oxygen carriers that are active at low temperatures might not intersect with the set that is

selective. A solution was proposed, where a selective catalyst might be deposited on the surface of an oxygen carrier, which broadens the applicable set of materials. This was demonstrated with the preparation of a set of oxygen carriers composed of bismuth oxide supported on ceria-zirconia. The target reaction was the selective combustion of hydrogen in the presence of hydrocarbons, which may be applied in an embodiment of the oxidative dehydrogenation of light alkanes. It was found that the kinetics and selectivity of the prepared materials were independent of the properties of the support, whether the support was inert or active. In other words, the surface chemistry of the resulting composite particulate material was decoupled from its bulk properties. This finding was exploited in a subsequent study on the epoxidation of ethylene. Chapter 3 also demonstrated, for the first time, the combination of selective combustion of hydrogen (performed using bismuth oxide supported on ceria-zirconia) with the dehydrogenation of ethane (performed using a proprietary Pt-based catalyst) to produce ethylene, thereby achieving overall oxidative dehydrogenation of ethane. Unfortunately, it was found that the specific reactor configuration employed (a packed bed of a heterogeneous mixture of particles of bismuth oxide on ceria-zirconia and particles of the Pt catalyst) was unstable and deactivated rapidly with cycling. Investigations demonstrated that volatilisation of bismuth was feasible and probably caused the deactivation. Volatilisation of bismuth was not identified in prior studies on bismuth oxide in its application for the selective combustion of hydrogen.

Chapter 4 applied the findings of the previous chapters to an industrially-significant process, the epoxidation of ethylene. A novel oxygen carrier was prepared, composed of silver supported on $SrFeO_3$. Silver was chosen for its unique catalytic properties in the epoxidation of ethylene, and $SrFeO_3$, a perovskite, was chosen for its favourable pO_2 at low temperatures. By using this composite oxygen carrier, this study demonstrated, for the first time, that epoxidation can be performed in a chemical looping reactor. The observations formed a basis for a proposed reaction mechanism, wherein the oxygen from $SrFeO_3$ diffused through its lattice to the surface of the crystallites of silver to be presented as oxygen adatoms. These oxygen adatoms were then able to oxidise selectively the ethylene to the epoxide. Whilst the selectivity of the oxygen carrier was inferior to state-of-the-art catalysts used in the conventional process, the prepared samples were still comparable to unpromoted silver. This suggests that a competitive formulation might be developed with the use of *e.g.* conventional promoters such as alkali metals or organic chlorides. The chemical looping process has inherent advantages over the conventional

process, namely that an air separation plant is no longer required, so further development might be of commercial interest.

Chapter 5 was a theoretical study, initially motivated by the phenomenon of ‘global enhancement’, wherein a modulated input to a nonlinear system can achieve an enhanced performance over the (‘global’) optimal steady state performance. The performance might be measured by the rate of reaction, conversion or selectivity. A frequently encountered problem is predicting how a nonlinear system behaves with varying frequency of its modulated inputs, *i.e.* the nonlinear frequency response, in order to determine when global enhancement is achieved. The governing system of time-dependent nonlinear differential equations could be solved numerically, but this requires the sampling of a large discrete set of frequencies which could span several orders of magnitude. This would be computationally expensive, and resonant phenomena could be missed in the discrete sampling. Nonlinear frequency response theory, which has been recently applied to chemical engineering problems, was investigated for its novel application to non-catalytic gas-solid reactions, of which chemical looping reactions are a subset. The motivation for using this theory was that the frequency response might be obtained more readily as a continuous function of frequency. In this chapter, an idealised, generic model of a reactor was formulated and solved using either nonlinear frequency response theory or a numerical method. It was found that the size of the errors varied with the degree of nonlinearity of the system, which could preclude the application of this theory to real systems such as chemical looping reactors (where the conversion of the solid can approach zero or unity and behave highly nonlinearly). Instead, it was suggested that this theory could be applied in dynamic measurements of reaction kinetics.

In summary, this Dissertation has identified principles in the formulation of selective oxygen carriers. These were applied in a demonstration for the epoxidation of ethylene, resulting in a novel selective oxygen carrier, which might be of commercial interest. Nonlinear frequency response theory was developed for the application to gas-solid reactions, which might be a viable tool in the analysis of dynamic measurements of reaction kinetics.

7 FUTURE WORK

The study on epoxidation posited that oxygen carriers with high pO_2 will be favourable, mainly on the basis that the working catalyst in industrial conditions is exposed to high pO_2 from the gas-phase. This was not actually proven. Therefore, it will be interesting to conduct a study varying only the pO_2 of the oxygen carrier and measure the resulting performance (*e.g.* selectivity) upon depositing with silver. Fine control of pO_2, without introducing too many confounding factors, might be achieved by doping of the oxygen carrier (*e.g.* either on the A- or B-site of $SrFeO_3$, or another base material altogether). The results of this study will inform whether materials with even higher pO_2 are worth pursuing for this application (recalling that the pO_2 of $SrFeO_3$ is much lower than industrial epoxidation conditions, despite being much higher than most currently known materials).

Whilst the conventional process for the epoxidation of ethylene has had the benefit of several decades' worth intense research and development, the chemical looping process conceived in this Dissertation can probably access much of that body of knowledge for itself. This includes the wealth of promoters, their effects and how they may be dosed (but the effects on the surface of the oxygen carrier must also be determined, which are unlikely to have been characterised). Factors such as the size and shape of the silver crystallites have shown to be of critical importance (Christopher and Linic, 2010), as well as how they might be controlled with the appropriate methods of preparation.

Commercial viability of chemical looping epoxidation will also require highly active materials to minimise the capital cost of the reactor. The slow reoxidation of $Ag/SrFeO_3$ was identified in chapter 4, which can present a severe bottleneck to the overall

productivity of a chemical looping cycle. The use of dopants, both on the surface and in the lattice of the oxygen carrier, might be beneficial here. Another solution is the use of elevated pressures, which is already used in the conventional process. Higher pressures of air might accelerate the reoxidation of the material. Furthermore, depending on the chemistry of the oxygen carrier, this could allow pO_2 higher than 0.21 bar (the limiting value of air at sea level) to be effected during the reduction step (*viz.* reaction with ethylene).

Another aspect in the operation of chemical looping epoxidation is the duration of the purge of the reactor. Chapter 4 had used two minutes to purge in between each reduction and oxidation step, which is an exaggerated length chosen to unambiguously establish that no gas-phase oxygen was present during the reduction step. However, during this purge, some oxygen could have desorbed, reducing the oxygen carrier and lower the pO_2 effected during the reduction step. Some preliminary studies, not shown in this Dissertation, does suggest that a shorter purge time can significantly improve the performance of the reaction.

The reactions of ethylene oxide with the oxygen carrier material is important (*i.e.* the secondary chemistry of the epoxidation of ethylene). Whilst this has been researched thoroughly on silver, alumina, and alumina-supported silver, the chemistry of ethylene oxide with an oxygen carrier, *e.g.* $SrFeO_3$, is unknown. The results of such a study will inform whether it is necessary to inhibit the interaction between the gas and the oxygen carrier.

Mechanistic details of the oxygen carrier-supported silver materials are important. What are the pathways of oxygen between the bulk of the oxygen carrier to the surface of silver? Does oxygen diffuse mainly along the surface of the oxide towards the silver crystallites at the triple-phase boundary, or does it diffuse mainly through the oxide-silver interface beneath the surface? This knowledge will inform how best to nanostructure the materials (*e.g.* if surface diffusion turns out to be dominant, then blocking the oxide surface might not be viable). *In situ* techniques such as Raman spectroscopy and “high” pressure XPS have proven to be useful in studying epoxidation, and so are interesting techniques for chemical looping epoxidation. This could also reveal information on the distribution of oxygen species in co-feeding mode compared to chemical looping mode.

Recent developments of highly stable supported metal catalysts might be exploited by developing fluidisable oxygen carriers for epoxidation. Fluidised epoxidation reactors

been examined in the past, including a pilot-scale plant in 1953 (Dever *et al.*, 2000). Although it is unclear why the fluidised bed reactor approach has been abandoned (it might be speculated that the attrition of expensive silver outweighs any benefits), it does offer benefits of improved temperature control and inhibition of side reactions (Dever *et al.*, 2000). Since chemical looping is naturally suited for circulating fluidised beds, it might be worthwhile revisiting this technology for epoxidation.

The direct epoxidation of higher alkenes such as propylene has long been researched as a greener route to higher epoxides, compared to the currently predominant routes based on chlorohydrins and hydroperoxides (Khatib and Oyama, 2015). A chemical looping mode of operation might achieve commercially viable selectivities. Other selective oxidations, with different combinations of catalysts and oxygen carriers, are largely unexplored using chemical looping.

The theoretical work using nonlinear frequency response theory will require experimental validation. Afterwards, it might be used to develop a kinetic model for the epoxidation of ethylene, which can then be used to investigate global enhancement. It was shown that the selectivity of epoxidation can improve with input modulation (Renken *et al.*, 1976).

8 REFERENCES

Amorim de Carvalho, M.C.N., Passos, F.B. and Schmal, M., 2007. Study of the active phase of silver catalysts for ethylene epoxidation, *J. Catal.*, **248**, 124–129. doi: 10.1016/j.jcat.2006.10.030.

Arnold, S.C., Gaffney, A.M., Song, R. and Yeh, C.Y., 2009. Process for Producing Ethylene Via Oxidative Dehydrogenation (ODH) of Ethane, US8519210B2.

Assal, J., Hallstedt, B. and Gauckler, L.J., 1997. Thermodynamic Assessment of the Silver-Oxygen System, *J. Am. Ceram. Soc.*, **80**, 3054–3060. doi: 10.1111/j.1151-2916.1997.tb03232.x.

Barin, I., 1995. *Thermochemical Data of Pure Substances*. Edited by I. Barin. Weinheim, Germany: Wiley-VCH Verlag GmbH. doi: 10.1002/9783527619825.

Baroi, C., Gaffney, A.M. and Fushimi, R., 2017. Process economics and safety considerations for the oxidative dehydrogenation of ethane using the M1 catalyst, *Catal. Today*, **298**, 138–144. doi: 10.1016/j.cattod.2017.05.041.

Beckers, J., Lee, A.F. and Rothenberg, G., 2009. Bismuth-doped ceria, Ce0.90Bi0.10O2: A selective and stable catalyst for clean hydrogen combustion, *Adv. Synth. Catal.*, **351**, 1557–1566. doi: 10.1002/adsc.200900089.

Beckers, J. and Rothenberg, G., 2010. Sustainable selective oxidations using ceria-based materials, *Green Chem.*, **12**, 939. doi: 10.1039/c000191k.

Berger, R.J., Pérez-Ramírez, J., Kapteijn, F. and Moulijn, J.A., 2002. Catalyst performance testing: bed dilution revisited, *Chem. Eng. Sci.*, **57**, 4921–4932. doi:

10.1016/S0009-2509(02)00273-7.

Bird, R.B., Stewart, W.E. and Lightfoot, E.N., 2007. *Transport Phenomena*. Revd. 2nd. John Wiley & Sons.

Blank, J.H., Beckers, J., Collignon, P.F. and Rothenberg, G., 2007. Redox kinetics of ceria-based mixed oxides in selective hydrogen combustion., *Chemphyschem*, **8**, 2490–7. doi: 10.1002/cphc.200700431.

Bohn, C.D., Müller, C.R., Cleeton, J.P., Hayhurst, A.N., Davidson, J.F., Scott, S.A. and Dennis, J.S., 2008. Production of very pure hydrogen with simultaneous capture of carbon dioxide using the redox reactions of iron oxides in packed beds, *Ind. Eng. Chem. Res.*, **47**, 7623–7630. doi: 10.1021/ie800335j.

Boodhoo, K. and Harvey, A., 2013. *Process Intensification Technologies for Green Chemistry: Engineering Solutions for Sustainable Chemical Processing*. Edited by K. Boodhoo and A. Harvey. Wiley.

Brunauer, S., Emmett, P.H. and Teller, E., 1938. Adsorption of Gases in Multimolecular Layers, *J. Am. Chem. Soc.*, **60**, 309–319. doi: 10.1021/ja01269a023.

Bukhtiyarov, V.I. and Knop-Gericke, A., 2011. Ethylene Epoxidation Over Silver Catalysts, in Hess, C. and Schlögl, R. (eds) *Nanostructured Catalysts: Selective Oxidations*. Cambridge: Royal Society of Chemistry, 214–247. doi: 10.1039/9781847559876-00214.

Busser, G.W., Hinrichsen, O. and Muhler, M., 2002. The temperature-programmed desorption of oxygen from an alumina-supported silver catalyst, *Catal. Letters*, **79**, 49–54. doi: 10.1023/A:1015300520227.

Caspary, K.J., Gehrke, H., Adrian, M.H. and Schwefer, M., 2008. Dehydrogenation of Alkanes, in Ertl, G., Knözinger, H., Schüth, F., and Weitkamp, J. (eds) *Handbook of Heterogeneous Catalysis*. Weinheim, Germany: Wiley-VCH Verlag GmbH, 3206–3229. doi: 10.1002/9783527610044.hetcat0162.

Cavani, F., Ballarini, N. and Cericola, A., 2007. Oxidative dehydrogenation of ethane and propane: How far from commercial implementation?, *Catal. Today*, **127**, 113–131. doi: 10.1016/j.cattod.2007.05.009.

Charpentier, J.-C., 2007. In the frame of globalization and sustainability, process intensification, a path to the future of chemical and process engineering (molecules into money), *Chem. Eng. J.*, **134**, 84–92. doi: 10.1016/j.cej.2007.03.084.

Chen, C.-J., Harris, J.W. and Bhan, A., 2018. Kinetics of ethylene epoxidation on a promoted Ag/α-Al2O3 catalyst - the effects of product and chloride co-feeds on rates and selectivity, *Chem. Eur. J.*, **5**, 644–656. doi: 10.1002/chem.201801356.

Chen, X.L. and Eysel, W., 1996. The Stabilization of β-Bi2O3 by CeO2, *J. Solid State Chem.*, **127**, 128–130. doi: 10.1006/jssc.1996.0367.

Cheng, C.M., Peng, Z.K., Zhang, W.M. and Meng, G., 2017. Volterra-series-based nonlinear system modeling and its engineering applications: A state-of-the-art review, *Mech. Syst. Signal Process.*, **87**, 340–364. doi: 10.1016/j.ymssp.2016.10.029.

Christopher, P. and Linic, S., 2010. Shape- and Size-Specific Chemistry of Ag Nanostructures in Catalytic Ethylene Epoxidation, *ChemCatChem*, **2**, 78–83. doi: 10.1002/cctc.200900231.

Chung, E.Y., Wang, W.K., Nadgouda, S.G., Baser, D.S., Sofranko, J.A. and Fan, L.-S., 2016. Catalytic Oxygen Carriers and Process Systems for Oxidative Coupling of Methane Using the Chemical Looping Technology, *Ind. Eng. Chem. Res.*, **55**, 12750–12764. doi: 10.1021/acs.iecr.6b03304.

Collett, C.H. and McGregor, J., 2016. Things go better with coke: the beneficial role of carbonaceous deposits in heterogeneous catalysis, *Catal. Sci. Technol.*, **6**, 363–378. doi: 10.1039/C5CY01236H.

Contractor, R.M., 1999. Dupont's CFB technology for maleic anhydride, *Chem. Eng. Sci.*, **54**, 5627–5632. doi: 10.1016/S0009-2509(99)00295-X.

Contractor, R.M., Bergna, H.E., Horowitz, H.S., Blackstone, C.M., Chowdhry, U. and Sleight, A.W., 1988. Butane Oxidation to Maleic Anhydride in A Recirculating Solids Reactor, in *Stud. Surf. Sci. Catal.* Academic Press Inc., 645–654. doi: 10.1016/S0167-2991(09)60694-7.

Creaser, D., Andersson, B., Hudgins, R.R. and Silveston, P.L., 1999. Cyclic operation of the oxidative dehydrogenation of propane, *Chem. Eng. Sci.*, **54**, 4437–4448. doi: 10.1016/S0009-2509(99)00135-9.

Cushing, B.L., Kolesnichenko, V.L. and O'Connor, C.J., 2004. Recent Advances in the Liquid-Phase Syntheses of Inorganic Nanoparticles, *Chem. Rev.*, **104**, 3893–3946. doi: 10.1021/cr030027b.

Dai, Y., Chen, Z., Guo, Y., Lu, G., Zhao, Y., Wang, H. and Hu, P., 2017. Significant

enhancement of the selectivity of propylene epoxidation for propylene oxide: a molecular oxygen mechanism, *Phys. Chem. Chem. Phys.*, **19**, 25129–25139. doi: 10.1039/C7CP02892J.

Davies, R., Dinsdale, A., Gisby, J., Robinson, J. and Martin, S., 2002. MTDATA - thermodynamic and phase equilibrium software from the national physical laboratory, *CALPHAD*, **26**, 229–271. doi: 10.1016/S0364-5916(02)00036-6.

Delgado, J.M.P.Q., 2006. A critical review of dispersion in packed beds, *Heat Mass Transfer*, **42**, 279–310. doi: 10.1007/s00231-005-0019-0.

Dennis, J. and Scott, S., 2010. In situ gasification of a lignite coal and CO2 separation using chemical looping with a Cu-based oxygen carrier, *Fuel*, **89**, 1623–1640. doi: 10.1016/j.fuel.2009.08.019.

Dever, J.P., George, K.F., Hoffman, W.C. and Soo, H., 2000. Ethylene Oxide, *Kirk-Othmer Encycl. Chem. Technol.* doi: doi:10.1002/0471238961.0520082504052205.a01.

Dincer, I. and Acar, C., 2015. Review and evaluation of hydrogen production methods for better sustainability, *Int. J. Hydrogen Energy*, **40**, 11094–11111. doi: 10.1016/j.ijhydene.2014.12.035.

Von Dreele, R. and Larson, A., 2000. General structure analysis system (GSAS), *Los Alamos Natl. Lab. Rep. LAUR*, 86–748.

Dueso, C., Thompson, C. and Metcalfe, I., 2015. High-stability, high-capacity oxygen carriers: Iron oxide-perovskite composite materials for hydrogen production by chemical looping, *Appl. Energy*, **157**, 382–390. doi: 10.1016/j.apenergy.2015.05.062.

Elbadawi, A.H., Ba-Shammakh, M.S., Al-Ghamdi, S., Razzak, S.A., Hossain, M.M. and de Lasa, H.I., 2016. A fluidizable VOx/γ–Al2O3–ZrO2 catalyst for the ODH of ethane to ethylene operating in a gas phase oxygen free environment, *Chem. Eng. Sci.*, **145**, 59–70. doi: 10.1016/j.ces.2016.01.050.

EUROKIN_fixed-bed_html, 2012. *EUROKIN spreadsheet on requirements for measurement of intrinsic kinetics in the gas-solid fixed-bed reactor*.

Fan, L.-S., Zeng, L. and Luo, S., 2015. Chemical-looping technology platform, *AIChE J.*, **61**, 2–22. doi: 10.1002/aic.14695.

Fan, L.-S., Zeng, L., Wang, W. and Luo, S., 2012. Chemical looping processes for CO2 capture and carbonaceous fuel conversion – prospect and opportunity, *Energy Environ. Sci.*, **5**, 7254. doi: 10.1039/c2ee03198a.

Farrell, B.L., Igenegbai, V.O. and Linic, S., 2016. A Viewpoint on Direct Methane Conversion to Ethane and Ethylene Using Oxidative Coupling on Solid Catalysts, *ACS Catal.*, **6**, 4340–4346. doi: 10.1021/acscatal.6b01087.

Fleischer, V., Littlewood, P., Parishan, S. and Schomäcker, R., 2016. Chemical looping as reactor concept for the oxidative coupling of methane over a Na2WO4/Mn/SiO2 catalyst, *Chem. Eng. J.*, **306**, 646–654. doi: 10.1016/j.cej.2016.07.094.

Fornberg, B., 1988. Generation of finite difference formulas on arbitrarily spaced grids, *Math. Comput.*, **51**, 699–699. doi: 10.1090/S0025-5718-1988-0935077-0.

Froment, G.F., De Wilde, J. and Bischoff, K., 2011. *Chemical reactor analysis and design*. 3rd edn. Hoboken, N.J: Wiley.

Gaffney, A.M. and Mason, O.M., 2017. Ethylene production via Oxidative Dehydrogenation of Ethane using M1 catalyst, *Catal. Today*, **285**, 159–165. doi: 10.1016/j.cattod.2017.01.020.

Gao, Y., Neal, L.M. and Li, F., 2016. Li-Promoted LaxSr2– xFeO4−δ Core–Shell Redox Catalysts for Oxidative Dehydrogenation of Ethane under a Cyclic Redox Scheme, *ACS Catal.*, **6**, 7293–7302. doi: 10.1021/acscatal.6b01399.

Gärtner, C.A., van Veen, A.C. and Lercher, J.A., 2013. Oxidative Dehydrogenation of Ethane: Common Principles and Mechanistic Aspects, *ChemCatChem*, **5**, 3196–3217. doi: 10.1002/cctc.201200966.

Van Gerven, T. and Stankiewicz, A., 2009. Structure, Energy, Synergy, Time - The Fundamentals of Process Intensification, *Ind. Eng. Chem. Res.*, **48**, 2465–2474. doi: 10.1021/ie801501y.

Gerzeliev, I.M., Popov, A.Y. and Ostroumova, V.A., 2016. Oxidative dehydrogenation of ethane to ethylene in a system with circulating microspherical metal oxide oxygen carrier: 2. Ethylene production in a pilot unit with a riser reactor, *Pet. Chem.*, **56**, 724–729. doi: 10.1134/S0965544116080053.

Giddings, R.A. and Gordon, R.S., 1973. Review of Oxygen Activities and Phase Boundaries in Wustite as Determined by Electromotive-Force and Gravimetric Methods, *J. Am. Ceram. Soc.*, **56**, 111–116. doi: 10.1111/j.1151-

2916.1973.tb15423.x.

Gierman, H., 1988. Design of laboratory hydrotreating reactors, *Appl. Catal.*, **43**, 277–286. doi: 10.1016/S0166-9834(00)82732-3.

Godefroy, A., Patience, G.S., Cenni, R. and Dubois, J.-L., 2010. Regeneration studies of redox catalysts, *Chem. Eng. Sci.*, **65**, 261–266. doi: 10.1016/j.ces.2009.05.037.

de Graaf, E.A., Andreini, A., Hensen, E.J.M. and Bliek, A., 2004. Selective hydrogen oxidation in a mixture with ethane/ethene using cerium zirconium oxide, *Appl. Catal. A Gen.*, **262**, 201–206. doi: 10.1016/j.apcata.2003.11.027.

Grant, J.T., Carrero, C.A., Goeltl, F., Venegas, J., Mueller, P., Burt, S.P., Specht, S.E., McDermott, W.P., Chieregato, A. and Hermans, I., 2016. Selective oxidative dehydrogenation of propane to propene using boron nitride catalysts, *Science*, **354**, 1570–1573. doi: 10.1126/science.aaf7885.

Grant, J.T., Mcdermott, W.P., Venegas, J.M., Burt, S.P., Micka, J., Phivilay, S.P., Carrero, C.A. and Hermans, I., 2017. Boron and Boron-Containing Catalysts for the Oxidative Dehydrogenation of Propane, *ChemCatChem*, 1–5. doi: 10.1002/cctc.201701140.

Grasselli, R.K., 2002. Fundamental principles of selective heterogeneous oxidation catalysis, *Top. Catal.*, **21**, 79–88. doi: 10.1023/A:1020556131984.

Grasselli, R.K., 2014. Site isolation and phase cooperation: Two important concepts in selective oxidation catalysis: A retrospective, *Catal. Today*, **238**, 10–27. doi: 10.1016/j.cattod.2014.05.036.

Grasselli, R.K., Buttrey, D.J., Burrington, J.D., Andersson, A., Holmberg, J., Ueda, W., Kubo, J., Lugmair, C.G. and Volpe, A.F., 2006. Active centers, catalytic behavior, symbiosis and redox properties of MoV(Nb,Ta)TeO ammoxidation catalysts, *Top. Catal.*, **38**, 7–16. doi: 10.1007/s11244-006-0066-x.

Grasselli, R.K., Stern, D.L. and Tsikoyiannis, J.G., 1999a. Catalytic dehydrogenation (DH) of light paraffins combined with selective hydrogen combustion (SHC) I. DH-SHC-DH catalysts in series (co-fed process mode), *Appl. Catal. A Gen.*, **189**, 1–8. doi: 10.1016/S0926-860X(99)00224-0.

Grasselli, R.K., Stern, D.L. and Tsikoyiannis, J.G., 1999b. Catalytic dehydrogenation (DH) of light paraffins combined with selective hydrogen combustion (SHC) II. DH+SHC catalysts physically mixed (redox process mode), *Appl. Catal. A Gen.*, 1–

8. doi: 10.1016/S0926-860X(99)00195-7.

Gray, M.R. and McCaffrey, W.C., 2002. Role of chain reactions and olefin formation in cracking, hydroconversion, and coking of petroleum and bitumen fractions, *Energy and Fuels*, **16**, 756–766. doi: 10.1021/ef010243s.

Gryaznov, V.M., Gul'yanova, S.G. and Kanizius, S., 1973. Diffusion of Oxygen Through a Silver Membrane, *Russ. J. Phys. Chem.*, **47**, 1517–1518.

Häussinger, P., Lohmüller, R. and Watson, A.M., 2000. Hydrogen, 2. Production, in *Ullmann's Encycl. Ind. Chem.* Weinheim, Germany: Wiley-VCH Verlag GmbH & Co. KGaA. doi: 10.1002/14356007.o13_o03.

Haynes, W.M., 2017. *CRC Handbook of Chemistry and Physics*. 97th edn. Boca Raton, FL: CRC Press.

He, F. and Li, F., 2014. Hydrogen production from methane and solar energy - Process evaluations and comparison studies, *Int. J. Hydrogen Energy*, **39**, 18092–18102. doi: 10.1016/j.ijhydene.2014.05.089.

He, F. and Li, F., 2015. Perovskite promoted iron oxide for hybrid water-splitting and syngas generation with exceptional conversion, *Energy Environ. Sci.*, **8**, 535–539. doi: 10.1039/C4EE03431G.

He, J., Zhai, Q., Zhang, Q., Deng, W. and Wang, Y., 2013. Active site and reaction mechanism for the epoxidation of propylene by oxygen over CuOx/SiO2 catalysts with and without Cs+ modification, *J. Catal.*, **299**, 53–66. doi: 10.1016/j.jcat.2012.11.032.

Heidebrecht, P. and Sundmacher, K., 2009. Thermodynamic analysis of a cyclic water gas-shift reactor (CWGSR) for hydrogen production, *Chem. Eng. Sci.*, **64**, 5057–5065. doi: 10.1016/j.ces.2009.08.011.

Hermans, I., Grant, J.T., Carrero Marquez, C.A., Chieregato, A. and Venegas, J.M., 2015. Heterogeneous catalysts for the oxidative dehydrogenation of alkanes or oxidative coupling of methane, US20170066700A1.

House, M.P., Carley, A.F. and Bowker, M., 2007. Selective oxidation of methanol on iron molybdate catalysts and the effects of surface reduction, *J. Catal.*, **252**, 88–96. doi: 10.1016/j.jcat.2007.09.005.

Huang, R., Zhang, B., Wang, J., Wu, K.-H., Shi, W., Zhang, Y., Liu, Y., Zheng, A.,

Schlögl, R. and Su, D.S., 2017. Direct Insight into Ethane Oxidative Dehydrogenation over Boron Nitrides, *ChemCatChem*, **9**, 3293–3297. doi: 10.1002/cctc.201700725.

Hudgins, R.R., Silveston, P.L., Li, C.-Y. and Adesina, A.A., 2013. Partial Oxidation and Dehydrogenation of Hydrocarbons, in *Periodic Operation of Chemical Reactors*. Butterworth-Heinemann, 79–122. doi: 10.1016/B978-0-12-391854-3.00004-8.

Ismail, M., Liu, W. and Scott, S.A., 2014. The performance of Fe2O3-CaO Oxygen Carriers and the Interaction of Iron Oxides with CaO during Chemical Looping Combustion and H2 production, *Energy Procedia*, **63**, 87–97. doi: 10.1016/j.egypro.2014.11.010.

Jacob, K.T., Dasgupta, N. and Waseda, Y., 1999. Thermodynamic properties of the calcium ferrites CaFe2O4 and Ca2Fe2O5, *Zeitschrift für Met.*, **90**, 486–490.

Jensen, W.B., 2009. The Origin of the Brin Process for the Manufacture of Oxygen, *J. Chem. Educ.*, **86**, 1266. doi: 10.1021/ed086p1266.

Jovalekić, Č., Zdujić, M., Poleti, D., Karanović, L. and Mitrić, M., 2008. Structural and electrical properties of the 2Bi2O3·3ZrO2 system, *J. Solid State Chem.*, **181**, 1321–1329. doi: 10.1016/j.jssc.2008.02.038.

Kaspar, J., Fornasiero, P., Balducci, G., Di Monte, R., Hickey, N. and Sergo, V., 2003. Effect of ZrO2 content on textural and structural properties of CeO2–ZrO2 solid solutions made by citrate complexation route, *Inorganica Chim. Acta*, **349**, 217–226. doi: 10.1016/S0020-1693(03)00034-3.

Kathe, M. V., Empfield, A., Na, J., Blair, E. and Fan, L.-S., 2016. Hydrogen production from natural gas using an iron-based chemical looping technology: Thermodynamic simulations and process system analysis, *Appl. Energy*, **165**, 183–201. doi: 10.1016/j.apenergy.2015.11.047.

Khadzhiev, S.N., Usachev, N.Y., Gerzeliev, I.M., Belanova, E.P., Kalinin, V.P., Kharlamov, V. V., Kazakov, A. V., Kanaev, S.A., Starostina, T.S. and Popov, A.Y., 2015. Oxidative dehydrogenation of ethane to ethylene in a system with circulating microspherical metal oxide oxygen carrier: 1. Synthesis and study of the catalytic system, *Pet. Chem.*, **55**, 651–654. doi: 10.1134/S0965544115080125.

Khatib, S.J. and Oyama, S.T., 2015. Direct Oxidation of Propylene to Propylene Oxide with Molecular Oxygen: A Review, *Catal. Rev.*, **57**, 306–344. doi:

10.1080/01614940.2015.1041849.

Kim, T., Vohs, J.M. and Gorte, R.J., 2006. Thermodynamic Investigation of the Redox Properties of Ceria−Zirconia Solid Solutions, *Ind. Eng. Chem. Res.*, **45**, 5561–5565. doi: 10.1021/ie0511478.

Kim, Y., Park, L.K., Yiacoumi, S. and Tsouris, C., 2017. Modular Chemical Process Intensification: A Review, *Annu. Rev. Chem. Biomol. Eng.*, **8**, 359–380. doi: 10.1146/annurev-chembioeng-060816-101354.

Kobayashi, M., 1980. Transient behavior of the oxidation of propylene over a modified silver oxide, *Can. J. Chem. Eng.*, **58**, 588–593. doi: 10.1002/cjce.5450580507.

Kocoń, M., Michorczyk, P. and Ogonowski, J., 2005. Effect of supports on catalytic activity of chromium oxide-based catalysts in the dehydrogenation of propane with CO2, *Catal. Letters*, **101**, 53–57. doi: 10.1007/s10562-004-3749-6.

Kogan, S.B., Schramm, H. and Herskowitz, M., 2001. Dehydrogenation of propane on modified Pt/θ-alumina Performance in hydrogen and steam environment, *Appl. Catal. A Gen.*, **208**, 185–191. doi: 10.1016/S0926-860X(00)00703-1.

Kuang, W., Fan, Y., Chen, K. and Chen, Y., 1999. Partial Oxidation of Toluene over Ultrafine Mixed Mo-Based Oxide Particles, *J. Catal.*, **186**, 310–317. doi: 10.1006/jcat.1999.2559.

Lambert, R.M., Williams, F.J., Cropley, R.L. and Palermo, A., 2005. Heterogeneous alkene epoxidation: past, present and future, *J. Mol. Catal. A Chem.*, **228**, 27–33. doi: 10.1016/j.molcata.2004.09.077.

Larsson, M., Henriksson, N. and Andersson, B., 1998. Investigation of the kinetics of a deactivating system by transient experiments, *Appl. Catal. A Gen.*, **166**, 9–19. doi: 10.1016/S0926-860X(97)00233-0.

Larsson, M., Hultén, M., Blekkan, E.A. and Andersson, B., 1996. The Effect of Reaction Conditions and Time on Stream on the Coke Formed during Propane Dehydrogenation, *J. Catal.*, **164**, 44–53. doi: 10.1006/jcat.1996.0361.

Lau, C.Y., Dunstan, M.T., Hu, W., Grey, C.P. and Scott, S.A., 2017. Large scale in silico screening of materials for carbon capture through chemical looping, *Energy Environ. Sci.*, **10**, 818–831. doi: 10.1039/C6EE02763F.

Li, L.M. and Billings, S.A., 2006. Generalized frequency response functions and output

response synthesis for MIMO non-linear systems, *Int. J. Control*, **79**, 53–62. doi: 10.1080/00207170500428794.

Linic, S. and Barteau, M.A., 2003. Control of Ethylene Epoxidation Selectivity by Surface Oxametallacycles, *J. Am. Chem. Soc.*, **125**, 4034–4035. doi: 10.1021/ja029076g.

Linic, S., Piao, H., Adib, K. and Barteau, M.A., 2004. Ethylene Epoxidation on Ag: Identification of the Crucial Surface Intermediate by Experimental and Theoretical Investigation of its Electronic Structure, *Angew. Chemie Int. Ed.*, **43**, 2918–2921. doi: 10.1002/anie.200353584.

Lintz, H. and Reitzmann, A., 2007. Alternative Reaction Engineering Concepts in Partial Oxidations on Oxidic Catalysts, *Catal. Rev.*, **49**, 1–32. doi: 10.1080/01614940600983467.

Liu, W., Dennis, J.S. and Scott, S.A., 2012. The effect of addition of ZrO2 to Fe2O3 for hydrogen production by chemical looping, *Ind. Eng. Chem. Res.*, **51**, 16597–16609. doi: 10.1021/ie302626x.

Lu, J., Bravo-Suárez, J.J., Takahashi, A., Haruta, M. and Oyama, S.T., 2005. In situ UV-vis studies of the effect of particle size on the epoxidation of ethylene and propylene on supported silver catalysts with molecular oxygen, *J. Catal.*, **232**, 85–95. doi: 10.1016/j.jcat.2005.02.013.

Lwin, S., Diao, W., Baroi, C., Gaffney, A. and Fushimi, R., 2017. Characterization of MoVTeNbOx Catalysts during Oxidation Reactions Using In Situ/Operando Techniques: A Review, *Catalysts*, **7**, 109. doi: 10.3390/catal7040109.

Lyngfelt, A., 2014. Chemical-looping combustion of solid fuels – Status of development, *Appl. Energy*, **113**, 1869–1873. doi: 10.1016/j.apenergy.2013.05.043.

Marimuthu, A., Zhang, J. and Linic, S., 2013. Tuning Selectivity in Propylene Epoxidation by Plasmon Mediated Photo-Switching of Cu Oxidation State, *Science*, **339**, 1590–1593. doi: 10.1126/science.1231631.

Marković, A., Morgenstern, A.-S. and Petkovska, M., 2008. Evaluation of the potential of periodically operated reactors based on the second order frequency response function, *Chem. Eng. Res. Des.*, **86**, 682–691. doi: 10.1016/j.cherd.2008.02.003.

Mars, P. and van Krevelen, D.W., 1954. Oxidations carried out by means of vanadium oxide catalysts, *Chem. Eng. Sci.*, **3**, 41–59. doi: 10.1016/S0009-2509(54)80005-4.

McAteer, C.H., Murugan, R. and Subba Rao, Y. V., 2017. Heterogeneously Catalyzed Synthesis of Heterocyclic Compounds, in *Adv. Heterocycl. Chem.* Elsevier Ltd, 173–205. doi: 10.1016/bs.aihch.2016.03.003.

Mears, D.E., 1971a. Diagnostic criteria for heat transport limitations in fixed bed reactors, *J. Catal.*, **20**, 127–131. doi: 10.1016/0021-9517(71)90073-X.

Mears, D.E., 1971b. The role of axial dispersion in trickle-flow laboratory reactors, *Chem. Eng. Sci.*, **26**, 1361–1366. doi: 10.1016/0009-2509(71)80056-8.

Messerschmitt, A., 1908. Process of producing hydrogen., US971206A.

Michaelides, A., Bocquet, M.L., Sautet, P., Alavi, A. and King, D.A., 2003. Structures and thermodynamic phase transitions for oxygen and silver oxide phases on Ag{1 1 1}, *Chem. Phys. Lett.*, **367**, 344–350. doi: 10.1016/S0009-2614(02)01699-8.

Montini, T., Melchionna, M., Monai, M. and Fornasiero, P., 2016. Fundamentals and Catalytic Applications of CeO2-Based Materials, *Chem. Rev.*, **116**, 5987–6041. doi: 10.1021/acs.chemrev.5b00603.

Mullins, D.R., 2015. The surface chemistry of cerium oxide, *Surf. Sci. Rep.*, **70**, 42–85. doi: 10.1016/j.surfrep.2014.12.001.

Neal, L.M., Yusuf, S., Sofranko, J.A. and Li, F., 2016. Oxidative Dehydrogenation of Ethane: A Chemical Looping Approach, *Energy Technol.*, **4**, 1200–1208. doi: 10.1002/ente.201600074.

Nijhuis, T.A., Makkee, M., Moulijn, J.A. and Weckhuysen, B.M., 2006. The Production of Propene Oxide: Catalytic Processes and Recent Developments, *Ind. Eng. Chem. Res.*, **45**, 3447–3459. doi: 10.1021/ie0513090.

Nikolić, D., Seidel-Morgenstern, A. and Petkovska, M., 2015. Nonlinear frequency response analysis of forced periodic operation of non-isothermal CSTR with simultaneous modulation of inlet concentration and inlet temperature, *Chem. Eng. Sci.*, **137**, 40–58. doi: 10.1016/j.ces.2015.06.018.

Nikolic Paunic, D. and Petkovska, M., 2013. Evaluation of periodic processes with two modulated inputs based on nonlinear frequency response analysis. Case study: CSTR with modulation of the inlet concentration and flow-rate, *Chem. Eng. Sci.*, **104**, 208–219. doi: 10.1016/j.ces.2013.09.009.

Nilsson, O., Mehling, H., Horn, R., Fricke, J., Hofmann, R., Müller, S.G., Eckstein, R.

and Hofmann, D., 1997. Determination of the thermal diffusivity and conductivity of monocrystalline silicon carbide (300 - 2300 K), *High Temp. High Press.*, **29**, 73–79.

Noronha, F.B., Fendley, E.C., Soares, R.R., Alvarez, W.E. and Resasco, D.E., 2001. Correlation between catalytic activity and support reducibility in the CO2 reforming of methane over Pt/CexZr1−xO2 catalysts, *Chem. Eng. J.*, **82**, 21–31. doi: 10.1016/S1385-8947(00)00368-5.

Özbek, M.O. and van Santen, R.A., 2013. The Mechanism of Ethylene Epoxidation Catalysis, *Catal. Letters*, **143**, 131–141. doi: 10.1007/s10562-012-0957-3.

Park, D.M., Ghazali, S. and Gau, G., 1983. A cyclic reactor study of ethylene epoxidation, *Appl. Catal.*, **6**, 175–193. doi: 10.1016/0166-9834(83)80263-2.

Patience, G.S. and Bockrath, R.E., 2010. Butane oxidation process development in a circulating fluidized bed, *Appl. Catal. A Gen.*, **376**, 4–12. doi: 10.1016/j.apcata.2009.10.023.

Pechini, M.P., 1963. Method of preparing lead and alkaline earth titanates and niobates and coating method using the same to form a capacitor, US3330697A.

Peplow, M., 2017. How fracking is upending the chemical industry, *Nature*, **550**, 26–28. doi: 10.1038/550026a.

Petkovska, M. and Morgenstern, A.-S., 2013. Evaluation of Periodic Processes, in Silveston, P. L. and Hudgins, R. R. (eds) *Periodic Operation of Chemical Reactors*. 1st edn. Oxford: Butterworth-Heinemann, 387–412.

Piccinin, S., Zafeiratos, S., Stampfl, C., Hansen, T.W., Hävecker, M., Teschner, D., Bukhtiyarov, V.I., Girgsdies, F., Knop-Gericke, A., Schlögl, R. and Scheffler, M., 2010. Alloy catalyst in a reactive environment: The example of Ag-Cu particles for ethylene epoxidation, *Phys. Rev. Lett.*, **104**, 1–4. doi: 10.1103/PhysRevLett.104.035503.

Popa, N.C. and Balzar, D., 2002. An analytical approximation for a size-broadened profile given by the lognormal and gamma distributions, *J. Appl. Crystallogr.*, **35**, 338–346. doi: 10.1107/S0021889802004156.

Pulido, A., Concepción, P., Boronat, M. and Corma, A., 2012. Aerobic epoxidation of propene over silver (111) and (100) facet catalysts, *J. Catal.*, **292**, 138–147. doi: 10.1016/j.jcat.2012.05.006.

Rebsdat, S. and Mayer, D., 2012. Ethylene Oxide, *Ullmann's Encycl. Ind. Chem.* Weinheim, Germany: Wiley-VCH Verlag GmbH & Co. KGaA. doi: 10.1002/14356007.a10_117.

Reichelt, R., Günther, S., Rößler, M., Wintterlin, J., Kubias, B., Jakobi, B. and Schlögl, R., 2007. High-pressure STM of the interaction of oxygen with Ag(111), *Phys. Chem. Chem. Phys.*, **9**, 3590–3599. doi: 10.1039/B700432J.

Renken, A., Hudgins, R.R. and Silveston, P.L., 2013. Use of Modulation in Mechanistic Studies, in Silveston, P. L. and Hudgins, R. R. (eds) *Periodic Operation of Chemical Reactors*. 1st edn. Oxford: Elsevier, 369–386. doi: 10.1016/B978-0-12-391854-3.00013-9.

Renken, A., Mueller, M. and Wandrey, C., 1976. Experimental studies on the improvement of fixed-bed reactors by periodic operation - the catalytic oxidation of ethylene, in *Chem. React. Eng.*, 107–116.

Rollman, W.F., 1949. Selective oxidation with suspended catalyst, US2604479A.

Rothenberg, G., de Graaf, E.A. and Bliek, A., 2003. Solvent-Free Synthesis of Rechargeable Solid Oxygen Reservoirs for Clean Hydrogen Oxidation, *Angew. Chemie Int. Ed.*, **42**, 3366–3368. doi: 10.1002/anie.200351545.

Satterfield, C.N., 1991. *Heterogeneous catalysis in industrial practice. 2nd edition*. United States: New York, NY (United States); McGraw Hill Book Co.

Sattler, J.J.H.B., Ruiz-Martinez, J., Santillan-Jimenez, E. and Weckhuysen, B.M., 2014. Catalytic Dehydrogenation of Light Alkanes on Metals and Metal Oxides, *Chem. Rev.*, **114**, 10613–10653. doi: 10.1021/cr5002436.

Scanlon, J.T. and Willis, D.E., 1985. Calculation of flame ionization detector relative response factors using the effective carbon number concept, *J. Chromatogr. Sci.*, **23**, 333–340. doi: 10.1093/chromsci/23.8.333.

Schneider, C.A., Rasband, W.S. and Eliceiri, K.W., 2012. NIH Image to ImageJ: 25 years of image analysis, *Nat. Methods*, **9**, 671–675. doi: 10.1038/nmeth.2089.

Schnellmann, M.A., Heuberger, C.F., Scott, S.A., Dennis, J.S. and Mac Dowell, N., 2018. Quantifying the role and value of chemical looping combustion in future electricity systems via a retrosynthetic approach, *Int. J. Greenh. Gas Control*, **73**, 1–15. doi: 10.1016/j.ijggc.2018.03.016.

Seyedmonir, S.R., Plischke, J.K., Vannice, M.A. and Young, H.W., 1990. Ethylene oxidation over small silver crystallites, *J. Catal.*, **123**, 534–549. doi: 10.1016/0021-9517(90)90149-E.

Shekari, A. and Patience, G.S., 2010. Maleic anhydride yield during cyclic n-butane/oxygen operation, *Catal. Today*, **157**, 334–338. doi: 10.1016/j.cattod.2010.03.011.

Shi, L., Wang, D. and Lu, A., 2018. A viewpoint on catalytic origin of boron nitride in oxidative dehydrogenation of light alkanes, *Chinese J. Catal.*, **39**, 908–913. doi: 10.1016/S1872-2067(18)63060-8.

Shi, L., Wang, D., Song, W., Shao, D., Zhang, W.-P. and Lu, A.-H., 2017a. Edge Hydroxylated Boron Nitride for Oxidative Dehydrogenation of Propane to Propylene, *ChemCatChem*, 1788–1793. doi: 10.1002/cctc.201700004.

Shi, L., Yan, B., Shao, D., Jiang, F., Wang, D. and Lu, A.-H., 2017b. Selective oxidative dehydrogenation of ethane to ethylene over a hydroxylated boron nitride catalyst, *Chinese J. Catal.*, **38**, 389–395. doi: 10.1016/S1872-2067(17)62786-4.

Silveston, P.L., Hudgins, R.R. and Renken, A., 1995. Periodic Operation of Catalytic Reactors - Introduction and Overview, *Catal. Today*, **25**, 91–112. doi: 10.1016/0920-5861(95)00101-K.

Specchia, V., Baldi, G. and Sicardi, S., 1980. Heat transfer in packed bed reactors with one phase flow, *Chem. Eng. Commun.*, **4**, 361–380. doi: 10.1080/00986448008935916.

Stegelmann, C., Schiødt, N.C., Campbell, C.T. and Stoltze, P., 2004. Microkinetic modeling of ethylene oxidation over silver, *J. Catal.*, **221**, 630–649. doi: 10.1016/j.jcat.2003.10.004.

Stephanopoulos, G., 1983. *Chemical Process Control: An Introduction to Theory and Practice*. New Jersey: Prentice Hall.

Takanabe, K. and Iglesia, E., 2009. Mechanistic Aspects and Reaction Pathways for Oxidative Coupling of Methane on Mn/Na2WO4/SiO2 Catalysts, *J. Phys. Chem. C*, **113**, 10131–10145. doi: 10.1021/jp9001302.

Tan, S.A., Grant, R.B. and Lambert, R.M., 1987. Secondary chemistry in the selective oxidation of ethylene: Effect of Cl and Cs promoters on the adsorption, isomerisation, and combustion of ethylene oxide on Ag(111), *J. Catal.*, **106**, 54–64.

doi: 10.1016/0021-9517(87)90210-7.

Thursfield, A., Murugan, A., Franca, R. and Metcalfe, I.S., 2012. Chemical looping and oxygen permeable ceramic membranes for hydrogen production – a review, *Energy Environ. Sci.*, **5**, 7421. doi: 10.1039/c2ee03470k.

Toby, B.H., 2001. EXPGUI, a graphical user interface for GSAS, *J. Appl. Crystallogr.*, **34**, 210–213. doi: 10.1107/S0021889801002242.

Torres, D., Lopez, N., Illas, F. and Lambert, R.M., 2007. Low-basicity oxygen atoms: A key in the search for propylene epoxidation catalysts, *Angew. Chemie - Int. Ed.*, **46**, 2055–2058. doi: 10.1002/anie.200603803.

Tsikoyiannis, J.G., Stern, D.L. and Grasselli, R.K., 1999. Metal Oxides As Selective Hydrogen Combustion (SHC) Catalysts and Their Potential in Light Paraffin Dehydrogenation, *J. Catal.*, **184**, 77–86. doi: 10.1006/jcat.1998.2363.

Vannice, M.A., 2005. *Kinetics of Catalytic Reactions*. Boston, MA: Springer US. doi: 10.1007/b136380.

Volterra, V., 1959. *Theory of Functionals and of Integral and Integro-differential Equations*. New York: Dover.

Vrieland, G.E. and Murchison, C.B., 1996. Anaerobic oxidation of butane to butadiene over magnesium molybdate catalysts. I. Magnesia supported catalysts, *Appl. Catal. A Gen.*, **134**, 101–121. doi: 10.1016/0926-860X(95)00213-8.

Wagner, C. and Hauffe, K., 1938. Untersuchungen über den stationären Zustand von Katalysatoren bei homogenen Reaktionen I, *Berichte der Bunsengesellschaft für Phys. Chemie*, **4**, 172–178. doi: 10.1002/bbpc.19380440303.

Wakao, N. and Funazkri, T., 1978. Effect of fluid dispersion coefficients on particle-to-fluid mass transfer coefficients in packed beds, *Chem. Eng. Sci.*, 1375–1384. doi: 10.1016/0009-2509(78)85120-3.

Wakao, N., Kaguei, S. and Funazkri, T., 1979. Effect of fluid dispersion coefficients on particle-to-fluid heat transfer coefficients in packed beds, *Chem. Eng. Sci.*, **34**, 325–336. doi: 10.1016/0009-2509(79)85064-2.

Waku, T., Biscardi, J. a. and Iglesia, E., 2004. Catalytic dehydrogenation of alkanes on Pt/Na-[Fe]ZSM5 and staged O2 introduction for selective H2 removal, *J. Catal.*, **222**, 481–492. doi: 10.1016/j.jcat.2003.12.011.

Weiner, D.D. and Spina, J.F., 1980. *Sinusoidal Analysis and Modeling of Weakly Nonlinear Circuits*. New York: Van Nostrand Reinhold.

Wolf, J., Anheden, M. and Yan, J., 2005. Comparison of nickel- and iron-based oxygen carriers in chemical looping combustion for CO2 capture in power generation, *Fuel*, **84**, 993–1006. doi: 10.1016/j.fuel.2004.12.016.

Wolfram Research Inc., 2017. Mathematica, Version 11.2. Champaign, Illinois: Wolfram Research, Inc., 11.2.

Yadav, R. and Rinker, R.G., 1989. The efficacy of concentration forcing, *Chem. Eng. Sci.*, **44**, 2191–2195. doi: 10.1016/0009-2509(89)85153-X.

Yates, J.G. and Lettieri, P., 2016. *Fluidized-Bed Reactors: Processes and Operating Conditions*. Cham: Springer (Particle Technology Series). doi: 10.1007/978-3-319-39593-7.

Yusuf, S., Neal, L., Haribal, V., Baldwin, M., Lamb, H.H. and Li, F., 2018. Manganese silicate based redox catalysts for greener ethylene production via chemical looping – oxidative dehydrogenation of ethane, *Appl. Catal. B Environ.*, **232**, 77–85. doi: 10.1016/j.apcatb.2018.03.037.

Yusuf, S., Neal, L.M. and Li, F., 2017. Effect of Promoters on Manganese-Containing Mixed Metal Oxides for Oxidative Dehydrogenation of Ethane via a Cyclic Redox Scheme, *ACS Catal.*, **7**, 5163–5173. doi: 10.1021/acscatal.7b02004.

Zhao, Z., Iloeje, C.O., Chen, T. and Ghoniem, A.F., 2014. Design of a rotary reactor for chemical-looping combustion. Part 1: Fundamentals and design methodology, *Fuel*, **121**, 327–343. doi: 10.1016/j.fuel.2013.11.056.

Zimmermann, H. and Walzl, R., 2009. Ethylene, in *Ullmann's Encycl. Ind. Chem.* Weinheim, Germany: Wiley-VCH Verlag GmbH & Co. KGaA, 465–530. doi: 10.1002/14356007.a10_045.pub3.

Zurcher, F.R., Scher, E.C., Cizeron, J.M., Schammel, W.P., Tkachenko, A., Gamoras, J., Karshtedt, D., Nyce, G., Rumplecker, A., McCormick, J., Merzlyak, A., Alcid, M., Rosenberg, D. and Ras, E.-J., 2011. Nanowire catalysts and methods for their use and preparation, US9751818B2.

9 APPENDIX

GENERALISED FREQUENCY RESPONSE FUNCTIONS

This appendix expresses the generalised frequency response functions (GFRFs) that were computed for the idealised reactor model in chapter 5. The font size has been decreased because of the size of the expressions. The electronic version of this Dissertation displays these GFRFs more clearly. Note that the third order GFRFs have been expressed in terms of the first and second order GFRFs, for brevity.

First order GFRFs

$$F_{x1}[\omega] \to \frac{i\, c_{A0s}\, (-(-i+\omega)\, (\omega - i\tau k_A \alpha_A) + \tau k_B\, (X_s\, (i\omega + \tau k_A \alpha_A) + (1 + i\omega)\, \alpha_B))}{c_{As}\, \left(-i\, (-i+\omega)\, ((1+i\omega)\, \omega + \tau k_B\, (\omega X_s + (-i+\omega)\, \alpha_B)) + \tau k_A \left(\tau \omega k_B X_s^2 - i\, (-i+\omega)\, (\omega + (-i+\omega)\, \alpha_A - i\tau k_B \alpha_B) + X_s\, ((1+i\omega)\, \omega - \tau k_B\, (\omega + (-i+\omega)\, \alpha_A - (-i+\omega)\, \alpha_B))\right)\right)}$$

$$G_{x1}[\omega] \to \frac{i\tau^2\, c_{A0s}\, k_A\, k_B\, (-1+X_s)\, \alpha_A}{c_{As}\, \left(-i\, (-i+\omega)\, ((1+i\omega)\, \omega + \tau k_B\, (\omega X_s + (-i+\omega)\, \alpha_B)) + \tau k_A \left(\tau \omega k_B X_s^2 - i\, (-i+\omega)\, (\omega + (-i+\omega)\, \alpha_A - i\tau k_B \alpha_B) + X_s\, ((1+i\omega)\, \omega - \tau k_B\, (\omega + (-i+\omega)\, \alpha_A - (-i+\omega)\, \alpha_B))\right)\right)}$$

$$H_{x1}[\omega] \to \frac{\tau\, c_{A0s}\, k_A\, (-1+X_s)\, (-i+\omega - i\tau k_B X_s)\, \alpha_A}{c_{As}\, X_s\, \left(-i\, (-i+\omega)\, ((1+i\omega)\, \omega + \tau k_B\, (\omega X_s + (-i+\omega)\, \alpha_B)) + \tau k_A \left(\tau \omega k_B X_s^2 - i\, (-i+\omega)\, (\omega + (-i+\omega)\, \alpha_A - i\tau k_B \alpha_B) + X_s\, ((1+i\omega)\, \omega - \tau k_B\, (\omega + (-i+\omega)\, \alpha_A - (-i+\omega)\, \alpha_B))\right)\right)}$$

$$F_{x1}[-\omega] \to \frac{i\, c_{A0s}\, ((i+\omega)\, (\omega + i\tau k_A \alpha_A) - \tau k_B\, (X_s\, (-i\omega + \tau k_A \alpha_A) + (1 - i\omega)\, \alpha_B))}{c_{As}\, \left((i+\omega)\, (\omega\, (i+\omega) + i\tau k_B\, (\omega X_s + (i+\omega)\, \alpha_B)) + \tau k_A \left(\tau \omega k_B X_s^2 + i\, (i+\omega)\, (\omega + (i+\omega)\, \alpha_A + i\tau k_B \alpha_B) + X_s\, ((1 - i\omega)\, \omega - \tau k_B\, (\omega + (i+\omega)\, \alpha_A - (i+\omega)\, \alpha_B))\right)\right)}$$

$$G_{x1}[-\omega] \to -\frac{i\tau^2\, c_{A0s}\, k_A\, k_B\, (-1+X_s)\, \alpha_A}{c_{As}\, \left((i+\omega)\, (\omega\, (i+\omega) + i\tau k_B\, (\omega X_s + (i+\omega)\, \alpha_B)) + \tau k_A \left(\tau \omega k_B X_s^2 + i\, (i+\omega)\, (\omega + (i+\omega)\, \alpha_A + i\tau k_B \alpha_B) + X_s\, ((1 - i\omega)\, \omega - \tau k_B\, (\omega + (i+\omega)\, \alpha_A - (i+\omega)\, \alpha_B))\right)\right)}$$

$$H_{x1}[-\omega] \to \frac{\tau\, c_{A0s}\, k_A\, (-1+X_s)\, (i+\omega + i\tau k_B X_s)\, \alpha_A}{c_{As}\, X_s\, \left((i+\omega)\, (\omega\, (i+\omega) + i\tau k_B\, (\omega X_s + (i+\omega)\, \alpha_B)) + \tau k_A \left(\tau \omega k_B X_s^2 + i\, (i+\omega)\, (\omega + (i+\omega)\, \alpha_A + i\tau k_B \alpha_B) + X_s\, ((1 - i\omega)\, \omega - \tau k_B\, (\omega + (i+\omega)\, \alpha_A - (i+\omega)\, \alpha_B))\right)\right)}$$

$$F_{z1}[u] \to -\frac{i\tau^2\, c_{B0s}\, k_A\, k_B\, X_s\, \alpha_B}{c_{Bs}\, \left((-i+u)\, (u\, (-i+u) - i\tau k_B\, (u X_s + (-i+u)\, \alpha_B)) + \tau k_A \left(u \tau k_B X_s^2 - i\, (-i+u)\, (u + (-i+u)\, \alpha_A - i\tau k_B \alpha_B) + X_s\, ((1+iu)\, u - \tau k_B\, (u + (-i+u)\, \alpha_A - (-i+u)\, \alpha_B))\right)\right)}$$

$$G_{z1}[u] \to \frac{c_{B0s}\, (-i\, (-i+u)\, (u - i\tau k_B \alpha_B) + \tau k_A\, (-u - (-i+u)\, \alpha_A + i\tau k_B \alpha_B + X_s\, (u - i\tau k_B \alpha_B)))}{c_{Bs}\, \left((-i+u)\, (u\, (-i+u) - i\tau k_B\, (u X_s + (-i+u)\, \alpha_B)) + \tau k_A \left(u \tau k_B X_s^2 - i\, (-i+u)\, (u + (-i+u)\, \alpha_A - i\tau k_B \alpha_B) + X_s\, ((1+iu)\, u - \tau k_B\, (u + (-i+u)\, \alpha_A - (-i+u)\, \alpha_B))\right)\right)}$$

$$H_{z1}[u] \to \frac{\tau\, c_{B0s}\, k_B\, (-i+u+i\tau k_A\, (-1+X_s))\, \alpha_B}{c_{Bs}\, \left((-i+u)\, (u\, (-i+u) - i\tau k_B\, (u X_s + (-i+u)\, \alpha_B)) + \tau k_A \left(u \tau k_B X_s^2 - i\, (-i+u)\, (u + (-i+u)\, \alpha_A - i\tau k_B \alpha_B) + X_s\, ((1+iu)\, u - \tau k_B\, (u + (-i+u)\, \alpha_A - (-i+u)\, \alpha_B))\right)\right)}$$

$$F_{z1}[-u] \to \frac{i\tau^2\, c_{B0s}\, k_A\, k_B\, X_s\, \alpha_B}{c_{Bs}\, \left((i+u)\, (u\, (i+u) + i\tau k_B\, (u X_s + (i+u)\, \alpha_B)) + \tau k_A \left(u \tau k_B X_s^2 + i\, (i+u)\, (u + (i+u)\, \alpha_A + i\tau k_B \alpha_B) + X_s\, ((1 - iu)\, u - \tau k_B\, (u + (i+u)\, \alpha_A - (i+u)\, \alpha_B))\right)\right)}$$

$$G_{z1}[-u] \to \frac{i\, c_{B0s}\, ((i+u)\, (u + i\tau k_B \alpha_B) + \tau k_A\, (i\, (u + (i+u)\, \alpha_A + i\tau k_B \alpha_B) + X_s\, (-iu + \tau k_B \alpha_B)))}{c_{Bs}\, \left((i+u)\, (u\, (i+u) + i\tau k_B\, (u X_s + (i+u)\, \alpha_B)) + \tau k_A \left(u \tau k_B X_s^2 + i\, (i+u)\, (u + (i+u)\, \alpha_A + i\tau k_B \alpha_B) + X_s\, ((1 - iu)\, u - \tau k_B\, (u + (i+u)\, \alpha_A - (i+u)\, \alpha_B))\right)\right)}$$

$$H_{z1}[-u] \to \frac{\tau\, c_{B0s}\, k_B\, (i+u-i\tau k_A\, (-1+X_s))\, \alpha_B}{c_{Bs}\, \left((i+u)\, (u\, (i+u) + i\tau k_B\, (u X_s + (i+u)\, \alpha_B)) + \tau k_A \left(u \tau k_B X_s^2 + i\, (i+u)\, (u + (i+u)\, \alpha_A + i\tau k_B \alpha_B) + X_s\, ((1 - iu)\, u - \tau k_B\, (u + (i+u)\, \alpha_A - (i+u)\, \alpha_B))\right)\right)}$$

Second order GFRFs

$$F_{xx2}[\omega,\omega] \to \left(\tau^2 c_{A\theta s}^2 k_A^2 (-1+X_s)\ (-i+\omega-i\tau k_B X_s)\ \alpha_A \left(-2\omega\left(-1-3i\omega+2\omega^2\right)\ (\omega-i\tau k_A\alpha_A)+\tau k_B\left(2\,(2+3i\omega)\,\omega X_s\ (\omega-i\tau k_A\alpha_A)+\left(-1-3i\omega+2\omega^2\right)\ (3i\omega+\tau k_A\alpha_A)\,\alpha_B\right)+\tau^2 k_B^2\left(2\omega X_s^2\ (\omega-i\tau k_A\alpha_A)+\omega\,(-3i+4\omega)\,X_s\,\alpha_B-i\,(-i+2\omega)\,\alpha_B\,(\tau k_A\alpha_A+(1+i\omega)\,\alpha_B)\right)\right)\right)\Big/ \left(c_{As}^2\left(-i\,(-i+\omega)\ ((1+i\omega)\,\omega+\tau k_B\,(\omega X_s+(-i+\omega)\,\alpha_B))+\tau k_A\left(\tau\omega k_B X_s^2-i\,(-i+\omega)\ (\omega+(-i+\omega)\,\alpha_A-i\tau k_B\alpha_B)+X_s\ ((1+i\omega)\,\omega-\tau k_B\,(\omega+(-i+\omega)\,\alpha_A-(-i+\omega)\,\alpha_B))\right)\right)^2\left(-i+2\omega\right)\ (2\omega\,(-i+2\omega)-i\tau k_B\,(2\omega X_s+(-i+2\omega)\,\alpha_B))+\tau k_A\left(2\tau\omega k_B X_s^2-i\,(-i+2\omega)\ (2\omega+(-i+2\omega)\,\alpha_A-i\tau k_B\alpha_B)+X_s\,(2\,(1+2i\omega)\,\omega+\tau k_B\,(-2\omega+(i-2\omega)\,\alpha_A+(-i+2\omega)\,\alpha_B))\right)\right)\right)$$

$$G_{xx2}[\omega,\omega] \to -\left(\left(\tau^3 c_{A\theta s}^2 k_A^2 k_B\ (-1+X_s)\ (1+i\omega+\tau k_B X_s)\ \alpha_A^2\left(-\left(-1-3i\omega+2\omega^2\right)\ (\omega-i\tau k_A\alpha_A)+\tau k_B\left(\tau k_A\left(2\omega-4\omega X_s+2\omega X_s^2+(-i+2\omega)\,\alpha_A\right)+(-i+2\omega)\ (2i\omega-i\omega X_s+(1+i\omega)\,\alpha_B)\right)\right)\right)\Big/ \left(c_{As}^2\left(-i\,(-i+\omega)\ ((1+i\omega)\,\omega+\tau k_B\,(\omega X_s+(-i+\omega)\,\alpha_B))+\tau k_A\left(\tau\omega k_B X_s^2-i\,(-i+\omega)\ (\omega+(-i+\omega)\,\alpha_A-i\tau k_B\alpha_B)+X_s\ ((1+i\omega)\,\omega-\tau k_B\,(\omega+(-i+\omega)\,\alpha_A-(-i+\omega)\,\alpha_B))\right)\right)^2\left(-i+2\omega\right)\ (2\omega\,(-i+2\omega)-i\tau k_B\,(2\omega X_s+(-i+2\omega)\,\alpha_B))+\tau k_A\left(2\tau\omega k_B X_s^2-i\,(-i+2\omega)\ (2\omega+(-i+2\omega)\,\alpha_A-i\tau k_B\alpha_B)+X_s\,(2\,(1+2i\omega)\,\omega+\tau k_B\,(-2\omega+(i-2\omega)\,\alpha_A+(-i+2\omega)\,\alpha_B))\right)\right)\right)\right)$$

$$H_{xx2}[\omega,\omega] \to \left(\tau^2\ (-i+2\omega)\ c_{A\theta s}^2 k_A^2\ (-1+X_s)\ (1+i\omega+\tau k_B X_s)\ \alpha_A^2\left(-i\left(-1-3i\omega+2\omega^2\right)\ (\omega-i\tau k_A\alpha_A)+\tau k_B\left(-(-2i+3\omega)\ X_s\ (\omega-i\tau k_A\alpha_A)+\left(1+3i\omega-2\omega^2\right)\alpha_B\right)+\tau^2 k_B^2\left(X_s^2\ (i\omega+\tau k_A\,(\alpha_A-\alpha_B))+(-1-2i\omega-\tau k_A)\,\alpha_B+(2+3i\omega+2\tau k_A)\,X_s\,\alpha_B\right)\right)\Big/ \left(c_{As}^2 X_s\left(-i\,(-i+\omega)\ ((1+i\omega)\,\omega+\tau k_B\,(\omega X_s+(-i+\omega)\,\alpha_B))+\tau k_A\left(\tau\omega k_B X_s^2-i\,(-i+\omega)\ (\omega+(-i+\omega)\,\alpha_A-i\tau k_B\alpha_B)+X_s\ ((1+i\omega)\,\omega-\tau k_B\,(\omega+(-i+\omega)\,\alpha_A-(-i+\omega)\,\alpha_B))\right)\right)^2\left(-i+2\omega\right)\ (2\omega\,(-i+2\omega)-i\tau k_B\,(2\omega X_s+(-i+2\omega)\,\alpha_B))+\tau k_A\left(2\tau\omega k_B X_s^2-i\,(-i+2\omega)\ (2\omega+(-i+2\omega)\,\alpha_A-i\tau k_B\alpha_B)+X_s\,(2\,(1+2i\omega)\,\omega+\tau k_B\,(-2\omega+(i-2\omega)\,\alpha_A+(-i+2\omega)\,\alpha_B))\right)\right)\right)\right)$$

$$F_{xx2}[\omega,-\omega] \to -\left(\left(\tau^3 c_{A\theta s}^2 k_A^2 k_B\ (-1+X_s)\ \alpha_A\,\alpha_B\left(k_A\left(1+\omega^2+\tau^2 k_B^2 X_s+\tau k_B\,(1+X_s)\right)\alpha_A+k_B\left(1+\omega^2+\tau k_B X_s\right)\alpha_B\right)\right)\Big/ \left(c_{As}^2\,(k_B\alpha_B+k_A\,((1+\tau k_B X_s)\,\alpha_A-\tau k_B\,(-1+X_s)\,\alpha_B))\left(i\,(-i+\omega)\ ((1+i\omega)\,\omega+\tau k_B\,(\omega X_s+(-i+\omega)\,\alpha_B))+\tau k_A\left(-\tau\omega k_B X_s^2+(-i+\omega)\ (i\omega+(1+i\omega)\,\alpha_A+\tau k_B\alpha_B)+X_s\ ((-1-i\omega)\,\omega+\tau k_B\,(\omega+(-i+\omega)\,\alpha_A-(-i+\omega)\,\alpha_B))\right)\right)\left(-(i+\omega)\ (\omega\,(i+\omega)+i\tau k_B\,(\omega X_s+(i+\omega)\,\alpha_B))+\tau k_A\left(-\tau\omega k_B X_s^2+(i+\omega)\ (-i\omega+(1-i\omega)\,\alpha_A+\tau k_B\alpha_B)+X_s\,(i\omega\,(i+\omega)+\tau k_B\,(\omega+(i+\omega)\,\alpha_A-(i+\omega)\,\alpha_B))\right)\right)\right)$$

$$G_{xx2}[\omega,-\omega] \to -\left(\left(\tau^3 c_{A\theta s}^2 k_A^2 k_B\ (-1+X_s)\ \alpha_A^2\left(k_A\left(1+\omega^2+\tau^2 k_B^2 X_s+\tau k_B\,(1+X_s)\right)\alpha_A+k_B\left(1+\omega^2+\tau k_B X_s\right)\alpha_B\right)\right)\Big/ \left(c_{As}^2\,(k_B\alpha_B+k_A\,((1+\tau k_B X_s)\,\alpha_A-\tau k_B\,(-1+X_s)\,\alpha_B))\left(i\,(-i+\omega)\ ((1+i\omega)\,\omega+\tau k_B\,(\omega X_s+(-i+\omega)\,\alpha_B))+\tau k_A\left(-\tau\omega k_B X_s^2+(-i+\omega)\ (i\omega+(1+i\omega)\,\alpha_A+\tau k_B\alpha_B)+X_s\ ((-1-i\omega)\,\omega+\tau k_B\,(\omega+(-i+\omega)\,\alpha_A-(-i+\omega)\,\alpha_B))\right)\right)\left(-(i+\omega)\ (\omega\,(i+\omega)+i\tau k_B\,(\omega X_s+(i+\omega)\,\alpha_B))+\tau k_A\left(-\tau\omega k_B X_s^2+(i+\omega)\ (-i\omega+(1-i\omega)\,\alpha_A+\tau k_B\alpha_B)+X_s\,(i\omega\,(i+\omega)+\tau k_B\,(\omega+(i+\omega)\,\alpha_A-(i+\omega)\,\alpha_B))\right)\right)\right)$$

$$H_{xx2}[\omega,-\omega] \to \left(\tau^2 c_{A\theta s}^2 k_A^2\ (-1+X_s)\ (1+\tau k_B X_s)\ \alpha_A^2\left(k_B\left(1+\omega^2+\tau k_B\,(-1+2X_s)\right)\alpha_B+k_A\left(\left(1+\omega^2+2\tau k_B X_s+\tau^2 k_B^2 X_s^2\right)\alpha_A-\tau^2 k_B^2\,(-1+X_s)^2\,\alpha_B\right)\right)\Big/ \left(c_{As}^2\,X_s\,(k_B\alpha_B+k_A\,((1+\tau k_B X_s)\,\alpha_A-\tau k_B\,(-1+X_s)\,\alpha_B))\left(-i\,(-i+\omega)\ ((1+i\omega)\,\omega+\tau k_B\,(\omega X_s+(-i+\omega)\,\alpha_B))+\tau k_A\left(\tau\omega k_B X_s^2-i\,(-i+\omega)\ (\omega+(-i+\omega)\,\alpha_A-i\tau k_B\alpha_B)+X_s\ ((1+i\omega)\,\omega-\tau k_B\,(\omega+(-i+\omega)\,\alpha_A-(-i+\omega)\,\alpha_B))\right)\right)\left((i+\omega)\ (\omega\,(i+\omega)+i\tau k_B\,(\omega X_s+(i+\omega)\,\alpha_B))+\tau k_A\left(\tau\omega k_B X_s^2+i\,(i+\omega)\ (\omega+(i+\omega)\,\alpha_A+i\tau k_B\alpha_B)+X_s\,((1-i\omega)\,\omega-\tau k_B\,(\omega+(i+\omega)\,\alpha_A-(i+\omega)\,\alpha_B))\right)\right)\right)$$

$$F_{xx2}[-\omega,\omega] \to -\left(\left(\tau^3 c_{A\theta s}^2 k_A^2 k_B\ (-1+X_s)\ \alpha_A\,\alpha_B\left(k_A\left(1+\omega^2+\tau^2 k_B^2 X_s+\tau k_B\,(1+X_s)\right)\alpha_A+k_B\left(1+\omega^2+\tau k_B X_s\right)\alpha_B\right)\right)\Big/ \left(c_{As}^2\,(k_B\alpha_B+k_A\,((1+\tau k_B X_s)\,\alpha_A-\tau k_B\,(-1+X_s)\,\alpha_B))\left(i\,(-i+\omega)\ ((1+i\omega)\,\omega+\tau k_B\,(\omega X_s+(-i+\omega)\,\alpha_B))+\tau k_A\left(-\tau\omega k_B X_s^2+(-i+\omega)\ (i\omega+(1+i\omega)\,\alpha_A+\tau k_B\alpha_B)+X_s\ ((-1-i\omega)\,\omega+\tau k_B\,(\omega+(-i+\omega)\,\alpha_A-(-i+\omega)\,\alpha_B))\right)\right)\left(-(i+\omega)\ (\omega\,(i+\omega)+i\tau k_B\,(\omega X_s+(i+\omega)\,\alpha_B))+\tau k_A\left(-\tau\omega k_B X_s^2+(i+\omega)\ (-i\omega+(1-i\omega)\,\alpha_A+\tau k_B\alpha_B)+X_s\,(i\omega\,(i+\omega)+\tau k_B\,(\omega+(i+\omega)\,\alpha_A-(i+\omega)\,\alpha_B))\right)\right)\right)$$

$$G_{xx2}[-\omega,\omega] \to -\left(\left(\tau^3 c_{A\theta s}^2 k_A^2 k_B\ (-1+X_s)\ \alpha_A^2\left(k_A\left(1+\omega^2+\tau^2 k_B^2 X_s+\tau k_B\,(1+X_s)\right)\alpha_A+k_B\left(1+\omega^2+\tau k_B X_s\right)\alpha_B\right)\right)\Big/ \left(c_{As}^2\,(k_B\alpha_B+k_A\,((1+\tau k_B X_s)\,\alpha_A-\tau k_B\,(-1+X_s)\,\alpha_B))\left(i\,(-i+\omega)\ ((1+i\omega)\,\omega+\tau k_B\,(\omega X_s+(-i+\omega)\,\alpha_B))+\tau k_A\left(-\tau\omega k_B X_s^2+(-i+\omega)\ (i\omega+(1+i\omega)\,\alpha_A+\tau k_B\alpha_B)+X_s\ ((-1-i\omega)\,\omega+\tau k_B\,(\omega+(-i+\omega)\,\alpha_A-(-i+\omega)\,\alpha_B))\right)\right)\left(-(i+\omega)\ (\omega\,(i+\omega)+i\tau k_B\,(\omega X_s+(i+\omega)\,\alpha_B))+\tau k_A\left(-\tau\omega k_B X_s^2+(i+\omega)\ (-i\omega+(1-i\omega)\,\alpha_A+\tau k_B\alpha_B)+X_s\,(i\omega\,(i+\omega)+\tau k_B\,(\omega+(i+\omega)\,\alpha_A-(i+\omega)\,\alpha_B))\right)\right)\right)$$

$$H_{xx2}[-\omega,\omega] \to \left(\tau^2 c_{A\theta s}^2 k_A^2\ (-1+X_s)\ (1+\tau k_B X_s)\ \alpha_A^2\left(k_B\left(1+\omega^2+\tau k_B\,(-1+2X_s)\right)\alpha_B+k_A\left(\left(1+\omega^2+2\tau k_B X_s+\tau^2 k_B^2 X_s^2\right)\alpha_A-\tau^2 k_B^2\,(-1+X_s)^2\,\alpha_B\right)\right)\Big/ \left(c_{As}^2\,X_s\,(k_B\alpha_B+k_A\,((1+\tau k_B X_s)\,\alpha_A-\tau k_B\,(-1+X_s)\,\alpha_B))\left(-i\,(-i+\omega)\ ((1+i\omega)\,\omega+\tau k_B\,(\omega X_s+(-i+\omega)\,\alpha_B))+\tau k_A\left(\tau\omega k_B X_s^2-i\,(-i+\omega)\ (\omega+(-i+\omega)\,\alpha_A-i\tau k_B\alpha_B)+X_s\ ((1+i\omega)\,\omega-\tau k_B\,(\omega+(-i+\omega)\,\alpha_A-(-i+\omega)\,\alpha_B))\right)\right)\left((i+\omega)\ (\omega\,(i+\omega)+i\tau k_B\,(\omega X_s+(i+\omega)\,\alpha_B))+\tau k_A\left(\tau\omega k_B X_s^2+i\,(i+\omega)\ (\omega+(i+\omega)\,\alpha_A+i\tau k_B\alpha_B)+X_s\,((1-i\omega)\,\omega-\tau k_B\,(\omega+(i+\omega)\,\alpha_A-(i+\omega)\,\alpha_B))\right)\right)\right)$$

$$F_{zz2}[u,-u] \to -\left(\left(\tau^3 c_{B\theta s}^2 k_A k_B^2 X_s\,\alpha_B^2\left(-\left(1+u^2\right)k_A\,\alpha_A-\left(1+u^2\right)k_B\,\alpha_B+\tau k_A k_B\,(-2+X_s)\,\alpha_B+\tau k_A^2\,(-1+X_s)\,(\alpha_A+\tau k_B\alpha_B)\right)\right)\Big/ \left(c_{Bs}^2\,(k_B\alpha_B+k_A\,((1+\tau k_B X_s)\,\alpha_A-\tau k_B\,(-1+X_s)\,\alpha_B))\left(-(-i+u)\ (u\,(-i+u)-i\tau k_B\,(u X_s+(-i+u)\,\alpha_B))+\tau k_A\left(-u\tau k_B X_s^2+(-i+u)\ (i\,u+(1+i\,u)\,\alpha_A+\tau k_B\alpha_B)+X_s\ ((-1-i\,u)\,u+\tau k_B\,(u+(-i+u)\,\alpha_A-(-i+u)\,\alpha_B))\right)\right)\left(-(i+u)\ (u\,(i+u)+i\tau k_B\,(u X_s+(i+u)\,\alpha_B))+\tau k_A\left(-u\tau k_B X_s^2+(i+u)\ (-i\,u+(1-i\,u)\,\alpha_A+\tau k_B\alpha_B)+X_s\,(i\,u\,(i+u)+\tau k_B\,(u+(i+u)\,\alpha_A-(i+u)\,\alpha_B))\right)\right)\right)$$

$$G_{zz2}[u,-u] \to -\left(\left(\tau^3 c_{B\theta s}^2 k_A k_B^2 X_s\,\alpha_A\,\alpha_B\left(-\left(1+u^2\right)k_A\,\alpha_A-\left(1+u^2\right)k_B\,\alpha_B+\tau k_A k_B\,(-2+X_s)\,\alpha_B+\tau k_A^2\,(-1+X_s)\,(\alpha_A+\tau k_B\alpha_B)\right)\right)\Big/ \left(c_{Bs}^2\,(k_B\alpha_B+k_A\,((1+\tau k_B X_s)\,\alpha_A-\tau k_B\,(-1+X_s)\,\alpha_B))\left(-(-i+u)\ (u\,(-i+u)-i\tau k_B\,(u X_s+(-i+u)\,\alpha_B))+\tau k_A\left(-u\tau k_B X_s^2+(-i+u)\ (i\,u+(1+i\,u)\,\alpha_A+\tau k_B\alpha_B)+X_s\ ((-1-i\,u)\,u+\tau k_B\,(u+(-i+u)\,\alpha_A-(-i+u)\,\alpha_B))\right)\right)\left(-(i+u)\ (u\,(i+u)+i\tau k_B\,(u X_s+(i+u)\,\alpha_B))+\tau k_A\left(-u\tau k_B X_s^2+(i+u)\ (-i\,u+(1-i\,u)\,\alpha_A+\tau k_B\alpha_B)+X_s\,(i\,u\,(i+u)+\tau k_B\,(u+(i+u)\,\alpha_A-(i+u)\,\alpha_B))\right)\right)\right)$$

$$H_{zz2}[u,-u] \to -\left(\left(\tau^2 c_{B\theta s}^2 k_B^2\ (-1+\tau k_A\,(-1+X_s))\ \alpha_B^2\left(\left(1+u^2\right)k_B\,\alpha_B+k_A\left(\left(1+u^2\right)\alpha_A-2\tau k_B\,(-1+X_s)\,\alpha_B\right)+\tau k_A^2\left(-\left(-1+2X_s+\tau k_B X_s^2\right)\alpha_A+\tau k_B\,(-1+X_s)^2\,\alpha_B\right)\right)\right)\Big/ \left(c_{Bs}^2\,(k_B\alpha_B+k_A\,((1+\tau k_B X_s)\,\alpha_A-\tau k_B\,(-1+X_s)\,\alpha_B))\left(-(-i+u)\ (u\,(-i+u)-i\tau k_B\,(u X_s+(-i+u)\,\alpha_B))+\tau k_A\left(-u\tau k_B X_s^2+(-i+u)\ (i\,u+(1+i\,u)\,\alpha_A+\tau k_B\alpha_B)+X_s\ ((-1-i\,u)\,u+\tau k_B\,(u+(-i+u)\,\alpha_A-(-i+u)\,\alpha_B))\right)\right)\left(-(i+u)\ (u\,(i+u)+i\tau k_B\,(u X_s+(i+u)\,\alpha_B))+\tau k_A\left(-u\tau k_B X_s^2+(i+u)\ (-i\,u+(1-i\,u)\,\alpha_A+\tau k_B\alpha_B)+X_s\,(i\,u\,(i+u)+\tau k_B\,(u+(i+u)\,\alpha_A-(i+u)\,\alpha_B))\right)\right)\right)$$

$$F_{zz2}[-u,u] \to -\Big(\Big(\tau^3 c_{B0s}^2 k_A k_B^2 X_s \alpha_B^2\Big(-\big(1+u^2\big) k_A \alpha_A - \big(1+u^2\big) k_B \alpha_B + \tau k_A k_B (-2+X_s)\alpha_B + \tau k_A^2 (-1+X_s)(\alpha_A + \tau k_B \alpha_B)\Big)\Big)\Big/\Big(c_{Bs}^2 (k_B \alpha_B + k_A ((1+\tau k_B X_s)\alpha_A - \tau k_B (-1+X_s)\alpha_B)) \Big(-(-i+u)(u(-i+u) - i\tau k_B (u X_s + (-i+u)\alpha_B)) + \tau k_A\Big(-u\tau k_B X_s^2 + (-i+u)(i u + (1+i u)\alpha_A + \tau k_B \alpha_B) + X_s((-1-i u)u + \tau k_B (u+(-i+u)\alpha_A - (-i+u)\alpha_B))\Big)\Big)\Big(-(i+u)(u(i+u) + i\tau k_B (u X_s + (i+u)\alpha_B)) + \tau k_A\Big(-u\tau k_B X_s^2 + (i+u)(-i u + (1-i u)\alpha_A + \tau k_B \alpha_B) + X_s(i u(i+u) + \tau k_B (u+(i+u)\alpha_A - (i+u)\alpha_B))\Big)\Big)\Big)$$

$$G_{zz2}[-u,u] \to -\Big(\Big(\tau^3 c_{B0s}^2 k_A k_B^2 X_s \alpha_A \alpha_B\Big(-\big(1+u^2\big) k_A \alpha_A - \big(1+u^2\big) k_B \alpha_B + \tau k_A k_B (-2+X_s)\alpha_B + \tau k_A^2 (-1+X_s)(\alpha_A + \tau k_B \alpha_B)\Big)\Big)\Big/\Big(c_{Bs}^2 (k_B \alpha_B + k_A ((1+\tau k_B X_s)\alpha_A - \tau k_B (-1+X_s)\alpha_B)) \Big(-(-i+u)(u(-i+u) - i\tau k_B (u X_s + (-i+u)\alpha_B)) + \tau k_A\Big(-u\tau k_B X_s^2 + (-i+u)(i u + (1+i u)\alpha_A + \tau k_B \alpha_B) + X_s((-1-i u)u + \tau k_B (u+(-i+u)\alpha_A - (-i+u)\alpha_B))\Big)\Big)\Big(-(i+u)(u(i+u) + i\tau k_B (u X_s + (i+u)\alpha_B)) + \tau k_A\Big(-u\tau k_B X_s^2 + (i+u)(-i u + (1-i u)\alpha_A + \tau k_B \alpha_B) + X_s(i u(i+u) + \tau k_B (u+(i+u)\alpha_A - (i+u)\alpha_B))\Big)\Big)\Big)$$

$$H_{zz2}[-u,u] \to -\Big(\Big(\tau^2 c_{B0s}^2 k_B^2 (-1+\tau k_A (-1+X_s))\alpha_B^2\Big(\big(1+u^2\big) k_B \alpha_B + k_A\Big(\big(1+u^2\big)\alpha_A - 2\tau k_B (-1+X_s)\alpha_B\Big) + \tau k_A^2\Big(-\big(-1+2X_s+\tau k_B X_s^2\big)\alpha_A + \tau k_B (-1+X_s)^2 \alpha_B\Big)\Big)\Big)\Big/\Big(c_{Bs}^2 (k_B \alpha_B + k_A ((1+\tau k_B X_s)\alpha_A - \tau k_B (-1+X_s)\alpha_B)) \Big(-(-i+u)(u(-i+u) - i\tau k_B (u X_s + (-i+u)\alpha_B)) + \tau k_A\Big(-u\tau k_B X_s^2 + (-i+u)(i u + (1+i u)\alpha_A + \tau k_B \alpha_B) + X_s((-1-i u)u + \tau k_B (u+(-i+u)\alpha_A - (-i+u)\alpha_B))\Big)\Big)\Big(-(i+u)(u(i+u) + i\tau k_B (u X_s + (i+u)\alpha_B)) + \tau k_A\Big(-u\tau k_B X_s^2 + (i+u)(-i u + (1-i u)\alpha_A + \tau k_B \alpha_B) + X_s(i u(i+u) + \tau k_B (u+(i+u)\alpha_A - (i+u)\alpha_B))\Big)\Big)\Big)$$

$$F_{zz2}[u,u] \to -\Big(\Big(\tau^3 c_{B0s}^2 k_A k_B^2 (-1-i u+\tau k_A (-1+X_s)) X_s \alpha_B^2\Big(-\big(-1-3i u+2u^2\big)(u - i\tau k_B \alpha_B) + \tau k_A\Big((1+2i u) u X_s + 2u\tau k_B X_s^2 + (-i+2u)(i u + \alpha_A + i u\alpha_A + \tau k_B \alpha_B)\Big)\Big)\Big)\Big/$$
$$\Big(c_{Bs}^2\Big((-i+u)(u(-i+u) - i\tau k_B (u X_s + (-i+u)\alpha_B)) + \tau k_A\Big(u\tau k_B X_s^2 - i(-i+u)(u + (-i+u)\alpha_A - i\tau k_B \alpha_B) + X_s((1+i u)u - \tau k_B (u+(-i+u)\alpha_A - (-i+u)\alpha_B))\Big)\Big)^2\Big((-i+2u)(2u(-i+2u) - i\tau k_B (2u X_s + (-i+2u)\alpha_B)) + \tau k_A\Big(2u\tau k_B X_s^2 - i(-i+2u)(2u + (-i+2u)\alpha_A - i\tau k_B \alpha_B) + X_s(2(1+2i u)u + \tau k_B (-2u + (i-2u)\alpha_A + (-i+2u)\alpha_B))\Big)\Big)\Big)$$

$$G_{zz2}[u,u] \to \Big(\tau^2 c_{B0s}^2 k_B^2 (-i+u+i\tau k_A (-1+X_s)) X_s \alpha_B\Big(2u\big(-1-3i u+2u^2\big)(u - i\tau k_B \alpha_B) + \tau^2 k_A^2\Big(-2u X_s^2 (u - i\tau k_B \alpha_B) - (2u+(-i+2u)\alpha_A)(u + (-i+u)\alpha_A - i\tau k_B \alpha_B) + u X_s((-3i+4u)\alpha_A + 4(u - i\tau k_B \alpha_B))\Big) + \tau k_A\Big(2(2+3i u) u X_s (u - i\tau k_B \alpha_B) - i\Big(2u(-2i+3u)(u - i\tau k_B \alpha_B) + \big(-1-3i u+2u^2\big)\alpha_A (3u - i\tau k_B \alpha_B)\Big)\Big)\Big)\Big/$$
$$\Big(c_{Bs}^2\Big((-i+u)(u(-i+u) - i\tau k_B (u X_s + (-i+u)\alpha_B)) + \tau k_A\Big(u\tau k_B X_s^2 - i(-i+u)(u + (-i+u)\alpha_A - i\tau k_B \alpha_B) + X_s((1+i u)u - \tau k_B (u+(-i+u)\alpha_A - (-i+u)\alpha_B))\Big)\Big)^2\Big((-i+2u)(2u(-i+2u) - i\tau k_B (2u X_s + (-i+2u)\alpha_B)) + \tau k_A\Big(2u\tau k_B X_s^2 - i(-i+2u)(2u + (-i+2u)\alpha_A - i\tau k_B \alpha_B) + X_s(2(1+2i u)u + \tau k_B (-2u + (i-2u)\alpha_A + (-i+2u)\alpha_B))\Big)\Big)\Big)$$

$$H_{zz2}[u,u] \to \Big((-i+2u)\tau^2 c_{B0s}^2 k_B^2 (-i+u+i\tau k_A (-1+X_s))\alpha_B^2\Big(\big(-1-3i u+2u^2\big)(u - i\tau k_B \alpha_B) + i\tau k_A\Big(\big(1+3i u-2u^2\big)\alpha_A - (-2i+3u)(u - i\tau k_B \alpha_B) + (-2i+3u) X_s (u - i\tau k_B \alpha_B)\Big) - \tau^2 k_A^2\Big(u + (-i+u)\alpha_A + X_s^2 (u + i\tau k_B (\alpha_A - \alpha_B)) - i\tau k_B \alpha_B + X_s(-2u + (2i-3u)\alpha_A + 2i\tau k_B \alpha_B)\Big)\Big)\Big)\Big/$$
$$\Big(c_{Bs}^2\Big((-i+u)(u(-i+u) - i\tau k_B (u X_s + (-i+u)\alpha_B)) + \tau k_A\Big(u\tau k_B X_s^2 - i(-i+u)(u + (-i+u)\alpha_A - i\tau k_B \alpha_B) + X_s((1+i u)u - \tau k_B (u+(-i+u)\alpha_A - (-i+u)\alpha_B))\Big)\Big)^2\Big((-i+2u)(2u(-i+2u) - i\tau k_B (2u X_s + (-i+2u)\alpha_B)) + \tau k_A\Big(2u\tau k_B X_s^2 - i(-i+2u)(2u + (-i+2u)\alpha_A - i\tau k_B \alpha_B) + X_s(2(1+2i u)u + \tau k_B (-2u + (i-2u)\alpha_A + (-i+2u)\alpha_B))\Big)\Big)\Big)$$

$$F_{xz2}[\omega,u] \to$$
$$\Big(\tau^2 c_{A0s} c_{B0s} k_A k_B \alpha_B\Big(\tau^3 (u+\omega) k_A k_B^2 X_s^4 (i\omega + 2\tau k_A \alpha_A) + \tau(-i+\omega)(-i+u+\omega) k_A \alpha_A (\tau k_A (u+(-i+u)\alpha_A - i\tau k_B \alpha_B) + (-i+u)(i u + \tau k_B \alpha_B)) + \tau^2 k_B X_s^3\Big((-i+u)\omega(u+\omega) k_B + \tau k_A^2\Big(i u^2 + u(3+5i\omega) + 4(1+i\omega) - 2\tau(u+\omega) k_B\Big)\alpha_A - k_A\Big(\omega\big(u^2 + 2\omega(-i+\omega) + u(-2i+3\omega)\big) + i\tau k_B (\omega(u+\omega) + (-i+u)(u+\omega)\alpha_A + (u(i-2\omega) - 2\omega(-i+\omega))\alpha_B)\Big)\Big) +$$
$$\tau X_s^2\Big((-i+u) k_B\Big(\omega\Big(i u^2 + u(2+3i\omega) + 2(1+i\omega)\omega\Big) + \tau(2\omega(-i+\omega) + u(-i+2\omega)) k_B \alpha_B\Big) + \tau k_A^2 \alpha_A\Big(-(-i+\omega)\big(u^2 + 2\omega(-i+\omega) + u(-i+3\omega)\big) + 2\tau^2 (-i+u+\omega) k_B^2 \alpha_B + \tau k_B\Big(-2u - 4\omega - 4i u\omega - 4i\omega^2 + (1+i u)(-i+u+\omega)\alpha_A + (1+i\omega)(-i+u+\omega)\alpha_B\Big)\Big) +$$
$$k_A\Big(-i\omega(-i+\omega)\big(u^2 + \omega(-i+\omega) + u(-i+2\omega)\big) + \tau^2 k_B^2 \alpha_B\Big(-u - 2\omega - 2i u\omega - 2i\omega^2 + (1+i u)(-i+u+\omega)\alpha_A + (1+i\omega)(-i+u+\omega)\alpha_B\Big) + \tau k_B\Big(\omega\big(u^2 + 2\omega(-i+\omega) + u(-2i+3\omega)\big) + (-i+u)(2\omega(-i+\omega) + u(-i+2\omega))\alpha_A - (-i+\omega)\big(u^2 + 2\omega(-i+\omega) + u(-i+3\omega)\big)\alpha_B\Big)\Big) -$$
$$(-i+u+\omega) X_s\Big((-i+u)(-i+\omega)(\omega - i\tau k_B \alpha_B)(u+\omega - i\tau k_B \alpha_B) + \tau^2 k_A^2 \alpha_A\Big(\tau k_B (i u + (1+i u)\alpha_A) - (-i+\omega)(2\omega - (-i+u)\alpha_A) + 2\tau^2 k_B^2 \alpha_B\Big) - \tau k_A\Big((-i+\omega)(u+\omega - i\tau k_B \alpha_B)(i\omega + \tau k_B \alpha_B) + (-i+u)\alpha_A\big(\omega + i\omega^2 + u\tau k_B - 2i\tau^2 k_B^2 \alpha_B\big)\Big)\Big)\Big)\Big/$$
$$\Big(c_{As} c_{Bs}\Big((-i+u)(u(-i+u) - i\tau k_B (u X_s + (-i+u)\alpha_B)) + \tau k_A\Big(u\tau k_B X_s^2 - i(-i+u)(u + (-i+u)\alpha_A - i\tau k_B \alpha_B) + X_s((1+i u)u - \tau k_B (u+(-i+u)\alpha_A - (-i+u)\alpha_B))\Big)\Big)\Big(-i(-i+\omega)\big((1+i\omega)\omega + \tau k_B (\omega X_s + (-i+\omega)\alpha_B)\big) + \tau k_A\Big(\tau\omega k_B X_s^2 - i(-i+\omega)(\omega + (-i+\omega)\alpha_A - i\tau k_B \alpha_B) + X_s((1+i\omega)\omega - \tau k_B (\omega + (-i+\omega)\alpha_A - (-i+\omega)\alpha_B))\Big)\Big)$$
$$\Big((-i+u+\omega)\big(u^2 + \omega(-i+\omega) + u(-i+2\omega) - i\tau k_B ((u+\omega) X_s + (-i+u+\omega)\alpha_B)\big) + \tau k_A\Big(\tau(u+\omega) k_B X_s^2 - i(-i+u+\omega)(u+\omega+(-i+u+\omega)\alpha_A - i\tau k_B \alpha_B) + X_s\big(u i u^2 + \omega + 2i u\omega + i\omega^2 - \tau k_B (u+\omega+(-i+u+\omega)\alpha_A - (-i+u+\omega)\alpha_B)\big)\Big)\Big)\Big)$$

$$G_{xz2}[\omega,u] \to -\Big(\Big(i\tau^2 c_{A0s} c_{B0s} k_A k_B \alpha_A\Big((-i+u)(-i+u+\omega)\Big(-i(-i+\omega)(u+\omega)(u - i\tau k_B \alpha_B) + \tau k_B X_s^2 (u(u+\omega) - i\tau(2u+\omega) k_B \alpha_B) + X_s\Big(u(1+i\omega)(u+\omega) + \tau^2 k_B^2 \alpha_B (2i(u+\omega) + (1+i\omega)\alpha_B) - u\tau k_B (u+\omega-(-i+\omega)\alpha_B)\Big)\Big) + \tau k_A\Big(\tau k_B X_s^3\Big(u\big(2i u^2 + u(2+3i\omega) + (2+i\omega)\omega\big) + \tau\big(4u^2 + \omega(-3i+\omega) + u(-4i+5\omega)\big) k_B \alpha_B\Big) -$$
$$X_s^2\Big(u(-i+\omega)\big(2u^2 + \omega(-2i+\omega) + u(-2i+3\omega)\big) + \tau^2 k_B^2 \alpha_B\big(-8i u + 8u^2 - 7i\omega + 11u\omega + 3\omega^2 + (-i+u)(-i+u+\omega)\alpha_A + (-i+\omega)(-i+u+\omega)\alpha_B\big) + i\tau k_B\Big(2u\big(2u^2 + \omega(-2i+\omega) + u(-2i+3\omega)\big) + (-i+u)\big(2u^2 + \omega(-i+\omega) + u(-2i+3\omega)\big)\alpha_A - (-i+\omega)\big(2u^2 - i\omega + 2u(-i+\omega)\big)\alpha_B\Big)\Big) +$$
$$X_s\Big(-i+\omega)\Big(2u\big(2u^2 + \omega(-2i+\omega) + u(-2i+3\omega)\big) + (-i+u)\big(2u^2 + \omega(-i+\omega) + u(-2i+3\omega)\big)\alpha_A\Big) + \tau^2 k_B^2 \alpha_B\big(4u^2 + 2\omega(-2i+\omega) + 2u(-2i+3\omega) + 2(-i+u)(-i+u+\omega)\alpha_A + (-i+\omega)(-i+u+\omega)\alpha_B\big) + i\tau k_B\Big(u\big(2u^2 + \omega(-2i+\omega) + u(-2i+3\omega)\big) + (-i+u)\big(2u^2 + \omega(-i+\omega) + u(-2i+3\omega)\big)\alpha_A - (-i+\omega)\big(4u^2 + \omega(-3i+\omega) + u(-4i+5\omega)\big)\alpha_B\Big) -$$
$$(-i+\omega)\Big(\big(2u^2 + \omega(-2i+\omega) + u(-2i+3\omega)\big)(u - i\tau k_B \alpha_B) + (-i+u)(-i+u+\omega)\alpha_A (2u+\omega - i\tau k_B \alpha_B)\Big) - \tau^2 k_A^2 (-1+X_s)\Big(\tau(u+\omega) k_B X_s^3 (u - 2i\tau k_B \alpha_B) + (-i+\omega)(u+\omega+(-i+u+\omega)\alpha_A)(i u + (1+i u)\alpha_A + \tau k_B \alpha_B) +$$
$$X_s^2\Big(u(1+i\omega)(u+\omega) + 4i\tau^2 (u+\omega) k_B^2 \alpha_B + \tau k_B\Big(\big(-2u^2 + i\omega - 2u(-i+\omega)\big)\alpha_A - (u+\omega)(2u - (-i+\omega)\alpha_B)\Big) - i X_s\Big((-i+\omega)\Big(2u(u+\omega) + \big(2u^2 - i\omega + 2u(-i+\omega)\big)\alpha_A\Big) + 2\tau^2 k_B^2 (u+\omega+(-i+u+\omega)\alpha_A)\alpha_B + i\tau k_B\Big((-i+u)(-i+u+\omega)\alpha_A^2 + (u+\omega)(u - 2(-i+\omega)\alpha_B) + \alpha_A\big(2u^2 - i\omega + 2u(-i+\omega) + (-i+\omega)(-i+u+\omega)\alpha_B\big)\Big)\Big)\Big)\Big)\Big/$$
$$\Big(c_{As} c_{Bs}\Big((-i+u)(u(-i+u) - i\tau k_B (u X_s + (-i+u)\alpha_B)) + \tau k_A\Big(u\tau k_B X_s^2 - i(-i+u)(u + (-i+u)\alpha_A - i\tau k_B \alpha_B) + X_s((1+i u)u - \tau k_B (u+(-i+u)\alpha_A - (-i+u)\alpha_B))\Big)\Big)\Big(-i(-i+\omega)\big((1+i\omega)\omega + \tau k_B (\omega X_s + (-i+\omega)\alpha_B)\big) + \tau k_A\Big(\tau\omega k_B X_s^2 - i(-i+\omega)(\omega + (-i+\omega)\alpha_A - i\tau k_B \alpha_B) + X_s((1+i\omega)\omega - \tau k_B (\omega + (-i+\omega)\alpha_A - (-i+\omega)\alpha_B))\Big)\Big)$$
$$\Big((-i+u+\omega)\big(u^2 + \omega(-i+\omega) + u(-i+2\omega) - i\tau k_B ((u+\omega) X_s + (-i+u+\omega)\alpha_B)\big) + \tau k_A\Big(\tau(u+\omega) k_B X_s^2 - i(-i+u+\omega)(u+\omega+(-i+u+\omega)\alpha_A - i\tau k_B \alpha_B) + X_s\big(u i u^2 + \omega + 2i u\omega + i\omega^2 - \tau k_B (u+\omega+(-i+u+\omega)\alpha_A - (-i+u+\omega)\alpha_B)\big)\Big)\Big)\Big)$$

$$H_{xz2}[\omega,u] \to -\Big(\Big(i\tau^2 (-i+u+\omega) c_{A0s} c_{B0s} k_A k_B \alpha_A \alpha_B\Big((1+i u)\Big(-\tau^2 \omega k_B^2 X_s^3 - (-i+\omega)(-i+u+\omega)(u - i\tau k_B \alpha_B) - \tau k_B X_s^2\Big(u + i u^2 + 2i u\omega + 2(1+i\omega)\omega + \tau(-3i+2u+3\omega) k_B \alpha_B\Big) + (-i+u-\tau) X_s\Big((-i+\omega)(u+\omega) + 2\tau^2 k_B^2 \alpha_B + i\tau k_B (u - 2(-i+\omega)\alpha_B)\Big)\Big) -$$
$$\tau^2 k_A^2 (-1+X_s)\Big(\tau k_B X_s^3 (u+2i\tau k_B (\alpha_A - \alpha_B)) + (-i+\omega)(i u + (1+i u)\alpha_A + \tau k_B \alpha_B) + X_s\Big(-i(-i+\omega)(2u + (-3i+3u+2\omega)\alpha_A) - 2i\tau^2 k_B^2 \alpha_B + \tau k_B (u+(-i+u)\alpha_A - 2(-i+\omega)\alpha_B)\Big) + X_s^2\Big(u+i u\omega+4i\tau^2 k_B^2 \alpha_B + \tau k_B (-2u + (5i-3u-4\omega)\alpha_A + (-i+\omega)\alpha_B)\Big)\Big) +$$
$$\tau k_A\Big(\tau^2 \omega k_B^2 X_s^4 - X_s^2\Big((-i+\omega)\big(2u^2 + 2u(-i+\omega) + \omega(-i+\omega)\big) + \tau^2 (-9i+8u+5\omega) k_B^2 \alpha_B + \tau k_B\big(4u+4i u^2 + 2\omega + 3i u\omega + 2i\omega^2 + (-i+u)(3+2i u+3i\omega)\alpha_A - i(-i+\omega)(-3i+3u+2\omega)\alpha_B\big) + \tau k_B X_s^3\Big(2i\big(u^2 + u(-i+\omega) + \omega(-i+\omega)\big) + \tau k_B (-\omega - (-i+u)\alpha_A + (-5i+4u+3\omega)\alpha_B)\Big) +$$
$$X_s\Big((-i+\omega)\big(4u^2 + \omega(-i+\omega) + u(-4i+3\omega) + 2(-i+u)(-i+u+\omega)\alpha_A\big) + 2\tau^2 (-2i+2u+\omega) k_B^2 \alpha_B + i\tau k_B (u(-2i+2u+\omega) + (-i+u)(-i+u+\omega)\alpha_A - (-i+\omega)(-5i+5u+3\omega)\alpha_B)\Big) - (-i+\omega)\big((-i+u)(-i+u+\omega)\alpha_A + (-2i+2u+\omega)(u - i\tau k_B \alpha_B)\big)\Big)\Big)\Big/$$
$$\Big(c_{As} c_{Bs} X_s\Big((-i+u)(u(-i+u) - i\tau k_B (u X_s + (-i+u)\alpha_B)) + \tau k_A\Big(u\tau k_B X_s^2 - i(-i+u)(u + (-i+u)\alpha_A - i\tau k_B \alpha_B) + X_s((1+i u)u - \tau k_B (u+(-i+u)\alpha_A - (-i+u)\alpha_B))\Big)\Big)\Big(-i(-i+\omega)\big((1+i\omega)\omega + \tau k_B (\omega X_s + (-i+\omega)\alpha_B)\big) + \tau k_A\Big(\tau\omega k_B X_s^2 - i(-i+\omega)(\omega + (-i+\omega)\alpha_A - i\tau k_B \alpha_B) + X_s((1+i\omega)\omega - \tau k_B (\omega + (-i+\omega)\alpha_A - (-i+\omega)\alpha_B))\Big)\Big)$$
$$\Big((-i+u+\omega)\big(u^2 + \omega(-i+\omega) + u(-i+2\omega) - i\tau k_B ((u+\omega) X_s + (-i+u+\omega)\alpha_B)\big) + \tau k_A\Big(\tau(u+\omega) k_B X_s^2 - i(-i+u+\omega)(u+\omega+(-i+u+\omega)\alpha_A - i\tau k_B \alpha_B) + X_s\big(u i u^2 + \omega + 2i u\omega + i\omega^2 - \tau k_B (u+\omega+(-i+u+\omega)\alpha_A - (-i+u+\omega)\alpha_B)\big)\Big)\Big)\Big)$$

$$F_{xz2}[\omega, -u] \to \Big(\tau^2 c_{A0s} c_{B0s} k_A k_B \sigma_B \Big(-\tau^3 (u-\omega) k_A k_B^2 X_s^4 (i\omega + 2\tau k_A \sigma_A) + \tau (i+u-\omega)(-i+\omega) k_A \sigma_A (\tau k_A (u + (i+u)\sigma_A + i\tau k_B \sigma_B) + (i+u)(-iu+\tau k_B \sigma_B)) - i\tau X_s^2 \Big((i+u) k_B \Big(\omega\big(u^2 + u(2i-3)\omega + 2\omega(-i+\omega)\big) + \tau(u+2iu\omega-2i\omega(-i+\omega))k_B\sigma_B\Big) + \tau k_A^2\sigma_A\Big((-i+\omega)\big(u-iu^2+3iu\omega-2i\omega(-i+\omega)\big) + 2\tau^2(1-iu+i\omega)k_B^2\sigma_B + \tau k_B\big(2iu-4i\omega-4u\omega+4\omega^2-(i+u)(i+u-\omega)\sigma_A + (i+u-\omega)(-i+\omega)\sigma_B\big)\Big) + k_A\Big(\omega(-i+\omega)\big(u^2+u(i-2\omega)+\omega(-i+\omega)\big) + \tau^2 k_B^2\sigma_B\big(iu-2iu\omega-2u\omega+2\omega^2-(i+u)(i+u-\omega)\sigma_A + (i+u-\omega)(-i+\omega)\sigma_B\big) + i\tau k_B\Big(\omega\big(u^2+u(2i-3\omega)+2\omega(-i+\omega)\big) + (i+u)(-2\omega(-i+\omega)+u(-i+2\omega))\sigma_A - (-i+\omega)\big(u^2+u(i-3\omega)+2\omega(-i+\omega)\big)\sigma_B\Big)\Big)\Big) + \tau^2 k_B X_s^2\Big((i+u)(u-\omega)\omega k_B + \tau k_A^2\big(iu^2+u(-3-5i\omega)+4(1+i\omega)\omega+2\tau(u-\omega)k_B\big)\sigma_A - k_A\Big(\omega\big(u^2+u(2i-3\omega)+2\omega(-i+\omega)\big) + i\tau k_B(\omega(-u+\omega)+(i+u)(u-\omega)\sigma_A + (-2u(-i+\omega)+u(-i+2\omega))\sigma_B)\Big) + (i+u-\omega)X_s\Big((i+u)(-i+\omega)(\omega - i\tau k_B\sigma_B)(u-\omega+i\tau k_B\sigma_B) + \tau^2 k_A^2\sigma_A\big(\tau k_B(-iu+(1-i\omega)\sigma_A) - (-i+\omega)(2\omega+(i+u)\sigma_A) + 2\tau^2 k_B^2\sigma_B\big) + \tau k_A\Big((-i+\omega)(u-\omega+i\tau k_B\sigma_B)(i\omega+\tau k_B\sigma_B) + (i+u)\sigma_A\big(\omega+i\omega^2-u\tau k_B - 2i\tau^2 k_B^2\sigma_B\big)\Big)\Big)\Big)\Big)\Big/ \Big(c_{As}c_{Bs}\Big((i+u)(u(i+u)+i\tau k_B(uX_s+(i+u)\sigma_B)) + \tau k_A\Big(u\tau k_B X_s^2 + i(i+u)(u+(i+u)\sigma_A + i\tau k_B\sigma_B) + X_s((1-iu)u-\tau k_B(u+(i+u)\sigma_A-(i+u)\sigma_B))\Big)\Big)\Big((i+u-\omega)\Big(u^2+u(i-2\omega)+\omega(-i+\omega)+i\tau k_B((u-\omega)X_s+(i+u-\omega)\sigma_B)\Big) + \tau k_A\Big(\tau(u-\omega)k_B X_s^2 - i(-i+\omega)(\omega+(-i+\omega)\sigma_A - i\tau k_B\sigma_B) + X_s((1+i\omega)\omega-\tau k_B(\omega+(-i+\omega)\sigma_A-(-i+\omega)\sigma_B))\Big)\Big)\Big)$$

$$G_{xz2}[\omega, -u] \to -\Big(\Big(i\tau^2 c_{A0s} c_{B0s} k_A k_B \sigma_A\Big((i+u)(i+u-\omega)\Big((u-\omega)(-i+\omega)(-iu+\tau k_B\sigma_B) + \tau k_B X_s^2(u(u-\omega)(1+i\omega)+\tau^2 k_B^2\sigma_B(-2i(u-\omega)+(1+i\omega)\sigma_B) + u\tau k_B(-u+\omega-(-i+\omega)\sigma_B))\Big) + \tau k_A\Big(\tau k_B X_s^3\big(u\big(-2iu^2+u(2+3i\omega)+(-2-i\omega)\omega\big) + \tau\big(4u^2+u(4i-5\omega)+\omega(-3i+\omega)\big)k_B\sigma_B\big) + X_s^2\big(u(-i+\omega)\big(2u^2+u(2i-3\omega)+\omega(-2i+\omega)\big) + \tau^2 k_B^2\sigma_B\big(-8iu-8u^2+7i\omega+11u\omega-3\omega^2-(i+u)(i+u-\omega)\sigma_A + (i+u-\omega)(-i+\omega)\sigma_B\big) + i\tau k_B\big(2u\big(2u^2+u(2i-3\omega)+\omega(-2i+\omega)\big) + (i+u)\big(2u^2+u(2i-3\omega)+\omega(-i+\omega)\big)\sigma_A + (-i+\omega)\big(2u^2+u(2i-3\omega)+\omega(-i+\omega)\big)\sigma_B\big)\big) - X_s\Big((-i+\omega)\big(2u\big(2u^2+u(2i-3\omega)+\omega(-2i+\omega)\big) + (i+u)\big(2u^2+u(2i-3\omega)+\omega(-i+\omega)\big)\sigma_A\big) + \tau^2 k_B^2\sigma_B\big(-2\big(2u^2+u(2i-3\omega)+\omega(2-i\omega)\big) - 2(i+u)(i+u-\omega)\sigma_A + (i+u-\omega)(-i+\omega)\sigma_B\big) + i\tau k_B\Big(u\big(2u^2+u(2i-3\omega)+\omega(-2i+\omega)\big) + (i+u)\big(2u^2+u(2i-3\omega)+\omega(-i+\omega)\big)\sigma_A + (-i+\omega)\big(4u^2+u(4i-5\omega)+\omega(-3i+\omega)\big)\sigma_B\Big)\Big) + (-i+\omega)\Big(\big(2u^2+u(2i-3\omega)+\omega(-2i+\omega)\big)(u+i\tau k_B\sigma_B) + (i+u)(i+u-\omega)\sigma_A(2u-\omega+i\tau k_B\sigma_B)\Big)\Big) + \tau^2 k_A^2(-1+X_s)\Big(-\tau(u-\omega)k_B X_s^3(u+2i\tau k_B\sigma_B) + (-i+\omega)(u-\omega+(i+u-\omega)\sigma_A)(-iu+(1-iu)\sigma_A+\tau k_B\sigma_B) + X_s^2\Big(-iu(u-\omega)(-i+\omega)+4i\tau^2(u-\omega)k_B^2\sigma_B + \tau k_B\big(\big(2u^2-i\omega-2u(-i+\omega)\big)\sigma_A + (u-\omega)(2u+(-i+\omega)\sigma_B)\big)\Big) + X_s\Big((-i+\omega)\big(2iu(u-\omega)+\big(2iu^2+u(-2-2i\omega)+\omega\big)\sigma_A\big) - 2i\tau^2 k_B^2(u-\omega+(i+u-\omega)\sigma_A)\sigma_B + \tau k_B\big(-(i+u)(i+u-\omega)\sigma_A^2 - (u-\omega)(u+2(-i+\omega)\sigma_B) + \sigma_A\big(-2u^2+i\omega+2u(-i+\omega)+(i+u-\omega)(-i+\omega)\sigma_B\big)\big)\Big)\Big)\Big)\Big)\Big/ \Big(c_{As}c_{Bs}\Big((i+u)(u(i+u)+i\tau k_B(uX_s+(i+u)\sigma_B)) + \tau k_A\Big(u\tau k_B X_s^2 + i(i+u)(u+(i+u)\sigma_A+i\tau k_B\sigma_B) + X_s((1-iu)u-\tau k_B(u+(i+u)\sigma_A-(i+u)\sigma_B))\Big)\Big)\Big((i+u-\omega)\Big(u^2+u(i-2\omega)+\omega(-i+\omega)+i\tau k_B((u-\omega)X_s+(i+u-\omega)\sigma_B)\Big) + \tau k_A\Big(\tau(u-\omega)k_B X_s^2 - i(-i+\omega)(\omega+(-i+\omega)\sigma_A - i\tau k_B\sigma_B) + X_s((1+i\omega)\omega-\tau k_B(\omega+(-i+\omega)\sigma_A-(-i+\omega)\sigma_B))\Big)\Big)\Big)$$

$$H_{xz2}[\omega, -u] \to -\Big(\Big(i\tau^2(i+u-\omega)c_{A0s}c_{B0s}k_A k_B\sigma_A\sigma_B\Big((i+u)\Big(-i\tau^2\omega k_B^2 X_s^3 + (i+u-\omega)(-i+\omega)(-iu+\tau k_B\sigma_B) + \tau k_B X_s^2\big(u^2+u(i-2\omega)+2\omega(-i+\omega)+i\tau(3i+2u-3\omega)k_B\sigma_B\big) + (i+u-\omega)X_s\big((u-\omega)(1+i\omega)-2i\tau^2 k_B^2\sigma_B - \tau k_B(u+2(-i+\omega)\sigma_B)\big)\Big) + \tau^2 k_A^2(-1+X_s)\Big(\tau k_B X_s^3(u-2i\tau k_B(\sigma_A-\sigma_B)) + (1+i\omega)(u+(i+u)\sigma_A+i\tau k_B\sigma_B) + X_s^2\Big(u+iu\omega-4i\tau^2 k_B^2\sigma_B - \tau k_B(2u+(5i+3u-4\omega)\sigma_A + (-i+\omega)\sigma_B)\Big) + X_s\Big((1+i\omega)(-2u+(-3i-3u+2\omega)\sigma_A) + 2i\tau^2 k_B^2\sigma_B + \tau k_B(u+(i+u)\sigma_A+2(-i+\omega)\sigma_B)\Big)\Big) + \tau k_A\Big(-\tau^2\omega k_B^2 X_s^4 + \tau k_B X_s^3\big(-2i\big(u^2-u(-i+\omega)+\omega(-i+\omega)\big) + \tau k_B(\omega-(i+u)\sigma_A + (5i+4u-3\omega)\sigma_B)\big) + X_s\Big(-(-i+\omega)\big(4u^2+u(4i-3\omega)+\omega(-i+\omega)+2(i+u)(i+u-\omega)\sigma_A\big) + 2\tau^2(2i+2u-\omega)k_B^2\sigma_B - i\tau k_B(u(2i+2u-\omega)+(i+u)(i+u-\omega)\sigma_A + (5i+5u-3\omega)(-i+\omega)\sigma_B)\Big) + X_s^2\Big((-i+\omega)\big(2u^2-2u(-i+\omega)+\omega(-i+\omega)\big) + \tau^2(-9i-8u+5\omega)k_B^2\sigma_B + i\tau k_B\big(4iu+4u^2-2i\omega-3u\omega+2\omega^2+(i+u)(3i+2u-3\omega)\sigma_A + (3i+3u-2\omega)(-i+\omega)\sigma_B\big)\Big) - (-i+\omega)(-(i+u)(i+u-\omega)\sigma_A - (2i+2u-\omega)(u+i\tau k_B\sigma_B))\Big)\Big)\Big)\Big/ \Big(c_{As}c_{Bs}X_s\Big((i+u)(u(i+u)+i\tau k_B(uX_s+(i+u)\sigma_B)) + \tau k_A\Big(u\tau k_B X_s^2 + i(i+u)(u+(i+u)\sigma_A+i\tau k_B\sigma_B) + X_s((1-iu)u-\tau k_B(u+(i+u)\sigma_A-(i+u)\sigma_B))\Big)\Big)\Big((i+u-\omega)\Big(u^2+u(i-2\omega)+\omega(-i+\omega)+i\tau k_B((u-\omega)X_s+(i+u-\omega)\sigma_B)\Big) + \tau k_A\Big(\tau(u-\omega)k_B X_s^2 - i(-i+\omega)(\omega+(-i+\omega)\sigma_A - i\tau k_B\sigma_B) + X_s((1+i\omega)\omega-\tau k_B(\omega+(-i+\omega)\sigma_A-(-i+\omega)\sigma_B))\Big)\Big)\Big)$$

$$F_{xz2}[-\omega, u] \to \Big(\tau^2 c_{A0s} c_{B0s} k_A k_B \sigma_B\Big(i\tau^3(u-\omega)k_A k_B^2 X_s^4(\omega+2i\tau k_A\sigma_A) + \tau(-i+u-\omega)(i+\omega)k_A\sigma_A(\tau k_A(u+(-i+u)\sigma_A - i\tau k_B\sigma_B) + (-i+u)(iu+\tau k_B\sigma_B)) + \tau^2 k_B X_s^3\Big((-i+u)(u-\omega)\omega k_B + \tau k_A^2\Big(-iu^2+u(-3+5i\omega)+4(1-i\omega)\omega+2\tau(u-\omega)k_B\Big)\sigma_A - k_A\Big(\omega\big(u^2+2\omega(i+\omega)-u(2i+3\omega)\big) + \tau k_B(i(u-\omega)\omega - i(-i+u)(u-\omega)\sigma_A + (u-2iu\omega+2i\omega(i+\omega))\sigma_B)\Big)\Big) + i\tau X_s^2\Big((-i+u)k_B\Big(\omega\big(u^2+2\omega(i+\omega)-u(2i+3\omega)\big) + \tau(u-2iu\omega+2i\omega(i+\omega))k_B\sigma_B\Big) + \tau k_A^2\sigma_A\Big((i+\omega)\big(u+iu^2-3iu\omega+2i\omega(i+\omega)\big) + 2\tau^2(1+iu-i\omega)k_B^2\sigma_B + \tau k_B\big(-2iu+4i\omega-4u\omega+4\omega^2-(-i+u)(-i+u-\omega)\sigma_A + (-i+u-\omega)(i+\omega)\sigma_B\big)\Big) + k_A\Big(\omega(i+\omega)\big(u^2+\omega(i+\omega)-u(i+2\omega)\big) + \tau^2 k_B^2\sigma_B\big(-iu+2iu\omega-2u\omega+2\omega^2-(-i+u)(-i+u-\omega)\sigma_A + (-i+u-\omega)(i+\omega)\sigma_B\big) - i\tau k_B\Big(\omega\big(u^2+2\omega(i+\omega)-u(2i+3\omega)\big) + (-i+u)(-2\omega(i+\omega)+u(i+2\omega))\sigma_A - (i+\omega)\big(u^2+2\omega(i+\omega)-u(i+3\omega)\big)\sigma_B\Big)\Big) + (-i+u-\omega)X_s\Big((-i+u)(i+\omega)(u-\omega-i\tau k_B\sigma_B)(\omega+i\tau k_B\sigma_B) + \tau^2 k_A^2\sigma_A\big(\tau k_B(iu+(1+iu)\sigma_A) - (i+\omega)(2\omega+(-i+u)\sigma_A) + 2\tau^2 k_B^2\sigma_B\big) + \tau k_A\Big(i(i+\omega)(\omega+i\tau k_B\sigma_B)(-u+\omega+i\tau k_B\sigma_B) + (-i+u)\sigma_A\big(\omega-iu^2-u\tau k_B+2i\tau^2 k_B^2\sigma_B\big)\Big)\Big)\Big)\Big/ \Big(c_{As}c_{Bs}\Big((-i+u)(u(-i+u)-i\tau k_B(uX_s+(-i+u)\sigma_B)) + \tau k_A\Big(u\tau k_B X_s^2 - i(-i+u)(u+(-i+u)\sigma_A - i\tau k_B\sigma_B) + X_s((1+iu)u-\tau k_B(u+(-i+u)\sigma_A-(-i+u)\sigma_B))\Big)\Big)\Big((-i+u-\omega)\Big(u^2+\omega(i+\omega)-u(i+2\omega)-i\tau k_B((u-\omega)X_s+(-i+u-\omega)\sigma_B)\Big) + \tau k_A\Big(\tau(u-\omega)k_B X_s^2 - i(-i+u-\omega)(u-\omega+(-i+u-\omega)\sigma_A - i\tau k_B\sigma_B) + X_s\Big(u+iu^2-\omega-2iu\omega+i\omega^2+\tau k_B(-u+\omega+(i-u+\omega)\sigma_A+(-i+u-\omega)\sigma_B)\Big)\Big)\Big)$$

$$G_{xz2}[-\omega, u] \to \Big(i\tau^2 c_{A0s} c_{B0s} k_A k_B \sigma_A\Big((-i+u)(-i+u-\omega)\Big((u-\omega)(i+\omega)(iu+\tau k_B\sigma_B) + \tau k_B X_s^2(u(u-\omega)-i\tau(2u-\omega)k_B\sigma_B) + X_s\Big(u(u-\omega)(1-i\omega)+\tau^2 k_B^2\sigma_B(2i(u-\omega)+(1-i\omega)\sigma_B) - u\tau k_B(u-\omega+(i+\omega)\sigma_B)\Big)\Big) + \tau k_A\Big(\tau k_B X_s^3\Big(u\big(2iu^2+u(2-3i\omega)+i\omega(2i+\omega)\big) + \tau\big(4u^2+\omega(3i+\omega)-u(4i+5\omega)\big)k_B\sigma_B\Big) + X_s^2\Big(u(i+\omega)\big(2u^2+\omega(2i+\omega)-u(2i+3\omega)\big) + \tau^2 k_B^2\sigma_B\big(8iu-8u^2-7i\omega+11u\omega-3\omega^2-(-i+u)(-i+u-\omega)\sigma_A + (-i+u-\omega)(i+\omega)\sigma_B\big) - i\tau k_B\big(2u\big(2u^2+\omega(2i+\omega)-u(2i+3\omega)\big) + (-i+u)\big(2u^2+\omega(i+\omega)-u(2i+3\omega)\big)\sigma_A + (i+\omega)\big(2u^2+i\omega-2u(i+\omega)\big)\sigma_B\big)\Big) - X_s\Big((i+\omega)\big(2u\big(2u^2+\omega(2i+\omega)-u(2i+3\omega)\big) + (-i+u)\big(2u^2+\omega(i+\omega)-u(2i+3\omega)\big)\sigma_A\big) + \tau^2 k_B^2\sigma_B\big(-4u^2-2\omega(2i+\omega)+u(4i+6\omega)-2(-i+u)(-i+u-\omega)\sigma_A + (-i+u-\omega)(i+\omega)\sigma_B\big) - i\tau k_B\Big(u\big(2u^2+\omega(2i+\omega)-u(2i+3\omega)\big) + (-i+u)\big(2u^2+\omega(i+\omega)-u(2i+3\omega)\big)\sigma_A + (i+\omega)\big(4u^2+\omega(3i+\omega)-u(4i+5\omega)\big)\sigma_B\Big)\Big) + (i+\omega)\Big(\big(2u^2+\omega(2i+\omega)-u(2i+3\omega)\big)(u-iu\tau k_B\sigma_B) + (-i+u)(-i+u-\omega)\sigma_A(2u-\omega-i\tau k_B\sigma_B)\Big)\Big) + \tau^2 k_A^2(-1+X_s)\Big(-\tau(u-\omega)k_B X_s^3(u-2i\tau k_B\sigma_B) + (i+\omega)(u-\omega+(-i+u-\omega)\sigma_A)(iu+(1+iu)\sigma_A+\tau k_B\sigma_B) + X_s^2\Big(iu(u-\omega)(i+\omega)-4i\tau^2(u-\omega)k_B^2\sigma_B + \tau k_B\big(\big(2u^2+i\omega-2u(i+\omega)\big)\sigma_A + (u-\omega)(2u+(i+\omega)\sigma_B)\big)\Big) + X_s\Big((i+\omega)\big(-2u\big(2u^2+\omega(2i+\omega)-u(2i+3\omega)\big) + \tau k_B(\omega-(i+u)\sigma_A + (5i+4u-3\omega)\sigma_B)\big) + (i+\omega)(-(-i+u)(-i+u-\omega)\sigma_A - (-2i+2u-\omega)(u-iu\tau k_B\sigma_B))\Big) + i\tau^2 k_A^2(-1+X_s)\Big((i+\omega)(u+(-i+u)\sigma_A - i\tau k_B\sigma_B) + \tau k_B X_s^3(iu+2\tau k_B(-\sigma_A+\sigma_B)) + X_s^2\Big(u(i+\omega)-4\tau^2 k_B^2\sigma_B - i\tau k_B(2u+(-5i+3u-4\omega)\sigma_A + (i+\omega)\sigma_B)\Big) + X_s\Big((i+\omega)(-2u+(3i-3u+2\omega)\sigma_A) + 2\tau^2 k_B^2\sigma_B + \tau k_B((1+iu)\sigma_A + i(u+2(i+\omega)\sigma_B))\Big)\Big)\Big)\Big)\Big/ \Big(c_{As}c_{Bs}X_s\Big((-i+u)(u(-i+u)-i\tau k_B(uX_s+(-i+u)\sigma_B)) + \tau k_A\Big(u\tau k_B X_s^2 - i(-i+u)(u+(-i+u)\sigma_A - i\tau k_B\sigma_B) + X_s((1+iu)u-\tau k_B(u+(-i+u)\sigma_A-(-i+u)\sigma_B))\Big)\Big)\Big((-i+u-\omega)\Big(u^2+\omega(i+\omega)-u(i+2\omega)-i\tau k_B((u-\omega)X_s+(-i+u-\omega)\sigma_B)\Big) + \tau k_A\Big(\tau(u-\omega)k_B X_s^2 - i(-i+u-\omega)(u-\omega+(-i+u-\omega)\sigma_A - i\tau k_B\sigma_B) + X_s\Big(u+iu^2-\omega-2iu\omega+i\omega^2+\tau k_B(-u+\omega+(i-u+\omega)\sigma_A+(-i+u-\omega)\sigma_B)\Big)\Big)\Big)$$

$$H_{xz2}[-\omega, u] \to \Big(i\tau^2(-i+u-\omega)c_{A0s}c_{B0s}k_A k_B\sigma_A\sigma_B\Big((-i+u)\Big(i\tau^2\omega k_B^2 X_s^3 + (-i+u-\omega)(i+\omega)(iu+\tau k_B\sigma_B) + \tau k_B X_s^2\big(u^2+2\omega(i+\omega)-u(i+2\omega)+\tau(-3-2iu+3i\omega)k_B\sigma_B\big) + (-i+u-\omega)X_s\big((u-\omega)(1-i\omega)+2i\tau^2 k_B^2\sigma_B - \tau k_B(u+2(i+\omega)\sigma_B)\big)\Big) - \tau^2\omega k_B^2 X_s^4 + X_s\Big((i+\omega)\big(4u^2+\omega(i+\omega)-u(4i+3\omega)+2(-i+u)(-i+u-\omega)\sigma_A\big) + 2\tau^2(2i-2u+\omega)k_B^2\sigma_B - i\tau k_B(u(-2i+2u-\omega)+(-i+u)(-i+u-\omega)\sigma_A + (-5i+5u-3\omega)(i+\omega)\sigma_B)\Big) - X_s^2\Big((i+\omega)\big(2u^2-2u(i+\omega)+\omega(i+\omega)\big) + \tau^2(9i-8u+5\omega)k_B^2\sigma_B - i\tau k_B\big(-4iu+4u^2+2i\omega-3u\omega+2\omega^2+(-i+u)(2u-3(i+\omega))\sigma_A + (-3i+3u-2\omega)(i+\omega)\sigma_B\big)\Big) + \tau k_B X_s^3\Big(-2i\big(u^2-u(i+\omega)+\omega(i+\omega)\big) + \tau k_B(-\omega+(-i+u)\sigma_A + (5i-4u+3\omega)\sigma_B)\Big) + (i+\omega)(-(-i+u)(-i+u-\omega)\sigma_A - (-2i+2u-\omega)(u-i\tau k_B\sigma_B))\Big) + i\tau^2 k_A^2(-1+X_s)\Big((i+\omega)(u+(-i+u)\sigma_A - i\tau k_B\sigma_B) + \tau k_B X_s^3(iu+2\tau k_B(-\sigma_A+\sigma_B)) + X_s^2\Big(u(i+\omega)-4\tau^2 k_B^2\sigma_B - i\tau k_B(2u+(-5i+3u-4\omega)\sigma_A + (i+\omega)\sigma_B)\Big) + X_s\Big((i+\omega)(-2u+(3i-3u+2\omega)\sigma_A) + 2\tau^2 k_B^2\sigma_B + \tau k_B((1+iu)\sigma_A + i(u+2(i+\omega)\sigma_B))\Big)\Big)\Big)\Big)\Big/ \Big(c_{As}c_{Bs}X_s\Big((-i+u)(u(-i+u)-i\tau k_B(uX_s+(-i+u)\sigma_B)) + \tau k_A\Big(u\tau k_B X_s^2 - i(-i+u)(u+(-i+u)\sigma_A - i\tau k_B\sigma_B) + X_s((1+iu)u-\tau k_B(u+(-i+u)\sigma_A-(-i+u)\sigma_B))\Big)\Big)\Big((-i+u-\omega)\Big(u^2+\omega(i+\omega)-u(i+2\omega)-i\tau k_B((u-\omega)X_s+(-i+u-\omega)\sigma_B)\Big) + \tau k_A\Big(\tau(u-\omega)k_B X_s^2 - i(-i+u-\omega)(u-\omega+(-i+u-\omega)\sigma_A - i\tau k_B\sigma_B) + X_s\Big(u+iu^2-\omega-2iu\omega+i\omega^2+\tau k_B(-u+\omega+(i-u+\omega)\sigma_A+(-i+u-\omega)\sigma_B)\Big)\Big)\Big)$$

Third order GFRFs

$$F_{xxx3}[\omega,\omega,-\omega] \to -\Big(\big(\tau\, k_A\, X_s\, \big(\big((1+i\,\omega)\,\omega+\tau\, k_B\,(\omega\, X_s+(-i+\omega)\,\alpha_B)\big)\, F_{xx2}[\omega,\omega]\, H_{x1}[-\omega]+(1+i\,\omega)\,\omega\,(F_{xx2}[-\omega,\omega]\, H_{x1}[\omega]+F_{xx2}[\omega,-\omega]\, H_{x1}[\omega]+F_{x1}[\omega]\, H_{xx2}[-\omega,\omega]+F_{x1}[-\omega]\, H_{xx2}[\omega,\omega])+\tau\, k_B\,(\omega\, X_s\,(F_{xx2}[-\omega,\omega]\, H_{x1}[\omega]+F_{xx2}[\omega,-\omega]\, H_{x1}[\omega]+F_{x1}[\omega]\, H_{xx2}[-\omega,\omega]+F_{x1}[-\omega]\, H_{xx2}[\omega,\omega])-(-i+\omega)\,\alpha_B\,(G_{xx2}[\omega,\omega]\, H_{x1}[-\omega]-F_{xx2}[-\omega,\omega]\, H_{x1}[\omega]-F_{xx2}[\omega,-\omega]\, H_{x1}[\omega]+G_{xx2}[-\omega,\omega]\, H_{x1}[\omega]+G_{xx2}[-\omega,\omega]\, H_{x1}[\omega]-F_{x1}[\omega]\, H_{xx2}[-\omega,\omega]+G_{x1}[\omega]\, H_{xx2}[-\omega,\omega]-F_{x1}[\omega]\, H_{xx2}[\omega,-\omega]+G_{x1}[-\omega]\, H_{xx2}[\omega,-\omega]-F_{x1}[-\omega]\, H_{xx2}[\omega,\omega]+G_{x1}[-\omega]\, H_{xx2}[\omega,\omega])))\big)\Big/\Big(-3\,i\,(-i+\omega)\,\big((1+i\,\omega)\,\omega+\tau\, k_B\,(\omega\, X_s+(-i+\omega)\,\alpha_B)\big)+3\,\tau\, k_A\,\big(\tau\,\omega\, k_B\, X_s^2-i\,(-i+\omega)\,(\omega+(-i+\omega)\,\alpha_A-i\,\tau\, k_B\,\alpha_B)+X_s\,\big((1+i\,\omega)\,\omega-\tau\, k_B\,(\omega+(-i+\omega)\,\alpha_A-(-i+\omega)\,\alpha_B)\big)\big)\Big)\Big)$$

$$G_{xxx3}[\omega,\omega,-\omega] \to (\tau\, k_B\, X_s\,\big((1+i\,\omega)\,\omega\,(G_{xx2}[\omega,\omega]\, H_{x1}[-\omega]+G_{xx2}[-\omega,\omega]\, H_{x1}[\omega]+G_{xx2}[\omega,-\omega]\, H_{x1}[\omega]+G_{x1}[\omega]\, H_{xx2}[-\omega,\omega]+G_{x1}[\omega]\, H_{xx2}[\omega,-\omega]+G_{x1}[-\omega]\, H_{xx2}[\omega,\omega])+\tau\, k_A\,(-(-i+\omega)\,\alpha_A\,(F_{xx2}[\omega,\omega]\, H_{x1}[-\omega]-G_{xx2}[\omega,\omega]\, H_{x1}[-\omega]+F_{xx2}[-\omega,\omega]\, H_{x1}[\omega]+F_{xx2}[\omega,-\omega]\, H_{x1}[\omega]-G_{xx2}[-\omega,\omega]\, H_{x1}[\omega]-G_{xx2}[\omega,-\omega]\, H_{x1}[\omega]+F_{x1}[\omega]\, H_{xx2}[-\omega,\omega]-G_{x1}[\omega]\, H_{xx2}[-\omega,\omega]+F_{x1}[\omega]\, H_{xx2}[\omega,-\omega]-G_{x1}[\omega]\, H_{xx2}[\omega,-\omega]+F_{x1}[-\omega]\, H_{xx2}[\omega,\omega])-\omega\,(-1+X_s)\,(G_{xx2}[\omega,\omega]\, H_{x1}[-\omega]+G_{xx2}[-\omega,\omega]\, H_{x1}[\omega]+G_{xx2}[\omega,-\omega]\, H_{x1}[\omega]+G_{x1}[\omega]\, H_{xx2}[-\omega,\omega]+G_{x1}[\omega]\, H_{xx2}[\omega,-\omega]+G_{x1}[-\omega]\, H_{xx2}[\omega,\omega])))\big)\Big/\Big(-3\,i\,(-i+\omega)\,\big((1+i\,\omega)\,\omega+\tau\, k_B\,(\omega\, X_s+(-i+\omega)\,\alpha_B)\big)+3\,\tau\, k_A\,\big(\tau\,\omega\, k_B\, X_s^2-i\,(-i+\omega)\,(\omega+(-i+\omega)\,\alpha_A-i\,\tau\, k_B\,\alpha_B)+X_s\,\big((1+i\,\omega)\,\omega-\tau\, k_B\,(\omega+(-i+\omega)\,\alpha_A-(-i+\omega)\,\alpha_B)\big)\big)\Big)\Big)$$

$$H_{xxx3}[\omega,\omega,-\omega] \to (\tau\,(-i+\omega)\,\big((1+i\,\omega)\, k_B\,\alpha_B\,(G_{xx2}[\omega,\omega]\, H_{x1}[-\omega]+G_{xx2}[-\omega,\omega]\, H_{x1}[\omega]+G_{xx2}[\omega,-\omega]\, H_{x1}[\omega]+G_{x1}[\omega]\, H_{xx2}[-\omega,\omega]+G_{x1}[\omega]\, H_{xx2}[\omega,-\omega]+G_{x1}[-\omega]\, H_{xx2}[\omega,\omega])+k_A\,\big((1+i\,\omega+\tau\, k_B\, X_s)\,\alpha_A\,(F_{xx2}[\omega,\omega]\, H_{x1}[-\omega]+F_{xx2}[-\omega,\omega]\, H_{x1}[\omega]+F_{xx2}[\omega,-\omega]\, H_{x1}[\omega]+F_{x1}[\omega]\, H_{xx2}[-\omega,\omega]+F_{x1}[\omega]\, H_{xx2}[\omega,-\omega]+F_{x1}[-\omega]\, H_{xx2}[\omega,\omega])-\tau\, k_B\,(-1+X_s)\,\alpha_B\,(G_{xx2}[\omega,\omega]\, H_{x1}[-\omega]+G_{xx2}[-\omega,\omega]\, H_{x1}[\omega]+G_{xx2}[\omega,-\omega]\, H_{x1}[\omega]+G_{x1}[\omega]\, H_{xx2}[-\omega,\omega]+G_{x1}[\omega]\, H_{xx2}[\omega,-\omega]+G_{x1}[-\omega]\, H_{xx2}[\omega,\omega])))\big)\Big/\Big(-3\,i\,(-i+\omega)\,\big((1+i\,\omega)\,\omega+\tau\, k_B\,(\omega\, X_s+(-i+\omega)\,\alpha_B)\big)+3\,\tau\, k_A\,\big(\tau\,\omega\, k_B\, X_s^2-i\,(-i+\omega)\,(\omega+(-i+\omega)\,\alpha_A-i\,\tau\, k_B\,\alpha_B)+X_s\,\big((1+i\,\omega)\,\omega-\tau\, k_B\,(\omega+(-i+\omega)\,\alpha_A-(-i+\omega)\,\alpha_B)\big)\big)\Big)\Big)$$

$$F_{xzz3}[\omega,u,-u] \to -\Big(\big(\tau\, k_A\, X_s\,\big(\big((1+i\,\omega)\,\omega+\tau\, k_B\,(\omega\, X_s+(-i+\omega)\,\alpha_B)\big)\, F_{zz2}[-u,u]\, H_{x1}[\omega]+\big((1+i\,\omega)\,\omega+\tau\, k_B\,(\omega\, X_s+(-i+\omega)\,\alpha_B)\big)\, F_{zz2}[u,-u]\, H_{x1}[\omega]+i\,\tau\, k_B\,\alpha_B\, G_{zz2}[-u,u]\, H_{x1}[\omega]-\tau\,\omega\, k_B\,\alpha_B\, G_{zz2}[-u,u]\, H_{x1}[\omega]+i\,\tau\, k_B\,\alpha_B\, G_{zz2}[u,-u]\, H_{x1}[\omega]-\tau\,\omega\, k_B\,\alpha_B\, G_{zz2}[u,-u]\, H_{x1}[\omega]+\omega\, F_{z1}[u]\, H_{xz2}[\omega,-u]+i\,\omega^2\, F_{z1}[u]\, H_{xz2}[\omega,-u]+\tau\,\omega\, k_B\, X_s\, F_{z1}[u]\, H_{xz2}[\omega,-u]-i\,\tau\, k_B\,\alpha_B\, F_{z1}[u]\, H_{xz2}[\omega,-u]+\tau\,\omega\, k_B\,\alpha_B\, F_{z1}[u]\, H_{xz2}[\omega,-u]+i\,\tau\, k_B\,\alpha_B\, G_{z1}[u]\, H_{xz2}[\omega,-u]-\tau\,\omega\, k_B\,\alpha_B\, G_{z1}[u]\, H_{xz2}[\omega,-u]+\omega\, F_{z1}[-u]\, H_{xz2}[\omega,u]+i\,\omega^2\, F_{z1}[-u]\, H_{xz2}[\omega,u]+\tau\,\omega\, k_B\, X_s\, F_{z1}[-u]\, H_{xz2}[\omega,u]-i\,\tau\, k_B\,\alpha_B\, F_{z1}[-u]\, H_{xz2}[\omega,u]+\tau\,\omega\, k_B\,\alpha_B\, F_{z1}[-u]\, H_{xz2}[\omega,u]+i\,\tau\, k_B\,\alpha_B\, G_{z1}[-u]\, H_{xz2}[\omega,u]-\tau\,\omega\, k_B\,\alpha_B\, G_{z1}[-u]\, H_{xz2}[\omega,u]+\omega\, F_{xz2}[\omega,u]\, H_{z1}[-u]+i\,\omega^2\, F_{xz2}[\omega,u]\, H_{z1}[-u]+\tau\,\omega\, k_B\, X_s\, F_{xz2}[\omega,u]\, H_{z1}[-u]-i\,\tau\, k_B\,\alpha_B\, F_{xz2}[\omega,u]\, H_{z1}[-u]+\tau\,\omega\, k_B\,\alpha_B\, F_{xz2}[\omega,u]\, H_{z1}[-u]+i\,\tau\, k_B\,\alpha_B\, G_{xz2}[\omega,u]\, H_{z1}[-u]-\tau\,\omega\, k_B\,\alpha_B\, G_{xz2}[\omega,u]\, H_{z1}[-u]+\omega\, F_{xz2}[\omega,-u]\, H_{z1}[u]+i\,\omega^2\, F_{xz2}[\omega,-u]\, H_{z1}[u]+\tau\,\omega\, k_B\, X_s\, F_{xz2}[\omega,-u]\, H_{z1}[u]-i\,\tau\, k_B\,\alpha_B\, F_{xz2}[\omega,-u]\, H_{z1}[u]+\tau\,\omega\, k_B\,\alpha_B\, F_{xz2}[\omega,-u]\, H_{z1}[u]+i\,\tau\, k_B\,\alpha_B\, G_{xz2}[\omega,-u]\, H_{z1}[u]-\tau\,\omega\, k_B\,\alpha_B\, G_{xz2}[\omega,-u]\, H_{z1}[u]+\omega\, F_{x1}[\omega]\, H_{zz2}[-u,u]+i\,\omega^2\, F_{x1}[\omega]\, H_{zz2}[-u,u]+\tau\,\omega\, k_B\, X_s\, F_{x1}[\omega]\, H_{zz2}[-u,u]-i\,\tau\, k_B\,\alpha_B\, F_{x1}[\omega]\, H_{zz2}[-u,u]+\tau\,\omega\, k_B\,\alpha_B\, F_{x1}[\omega]\, H_{zz2}[-u,u]+i\,\tau\, k_B\,\alpha_B\, G_{x1}[\omega]\, H_{zz2}[-u,u]-\tau\,\omega\, k_B\,\alpha_B\, G_{x1}[\omega]\, H_{zz2}[-u,u]+\omega\, F_{x1}[\omega]\, H_{zz2}[u,-u]+i\,\omega^2\, F_{x1}[\omega]\, H_{zz2}[u,-u]+\tau\,\omega\, k_B\, X_s\, F_{x1}[\omega]\, H_{zz2}[u,-u]-i\,\tau\, k_B\,\alpha_B\, F_{x1}[\omega]\, H_{zz2}[u,-u]+\tau\,\omega\, k_B\,\alpha_B\, F_{x1}[\omega]\, H_{zz2}[u,-u]+i\,\tau\, k_B\,\alpha_B\, G_{x1}[\omega]\, H_{zz2}[u,-u]-\tau\,\omega\, k_B\,\alpha_B\, G_{x1}[\omega]\, H_{zz2}[u,-u])\big)\Big/\Big(-2\,i\,(-i+\omega)\,\big((1+i\,\omega)\,\omega+\tau\, k_B\,(\omega\, X_s+(-i+\omega)\,\alpha_B)\big)+2\,\tau\, k_A\,\big(\tau\,\omega\, k_B\, X_s^2-i\,(-i+\omega)\,(\omega+(-i+\omega)\,\alpha_A-i\,\tau\, k_B\,\alpha_B)+X_s\,\big((1+i\,\omega)\,\omega-\tau\, k_B\,(\omega+(-i+\omega)\,\alpha_A-(-i+\omega)\,\alpha_B)\big)\big)\Big)\Big)$$

$$G_{xzz3}[\omega,u,-u] \to (\tau\, k_B\, X_s\,\big((1+i\,\omega)\,\omega\,(G_{zz2}[-u,u]\, H_{x1}[\omega]+G_{zz2}[u,-u]\, H_{x1}[\omega]+G_{z1}[u]\, H_{xz2}[\omega,-u]+G_{z1}[-u]\, H_{xz2}[\omega,u]+G_{xz2}[\omega,u]\, H_{z1}[-u]+G_{xz2}[\omega,-u]\, H_{z1}[u]+G_{x1}[\omega]\, H_{zz2}[-u,u]+G_{x1}[\omega]\, H_{zz2}[u,-u])+\tau\, k_A\,(-(-i+\omega)\,\alpha_A\,(F_{zz2}[-u,u]\, H_{x1}[\omega]+F_{zz2}[u,-u]\, H_{x1}[\omega]-G_{zz2}[-u,u]\, H_{x1}[\omega]-G_{zz2}[u,-u]\, H_{x1}[\omega]+F_{z1}[u]\, H_{xz2}[\omega,-u]-G_{z1}[u]\, H_{xz2}[\omega,-u]+F_{z1}[-u]\, H_{xz2}[\omega,u]-G_{z1}[-u]\, H_{xz2}[\omega,u]+F_{xz2}[\omega,u]\, H_{z1}[-u]-G_{xz2}[\omega,u]\, H_{z1}[-u]+F_{xz2}[\omega,-u]\, H_{z1}[u]-G_{xz2}[\omega,-u]\, H_{z1}[u]+F_{x1}[\omega]\, H_{zz2}[-u,u]-G_{x1}[\omega]\, H_{zz2}[-u,u]+F_{x1}[\omega]\, H_{zz2}[u,-u]-G_{x1}[\omega]\, H_{zz2}[u,-u])-\omega\,(-1+X_s)\,(G_{zz2}[-u,u]\, H_{x1}[\omega]+G_{zz2}[u,-u]\, H_{x1}[\omega]+G_{z1}[u]\, H_{xz2}[\omega,-u]+G_{z1}[-u]\, H_{xz2}[\omega,u]+G_{xz2}[\omega,u]\, H_{z1}[-u]+G_{xz2}[\omega,-u]\, H_{z1}[u]+G_{x1}[\omega]\, H_{zz2}[-u,u]+G_{x1}[\omega]\, H_{zz2}[u,-u])))\big)\Big/\Big(-2\,i\,(-i+\omega)\,\big((1+i\,\omega)\,\omega+\tau\, k_B\,(\omega\, X_s+(-i+\omega)\,\alpha_B)\big)+2\,\tau\, k_A\,\big(\tau\,\omega\, k_B\, X_s^2-i\,(-i+\omega)\,(\omega+(-i+\omega)\,\alpha_A-i\,\tau\, k_B\,\alpha_B)+X_s\,\big((1+i\,\omega)\,\omega-\tau\, k_B\,(\omega+(-i+\omega)\,\alpha_A-(-i+\omega)\,\alpha_B)\big)\big)\Big)\Big)$$

$$H_{xzz3}[\omega,u,-u] \to (\tau\,(-i+\omega)\,\big((1+i\,\omega)\, k_B\,\alpha_B\,(G_{zz2}[-u,u]\, H_{x1}[\omega]+G_{zz2}[u,-u]\, H_{x1}[\omega]+G_{z1}[u]\, H_{xz2}[\omega,-u]+G_{z1}[-u]\, H_{xz2}[\omega,u]+G_{xz2}[\omega,u]\, H_{z1}[-u]+G_{xz2}[\omega,-u]\, H_{z1}[u]+G_{x1}[\omega]\, H_{zz2}[-u,u]+G_{x1}[\omega]\, H_{zz2}[u,-u])+k_A\,\big((1+i\,\omega+\tau\, k_B\, X_s)\,\alpha_A\,(F_{zz2}[-u,u]\, H_{x1}[\omega]+F_{zz2}[u,-u]\, H_{x1}[\omega]+F_{z1}[u]\, H_{xz2}[\omega,-u]+F_{z1}[-u]\, H_{xz2}[\omega,u]+F_{xz2}[\omega,u]\, H_{z1}[-u]+F_{xz2}[\omega,-u]\, H_{z1}[u]+F_{x1}[\omega]\, H_{zz2}[-u,u]+F_{x1}[\omega]\, H_{zz2}[u,-u])-\tau\, k_B\,(-1+X_s)\,\alpha_B\,(G_{zz2}[-u,u]\, H_{x1}[\omega]+G_{zz2}[u,-u]\, H_{x1}[\omega]+G_{z1}[u]\, H_{xz2}[\omega,-u]+G_{z1}[-u]\, H_{xz2}[\omega,u]+G_{xz2}[\omega,u]\, H_{z1}[-u]+G_{xz2}[\omega,-u]\, H_{z1}[u]+G_{x1}[\omega]\, H_{zz2}[-u,u]+G_{x1}[\omega]\, H_{zz2}[u,-u])))\big)\Big/\Big(-2\,i\,(-i+\omega)\,\big((1+i\,\omega)\,\omega+\tau\, k_B\,(\omega\, X_s+(-i+\omega)\,\alpha_B)\big)+2\,\tau\, k_A\,\big(\tau\,\omega\, k_B\, X_s^2-i\,(-i+\omega)\,(\omega+(-i+\omega)\,\alpha_A-i\,\tau\, k_B\,\alpha_B)+X_s\,\big((1+i\,\omega)\,\omega-\tau\, k_B\,(\omega+(-i+\omega)\,\alpha_A-(-i+\omega)\,\alpha_B)\big)\big)\Big)\Big)$$

$$F_{zzz3}[u,\omega,-u] \to -\Big(\big(\tau\, k_A\, X_s\, \big(\big((1+i\,u)\,u+\tau\, k_B\,(u\,X_s+(-i+u)\,\alpha_B)\big)\,F_{zz2}[u,u]\,H_{z1}[-u]+(1+i\,u)\,u\,(F_{zz2}[-u,u]\,H_{z1}[u]+F_{zz2}[u,-u]\,H_{z1}[u]+F_{z1}[u]\,H_{zz2}[-u,u]+F_{z1}[u]\,H_{zz2}[u,-u]+F_{z1}[-u]\,H_{zz2}[u,u])+\tau\, k_B\,(u\,X_s\,(F_{zz2}[-u,u]\,H_{z1}[u]+F_{zz2}[u,-u]\,H_{z1}[u]+F_{z1}[u]\,H_{zz2}[-u,u]+F_{z1}[u]\,H_{zz2}[u,-u]+F_{z1}[-u]\,H_{zz2}[u,u])-(-i+u)\,\alpha_B\,(G_{zz2}[u,u]\,H_{z1}[-u]-F_{zz2}[-u,u]\,H_{z1}[u]-F_{zz2}[u,-u]\,H_{z1}[u]+G_{zz2}[-u,u]\,H_{z1}[u]+G_{zz2}[u,-u]\,H_{z1}[u]-F_{z1}[u]\,H_{zz2}[-u,u]+G_{z1}[u]\,H_{zz2}[-u,u]-F_{z1}[u]\,H_{zz2}[u,-u]+G_{z1}[u]\,H_{zz2}[u,-u]-F_{z1}[-u]\,H_{zz2}[u,u]+G_{z1}[-u]\,H_{zz2}[u,u])))\big)\Big/\Big(3\,\big((-i+u)\,(u\,(-i+u)-i\,\tau\, k_B\,(u\,X_s+(-i+u)\,\alpha_B))+\tau\, k_A\,\big(u\,\tau\, k_B\,X_s^2-i\,(-i+u)\,(u+(-i+u)\,\alpha_A-i\,\tau\, k_B\,\alpha_B)+X_s\,((1+i\,u)\,u-\tau\, k_B\,(u+(-i+u)\,\alpha_A-(-i+u)\,\alpha_B))\big)\big)\Big)$$

$$G_{zzz3}[u,\omega,-u] \to (\tau\, k_B\, X_s\,((1+i\,u)\,u\,(G_{zz2}[u,u]\,H_{z1}[-u]+G_{zz2}[-u,u]\,H_{z1}[u]+G_{zz2}[u,-u]\,H_{z1}[u]+G_{z1}[u]\,H_{zz2}[-u,u]+G_{z1}[u]\,H_{zz2}[u,-u]+G_{z1}[-u]\,H_{zz2}[u,u])+\tau\, k_A\,(-(-i+u)\,\alpha_A\,(F_{zz2}[u,u]\,H_{z1}[-u]-G_{zz2}[u,u]\,H_{z1}[-u]+F_{zz2}[-u,u]\,H_{z1}[u]+F_{zz2}[u,-u]\,H_{z1}[u]-G_{zz2}[-u,u]\,H_{z1}[u]-G_{zz2}[u,-u]\,H_{z1}[u]+F_{z1}[u]\,H_{zz2}[-u,u]-G_{z1}[u]\,H_{zz2}[-u,u]+F_{z1}[u]\,H_{zz2}[u,-u]-G_{z1}[u]\,H_{zz2}[u,-u]+F_{z1}[-u]\,H_{zz2}[u,u]-G_{z1}[-u]\,H_{zz2}[u,u])-u\,(-1+X_s)\,(G_{zz2}[u,u]\,H_{z1}[-u]+G_{zz2}[-u,u]\,H_{z1}[u]+G_{zz2}[u,-u]\,H_{z1}[u]+G_{z1}[u]\,H_{zz2}[-u,u]+G_{z1}[u]\,H_{zz2}[u,-u]+G_{z1}[-u]\,H_{zz2}[u,u]))\big)\Big/\Big(3\,\big((-i+u)\,(u\,(-i+u)-i\,\tau\, k_B\,(u\,X_s+(-i+u)\,\alpha_B))+\tau\, k_A\,\big(u\,\tau\, k_B\,X_s^2-i\,(-i+u)\,(u+(-i+u)\,\alpha_A-i\,\tau\, k_B\,\alpha_B)+X_s\,((1+i\,u)\,u-\tau\, k_B\,(u+(-i+u)\,\alpha_A-(-i+u)\,\alpha_B))\big)\big)\Big)$$

$$H_{zzz3}[u,\omega,-u] \to (i\,(-i+u)\,\tau\,((-i+u)\,k_B\,\alpha_B\,(G_{zz2}[u,u]\,H_{z1}[-u]+G_{zz2}[-u,u]\,H_{z1}[u]+G_{zz2}[u,-u]\,H_{z1}[u]+G_{z1}[u]\,H_{zz2}[-u,u]+G_{z1}[u]\,H_{zz2}[u,-u]+G_{z1}[-u]\,H_{zz2}[u,u])+k_A\,((-i+u-i\,\tau\, k_B\,X_s)\,\alpha_A\,(F_{zz2}[u,u]\,H_{z1}[-u]+F_{zz2}[-u,u]\,H_{z1}[u]+F_{zz2}[u,-u]\,H_{z1}[u]+F_{z1}[u]\,H_{zz2}[-u,u]+F_{z1}[u]\,H_{zz2}[u,-u]+F_{z1}[-u]\,H_{zz2}[u,u])+i\,\tau\, k_B\,(-1+X_s)\,\alpha_B\,(G_{zz2}[u,u]\,H_{z1}[-u]+G_{zz2}[-u,u]\,H_{z1}[u]+G_{zz2}[u,-u]\,H_{z1}[u]+G_{z1}[u]\,H_{zz2}[-u,u]+G_{z1}[u]\,H_{zz2}[u,-u]+G_{z1}[-u]\,H_{zz2}[u,u]))\big)\Big/\Big(3\,\big((-i+u)\,(u\,(-i+u)-i\,\tau\, k_B\,(u\,X_s+(-i+u)\,\alpha_B))+\tau\, k_A\,\big(u\,\tau\, k_B\,X_s^2-i\,(-i+u)\,(u+(-i+u)\,\alpha_A-i\,\tau\, k_B\,\alpha_B)+X_s\,((1+i\,u)\,u-\tau\, k_B\,(u+(-i+u)\,\alpha_A-(-i+u)\,\alpha_B))\big)\big)\Big)$$

$$F_{xxz3}[\omega,-\omega,u] \to -\Big(\big(\tau\, k_A\, X_s\,\big(\big((1+i\,u)\,u+\tau\, k_B\,(u\,X_s+(-i+u)\,\alpha_B)\big)\,F_{xz2}[\omega,u]\,H_{x1}[-\omega]+(1+i\,u)\,u\,(F_{xz2}[-\omega,u]\,H_{x1}[\omega]+F_{z1}[u]\,(H_{xx2}[-\omega,\omega]+H_{xx2}[\omega,-\omega])+F_{x1}[\omega]\,H_{xz2}[-\omega,u]+F_{x1}[-\omega]\,H_{xz2}[\omega,u]+F_{xx2}[-\omega,\omega]\,H_{z1}[u])+\tau\, k_B\,(u\,X_s\,(F_{xz2}[-\omega,u]\,H_{x1}[\omega]+F_{z1}[u]\,(H_{xx2}[-\omega,\omega]+H_{xx2}[\omega,-\omega])+F_{x1}[\omega]\,H_{xz2}[-\omega,u]+F_{x1}[-\omega]\,H_{xz2}[\omega,u]+F_{xx2}[-\omega,\omega]\,H_{z1}[u]+F_{xx2}[\omega,-\omega]\,H_{z1}[u])-(-i+u)\,\alpha_B\,(G_{xz2}[\omega,u]\,H_{x1}[-\omega]-F_{xz2}[-\omega,u]\,H_{x1}[\omega]+G_{xz2}[-\omega,u]\,H_{x1}[\omega]-F_{z1}[u]\,H_{xx2}[-\omega,\omega]+G_{z1}[u]\,H_{xx2}[-\omega,\omega]-F_{z1}[u]\,H_{xx2}[\omega,-\omega]+G_{z1}[u]\,H_{xx2}[\omega,-\omega]-F_{x1}[\omega]\,H_{xz2}[-\omega,u]+G_{x1}[\omega]\,H_{xz2}[-\omega,u]-F_{x1}[-\omega]\,H_{xz2}[\omega,u]+G_{x1}[-\omega]\,H_{xz2}[\omega,u]-F_{xx2}[-\omega,\omega]\,H_{z1}[u]-F_{xx2}[\omega,-\omega]\,H_{z1}[u]+G_{xx2}[-\omega,\omega]\,H_{z1}[u]+G_{xx2}[\omega,-\omega]\,H_{z1}[u])))\big)\Big/\Big(2\,\big((-i+u)\,(u\,(-i+u)-i\,\tau\, k_B\,(u\,X_s+(-i+u)\,\alpha_B))+\tau\, k_A\,\big(u\,\tau\, k_B\,X_s^2-i\,(-i+u)\,(u+(-i+u)\,\alpha_A-i\,\tau\, k_B\,\alpha_B)+X_s\,((1+i\,u)\,u-\tau\, k_B\,(u+(-i+u)\,\alpha_A-(-i+u)\,\alpha_B))\big)\big)\Big)$$

$$G_{xxz3}[\omega,-\omega,u] \to (\tau\, k_B\, X_s\,((1+i\,u)\,u\,(G_{xz2}[\omega,u]\,H_{x1}[-\omega]+G_{xz2}[-\omega,u]\,H_{x1}[\omega]+G_{z1}[u]\,H_{xx2}[-\omega,\omega]+G_{z1}[u]\,H_{xx2}[\omega,-\omega]+G_{x1}[\omega]\,H_{xz2}[-\omega,u]+G_{x1}[-\omega]\,H_{xz2}[\omega,u]+G_{xx2}[-\omega,\omega]\,H_{z1}[u]+G_{xx2}[\omega,-\omega]\,H_{z1}[u])+\tau\, k_A\,(-(-i+u)\,\alpha_A\,(F_{xz2}[\omega,u]\,H_{x1}[-\omega]-G_{xz2}[\omega,u]\,H_{x1}[-\omega]+F_{xz2}[-\omega,u]\,H_{x1}[\omega]-G_{xz2}[-\omega,u]\,H_{x1}[\omega]+F_{z1}[u]\,H_{xx2}[-\omega,\omega]-G_{z1}[u]\,H_{xx2}[-\omega,\omega]+F_{z1}[u]\,H_{xx2}[\omega,-\omega]-G_{z1}[u]\,H_{xx2}[\omega,-\omega]+F_{x1}[\omega]\,H_{xz2}[-\omega,u]-G_{x1}[\omega]\,H_{xz2}[-\omega,u]+F_{x1}[-\omega]\,H_{xz2}[\omega,u]-G_{x1}[-\omega]\,H_{xz2}[\omega,u]+F_{xx2}[-\omega,\omega]\,H_{z1}[u]+F_{xx2}[\omega,-\omega]\,H_{z1}[u]-G_{xx2}[-\omega,\omega]\,H_{z1}[u]-G_{xx2}[\omega,-\omega]\,H_{z1}[u])-u\,(-1+X_s)\,(G_{xz2}[\omega,u]\,H_{x1}[-\omega]+G_{xz2}[-\omega,u]\,H_{x1}[\omega]+G_{z1}[u]\,H_{xx2}[-\omega,\omega]+G_{z1}[u]\,H_{xx2}[\omega,-\omega]+G_{x1}[\omega]\,H_{xz2}[-\omega,u]+G_{x1}[-\omega]\,H_{xz2}[\omega,u]+G_{xx2}[-\omega,\omega]\,H_{z1}[u]+G_{xx2}[\omega,-\omega]\,H_{z1}[u]))\big)\Big/\Big(2\,\big((-i+u)\,(u\,(-i+u)-i\,\tau\, k_B\,(u\,X_s+(-i+u)\,\alpha_B))+\tau\, k_A\,\big(u\,\tau\, k_B\,X_s^2-i\,(-i+u)\,(u+(-i+u)\,\alpha_A-i\,\tau\, k_B\,\alpha_B)+X_s\,((1+i\,u)\,u-\tau\, k_B\,(u+(-i+u)\,\alpha_A-(-i+u)\,\alpha_B))\big)\big)\Big)$$

$$H_{xxz3}[\omega,-\omega,u] \to (i\,(-i+u)\,\tau\,((-i+u)\,k_B\,\alpha_B\,(G_{xz2}[\omega,u]\,H_{x1}[-\omega]+G_{xz2}[-\omega,u]\,H_{x1}[\omega]+G_{z1}[u]\,H_{xx2}[-\omega,\omega]+G_{z1}[u]\,H_{xx2}[\omega,-\omega]+G_{x1}[\omega]\,H_{xz2}[-\omega,u]+G_{x1}[-\omega]\,H_{xz2}[\omega,u]+G_{xx2}[-\omega,\omega]\,H_{z1}[u]+G_{xx2}[\omega,-\omega]\,H_{z1}[u])+k_A\,((-i+u-i\,\tau\, k_B\,X_s)\,\alpha_A\,(F_{xz2}[\omega,u]\,H_{x1}[-\omega]+F_{xz2}[-\omega,u]\,H_{x1}[\omega]+F_{z1}[u]\,H_{xx2}[-\omega,\omega]+F_{z1}[u]\,H_{xx2}[\omega,-\omega]+F_{x1}[\omega]\,H_{xz2}[-\omega,u]+F_{x1}[-\omega]\,H_{xz2}[\omega,u]+F_{xx2}[-\omega,\omega]\,H_{z1}[u]+F_{xx2}[\omega,-\omega]\,H_{z1}[u])+i\,\tau\, k_B\,(-1+X_s)\,\alpha_B\,(G_{xz2}[\omega,u]\,H_{x1}[-\omega]+G_{xz2}[-\omega,u]\,H_{x1}[\omega]+G_{z1}[u]\,H_{xx2}[-\omega,\omega]+G_{z1}[u]\,H_{xx2}[\omega,-\omega]+G_{x1}[\omega]\,H_{xz2}[-\omega,u]+G_{x1}[-\omega]\,H_{xz2}[\omega,u]+G_{xx2}[-\omega,\omega]\,H_{z1}[u]+G_{xx2}[\omega,-\omega]\,H_{z1}[u]))\big)\Big/\Big(2\,\big((-i+u)\,(u\,(-i+u)-i\,\tau\, k_B\,(u\,X_s+(-i+u)\,\alpha_B))+\tau\, k_A\,\big(u\,\tau\, k_B\,X_s^2-i\,(-i+u)\,(u+(-i+u)\,\alpha_A-i\,\tau\, k_B\,\alpha_B)+X_s\,((1+i\,u)\,u-\tau\, k_B\,(u+(-i+u)\,\alpha_A-(-i+u)\,\alpha_B))\big)\big)\Big)$$

$$F_{xxx3}[\omega,\omega,\omega] \to -\frac{\tau k_A X_s \left(\left(3\left(1+3 i \omega\right)\omega+\tau k_B\left(3\omega X_s+\left(-i+3\omega\right)\alpha_B\right)\right)F_{xx2}[\omega,\omega]H_{x1}[\omega]+3\left(1+3 i \omega\right)\omega F_{x1}[\omega]H_{xx2}[\omega,\omega]+\tau k_B\left(3\omega X_s F_{x1}[\omega]H_{xx2}[\omega,\omega]-\left(-i+3\omega\right)\alpha_B\left(G_{xx2}[\omega,\omega]H_{x1}[\omega]+\left(-F_{x1}[\omega]+G_{x1}[\omega]\right)H_{xx2}[\omega,\omega]\right)\right)\right)}{\left(-i+3\omega\right)\left(3\omega\left(-i+3\omega\right)-i\tau k_B\left(3\omega X_s+\left(-i+3\omega\right)\alpha_B\right)\right)+\tau k_A\left(3\tau\omega k_B X_s^2-i\left(-i+3\omega\right)\left(3\omega+\left(-i+3\omega\right)\alpha_A-i\tau k_B\alpha_B\right)+X_s\left(3\left(1+3 i \omega\right)\omega+\tau k_B\left(-3\omega+\left(i-3\omega\right)\alpha_A+\left(-i+3\omega\right)\alpha_B\right)\right)\right)}$$

$$G_{xxx3}[\omega,\omega,\omega] \to \frac{\tau k_B X_s\left(3\left(1+3 i \omega\right)\omega\left(G_{xx2}[\omega,\omega]H_{x1}[\omega]+G_{x1}[\omega]H_{xx2}[\omega,\omega]\right)+\tau k_A\left(-\left(-i+3\omega\right)\alpha_A\left(F_{xx2}[\omega,\omega]H_{x1}[\omega]-G_{xx2}[\omega,\omega]H_{x1}[\omega]+\left(F_{x1}[\omega]-G_{x1}[\omega]\right)H_{xx2}[\omega,\omega]\right)-3\omega\left(-1+X_s\right)\left(G_{xx2}[\omega,\omega]H_{x1}[\omega]+G_{x1}[\omega]H_{xx2}[\omega,\omega]\right)\right)\right)}{\left(-i+3\omega\right)\left(3\omega\left(-i+3\omega\right)-i\tau k_B\left(3\omega X_s+\left(-i+3\omega\right)\alpha_B\right)\right)+\tau k_A\left(3\tau\omega k_B X_s^2-i\left(-i+3\omega\right)\left(3\omega+\left(-i+3\omega\right)\alpha_A-i\tau k_B\alpha_B\right)+X_s\left(3\left(1+3 i \omega\right)\omega+\tau k_B\left(-3\omega+\left(i-3\omega\right)\alpha_A+\left(-i+3\omega\right)\alpha_B\right)\right)\right)}$$

$$H_{xxx3}[\omega,\omega,\omega] \to \frac{\tau\left(-i+3\omega\right)\left(\left(1+3 i \omega\right)k_B\alpha_B\left(G_{xx2}[\omega,\omega]H_{x1}[\omega]+G_{x1}[\omega]H_{xx2}[\omega,\omega]\right)+k_A\left(\left(1+3 i \omega+\tau k_B X_s\right)\alpha_A\left(F_{xx2}[\omega,\omega]H_{x1}[\omega]+F_{x1}[\omega]H_{xx2}[\omega,\omega]\right)-\tau k_B\left(-1+X_s\right)\alpha_B\left(G_{xx2}[\omega,\omega]H_{x1}[\omega]+G_{x1}[\omega]H_{xx2}[\omega,\omega]\right)\right)\right)}{\left(-i+3\omega\right)\left(3\omega\left(-i+3\omega\right)-i\tau k_B\left(3\omega X_s+\left(-i+3\omega\right)\alpha_B\right)\right)+\tau k_A\left(3\tau\omega k_B X_s^2-i\left(-i+3\omega\right)\left(3\omega+\left(-i+3\omega\right)\alpha_A-i\tau k_B\alpha_B\right)+X_s\left(3\left(1+3 i \omega\right)\omega+\tau k_B\left(-3\omega+\left(i-3\omega\right)\alpha_A+\left(-i+3\omega\right)\alpha_B\right)\right)\right)}$$

$$F_{zzz3}[u,u,u] \to -\frac{\tau k_A X_s\left(\left(3\left(1+3 i u\right)u+\tau k_B\left(3u X_s+\left(-i+3u\right)\alpha_B\right)\right)F_{zz2}[u,u]H_{z1}[u]+3\left(1+3 i u\right)u F_{z1}[u]H_{zz2}[u,u]+\tau k_B\left(3u X_s F_{z1}[u]H_{zz2}[u,u]-\left(-i+3u\right)\alpha_B\left(G_{zz2}[u,u]H_{z1}[u]+\left(-F_{z1}[u]+G_{z1}[u]\right)H_{zz2}[u,u]\right)\right)\right)}{\left(-i+3u\right)\left(3u\left(-i+3u\right)-i\tau k_B\left(3u X_s+\left(-i+3u\right)\alpha_B\right)\right)+\tau k_A\left(3u\tau k_B X_s^2-i\left(-i+3u\right)\left(3u+\left(-i+3u\right)\alpha_A-i\tau k_B\alpha_B\right)+X_s\left(3\left(1+3 i u\right)u+\tau k_B\left(-3u+\left(i-3u\right)\alpha_A+\left(-i+3u\right)\alpha_B\right)\right)\right)}$$

$$G_{zzz3}[u,u,u] \to \frac{\tau k_B X_s\left(3\left(1+3 i u\right)u\left(G_{zz2}[u,u]H_{z1}[u]+G_{z1}[u]H_{zz2}[u,u]\right)+\tau k_A\left(-\left(-i+3u\right)\alpha_A\left(F_{zz2}[u,u]H_{z1}[u]-G_{zz2}[u,u]H_{z1}[u]+\left(F_{z1}[u]-G_{z1}[u]\right)H_{zz2}[u,u]\right)-3u\left(-1+X_s\right)\left(G_{zz2}[u,u]H_{z1}[u]+G_{z1}[u]H_{zz2}[u,u]\right)\right)\right)}{\left(-i+3u\right)\left(3u\left(-i+3u\right)-i\tau k_B\left(3u X_s+\left(-i+3u\right)\alpha_B\right)\right)+\tau k_A\left(3u\tau k_B X_s^2-i\left(-i+3u\right)\left(3u+\left(-i+3u\right)\alpha_A-i\tau k_B\alpha_B\right)+X_s\left(3\left(1+3 i u\right)u+\tau k_B\left(-3u+\left(i-3u\right)\alpha_A+\left(-i+3u\right)\alpha_B\right)\right)\right)}$$

$$H_{zzz3}[u,u,u] \to \frac{i\left(-i+3u\right)\tau\left(\left(-i+3u\right)k_B\alpha_B\left(G_{zz2}[u,u]H_{z1}[u]+G_{z1}[u]H_{zz2}[u,u]\right)+k_A\left(\left(-i+3u-i\tau k_B X_s\right)\alpha_A\left(F_{zz2}[u,u]H_{z1}[u]+F_{z1}[u]H_{zz2}[u,u]\right)+i\tau k_B\left(-1+X_s\right)\alpha_B\left(G_{zz2}[u,u]H_{z1}[u]+G_{z1}[u]H_{zz2}[u,u]\right)\right)\right)}{\left(-i+3u\right)\left(3u\left(-i+3u\right)-i\tau k_B\left(3u X_s+\left(-i+3u\right)\alpha_B\right)\right)+\tau k_A\left(3u\tau k_B X_s^2-i\left(-i+3u\right)\left(3u+\left(-i+3u\right)\alpha_A-i\tau k_B\alpha_B\right)+X_s\left(3\left(1+3 i u\right)u+\tau k_B\left(-3u+\left(i-3u\right)\alpha_A+\left(-i+3u\right)\alpha_B\right)\right)\right)}$$

$$F_{xxz3}[\omega,\omega,u] \to -\Big(\Big(\tau k_A X_s\left(\left(u+i u^2+4 i u\omega+2\left(1+2 i \omega\right)\omega+\tau k_B\left(\left(u+2\omega\right)X_s+\left(-i+u+2\omega\right)\alpha_B\right)\right)F_{xx2}[\omega,u]H_{x1}[\omega]+\left(u+i u^2+4 i u\omega+2\left(1+2 i \omega\right)\omega\right)\left(F_{z1}[u]H_{xx2}[\omega,\omega]+F_{x1}[\omega]H_{xz2}[\omega,u]+F_{xx2}[\omega,\omega]H_{z1}[u]\right)+$$
$$\tau k_B\left(\left(u+2\omega\right)X_s\left(F_{z1}[u]H_{xx2}[\omega,\omega]+F_{x1}[\omega]H_{xz2}[\omega,u]+F_{xx2}[\omega,\omega]H_{z1}[u]\right)-\left(-i+u+2\omega\right)\alpha_B\left(G_{xz2}[\omega,u]H_{x1}[\omega]-F_{z1}[u]H_{xx2}[\omega,\omega]+G_{z1}[u]H_{xx2}[\omega,\omega]-F_{x1}[\omega]H_{xz2}[\omega,u]+G_{x1}[\omega]H_{xz2}[\omega,u]-F_{xx2}[\omega,\omega]H_{z1}[u]+G_{xx2}[\omega,\omega]H_{z1}[u]\right)\right)\Big)\Big/$$
$$\Big(\left(-i+u+2\omega\right)\left(u^2+2\omega\left(-i+2\omega\right)+u\left(-i+4\omega\right)-i\tau k_B\left(\left(u+2\omega\right)X_s+\left(-i+u+2\omega\right)\alpha_B\right)\right)+\tau k_A\Big(\tau\left(u+2\omega\right)k_B X_s^2-i\left(-i+u+2\omega\right)\left(u+2\omega+\left(-i+u+2\omega\right)\alpha_A-i\tau k_B\alpha_B\right)+$$
$$X_s\left(u+i u^2+2\omega+4 i u\omega+4 i\omega^2-\tau k_B\left(u+2\omega+\left(-i+u+2\omega\right)\alpha_A-\left(-i+u+2\omega\right)\alpha_B\right)\right)\Big)\Big)$$

$$G_{xxz3}[\omega,\omega,u] \to$$
$$\Big(\tau k_B X_s\left(\left(u+i u^2+4 i u\omega+2\left(1+2 i \omega\right)\omega\right)\left(G_{xz2}[\omega,u]H_{x1}[\omega]+G_{z1}[u]H_{xx2}[\omega,\omega]+G_{x1}[\omega]H_{xz2}[\omega,u]+G_{xx2}[\omega,\omega]H_{z1}[u]\right)+\tau k_A\left(-\left(-i+u+2\omega\right)\alpha_A\left(F_{xz2}[\omega,u]H_{x1}[\omega]-G_{xz2}[\omega,u]H_{x1}[\omega]+F_{z1}[u]H_{xx2}[\omega,\omega]-G_{z1}[u]H_{xx2}[\omega,\omega]+F_{x1}[\omega]H_{xz2}[\omega,u]-\right.\right.\right.$$
$$\left.\left.\left.G_{x1}[\omega]H_{xz2}[\omega,u]+F_{xx2}[\omega,\omega]H_{z1}[u]-G_{xx2}[\omega,\omega]H_{z1}[u]\right)-\left(u+2\omega\right)\left(-1+X_s\right)\left(G_{xz2}[\omega,u]H_{x1}[\omega]+G_{z1}[u]H_{xx2}[\omega,\omega]+G_{x1}[\omega]H_{xz2}[\omega,u]+G_{xx2}[\omega,\omega]H_{z1}[u]\right)\right)\right)\Big)\Big/\Big(\left(-i+u+2\omega\right)$$
$$\left(u^2+2\omega\left(-i+2\omega\right)+u\left(-i+4\omega\right)-i\tau k_B\left(\left(u+2\omega\right)X_s+\left(-i+u+2\omega\right)\alpha_B\right)\right)+\tau k_A\left(\tau\left(u+2\omega\right)k_B X_s^2-i\left(-i+u+2\omega\right)\left(u+2\omega+\left(-i+u+2\omega\right)\alpha_A-i\tau k_B\alpha_B\right)+X_s\left(u+i u^2+2\omega+4 i u\omega+4 i\omega^2-\tau k_B\left(u+2\omega+\left(-i+u+2\omega\right)\alpha_A-\left(-i+u+2\omega\right)\alpha_B\right)\right)\right)\Big)$$

$$H_{xxz3}[\omega,\omega,u] \to \left(\tau\left(-i+u+2\omega\right)\left(\left(1+i u+2 i\omega\right)k_B\alpha_B\left(G_{xz2}[\omega,u]H_{x1}[\omega]+G_{z1}[u]H_{xx2}[\omega,\omega]+G_{x1}[\omega]H_{xz2}[\omega,u]+G_{xx2}[\omega,\omega]H_{z1}[u]\right)+\right.\right.$$
$$k_A\left(\left(1+i u+2 i\omega+\tau k_B X_s\right)\alpha_A\left(F_{xz2}[\omega,u]H_{x1}[\omega]+F_{z1}[u]H_{xx2}[\omega,\omega]+F_{x1}[\omega]H_{xz2}[\omega,u]+F_{xx2}[\omega,\omega]H_{z1}[u]\right)-\tau k_B\left(-1+X_s\right)\alpha_B\left(G_{xz2}[\omega,u]H_{x1}[\omega]+G_{z1}[u]H_{xx2}[\omega,\omega]+G_{x1}[\omega]H_{xz2}[\omega,u]+G_{xx2}[\omega,\omega]H_{z1}[u]\right)\right)\Big)\Big/\Big(\left(-i+u+2\omega\right)$$
$$\left(u^2+2\omega\left(-i+2\omega\right)+u\left(-i+4\omega\right)-i\tau k_B\left(\left(u+2\omega\right)X_s+\left(-i+u+2\omega\right)\alpha_B\right)\right)+\tau k_A\left(\tau\left(u+2\omega\right)k_B X_s^2-i\left(-i+u+2\omega\right)\left(u+2\omega+\left(-i+u+2\omega\right)\alpha_A-i\tau k_B\alpha_B\right)+X_s\left(u+i u^2+2\omega+4 i u\omega+4 i\omega^2-\tau k_B\left(u+2\omega+\left(-i+u+2\omega\right)\alpha_A-\left(-i+u+2\omega\right)\alpha_B\right)\right)\right)\Big)$$

$$F_{xzz3}[\omega, u, u] \to -\Big(\big(\tau\, k_A X_s \big(\big(2u + 4\,i\,u^2 + \omega + 4\,i\,u\,\omega + i\,\omega^2 + \tau\, k_B\,((2u+\omega)\,X_s + (-i+2u+\omega)\,\alpha_B)\big)\,F_{zz2}[u,u]\,H_{x1}[\omega] + \big(2u + 4\,i\,u^2 + \omega + 4\,i\,u\,\omega + i\,\omega^2\big)\,(F_{z1}[u]\,H_{xz2}[\omega,u] + F_{xz2}[\omega,u]\,H_{z1}[u] + F_{x1}[\omega]\,H_{zz2}[u,u]) + \tau\, k_B\,((2u+\omega)\,X_s\,(F_{z1}[u]\,H_{xz2}[\omega,u] + F_{xz2}[\omega,u]\,H_{z1}[u] + F_{x1}[\omega]\,H_{zz2}[u,u]) - (-i+2u+\omega)\,\alpha_B\,(G_{zz2}[u,u]\,H_{x1}[\omega] - F_{z1}[u]\,H_{xz2}[\omega,u] + G_{z1}[u]\,H_{xz2}[\omega,u] - F_{xz2}[\omega,u]\,H_{z1}[u] + G_{xz2}[\omega,u]\,H_{z1}[u] - F_{x1}[\omega]\,H_{zz2}[u,u] + G_{x1}[\omega]\,H_{zz2}[u,u]))\big)\big)\Big/\Big((-i+2u+\omega)\,\big(4u^2 + \omega\,(-i+\omega) + u\,(-2i+4\omega) - i\,\tau\, k_B\,((2u+\omega)\,X_s + (-i+2u+\omega)\,\alpha_B)\big) + \tau\, k_A\,\big(\tau\,(2u+\omega)\,k_B\,X_s^2 - i\,(-i+2u+\omega)\,(2u+\omega+(-i+2u+\omega)\,\alpha_A - i\,\tau\, k_B\,\alpha_B) + X_s\,\big(2u + 4\,i\,u^2 + \omega + 4\,i\,u\,\omega + i\,\omega^2 - \tau\, k_B\,(2u+\omega+(-i+2u+\omega)\,\alpha_A - (-i+2u+\omega)\,\alpha_B)\big)\big)\big)\Big)$$

$$G_{xzz3}[\omega, u, u] \to \big(\tau\, k_B\, X_s\,\big(\big(2u + 4\,i\,u^2 + \omega + 4\,i\,u\,\omega + i\,\omega^2\big)\,(G_{zz2}[u,u]\,H_{x1}[\omega] + G_{z1}[u]\,H_{xz2}[\omega,u] + G_{xz2}[\omega,u]\,H_{z1}[u] + G_{x1}[\omega]\,H_{zz2}[u,u]) + \tau\, k_A\,(-(-i+2u+\omega)\,\alpha_A\,(F_{zz2}[u,u]\,H_{x1}[\omega] - G_{zz2}[u,u]\,H_{x1}[\omega] + F_{z1}[u]\,H_{xz2}[\omega,u] - G_{z1}[u]\,H_{xz2}[\omega,u] + F_{xz2}[\omega,u]\,H_{z1}[u] - G_{xz2}[\omega,u]\,H_{z1}[u] + F_{x1}[\omega]\,H_{zz2}[u,u] - G_{x1}[\omega]\,H_{zz2}[u,u]) - (2u+\omega)\,(-1+X_s)\,(G_{zz2}[u,u]\,H_{x1}[\omega] + G_{z1}[u]\,H_{xz2}[\omega,u] + G_{xz2}[\omega,u]\,H_{z1}[u] + G_{x1}[\omega]\,H_{zz2}[u,u]))\big)\big)\Big/\Big((-i+2u+\omega)\,\big(4u^2 + \omega\,(-i+\omega) + u\,(-2i+4\omega) - i\,\tau\, k_B\,((2u+\omega)\,X_s + (-i+2u+\omega)\,\alpha_B)\big) + \tau\, k_A\,\big(\tau\,(2u+\omega)\,k_B\,X_s^2 - i\,(-i+2u+\omega)\,(2u+\omega+(-i+2u+\omega)\,\alpha_A - i\,\tau\, k_B\,\alpha_B) + X_s\,\big(2u + 4\,i\,u^2 + \omega + 4\,i\,u\,\omega + i\,\omega^2 - \tau\, k_B\,(2u+\omega+(-i+2u+\omega)\,\alpha_A - (-i+2u+\omega)\,\alpha_B)\big)\big)\Big)$$

$$H_{xzz3}[\omega, u, u] \to (\tau\,(-i+2u+\omega)\,((1+2\,i\,u+i\,\omega)\,k_B\,\alpha_B\,(G_{zz2}[u,u]\,H_{x1}[\omega] + G_{z1}[u]\,H_{xz2}[\omega,u] + G_{xz2}[\omega,u]\,H_{z1}[u] + G_{x1}[\omega]\,H_{zz2}[u,u]) + k_A\,((1+2\,i\,u+i\,\omega+\tau\, k_B\, X_s)\,\alpha_A\,(F_{zz2}[u,u]\,H_{x1}[\omega] + F_{z1}[u]\,H_{xz2}[\omega,u] + F_{xz2}[\omega,u]\,H_{z1}[u] + F_{x1}[\omega]\,H_{zz2}[u,u]) - \tau\, k_B\,(-1+X_s)\,\alpha_B\,(G_{zz2}[u,u]\,H_{x1}[\omega] + G_{z1}[u]\,H_{xz2}[\omega,u] + G_{xz2}[\omega,u]\,H_{z1}[u] + G_{x1}[\omega]\,H_{zz2}[u,u])))\Big/\Big((-i+2u+\omega)\,\big(4u^2 + \omega\,(-i+\omega) + u\,(-2i+4\omega) - i\,\tau\, k_B\,((2u+\omega)\,X_s + (-i+2u+\omega)\,\alpha_B)\big) + \tau\, k_A\,\big(\tau\,(2u+\omega)\,k_B\,X_s^2 - i\,(-i+2u+\omega)\,(2u+\omega+(-i+2u+\omega)\,\alpha_A - i\,\tau\, k_B\,\alpha_B) + X_s\,\big(2u + 4\,i\,u^2 + \omega + 4\,i\,u\,\omega + i\,\omega^2 - \tau\, k_B\,(2u+\omega+(-i+2u+\omega)\,\alpha_A - (-i+2u+\omega)\,\alpha_B)\big)\big)\Big)$$

$$F_{xxz3}[\omega, \omega, -u] \to -\Big(\big(\tau\, k_A X_s\,\big(\big(u - i\,u^2 + 4\,i\,u\,\omega + 2\,(-1-2\,i\,\omega)\,\omega + \tau\, k_B\,((u-2\omega)\,X_s + (i+u-2\omega)\,\alpha_B)\big)\,F_{xz2}[\omega,-u]\,H_{x1}[\omega] + \big(u - i\,u^2 + 4\,i\,u\,\omega + 2\,(-1-2\,i\,\omega)\,\omega\big)\,(F_{z1}[-u]\,H_{xx2}[\omega,\omega] + F_{x1}[\omega]\,H_{xz2}[\omega,-u] + F_{xx2}[\omega,\omega]\,H_{z1}[-u]) + \tau\, k_B\,((u-2\omega)\,X_s\,(F_{z1}[-u]\,H_{xx2}[\omega,\omega] + F_{x1}[\omega]\,H_{xz2}[\omega,-u] + F_{xx2}[\omega,\omega]\,H_{z1}[-u]) - (i+u-2\omega)\,\alpha_B\,(G_{xz2}[\omega,-u]\,H_{x1}[\omega] - F_{z1}[-u]\,H_{xx2}[\omega,\omega] + G_{z1}[-u]\,H_{xx2}[\omega,\omega] - F_{x1}[\omega]\,H_{xz2}[\omega,-u] + G_{x1}[\omega]\,H_{xz2}[\omega,-u] - F_{xx2}[\omega,\omega]\,H_{z1}[-u] + G_{xx2}[\omega,\omega]\,H_{z1}[-u]))\big)\big)\Big/\Big((i+u-2\omega)\,\big(u^2 + u\,(i-4\omega) + 2\,\omega\,(-i+2\omega) + i\,\tau\, k_B\,((u-2\omega)\,X_s + (i+u-2\omega)\,\alpha_B)\big) + \tau\, k_A\,\big(\tau\,(u-2\omega)\,k_B\,X_s^2 + i\,(i+u-2\omega)\,(u-2\omega+(i+u-2\omega)\,\alpha_A + i\,\tau\, k_B\,\alpha_B) + X_s\,\big(u - i\,u^2 - 2\,\omega + 4\,i\,u\,\omega - 4\,i\,\omega^2 - \tau\, k_B\,(u-2\omega+(i+u-2\omega)\,\alpha_A - (i+u-2\omega)\,\alpha_B)\big)\big)\Big)$$

$$G_{xxz3}[\omega, \omega, -u] \to \big(\tau\, k_B\, X_s\,\big(\big(u - i\,u^2 + 4\,i\,u\,\omega + 2\,(-1-2\,i\,\omega)\,\omega\big)\,(G_{xz2}[\omega,-u]\,H_{x1}[\omega] + G_{z1}[-u]\,H_{xx2}[\omega,\omega] + G_{x1}[\omega]\,H_{xz2}[\omega,-u] + G_{xx2}[\omega,\omega]\,H_{z1}[-u]) + \tau\, k_A\,(-(i+u-2\omega)\,\alpha_A\,(F_{xz2}[\omega,-u]\,H_{x1}[\omega] - G_{xz2}[\omega,-u]\,H_{x1}[\omega] + F_{z1}[-u]\,H_{xx2}[\omega,\omega] - G_{z1}[-u]\,H_{xx2}[\omega,\omega] + F_{x1}[\omega]\,H_{xz2}[\omega,-u] - G_{x1}[\omega]\,H_{xz2}[\omega,-u] + F_{xx2}[\omega,\omega]\,H_{z1}[-u] - G_{xx2}[\omega,\omega]\,H_{z1}[-u]) - (u-2\omega)\,(-1+X_s)\,(G_{xz2}[\omega,-u]\,H_{x1}[\omega] + G_{z1}[-u]\,H_{xx2}[\omega,\omega] + G_{x1}[\omega]\,H_{xz2}[\omega,-u] + G_{xx2}[\omega,\omega]\,H_{z1}[-u]))\big)\big)\Big/\Big((i+u-2\omega)\,\big(u^2 + u\,(i-4\omega) + 2\,\omega\,(-i+2\omega) + i\,\tau\, k_B\,((u-2\omega)\,X_s + (i+u-2\omega)\,\alpha_B)\big) + \tau\, k_A\,\big(\tau\,(u-2\omega)\,k_B\,X_s^2 + i\,(i+u-2\omega)\,(u-2\omega+(i+u-2\omega)\,\alpha_A + i\,\tau\, k_B\,\alpha_B) + X_s\,\big(u - i\,u^2 - 2\,\omega + 4\,i\,u\,\omega - 4\,i\,\omega^2 - \tau\, k_B\,(u-2\omega+(i+u-2\omega)\,\alpha_A - (i+u-2\omega)\,\alpha_B)\big)\big)\Big)$$

$$H_{xxz3}[\omega, \omega, -u] \to -\Big((i\,\tau\,(i+u-2\omega)\,((i+u-2\omega)\,k_B\,\alpha_B\,(G_{xz2}[\omega,-u]\,H_{x1}[\omega] + G_{z1}[-u]\,H_{xx2}[\omega,\omega] + G_{x1}[\omega]\,H_{xz2}[\omega,-u] + G_{xx2}[\omega,\omega]\,H_{z1}[-u]) + k_A\,((i+u-2\omega+i\,\tau\, k_B\, X_s)\,\alpha_A\,(F_{xz2}[\omega,-u]\,H_{x1}[\omega] + F_{z1}[-u]\,H_{xx2}[\omega,\omega] + F_{x1}[\omega]\,H_{xz2}[\omega,-u] + F_{xz2}[\omega,\omega]\,H_{z1}[-u]) - i\,\tau\, k_B\,(-1+X_s)\,\alpha_B\,(G_{xz2}[\omega,-u]\,H_{x1}[\omega] + G_{z1}[-u]\,H_{xx2}[\omega,\omega] + G_{x1}[\omega]\,H_{xz2}[\omega,-u] + G_{xz2}[\omega,\omega]\,H_{z1}[-u])))\Big/\Big((i+u-2\omega)\,\big(u^2 + u\,(i-4\omega) + 2\,\omega\,(-i+2\omega) + i\,\tau\, k_B\,((u-2\omega)\,X_s + (i+u-2\omega)\,\alpha_B)\big) + \tau\, k_A\,\big(\tau\,(u-2\omega)\,k_B\,X_s^2 + i\,(i+u-2\omega)\,(u-2\omega+(i+u-2\omega)\,\alpha_A + i\,\tau\, k_B\,\alpha_B) + X_s\,\big(u - i\,u^2 - 2\,\omega + 4\,i\,u\,\omega - 4\,i\,\omega^2 - \tau\, k_B\,(u-2\omega+(i+u-2\omega)\,\alpha_A - (i+u-2\omega)\,\alpha_B)\big)\big)\Big)$$

$$F_{xzz3}[-\omega, u, u] \to -\Big(\big(\tau\, k_A X_s\,\big(\big(4\,i\,u^2 + u\,(2-4\,i\,\omega) + i\,\omega\,(i+\omega) + \tau\, k_B\,((2u-\omega)\,X_s + (-i+2u-\omega)\,\alpha_B)\big)\,F_{zz2}[u,u]\,H_{x1}[-\omega] + i\,\big(4u^2 + \omega\,(i+\omega) - 2u\,(i+2\omega)\big)\,(F_{z1}[u]\,H_{xz2}[-\omega,u] + F_{xz2}[-\omega,u]\,H_{z1}[u] + F_{x1}[-\omega]\,H_{zz2}[u,u]) + \tau\, k_B\,((2u-\omega)\,X_s\,(F_{z1}[u]\,H_{xz2}[-\omega,u] + F_{xz2}[-\omega,u]\,H_{z1}[u] + F_{x1}[-\omega]\,H_{zz2}[u,u]) - (-i+2u-\omega)\,\alpha_B\,(G_{zz2}[u,u]\,H_{x1}[-\omega] - F_{z1}[u]\,H_{xz2}[-\omega,u] + G_{z1}[u]\,H_{xz2}[-\omega,u] - F_{xz2}[-\omega,u]\,H_{z1}[u] + G_{xz2}[-\omega,u]\,H_{z1}[u] - F_{x1}[-\omega]\,H_{zz2}[u,u] + G_{x1}[-\omega]\,H_{zz2}[u,u]))\big)\big)\Big/\Big((-i+2u-\omega)\,\big(4u^2 + \omega\,(i+\omega) - 2u\,(i+2\omega) - i\,\tau\, k_B\,((2u-\omega)\,X_s + (-i+2u-\omega)\,\alpha_B)\big) + \tau\, k_A\,\big(\tau\,(2u-\omega)\,k_B\,X_s^2 - i\,(-i+2u-\omega)\,(2u-\omega+(-i+2u-\omega)\,\alpha_A - i\,\tau\, k_B\,\alpha_B) + X_s\,\big(2u + 4\,i\,u^2 - \omega - 4\,i\,u\,\omega + i\,\omega^2 + \tau\, k_B\,(-2u+\omega+(i-2u+\omega)\,\alpha_A + (-i+2u-\omega)\,\alpha_B)\big)\big)\Big)$$

$$G_{xzz3}[-\omega, u, u] \to \big(\tau\, k_B\, X_s\,\big(i\,\big(4u^2 + \omega\,(i+\omega) - 2u\,(i+2\omega)\big)\,(G_{zz2}[u,u]\,H_{x1}[-\omega] + G_{z1}[u]\,H_{xz2}[-\omega,u] + G_{xz2}[-\omega,u]\,H_{z1}[u] + G_{x1}[-\omega]\,H_{zz2}[u,u]) + \tau\, k_A\,(-(-i+2u-\omega)\,\alpha_A\,(F_{zz2}[u,u]\,H_{x1}[-\omega] - G_{zz2}[u,u]\,H_{x1}[-\omega] + F_{z1}[u]\,H_{xz2}[-\omega,u] - G_{z1}[u]\,H_{xz2}[-\omega,u] + F_{xz2}[-\omega,u]\,H_{z1}[u] - G_{xz2}[-\omega,u]\,H_{z1}[u] + F_{x1}[-\omega]\,H_{zz2}[u,u] - G_{x1}[-\omega]\,H_{zz2}[u,u]) - (2u-\omega)\,(-1+X_s)\,(G_{zz2}[u,u]\,H_{x1}[-\omega] + G_{z1}[u]\,H_{xz2}[-\omega,u] + G_{xz2}[-\omega,u]\,H_{z1}[u] + G_{x1}[-\omega]\,H_{zz2}[u,u]))\big)\big)\Big/\Big((-i+2u-\omega)\,\big(4u^2 + \omega\,(i+\omega) - 2u\,(i+2\omega) - i\,\tau\, k_B\,((2u-\omega)\,X_s + (-i+2u-\omega)\,\alpha_B)\big) + \tau\, k_A\,\big(\tau\,(2u-\omega)\,k_B\,X_s^2 - i\,(-i+2u-\omega)\,(2u-\omega+(-i+2u-\omega)\,\alpha_A - i\,\tau\, k_B\,\alpha_B) + X_s\,\big(2u + 4\,i\,u^2 - \omega - 4\,i\,u\,\omega + i\,\omega^2 + \tau\, k_B\,(-2u+\omega+(i-2u+\omega)\,\alpha_A + (-i+2u-\omega)\,\alpha_B)\big)\big)\Big)$$

$$H_{xzz3}[-\omega, u, u] \to (i\,\tau\,(-i+2u-\omega)\,((-i+2u-\omega)\,k_B\,\alpha_B\,(G_{zz2}[u,u]\,H_{x1}[-\omega] + G_{z1}[u]\,H_{xz2}[-\omega,u] + G_{xz2}[-\omega,u]\,H_{z1}[u] + G_{x1}[-\omega]\,H_{zz2}[u,u]) + k_A\,((-i+2u-\omega+i\,\tau\, k_B\, X_s)\,\alpha_A\,(F_{zz2}[u,u]\,H_{x1}[-\omega] + F_{z1}[u]\,H_{xz2}[-\omega,u] + F_{xz2}[-\omega,u]\,H_{z1}[u] + F_{x1}[-\omega]\,H_{zz2}[u,u]) + i\,\tau\, k_B\,(-1+X_s)\,\alpha_B\,(G_{zz2}[u,u]\,H_{x1}[-\omega] + G_{z1}[u]\,H_{xz2}[-\omega,u] + G_{xz2}[-\omega,u]\,H_{z1}[u] + G_{x1}[-\omega]\,H_{zz2}[u,u])))\Big/\Big((-i+2u-\omega)\,\big(4u^2 + \omega\,(i+\omega) - 2u\,(i+2\omega) - i\,\tau\, k_B\,((2u-\omega)\,X_s + (-i+2u-\omega)\,\alpha_B)\big) + \tau\, k_A\,\big(\tau\,(2u-\omega)\,k_B\,X_s^2 - i\,(-i+2u-\omega)\,(2u-\omega+(-i+2u-\omega)\,\alpha_A - i\,\tau\, k_B\,\alpha_B) + X_s\,\big(2u + 4\,i\,u^2 - \omega - 4\,i\,u\,\omega + i\,\omega^2 + \tau\, k_B\,(-2u+\omega+(i-2u+\omega)\,\alpha_A + (-i+2u-\omega)\,\alpha_B)\big)\big)\Big)$$